POTENTIAL FACTORS RESPONSIBLE FOR DISCREPANCIES IN JET NOISE MEASUREMENTS OF DIFFERENT STUDIES

A Dissertation
Presented to
The Academic Faculty

by

Aharon Zamir Karon

In Partial Fulfillment
of the Requirements for the Degree
Doctor of Philosophy in the
School of Aerospace Engineering

Georgia Institute of Technology
August 2016

POTENTIAL FACTORS RESPONSIBLE FOR DISCREPANCIES IN JET NOISE MEASUREMENTS OF DIFFERENT STUDIES

Approved by:

Dr. Krishan K. Ahuja, Advisor
School of Aerospace Engineering
Georgia Institute of Technology

Dr. Joseph Gavin
Gulfstream Aerospace
Savannah, Ga

Dr. Jechiel Jagoda
School of Aerospace Engineering
Georgia Institute of Technology

Dr. Donald Nance
NASA Marshall
Huntsville, Alabama

Dr. Lakshmi Sankar
School of Aerospace Engineering
Georgia Institute of Technology

Date Approved: 8/16/2016

For my wife Olivia and daughter Emunah

ACKNOWLEDGEMENTS

I give thanks to Dr. Krishan Ahuja for his endless guidance and support during my Ph.D. effort. His dedication to his students and their work is something that all advisors should strive to model.

Thanks are also given to Dr. Jeff Jagoda, Dr. Lakshmi Sankar, Dr. Joseph Gavin, and Dr. Donald Nance for taking the time to read my thesis and serving on my committee. I also would like to thank GTRI-Aerospace, Transportation, and Advanced Systems Laboratory (ATAS) for use of its facilities for the purposes of this research. Thanks also to Dr. Robert Funk, Dr. Donald Nance, Dr. Alessio Medda, Mr. Russell Young, Mr. David Alvord, and Mr. Kyle Carnahan for their advice during my research. I would like to also to acknowledge my fellow Graduate Students, Mr. Nick Breen, Mr. Darryl Dickey, and Mr. Shane Lympany, for their help and support during this effort. Also, I would like to acknowledge many of the undergraduate students and interns who helped me during my research that include: Mr. Connor Ellis, Mr. Kevin Quach, Ms. Rose McCarty, and Ms. Stephanie Moon. I would like to specially acknowledge Mr. John Carrigan, for his help, his engineering skills, and his friendship. John passed away during my time at Georgia Tech and will be deeply missed.

I give the deepest thanks to my wife Olivia for her love and support during this high stress time in my life. I would also like to thank my parents, Martin and Marcia Karon, for their endless support.

Last, but certainly not least, I would like to thank G-D for the gifts He has given me that have allowed me to come to this point.

TABLE OF CONTENTS

LIST OF TABLES

LIST OF FIGURES

NOMENCLATURE

A	= nozzle-exit area
a	= speed of sound in the jet
a_i	= internal rig speed of sound
a_0	= ambient speed of sound
B_i	= systematic uncertainty of measurement i
D_j	= nozzle-exit diameter
f	= frequency
H	= boundary layer shape factor
He	= Helmholtz number
I	= intensity
I_{ref}	= reference intensity
L_{BM}	= distance between the baffle and microphone plane
L_{NB}	= distance between the nozzle-exit and the baffle
L_{SN}	= distance between the frequency source and nozzle
M_c	= convection Mach number (0.65 *Mj)
M_i	= internal rig Mach number
M_j	= jet Mach number
$\dot{m}$	= mass flow rate
OASPL	= Overall Sound Pressure Level
p_t	= total pressure
p_a	= ambient pressure
p_i	= rig internal static pressure
R	= distance from the nozzle-exit
Re_D	= Reynolds Number with respect to diameter
R_i	= random uncertainty of measurement i
$\bar{R}$	= specific gas constant for air
SPL	= Sound Pressure Level
St	= Strouhal number
T_i	= rig internal static temperature
T_j	= static temperature in jet
T_t	= total temperature
U_i	= internal velocity
U_j	= jet velocity
ΔSPL	= change of SPL
Γ	= coefficient in boundary layer curve fit
δ^*	= displacement thickness
θ	= polar angle with respect to the downstream axis
θ^*	= momentum thickness
Ψ	= incidence angle of soundwave to microphone
ϕ	= shielding angle in shielding code
γ	= ratio of specific heats
ρ	= static density
ρ_0	= ambient density
Ω	= exponent in boundary layer curve fit

SUMMARY

Over the years, many jet noise studies have been performed in anechoic jet-facilities around the world. Often, the jet noise measurements from studies that were thought to be identical based on the jet settings and nozzle selection turn out to have differences in the spectra. Many researchers have claimed to have explanations for these differences, which range from differences in jet initial conditions to accusations of rig-noise contamination in the jet-facility. This study attempts to resolve these differences in the jet noise measurements by investigating some of these claims.

First, the issue of rig-noise contamination is investigated. A method for detecting rig-noise contamination, known as the Doubling-Diameter Method is evaluated. A case study using the GTRI Anechoic Jet-Facility is run to show how the method can be used for rig-noise detection. The initial conditions of the jet in terms of Reynolds number and nozzle-exit boundary layer state are investigated to explore their effect on jet noise. The ducting in the vicinity of the jet nozzle, mainly the plenum chamber and a secondary nozzle used either as a flight simulation nozzle or to simulate the bypass flow, are examined to see how they can cause differences in the noise measurements, with these surfaces acting either reflectors or shields. Lastly, a simple computational method is used to predict the shielding effects from the plenum chamber on the jet noise.

There are four main contributions of this work to the field of jet noise:

1. it provides a methodology for evaluating the quality of jet noise measurements,

2. it investigates the role of the Reynolds number with respect to diameter and how it relates to the ability to scale the jet noise based on the nozzle-exit diameter,
3. it explores the role of the nozzle-exit boundary layer on jet noise, and
4. it helps design facilities for accurate jet-mixing noise measurements.

The third contribution appears to be quite critical in that it was found that the jet mixing noise is highly dependent on the boundary layer thickness. These results help explain the differences in the noise amplitudes of different jet noise studies, most of which failed to provide the character of the nozzle-exit boundary layer. In turn, it is recommended that in future publications on jet mixing noise, the researchers must attempt to document the nozzle-exit boundary layer state for their results to be of utmost use.

CHAPTER 1

INTRODUCTION

Over the years, jet noise measurements have been acquired in a large number of jet-facilities around the world. These data have formed a global database that has been used in developing jet mixing noise prediction schemes and to understand the physics behind the generation and radiation of jet noise. Based on the results of the Lighthill[1-3] acoustic analogy, all frequency spectra that are formed from jet noise microphone-measurements should be able to be normalized to the same spectrum. This is such that the frequencies are normalized to Strouhal numbers (or Helmholtz numbers at low polar angles) and the amplitude at each Strouhal number is normalized to the same level for every spectrum. This scheme can also be used to scale jet noise spectra from different tests to one another in order for researchers to make comparisons, as well as scale jet noise measurements from model-scale nozzles to full-scale jet engines, i.e., used as part of a prediction scheme. When the frequency spectra of jet noise measurements from different jet-facilities, which were acquired at or corrected to similar conditions, are compared, the published spectra often show some differences. One such comparison was conducted by Viswanathan[4, 5], which is shown in Figure 1.1, where he compared his jet noise measurements acquired in the Boeing Low Speed Aeroacoustic Facility to that acquired by Tanna[6] in the Lockheed Anechoic Jet-Facility (henceforth referred to as the "Tanna Jet Noise Database"), which is now run by Georgia Tech Research Institute (GTRI). Viswanathan[4, 5] found that the Tanna Jet Noise Database measurements had higher high-

frequency levels compared to his data. He showed that the spectral levels of many other researchers were also higher than those obtained by his experiments[4, 5]. He concluded that the Tanna Jet Noise Database as well as data of many other well-known jet noise researchers[7, 8] were contaminated by high-frequency rig-noise.

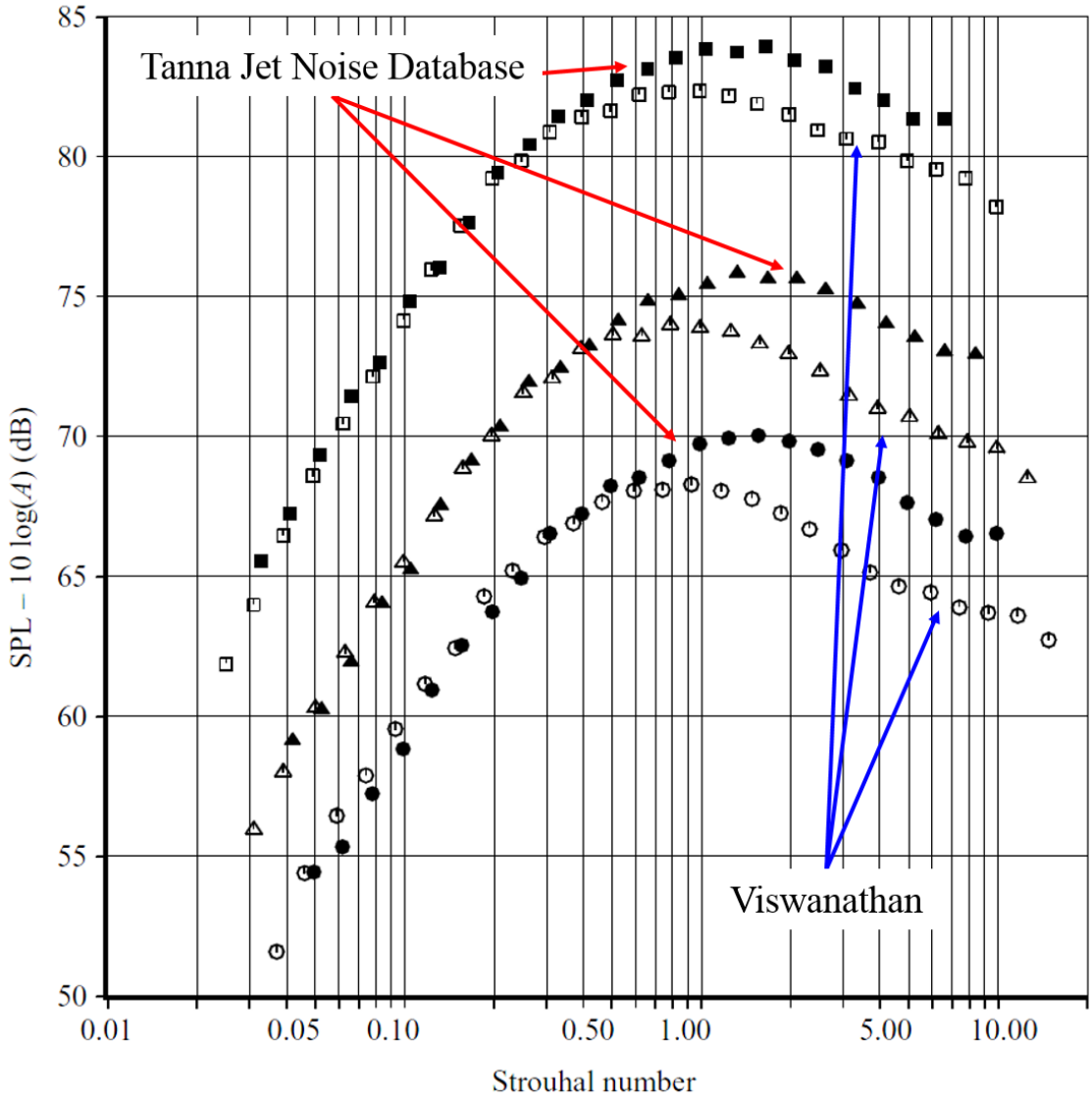

Figure 1.1: Comparison performed by Viswanathan[4] between his measurements and Tanna Jet Noise Database. Filled Symbols: Tanna, Open Symbols: Viswanathan. Circles: M = 0.62, Triangles: M = 0.74, Squares: M = 0.98.

This claim by Viswnathan in a number of his publications[4, 5, 9] has understandably generated a good amount of discussion at various aeroacoustics conferences and workshops over the last ten years. As the Tanna Jet Noise Database was acquired in the facility that is currently used by GTRI researchers, including the present author for this thesis, this claim was of concern to GTRI as well. The current thinking is that when comparing jet noise data from one facility to another, no account is taken of many factors that are typically different in different facilities. This includes the effects of, upstream turbulence in the main flow, the Reynolds number of the jet, the nozzle-exit boundary layer state of the jet, potential reflections from plenum chambers and other acoustically untreated structures inside of the jet-facility, and possible shielding by plenum chambers of measurements acquired in the forward arc. Another factor that has been of some debate for a while is the requirement that all jet noise data must be measured in the true geometric far-field[10, 11], which ensures that the whole jet can be treated as a point sound source so that data of different facilities can be extrapolated to the same distance by using the inverse square law applied to a distance between the microphone and the center of the nozzle-exit , a common practice when comparing jet noise of various investigators acquired at different distances.

Harper-Bourne[12] rejected Viswanathan's claim that others' data was contaminated with jet-rig-noise and argued that the noted differences had to be due to the jet initial conditions (nozzle-exit conditions). Harper-Bourne[12] explained that typical university-style anechoic jet-facilities (such as the GTRI Anechoic Jet-Facility) tend to have initial conditions that may create a uniform, laminar jet-flow. This flow state tends to be the product of a large contraction ratio between the plenum chambers and the jet nozzle. In addition, most university-style anechoic jet-facilities use nozzles that are built using the

design specifications of the American Society of Mechanical Engineers (these are referred to as ASME nozzles and are described in detail in Chapter 5), and these nozzles tend be smaller more compact nozzles, which is desirable given university-style anechoic jet-facilities tend to be smaller in size. Industrial size anechoic jet-facilities may have more turbulent initial conditions due to the larger size nozzles and smaller rig contraction-ratios. These nozzle-exit conditions can affect the jet flow development as the jet exhausts from the nozzle, and ultimately affect the overall noise measured at a farfield microphone.

Existing jet noise studies on the role of nozzle-exit boundary layer and other factors, such as Reynolds number, have been mainly qualitative in nature[13-19]; leading to little quantitative guidelines of how these factors affect the jet noise spectrum. A better understanding of both the effects the Reynolds number and nozzle-exit boundary layer state will bring reconciliation to the differences between jet noise measurements from different facilities, as the nozzle-exit flow state of each facility can be different in terms of Reynolds number, turbulence intensity, boundary layer displacement thickness, boundary layer momentum thickness, and boundary layer shape factor.

Additionally, a typical jet rig has a number of surfaces in the vicinity of the jet-exit. This includes the nozzle itself, the plenum chamber and associated flanges, and the air supply ducts. The region in the vicinity of jet-exit (referred to here as "surroundings") in each facility are often quite different from the perspective of possible contamination of the measured spectra by acoustic reflections, diffraction, scattering, or shielding by surfaces in the vicinity of the nozzle. The varying degree of geometrical details and acoustic treatment of many of these surfaces in different facilities can understandably cause differences in the measured spectra. All jet-facilities have a plenum (a large air reservoir) that supplies clean

air to the nozzle. If the plenum structure is inside the anechoic chamber and is rather large, which is common in multi-stream facilities, the plenum structure can act as shield for the microphones in the forward arc. Surfaces that are not acoustically treated can reflect, diffract and scatter the sound produced from the jet, and cause the microphones to not record clean jet noise. As the high-frequency jet noise is produced close to the nozzle-exit, the high-frequency noise will be particularly prone to reflections from the nozzle-surface if not covered and to shielding in the forward arc if the plenum chamber partially blocks the sound. Reflections could cause interference at different frequencies, and depending on the phase relationship could cause cancellation or amplification of the noise measured at the microphone (this will be explained in detail in Chapter 6). Diffraction and scattering by plenum chamber flanges and other surfaces can change the spectral shape of the measured spectrum.

The overall objective of the proposed study is to understand what makes jet noise spectra measured from different test facilities to be different. The study has four well-defined objectives, which deal with determining the roles of the following four factors on the jet noise spectra measured in an anechoic jet-facility:

1. Rig-noise contamination
2. Reynolds number of the jet
3. Nozzle-exit boundary layer
4. Acoustically untreated surfaces inside jet-facility

The first objective of the study is to verify that a method to determine the existence of rig-noise contamination in an anechoic jet-facility will accurately detect this contamination. This method will be used on jet noise acquired in the GTRI Anechoic Jet-

Facility as a case study to check the claims made by Viswnathan[4, 5, 9]. This claim must be investigated before any new jet noise measurements can be considered clean, and if noise-contamination is discovered, the problem must be addressed. This will be accomplished using the known jet noise scaling laws (described in Chapter 3).

The second objective is to explore the role of the Reynolds number on the jet noise frequency spectrum. This will be performed by measuring the jet noise generated from jets issuing from nozzles of varying diameters with varying jet velocities. The change in nozzle-exit diameters and jet velocities will ultimately change the Reynolds number. The Reynolds number will be varied between 5000 and 100000. Comparing the jet noise spectra from the jets generated from each nozzle and velocity after accounting for jet mixing noise dependence on jet-diameter, velocity, and the other important flow parameters will reveal how the Reynolds number affects jet noise.

The third objective of this effort is to study how the state of the nozzle-exit boundary layer affects jet noise. A number of studies, such as those conducted by Viswanathan and Clark[15] and Zaman[16], have shown that the state of the nozzle-exit boundary layer can have an effect on high-frequency jet noise. Therefore, a more exhaustive study into this factor can potentially shed some light on the differences seen by Viswanathan[4]. Jet noise measurements and nozzle-exit velocity measurements will be acquired to show how nozzle-exit boundary layer state affects different aspects of the jet noise spectrum, such as peak noise, overall sound pressure level (OASPL) and high-frequency noise.

The fourth and final objective is to examine the effects of the acoustically untreated surfaces inside of an anechoic jet-facility. Untreated surfaces near the jet nozzle, i.e., the

nozzle's surroundings, which include the plenum chamber front surface, will be examined as to their effect on jet noise measurement in terms of acting as both a reflector and a shield.

The results of this experimental program will help resolve the observed discrepancies between jet noise measured in different facilities for similar jet operating conditions. The results of this study will also enhance our understanding of how rig-noise and the jet surroundings can affect jet noise measurements. In addition, there will be a greater understanding of the effect of Reynolds number and initial conditions, in terms of the nozzle-exit boundary layer's displacement thickness, momentum thickness and shape factor, on the jet noise spectrum, as well as on the flow features of the jet. This will also provide benchmark jet noise data for validating computational aeroacoustics techniques for predicting jet mixing noise where appropriate account has been taken of the initial boundary conditions.

As the reader can see from the objectives listed above, the topics covered in this document are quite varied. In order to assist the reader, each topic is restricted to its own chapter. Thus, for each topic, a literature review, a description of the experimental facilities, a description of the experimentation, the results, and a brief conclusions section will be presented in the chapter about that topic. This is done so all the important information about a given topic is contained within the individual chapter. An overall summary of the literature review for each topic is first provided in Chapter 2. This is then followed by a detailed description of the prior the studies of the four topics described above in Chapters 3 – 6, respectively. In Chapter 7, the uncertainty analysis of the measurements that the calculations using those measurements is presented. Finally, in Chapter 8 the

conclusions of this study are stated. Suggestions for future research are also provided in the same chapter.

It should be mentioned here that the experiments described here were restricted to subsonic jet exit Mach numbers. As such, additional work would be required to extend the conclusions to the supersonic regime.

CHAPTER 2

OVERALL SUMMARY OF THE LITERATURE REVIEW

As stated at the end of Chapter 1, this research study is composed of four separate topics that relate to factors making jet noise spectra measured from different test facilities to be different. Because of the varying nature of these four topics, a separate chapter is dedicated to each topic. Within each of these chapters, there is a section devoted to an extensive literature review related to the chapter's topic. This is expected to allow the reader to more readily recall important information for a particular research topic. This chapter, provides a brief review of some of the basics of jet noise theory. A short summary of the literature review on each topic is also provided for which the details appear in each respective chapter.

2.1 The Lighthill Acoustic Analogy

In 1952, the first jet noise theory was developed by Lighthill[1-3] in the form of the acoustic analogy. This theory was created by combining the exact continuity and momentum equations and rearranging them to separate the linear propagation terms and the nonlinear source terms. Using this methodology, Lighthill created an acoustic analogy of the form:

$$\frac{\partial^2 \rho}{\partial t^2} - a_0^2 \frac{\partial^2 \rho}{\partial x_i^2} = \frac{\partial^2 T_{ij}}{\partial x_i \partial x_j} \tag{2.1}$$

where, the left-hand side of Equation 2.1 contains the propagation terms and the right-hand side contains the source terms, and T_{ij} is the Reynolds stress tensor, which is given by:

$$T_{ij} = \rho v_i v_j + p_{ij} - a_0^2 \rho \delta_{ij} \tag{2.2}$$

In Equations 2.1 and 2.2, ρ is the density, a_0 is the ambient speed of sound, v is the velocity, p_{ij} is the compressive stress tensor and δ_{ij} is the Kronecker delta. This theory initiated the field of aeroacoustics and was the first theory that had the potential of predicting jet noise. Others followed in Lighthill's footsteps and improved upon the theory or created their own acoustic analogies following the same methodology, but adding effects for which the original theory did not account. Proudman[20], Ribner[21], FFowcs-Williams[22], Lilley[23], Doak[24], Goldstein and Rosenbaum[25], and many others helped shape the acoustic analogy into a powerful theory. One of the major results of the acoustic analogy theory is the jet noise intensity scaling relationship:

$$I \sim \frac{\rho_m^2}{\rho_0}\frac{U_j^8}{a_0^5}\frac{D_j^2}{R^2}\,(1 - M_c\cos(\theta))^{-5} \tag{2.3}$$

where, ρ_m is the density of the jet mixing layer, ρ_0 is the ambient density, U_j is the jet velocity, a_0 is the ambient speed of sound, D_j is the nozzle-exit diameter, R is the distance between the nozzle-exit the measurement location, M_c is the convection Mach number (typically assumed to be $0.65M_j$, the jet Mach number), and θ is the polar angle (in this study this angle is measured with respect to the downstream jet axis). The jet noise intensity relation in Equation 2.3 has been the source for the jet noise scaling relationship and prediction schemes that continue to be used today.

For this scaling relationship to apply to jet noise measurements, these measurements must be acquired by microphones in the geometric farfield. The geometric farfield of a jet is considered to be the microphone distance from the nozzle-exit center where the whole jet can be considered to be a point source located at the nozzle-exit center and where the measured noise follows the Inverse Square Law. Given that jet noise is a distributed source that generates broadband noise, each frequency has a different distance

where it enters the farfield. Ahuja, Milway, and Churney[11] showed for frequencies of interest this distance is a minimum of 50 nozzle-exit diameters.

2.2 Tam's Two Source Model

In 1971, Champaign and Crow[26] discovered coherent large-scale turbulence structures inside of the jet shear-layer. As turbulence has always been considered the sound source of jet noise, this changed the physical model used by Lighthill[1-3] in his acoustic analogy, which did not account for the difference between small-scale turbulence and the coherent large-scale turbulence, and therefore the sound source. Based on this new physical understanding, Tam et al.[27-29] developed the so-called two-source model. This model is illustrated in Figure 2.1. As seen in Figure 2.1, Tam et al.[27-29] showed that the coherent large-scale structures radiate sound in the downstream direction in the form of Mach waves and the random small-scale turbulence radiates sound primarily in the sideline direction. Tam et al.[27-29] developed similarity spectra for the noise generated by the coherent large-scale turbulence and the random small-scale turbulence, and these are shown in Figure 2.2. These similarity spectra can be used to predict jet noise by combining them based on the dominance of small-scale turbulence noise versus large-scale turbulence noise and the physical state of the jet, i.e., nozzle diameter, jet velocity, etc. One can see

that the small-scale turbulence generates a broader frequency spectrum than the large-scale turbulence.

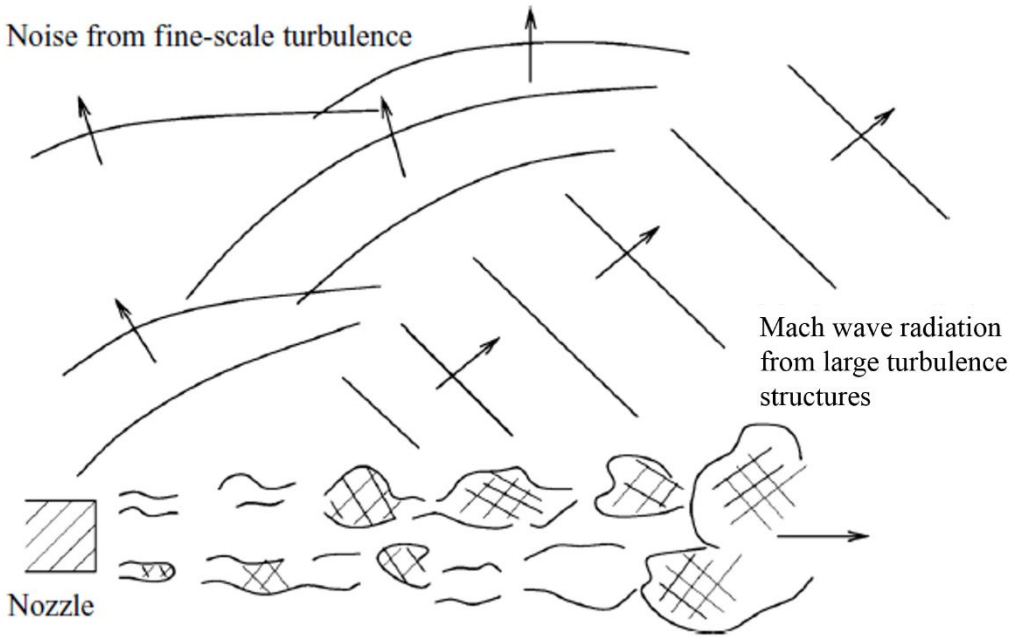

Figure 2.1: Physical model of Tam's two source model, which is reproduced from Tam et al.[30]

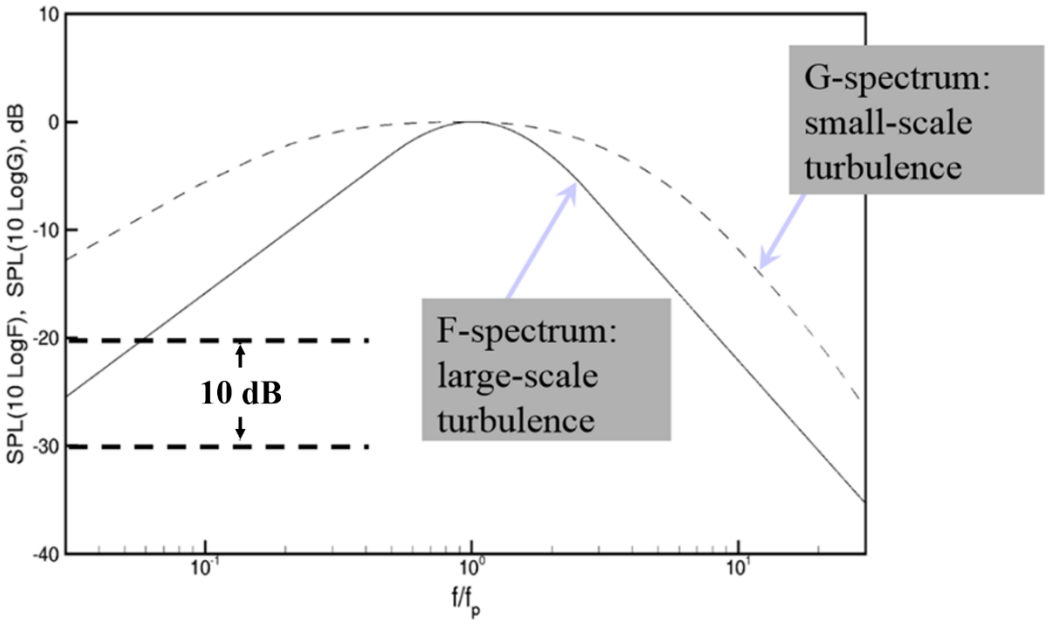

Figure 2.2: Similarity spectra developed by Tam[27].

2.3 Rig-noise Contamination of Jet Noise Measurements

Rig-noise is a noise source that falls into the category of "excess noise", which is any measured noise that is not generated by the jet. The existence of excess noise is typically determined when the measured noise does not scale with the jet noise intensity relationship, which is given in Equation 2.3. Ahuja[31] explored three possible sources of excess noise, which included noise produced upstream of the nozzle-exit by obstruction noise, turbulence, and swirl, respectively, and showed each one can cause additional noise with higher levels than would be expected from jet noise, and certainly does not scale with Equation 2.3. Subsequently, Ahuja[10] presented five different methods for testing for rig-noise contamination of jet noise measurements. The most notable of these methods in the Doubling-Diameter Method. While Ahuja[10] points to these methods as a way for testing for rig-noise contamination, they were not validated with experimentation. For the full review of the literature related to this topic see Chapter 3.

The current work will validate the Doubling-Diameter Method as a way to determine if rig-noise contamination exists in jet noise measurements. In addition, this method will be used on the GTRI Anechoic Jet-Facility as a case study.

2.4 Reynolds Number Effects on Jet Noise

The published works of Long and Arndt[17], Kastner et al.[18], and Bhat[19] show that jet noise is reduced as the Reynolds number of the jet is reduced. All of these studies derived different conclusions. For example, Long and Arndt[17] observed a 7 dB reduction across all frequencies between the low and high Reynolds number jets, whereas Kastner et al.[18] and Bhat[19] showed reduction only to the right of the spectral peak. The full literature review for this topic is provided in Chapter 4.

These studies only showed the effects of the Reynolds number on the jet noise from the qualitative standpoint. These studies did not discuss why the results showed the observed noise reductions at low Reynolds numbers. The present work adds some quantitative understanding to these effects.

2.5 Nozzle-exit Boundary Layer Effects on Jet Noise

Experimental studies by Powell[13], Ahuja[14], Viswanathan and Clark[15], and Zaman[16] indicate that jet noise levels are reduced as the nozzle-exit boundary layer becomes more developed. Although, Powell[13] and Ahuja[14] showed jet noise reduction across all frequencies, Viswanathan and Clark[15] and Zaman[16] showed jet noise reductions only at frequencies to the right of the spectral peak. Computational studies performed by Bogey et al.[32-37] are in agreement with the conclusion that jet noise is reduced as the nozzle-exit boundary layer becomes more developed. Prior work on this topic is fully reviewed in Chapter 5.

2.6 Reflection and Shielding Inside an Anechoic Jet-Facility

Reflections and shielding, which is made up of transmission loss, refraction, diffraction and scattering, are very well known concepts in acoustics literature. The effects on the jet noise from reflections from the surfaces occurs in the form of "waviness", as is discussed by Ahuja[10] and Viswanathan[38]. This is a continuing problem with jet noise measurements that cannot be completely eliminated but can be mitigated. No previous research has been conducted on how a plenum chamber or secondary nozzle could act as an acoustic shield for microphones in the forward arc. Although much work has been conducted by many authors for prediction of shielding effects in general. These shielding prediction scheme range from a simple monopole being shielded by a disk to full shielding

of jet noise by air frame components. In particular, Ahtye and McCulley[39] developed a code that can potentially be used to predict the shielding of jet noise by a plenum chamber. This code is based on a point source being shielded by a rectangular shield, and Ahtye and McCulley[39] used it for prediction of broadband shielding. The full literature review can be seen in Chapter 4.

This work will add to the existing literature by showing the potential shielding and reflection effects brought about by the presence of a plenum chamber inside of an anechoic jet-facility. The abilities of a simple shielding code to predict these shielding effecting will also be examined.

While the studies mentioned above indicate that the jet mixing noise is modified by thickening the boundary layer, they do not show how these reductions are related to the state of the boundary layer in terms of the boundary layer displacement thickness, momentum thickness and shape factor. In addition, how these reductions vary with frequency needs to be understood. The current work will add these elements to the existing literature.

CHAPTER 3

VALIDATING THE DOUBLING-DIAMETER METHOD FOR DETECTING OF RIG-NOISE CONTAMINATION IN JET NOISE MEASUREMENTS

Often jet noise spectra that have been acquired in different anechoic jet-facilities are compared and the spectra do not match. These spectra are from jets that are assumed to be at the same conditions or are corrected to the same conditions using the jet noise scaling laws, such as D_j^2 and U_j^8. Many have suggested a variety of reasons as to why these differences exist. One such explanation is the presence of rig-noise contamination. This is a harsh claim; as it creates doubt about any measurements acquired in the jet-facility in question. Viswanathan[4, 5] and Ahuja[10] brought up the important concern of rig-noise contamination of jet noise measurements. As will be seen below, Ahuja [10] proposed several techniques that can be used to determine if rig-noise contamination is present in jet noise measurements. One of these techniques will first be validated, and then used to determine if rig-noise contamination is in fact present in measurements acquired in the GTRI Anechoic Jet-Facility as a case study. The case study will determine if rig-noise exists in jet noise measurements acquired in this facility and will verify the validity of the measurements for all studies performed in the facility.

3.1 Previous Work

3.1.1 Jet Noise Scaling Relationships and Prediction Schemes

Some of the rig-noise detection methods require knowledge of the jet noise scaling relationships; these relationships are summarized here. One of the results of the Lighthill

Acoustic Analogy[1-3] was the jet noise intensity relationship, which is given by the expression:

$$I \sim \frac{\rho_m^2}{\rho_0} \frac{U_j^8}{a_0^5} \frac{D^2}{R^2} \left(1 - M_c \cos\theta\right)^{-5} \tag{3.1}$$

A scaling/normalization scheme, based on Equation 3.1 is commonly used by the jet noise community (for example, see Ahuja and Bushell[40] and Ahuja[8]). The SPL can be found from the intensity of a sound signal using the equation:

$$SPL = 10 \log\left(\frac{I}{I_{ref}}\right) \tag{3.2}$$

The frequencies of the jet noise spectrum can be normalized using the Strouhal number, which is defined as:

$$St = \frac{f D_j}{U_j} \tag{3.3}$$

The amplitude at each Strouhal number can be calculated by removing the effects from each of the parameters in Equation 3.1, using the expression:

$$A(St) = SPL - 80 \log\left(U_j\right) - 20 \log(D) - 20 \log\left(\frac{1}{R}\right) + 50 \log(1 - M_c \cos(\theta)) - 20 \log(\rho_m) - 10 \log(\rho_0) \tag{3.4}$$

When Equation 3.4 is used, the effects from these parameters are removed and the amplitude of a spectrum given by *A(St)* at each Strouhal number should be normalized to a constant value. This means that, in theory, every jet noise spectrum can be reduced to the same normalized spectrum. Equation 3.4 can be used in reverse to predict jet noise spectra for a jet at any desired conditions. This prediction scheme is still used today. The only change in this scheme in more recent years is that at low polar angles ($\theta < 40°$) the

frequencies are normalized using the Helmholtz number as shown in Ahuja[8] and Michel and Ahuja[41], which is given by the following the expression:

$$He = \frac{fD_j}{a_0} \tag{3.5}$$

Gaeta and Ahuja[42] revisited the scaling scheme that was presented in Equations 3.1 – 3.5. They showed that jet noise presented in 1/3-octave band spectra scales differently than jet noise presented in narrowband spectra. They showed that the scaling scheme shown in Equation 3.4 works for 1/3-octave band spectra, but not for narrowband spectra. To derive the proper scaling methodology for narrowband spectra, Gaeta and Ahuja[42] started with the full dimensional form of the intensity for spectral density, which was originally derived by Ffowcs-Williams[22] and later by Lush[7] and re-stated it in dimensional form as:

$$I(f) \propto \frac{D_j^3 f^4}{\rho_0 a_0^5 R^2} H(f_s) \tag{3.6}$$

The $H(f_s)$ term is the Fourier transform of the Lighthill's stress tensor correlation function, which has a dimensional form:

$$H(f_s) \propto \frac{\rho_0^2 U_j^4 D_j^3}{f_s} \tag{3.7}$$

Gaeta and Ahuja[42] reduced Equations 3.6 and 3.7 to the non-dimensional form:

$$I(f) \propto \frac{\rho_0 D_j^2 U_j^8}{a_0^5 R^2} \left[\frac{D_j}{U_j}\right] \frac{1}{|1 - M_c \cos(\theta)|^5} \tag{3.8}$$

Using this form of the intensity, the scaling scheme can be adjusted to:

$$A(St) = SPL - 10\log(\Delta f) - 70\log(U_j) - 30\log(D) - 20\log\left(\frac{1}{R}\right) + 50\log(1 - M_c\, cos(\theta)) - 20\log(\rho_m) - 10\log(\rho_0) \tag{3.9}$$

The Δf term in Equation 3.9 adds the requirement of all scaling must be performed with the spectrum in the form of Power Spectral Density (PSD or SPL per Hz). The extra D_j/U_j comes out of the math and is related to the Strouhal Number. Gaeta and Ahuja[42] showed that narrowband spectra collapses well using this method, when scaling jets of the same nozzle-exit diameter but different jet velocities. It is noted here that in the study presented by Gaeta and Ahuja[42] only velocity scaling was studied and that they showed that narrowband jet noise spectra scale with D_j^3 and U_j^7. Since only velocity scaling was studied, additional work is needed to confirm the third power of the diameter (D_j^3) scaling for the PSD of jet noise. (This has been shown to be true in the present work.)

3.1.2 Rig-noise and Proposed Rig-noise Detection Techniques

In order for jet noise measurements to be considered "clean", the measured noise must only be generated by the jet mixing itself taking place outside the nozzle. Noise generated over and above that generated by the jet mixing alone has been historically dubbed "excess noise" (See Bushell[43] and Ahuja[31]). The presence of excess noise has traditionally been detected using the jet noise scaling relationships that were presented above. Whenever jet noise did not follow these relationships, contamination of the noise measurements by excess noise was assumed. The portion of the measured noise that originally was considered excess noise contamination is now reasonably well defined. For example, Crighton[44] discussed shock noise in the context of excess noise, but this is now a well understood noise source. Most excess noise sources were typically seen at low velocities and were assumed to be present whenever the measured noise from a given jet followed a velocity scaling of U_j^n , where n was less than 8. At these velocities, the scaling was typically found to be between U_j^6 or U_j^4, corresponding to dipole and monopole

sources, respectively, as was shown in Bushell[45] and Ahuja[31]. Crighton[46, 47] showed one of the potential sources of excess noise to be what has become to be understood as "lip noise". Crighton[46, 47] showed that the shear layer of a jet can interact with the nozzle-exit lip and cause a monopole and dipole source to become prominent in the measured noise. This noise component was shown to scale with U_j^6. Ahuja[31] performed a study looking at the sources of excess noise. After finalizing a set of clean jet noise as a reference, he showed that flow obstructions upstream of the nozzle, additional turbulence generated upstream of the nozzle, and swirl generated upstream of the nozzle could be the sources of excess noise.

In order, to acquire clean anechoic jet noise measurements, the anechoic jet-facility must also be carefully designed so that the jet noise is not contaminated by "rig-noise". This type of noise is formed from bends in the plumbing, which connects the air supply to the jet, measurement devices, such as pressure probes and thermocouples, and especially the control valve, which is typically used to throttle the jet-flow. This is the type of noise that was claimed by Viswanathan[4, 5, 9] to be contaminating the Tanna Jet Noise Database[6]. Ahuja[10] presented a methodology for designing clean anechoic jet-facilities, and suggested five methods for testing for excess-noise: (1) examine changes in noise by testing three nozzles of different diameters at the same velocity (referred to as the Doubling-Diameter method), (2) compare newly measured data with well-established measured data or prediction for round jets, (3) add a duct extension to the nozzle to examine changes in far-

field noise, (4) examine jet noise coherence at widely spaced microphones, and (5) carry out a source location test.

The first methodology is the Doubling-Diameter Method. This technique is illustrated in Figure 3.1. This method is based on the jet noise scaling relationships, which are given in Equations 3.1 and 3.8. As explained above, if noise is being analyzed in either OASPL or 1/3-octave band spectra then Equation 3.1 is used, and the jet noise scales with D_j^2. Alternatively, if the noise is being analyzed in narrowband spectra then Equation 3.8 is used, and the jet noise scales with D_j^3. Using Equations 3.1 and 3.8, if the nozzle-exit diameter of a jet is doubled while keeping the velocity constant, noise should increase across the whole spectrum by 6 dB or 9 dB, depending on whether the noise is analyzed in 1/3-octave bands or narrowband, respectively. This implies that the jet noise is the dominant noise source and there is no rig-noise contamination or the rig-noise is completely masked by the jet noise. Alternately, if the jet noise from two nozzles, where one nozzle-exit is twice the other, can be normalized, or collapsed, by removing the

diameter component using the diameter term in Equations 3.4 or 3.9, this will indicate the same thing.

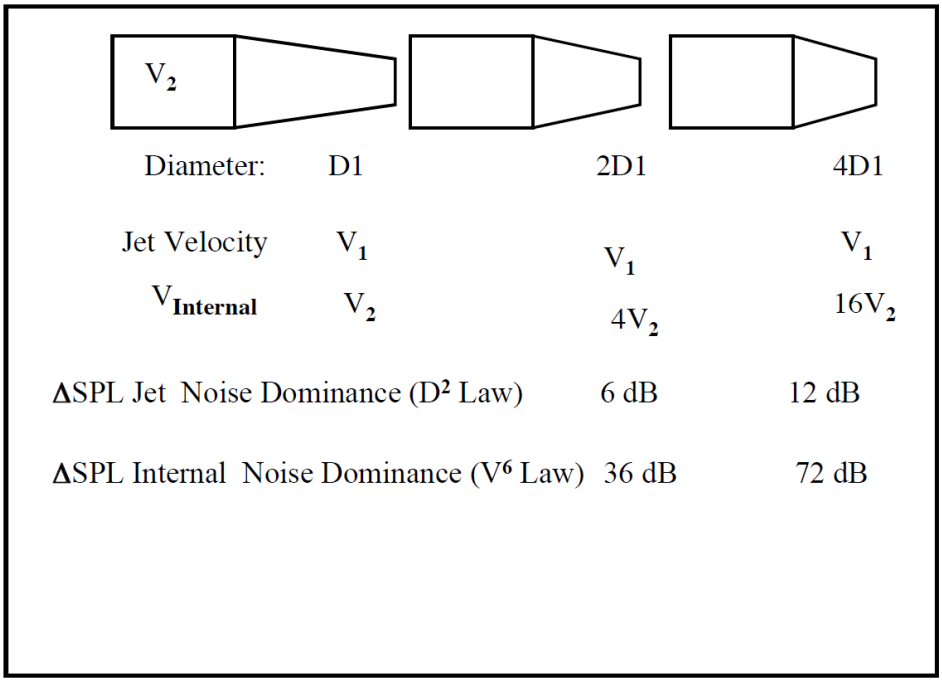

Figure 3.1: Methodology behind the double diameter technique, reproduced from Ahuja[10].

On the other hand, if rig-noise is the dominant noise source, doubling the nozzle-exit diameter will increase the mass flow rate through the jet-rig piping system by a factor of four. This mass flow rate increase will cause the velocity in the piping system to increase by up to a factor of four depending upon whether compressibility effects in the piping system are taken into account. This is because the mass flow rate of any fluid system is given by the equation:

$$\dot{m} = \rho U_i A \tag{3.10}$$

Since the pipe geometry will not change, and the density change will be a function of the velocity change, if incompressible flow is assumed in the plumbing the velocity in the pipes will increase by a factor of four. It should be noted, if the Mach number of the flow inside

the supply ducts increases above M_i = 0.3, compressibility effects will affect the actual velocity of the flow. Rig-noise, most notability valve noise, is a dipole noise source. Aerodynamic dipole sources are a result of a force flux, and noise caused by air moving over a body is a dipole sources due to the oscillating aerodynamic forces that result from this process. Dipole noise sources have been found to scale with the sixth power of the velocity of the flow over the body. So, as depicted in Figure 3.1 above, with this factor of four increase of the velocity inside the jet-rig plumbing due to the doubling of nozzle-exit diameter, the rig-noise will be expected to increase by 36 dB due to pipe velocity to sixth power dependence. This number assumes incompressible flow, but low velocities where excess noise has often been identified in the published literature, this will be a more accurate representation. In practice, a 36 dB increase may not be observed because of the incompressibility assumption and because typically anechoic jet-facilities have silencers deployed upstream of the nozzle-exit to attenuate the rig-noise. Using the collapse method described above, once the effects of nozzle-exit diameter is removed, any additional differences from doubling the nozzle diameter can be assumed to be upstream noise.

In this methodology, jet noise generated from nozzles of diameters D_j and $2D_j$ is measured and fully corrected into a lossless form as will be described below. At a given jet Mach number or jet velocity, if a 6 dB or 9 dB difference between the spectra is observed, depending on if 1/3-octave band spectra or narrowband spectra are being used, or the spectra collapse by removing the diameter effect on the jet noise, it implies that the facility is free of rig-noise contamination at that condition. If a larger decibel difference is observed, that implies that rig-noise contamination is present at that condition. Any jet

noise study in an anechoic chamber needs to have verification of the non-existence of rig-noise contamination over a range of jet operating conditions and nozzle-exit diameters.

Method 2, which involves comparing newly measured data with well-established measured data or prediction for round jets, is widely used in the jet noise research community, but is based upon a major assumption that the well-established measured database is in fact clean jet mixing noise. The problem with making this assumption is precisely the motivation behind the entirety of this work, in that other physical phenomena that are a function of the configuration of the jet-facility or the nozzle choice, such as the Reynolds number or nozzle-exit boundary layer state, which are investigated in Chapters 4 and 5, respectively, may in fact indicate noise contamination, even though that may not be the case.

In the third methodology, extensions are added to the straight section of a nozzle and changes in the farfield noise measurements are observed. Adding extensions to the straight section of the nozzle will cause the nozzle-exit boundary layer to become thicker. As will be explained in Chapter 5, this will reduce the jet noise, particularly at high-frequencies. Alternatively, the internal velocities will remain the same, meaning the rig-noise levels will be unchanged. If rig-noise is the dominant noise source, adding the duct extension, there may not show any noise reduction.

In the fourth methodology, the coherence of widely spaced microphones is measured. From the work of Nance et al.[48-52], this spacing was found to be 20°. Due to the fact that a jet is a distributed noise source that produces incoherent broadband noise associated with small-scale turbulence, the coherence of the noise measured from these microphones should be zero. Rig-noise is a coherent noise that will radiate from the nozzle-

exit. If rig-noise exists, a non-zero coherence value will be calculated between the microphones.

The fifth and final methodology consists of performing source location on the jet. Identifying what frequency noise is generated at what downstream location in a jet has been the topic of a limited number of studies[53-58]. Typically, it is found that high frequencies are generated near the nozzle-exit and low frequencies farther downstream. If jet noise is the dominant source, the source distribution should be similar to that measured in the previous works[53-58]. If rig-noise is the dominant noise source, more frequencies than would be typically seen in a jet noise source distribution will be located near the nozzle-exit. Due the complexity of this method, it is the least likely to be used by the common researcher therefore it was not studied as part of this effort, although it the topic of the doctoral thesis of another graduate student of Dr. Krishan K. Ahuja[53].

It would ideally be nice to try all of the five methods described above to determine if the GTRI facility is free of rig-noise. As other components of the present work required testing nozzles of a range of exit diameters anyway, it was felt that the author could leverage the Doubling-Diameter method most as the farfield noise data from nozzles of various diameters was already available. For this reason and in the interest of time, only the Doubling-Diameter Method is thus studied here in order to prove that the GTRI Anechoic Jet-Facility is in fact free of rig-noise contamination, and then suggest other phenomena that could be responsible for differences in jet noise measurements, as is done

in the following chapters. Analyzing each method in depth would be a thesis topic of its own and is left as a topic of future research by others.

3.1.3 Noise Produced by Obstruction Upstream of the Nozzle

In order to verify the Doubling-Diameter Method for this study, a known upstream aerodynamic noise source is required to be placed upstream of the nozzle-exit. For this purpose, cylindrical obstructions were placed upstream of the nozzle-exit. The generation of noise by these obstructions was discussed in Ahuja[31]. As air moves over the cylinder, the boundary layer between the air and the obstruction grows until separation occurs. When the flow separates from the obstruction, alternating vortices are formed, a phenomenon referred to as vortex shedding. These vortices cause alternating lift and drag forces on the obstruction, which produce well-defined tones. This is the dipole sound produced by obstructions in flows. When the flow created from the obstruction exits the nozzle, two phenomena occur: (1) the noise created by the dipole source radiates from the nozzle, which is made up of high-amplitude tones at the vortex-shedding frequency and its harmonics, and (2) the wake created from the obstruction merges with jet flow and raises the amplitude of the broadband noise.

Ahuja[31] performed considerable work on the impact of upstream cylinder obstruction on jet noise measurements. He used a circular and a rectangular obstruction and found that the measured noise increased by 40 dB for the circular obstruction and 10 dB for the rectangular obstruction. Similar obstructions were used in the present study to purposely add rig-noise and contaminate the measured jet noise. The Doubling-Diameter method was then utilized to see if this rig-noise could be detected as the source of jet noise contamination.

3.2 Experimental Program

3.2.1 Facility Description

A detailed description of the GTRI Anechoic Jet-Facility can be seen in publications by Burrin, Dean and Tanna[59], Burrin and Tanna[60], and Ahuja[10]. A concise description will be provided here. A picture of the jet-facility is shown in Figure 3.2. The jet-facility is capable of creating co-annular jet streams. High pressure air (a maximum of 100 psi) is fed to the chamber from a reservoir. A control valve is used to control the mass flow rate through the system. The air supplied to both the primary and secondary jets can be heated independently, using propane burners, up to 1200 °F. The air in each flow is sent through silencers upstream of the two plenum chambers to attenuate any noise created upstream of the jet nozzle, such as valve noise. The air is then passed through a plenum that has a contraction ratio of 36 and to which the various nozzles can be attached. The nozzles used in the experimental program will be described below. Figure 3.3 shows a sketch of the jet system. For more details, see Burrin, Dean and Tanna[59], Burrin and Tanna[60], and Ahuja[10].

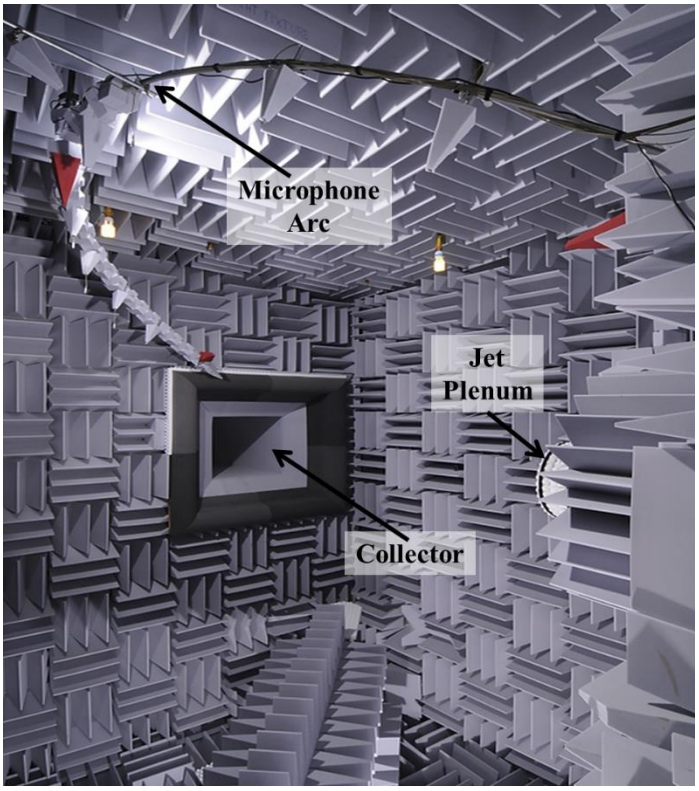

Figure 3.2: The GTRI Anechoic Jet-Facility.

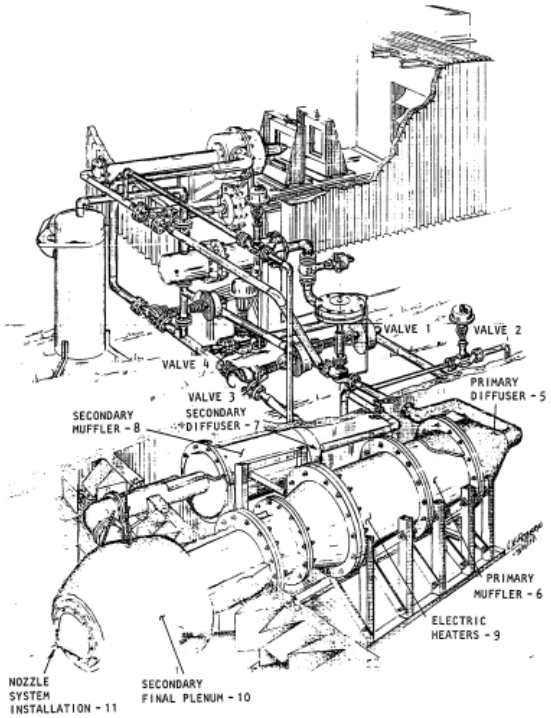

Figure 3.3: Schematic of the air flow system for the GTRI Anechoic Jet-Facility, reproduced from Burrin and Tanna[60].

Figure 3.4 shows a diagram of the experimental set-up inside of the GTRI Anechoic Jet-Facility. In this configuration, the desired nozzle is attached to the plenum of the primary jet-flow. The microphones used for measuring the jet noise are placed on a microphone arc, which is placed far enough away so the microphones are in the acoustic and geometric far-field, usually considered minimally 60 nozzle-exit diameters. These microphones are mounted at polar angles of 30°, 60° and 90°. Depending on the nozzle configuration used in a particular test, while the microphones were mounted at these polar angles, the distances from the nozzle-exit changed. These distances will be stated below where each experimental test is described. In addition, the microphones were not placed at a common distance from the nozzle-exit. The reason for this was to place the microphones as far into the farfield as possible, while being restricted by the dimensions of the room and the position of the microphone arc.

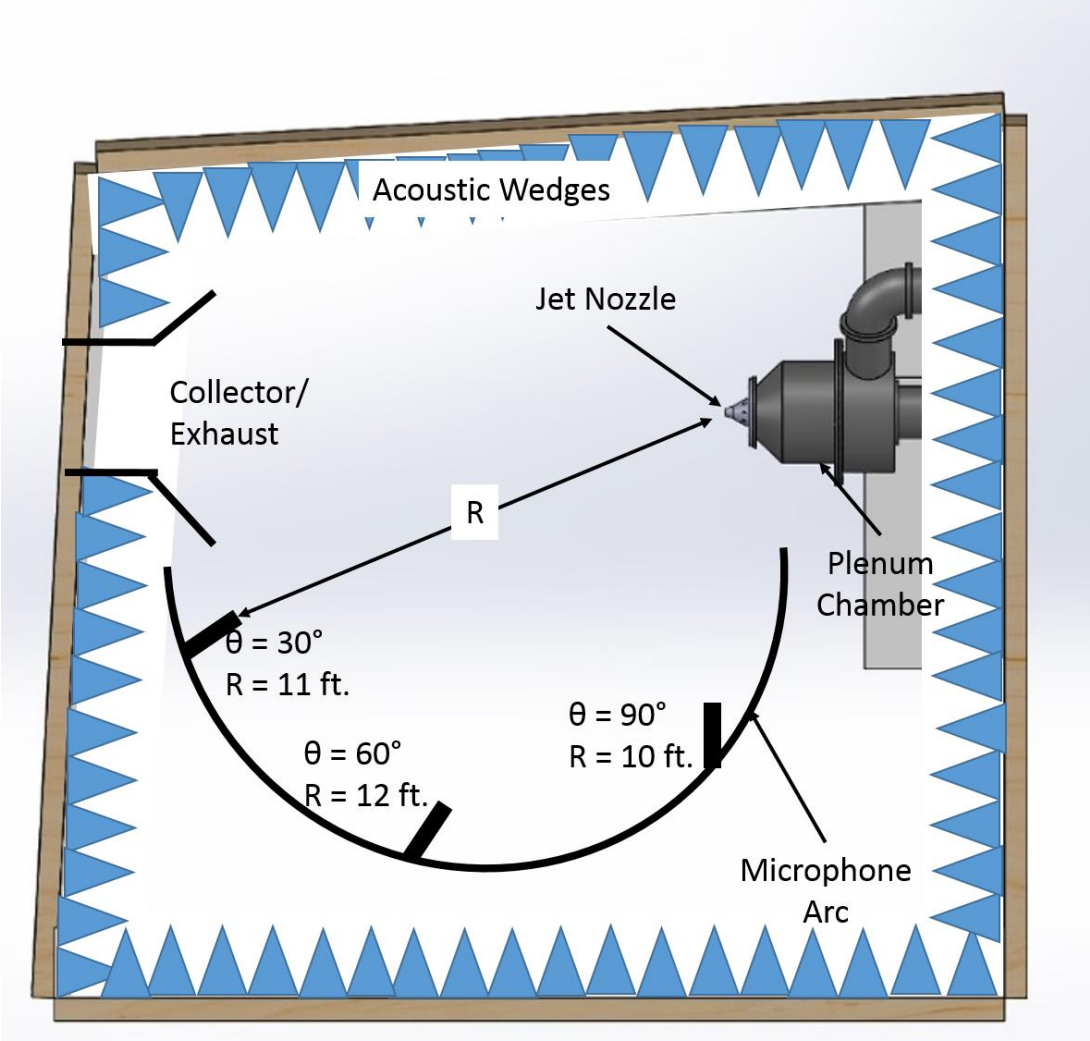

Figure 3.4: Experimental set-up inside of the GTRI Anechoic Jet-Facility.

The acoustic measurements were acquired using 4939 Bruel and Kjear (B&K) ¼-inch free-field microphones, which are attached to 2669 B&K preamplifiers. The 4939 microphones have a frequency range of 4 – 100,000 Hz. The ¼-inch microphone-preamplifier combinations are connected to B&K 2960-A-0S4 Nexus conditioning amplifiers that not only amplify the signal but serve as the microphones' 200 millivolt power supply. The signals are then fed into a National Instruments (NI) PXIe-4499 module

inside of an NI PXIe-1073 chassis. All the microphone measurements are processed in LabView, the NI programming language.

The pressure signals were processed into averaged frequency spectra. For these experiments, the sampling frequency used with the analyzer was 204.8 kHz; thus 204,800 samples of the acoustic pressure signal were acquired every second. These time signals were processed to provide averaged power spectra using a window size of 6400 samples, 50% overlap, and a Hanning window. This created a Δf of 32 Hz and a smooth spectral curve. These spectra were then corrected for a variety of conditions, as detailed in Ahuja[10]. The effects of microphone geometry, the microphone protective grid, microphone actuator response, and incidence of the microphone with respect to the source are accounted for as part of the microphone free-field frequency response. This correction, is a function of both frequency and the angle of incidence of the sound wave on the microphone, is lumped together and will be denoted by the variable $A(f, \Psi)$. In addition, a foam ball windscreen was used on the $\theta = 30°$ microphone, to prevent hydrodynamic fluctuations from affecting the measurements. The effects of windscreen on a broadband frequency spectrum was determined experimentally and is denoted by the variable $B(f)$. The effect of atmospheric attenuation was accounted for by using the method presented in ANSI S1.26-1995[61]. This atmospheric-attenuation correction methodology contains many equations and is too long to present here, but is shown in Appendix B. This method results in a frequency-dependent attenuation coefficient $\alpha(f)$, which has the units of dB/m. Removing the attenuation effects and applying all of the microphone related corrections described above provides the so-called "lossless spectra," which will be used throughout the analysis. The advantage of this form of the data is that it allows the data from different facilities, different microphones

and acquired on different days to be compared with one another. This also allows the theoretical predictions, which are independent of microphone responses, to be compared with the measured lossless data. Finally, the jet noise measurements are extrapolated to a common distance to help with needed comparisons. This distance was selected to be 72 nozzle-exit diameters and is performed using the inverse square law, which is part of Equation 3.1. Combining these effects, the free-field and lossless jet noise spectrum is calculated using the equation:

$$SPL(f)_{free-field,lossless} = SPL_{uncorrected} - A(f,\Psi) + B(f) + \alpha(f)R_1 + 20\log_{10}\left(\frac{R_1}{R_2}\right) \quad (3.11)$$

where R_1 is the distance between the nozzle-exit and the microphone at the time of measurement and R_2 is the extrapolated distance between the microphone and nozzle-exit used in the inverse square law. Corrections for any of the parameters shown in Equation 3.1 are simply done by removing that effect using Equations 3.4 or 3.9 and then adding the effect of the changed parameter back into the spectrum by using the reverse operation. An example of this correction process is shown in Appendix A. As an additional level of processing, the uncorrected measurements are compared to the ambient noise measurements. Any data point that is within a ΔSPL of the ambient noise measurements is disregarded due to ambient noise contamination.

The following is a description of the instrumentation used to acquire the jet operating conditions. The stagnation temperature, T_t, was measured using a K-type thermocouple located in the jet plenum chamber. This temperature measured was recorded using one of two devices depending on the availability of the instrumentation: (1) a thermocouple reader box, which outputs a 100 mV/°F DC voltage signal, which was

measured using the same PXIe DAQ that was used for the acoustic measurements; or (2) NI SCXI-1112 thermocouple cards inside of a NI SCXI-1001 chassis. The stagnation pressure, p_t, was measured using a pressure port in the jet plenum chamber that is read by a NetScanner Model 9816 pressure reader mounted inside a NetScanner Model 98RK chassis. The ambient pressure, p_a, of the chamber was measured using a NetScanner 9032 barometer. The chamber's ambient humidity, h, and temperature, T_a, were measured with a Newport Electronics ITHP-5-DB9 humidity and temperature probe. The jet properties were then calculated using the isentropic flow relationships. Since the ambient pressure for the jet is also the jet's static pressure, the jet Mach number, M_j, was calculated using the expression:

$$M_j = \left(\left(\left(\frac{p_t}{p_a} \right)^{\frac{\gamma-1}{\gamma}} - 1 \right) \frac{2}{\gamma-1} \right)^{\frac{1}{2}} \tag{3.12}$$

where, γ, is the ratio of specific heats, which is 1.4 for air. The jet static temperature, T_j, was then calculated using the equation:

$$T_j = \frac{T_t}{1+\frac{\gamma-1}{2} M_j^2} \tag{3.13}$$

The speed of sound, a, in the jet was calculated using the expression:

$$a = \sqrt{\gamma \bar{R} T_j} \tag{3.14}$$

where, $\bar{R}$ is the specific gas constant of air. This provided the jet exit velocity from:

$$U_j = M_j a \tag{3.15}$$

The ambient speed of sound, a_0, was calculated from:

$$a_0 = \sqrt{\gamma \bar{R} T_a} \tag{3.16}$$

When setting the jet conditions, the velocity, Mach number or ambient Mach number (U_j/a_0) are used.

3.2.2 Experimental Program Description

The study consisted of two parts: (1) the verification of the Doubling-Diameter Method as a method for determining the existence of rig-noise contamination in an anechoic jet-facility and (2) the application of this methodology to jet noise measurements acquired in the GTRI Anechoic Jet-Facility as a case study to determine if they were contaminated by rig-noise. In the first part of the study, upstream noise from a known aerodynamic source consisting of obstruction noise was purposely added to contaminate the jet noise measurements. This was accomplished by adding the obstruction in a separate, four-inch diameter, 5-inch long duct section mounted between the nozzle-exit and the plenum chamber as shown in Figure 3.5. A total of three flow obstructions were used: (1) a 1/8-inch diameter rod, (2) ¼-inch diameter rod, and (3) a 1-inch × 1-inch square cross-sectional rod. In addition, a baseline case was acquired without any flow obstruction upstream of the nozzle-exit. For each of these obstructions, two nozzles were used: (1) a two-inch diameter nozzle and (2) the four-inch diameter duct section exit itself. For each of the two cases, the obstructions were located 9.5 inches and 2.5 inches upstream of the

nozzle-exit, respectively. A total of 8 test configurations were thus tested, namely, 3 obstructions and no obstruction with 2 nozzle-exit diameters.

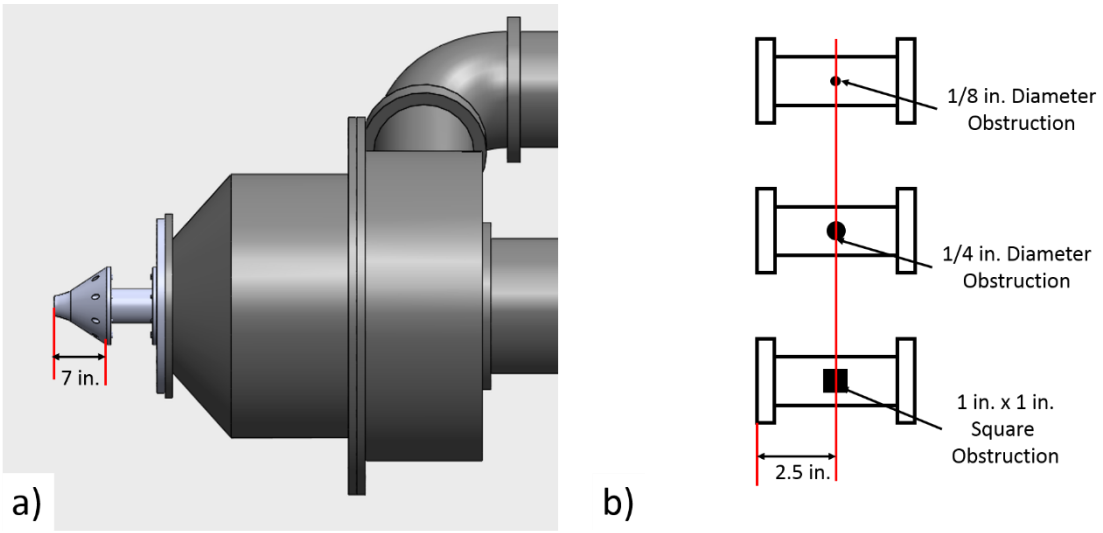

Figure 3.5: Nozzle/obstruction setups: a) the 2-inch nozzle-exit diameter mounted on the pipe extensions and b) the obstructions in the pipe extension.

Farfield acoustic measurements were acquired for these 8 configurations at polar angles of 30°, 60° and 90°. The microphone distances only varied with the nozzle attached to the pipe section. The distances of each of the microphones for the two nozzle configurations are shown in Table 3.1. The microphones were set-up as shown in Figure 3.4. The jet Mach number for each case was varied from M_j = 0.4 to M_j = 0.8.

Table 3.1: Distance of the microphones from the nozzle-exit for the first set of experimentation.

θ \ Nozzle	2 in. Nozzle		4 in. Nozzle	
	R (ft)	R/D	R (ft)	R/D
30°	10.33	62	10.71	32.1
60°	10.33	62	12.12	36.4
90°	10.33	62	12.5	37.5

In the second part of the study, which was the case study of the GTRI Anechoic Jet-Facility, jet noise was measured using ASME nozzles of the following nozzle-exit

diameters: (1) 0.25 inches, (2) 0.5 inches, (3) 1 inch, (4) 1.54 inches and (5) 2 inches. Jet Mach number was varied between 0.4 and 0.8. Microphone measurements were acquired at polar angles of 30°, 60° and 90°. The distances of the microphones from the nozzle-exit for the nozzles are listed in Table 3.2. This configuration is exactly what is shown in Figure 3.4.

Table 3.2: Distance of the microphones from the nozzle-exit for the second set of experimentation

θ \ Nozzle	0.25 in. Nozzle		0.5 in. Nozzle		1 in. Nozzle		1.5 in. Nozzle		2 in. Nozzle	
	R (ft)	R/D	R (ft)	R/D	R (ft)	R/D	R (ft)	R/D	R (ft)	R/D
30°	3.5	168	3.5	84	11	132	11	88	11	66
60°	2	96	2	48	12	144	12	96	12	72
90°	2	96	2	48	10	120	10	80	10	60

As a part of this study, the velocity upstream of the obstruction is calculated and used as part of the analysis. Figure 3.6 shows a diagram related to calculation of this velocity. This calculation is based on the isentropic flow equations and assume both stagnation temperature and stagnation pressure are constant. From isentropic theory, for a given jet Mach number there exists a ratio $(A/A^*)_j$. Since the cross-sectional areas of the nozzle-exit and the pipe section upstream of the obstruction are known, this same quantity, $(A/A^*)_i$, for the flow upstream of the obstruction can be calculated using the equation:

$$\left(\frac{A}{A^*}\right)_i = \left(\frac{A}{A^*}\right)_j \left(\frac{A_i}{A_j}\right) \tag{3.17}$$

where, A_j and A_i are cross-sectional area of the nozzle-exit and pipe upstream of the obstruction, respectively. The quantity $(A/A^*)_i$ is related to the internal Mach number, M_i,

using the isentropic flow tables. Given this Mach number the internal velocity, U_i, is calculated using the equations:

$$p_i = \frac{p_t}{\left(1+\frac{\gamma-1}{2}M_i^2\right)^{\frac{\gamma}{\gamma-1}}} \tag{3.18}$$

$$T_i = \frac{T_t}{\left(1+\frac{\gamma-1}{2}M_i^2\right)} \tag{3.19}$$

$$a_i = \sqrt{\gamma\, \bar{R}\, T_i} \tag{3.20}$$

$$U_i = M_i a_i \tag{3.21}$$

where, p_i, T_i, and a_i are the static pressure, static pressure, speed of sound upstream of the obstruction, respectively.

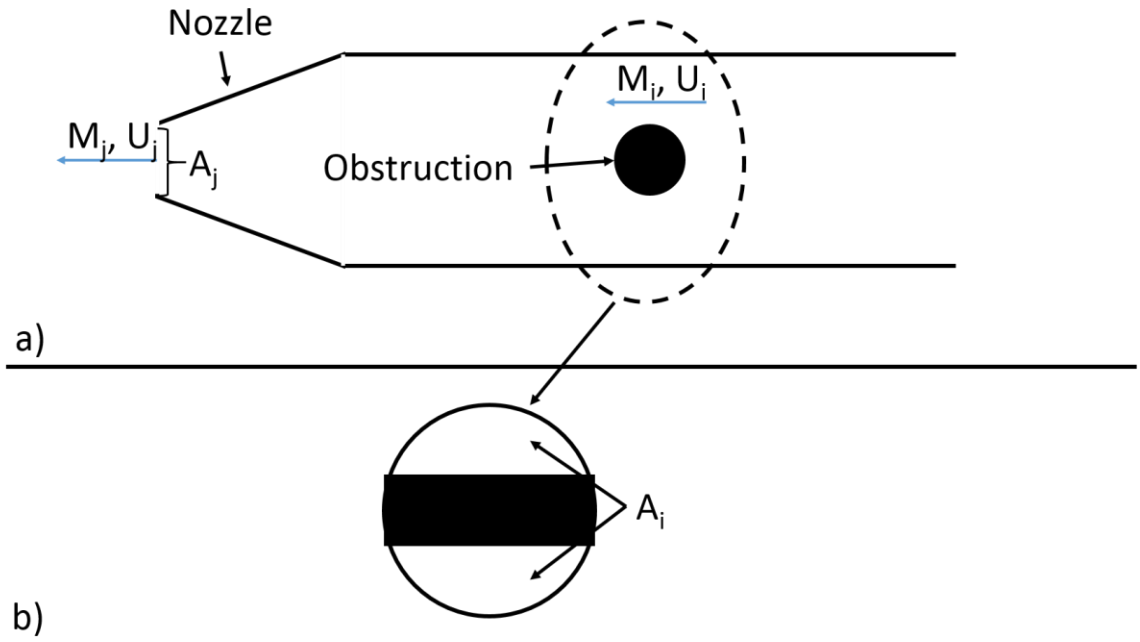

Figure 3.6: Diagram representing calculation of the internal velocity; a) side view and b) close up of the cross-section on obstruction.

The above methodology, makes two assumptions: (1) the flow field is isentropic and (2) the obstructions cause minimal blockage of the overall flow field. The first assumption

does not necessarily hold. The turbulent wake from the obstruction body creates a non-isentropic flow. But this effect is dependent on the blockage produce by the obstruction. The 1/8-inch diameter obstruction only blocks 5% of the cross-section of the four-inch pipe, so the non-isentropic will be weakest in this case. The ¼-inch diameter obstruction blocks 10% of the cross-section of the four-inch pipe, so the effects will be stronger than that of the 1/8-inch diameter obstruction. The 1-inch square obstructions will have the largest non-isentropic effects due to the obstruction wake.

The blockage effect will be ignored in the present calculations, but will be kept in mind in interpreting the data. Tables 3.3 and 3.4 show the jet and internal velocities for the cases studied. A few notes are made here about the calculations presented in Tables 3.2 and 3.4. Firstly, in the case of the two-inch diameter nozzle, the internal velocities are quite low as

Table 3.3: Jet and internal Mach and velocity calculations for the two-inch nozzle.

Obstruction Type	M_j	U_j (ft/sec)	M_i	U_i (ft/sec)
1/8-in. Diameter	0.41	455.0	0.10	109.8
	0.50	560.8	0.11	129.8
	0.60	656.6	0.13	145.1
	0.70	762.2	0.14	158.4
	0.80	853.3	0.15	166.6
1/4-in. Diameter	0.40	451.4	0.10	113.7
	0.50	556.6	0.12	134.7
	0.60	658.3	0.13	151.7
	0.70	763.6	0.15	165.4
	0.80	858.6	0.15	174.2
1-in. Square	0.40	451.4	0.14	154.2
	0.50	553.2	0.16	182.0
	0.60	657.0	0.18	206.1
	0.70	755.8	0.20	224.2
	0.80	855.2	0.21	237.3

shown Table 3.4. Because these internal velocities are so low it is predicted that the noise created by the obstructions will be low and even masked by the jet noise. In the case of the four-inch nozzle, the internal velocities are quite high. In some cases, the value of $(A/A^*)_i$ was found to be less than one. In these cases, the authors assumed the obstruction is causing the flow to choke as the air passes over it. A choked flow means that the flow speed is Mach 1 as the flow passes over the obstruction as is indicated in Table 3.4.

Table 3.4: Jet and internal Mach and velocity calculations for the four-inch nozzle.

Obstruction Type	M_j	U_j (ft/sec)	M_i	U_i (ft/sec)
1/8-in. Diameter	0.40	443.6	0.42	465.7
	0.50	553.1	0.54	584.6
	0.60	651.2	0.65	695.7
	0.71	756.5	0.78	828.7
	0.80	844.6	1.00	1022.0
1/4-in. Diameter	0.40	443.8	0.45	490.9
	0.50	547.0	0.56	613.9
	0.61	661.6	0.72	767.4
	0.70	752.7	0.93	960.9
	0.80	841.6	1.00	1022.3
1-in. Square	0.40	443.5	0.71	766.4
	0.50	551.9	1.00	1026.6
	0.61	656.6	1.00	1025.4
	0.70	753.5	1.00	1024.5
	0.80	843.3	1.00	1023.8

3.3 Results

3.3.1 Validating the double diameter method

A few comments are made before any of the measurements and analysis are presented. First, a large amount of jet noise measurements was acquired over the course

of this study. While the analysis is based on the whole dataset, in order to avoid repetition of showing many plots that show the same exact phenomenon, only a subset of the data is presented. Secondly, all normalization of the jet noise spectra is performed using the following methodology: (1) the frequencies are normalized in terms of Helmholtz number at a polar angle of 30° (see Equation 6.5), and by Strouhal number at larger polar angles (see Equation 3.3), and (2) the amplitude at each normalized frequency is normalized using Equation 3.9. Lastly, when spectra of the two-inch diameter nozzle and four-inch diameter nozzle are normalized for spectral collapse, internal noise produced by the upstream obstructions is not expected to reach the theoretical 36 dB difference stated above. The reason for this is since the normalization techniques subtracts off the diameter component of jet noise, this removes 9 dB from the spectra. This diameter dependence removal causes this theoretical 36 dB increase to become 27 dB.

Figure 3.7 compares the lossless jet noise spectra for the two-inch nozzle with and without obstructions. Spectra at polar angles of 30°, 60°, and 90° and a jet Mach number of 0.6 are shown in Figure 3.7. For each polar angle, data for three obstructions, namely, the two cylindrical obstructions (diameters: 1/8 in and ¼ in) and the 1-inch × 1-inch square obstruction, are shown. As seen in Figure 3.7, there is complete spectral collapse between noise produced by the two-inch nozzle alone and the noise produced by the two-inch nozzle with the two circular obstructions upstream of it. This means that any noise produced by these obstructions is completely masked by the noise produced by the jet mixing noise of nozzle flow without obstruction. In order words, the upstream noise produced by the two circular obstructions used here does not contaminate the jet noise produced by the two-inch nozzle. On the other hand, the square obstruction does contaminate the noise produced by

the two-inch nozzle by about 2 dB at most frequencies. This contamination is 6 dB at the tonal frequency associated with the noise produced by the obstruction. This is due to the fact that the square obstruction is much larger than the two circular obstructions. The noise produced by these obstructions is directly related their characteristic length as shown by Philips[62], Ahuja[31], and Martin and Ahuja[63]. In addition, as shown in Table 3.4, the internal velocity is typically higher for the square obstruction at a given jet exit Mach number, than the other two obstructions where the internal velocities are quite similar. This would increase the noise produced even by a low internal velocity to a level where it will contaminate the jet noise.

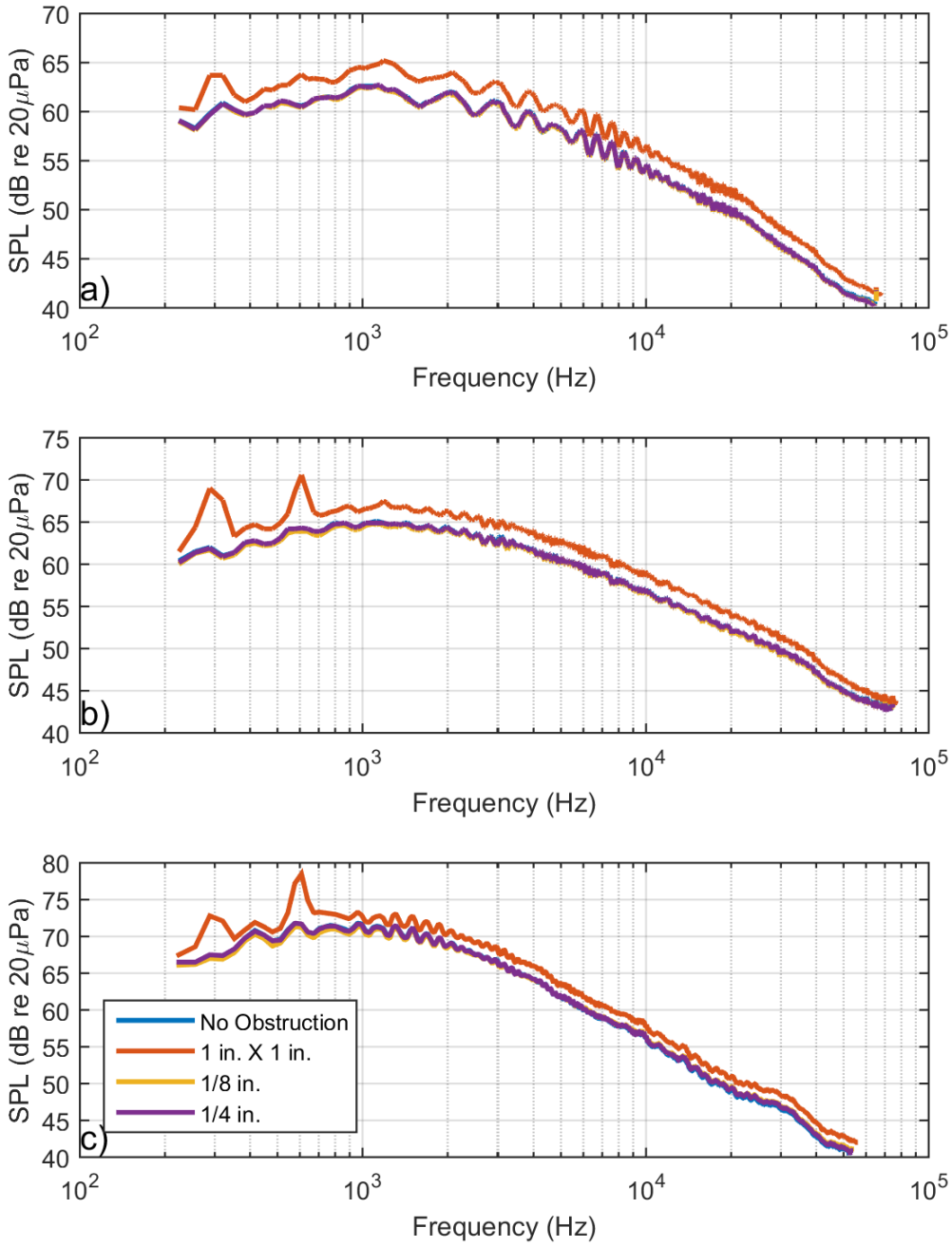

Figure 3.7: Farfield noise with and without obstructions for the two-inch diameter nozzle. a) θ = 30°, b) θ = 60°, and c) θ = 90°. M_j = 0.6, R = 12 ft., D = 2in., Δf = 32 Hz., lossless.

Figure 3.8 compares the lossless jet noise spectra for the four-inch nozzle with and without obstructions. As was done for the two-inch diameter nozzle, spectra at polar angles of 30°, 60°, and 90° and a jet Mach number of 0.6 are shown in this figure. Unlike the results for the smaller nozzle shown in Figure 3.7 above, the noise produced by the four-inch nozzle is affected quite significantly by the obstructions. First of all, the noise spectrum without any obstruction shows a well-defined high-frequency hump, which did not exist in the noise data shown above in Figure 3.7 for the two-inch nozzle. The first conclusion to be drawn here is that when a 4-in. nozzle-exit diameter nozzle is employed, rig noise, if present will show up. That is indeed the case and that is why this facility is not used for studying jet mixing noise much larger than 2–inch diameter nozzle. This hump does not represent a 36 dB increase as theoretically predicted above because the silencer upstream of the nozzle likely removed much of the rig-noise contamination. On the other hand, the noise produced by the obstructions do not have a silencer to remove any of the noise they produce. The square obstruction increases noise at almost all frequencies. At the tone frequency, the square obstruction generates 20 – 30 dB of contamination of the noise produced by the four-inch nozzle without obstruction. Even the broadband noise is increased by 5 – 10 dB by the square obstruction. The circular obstructions, do not seem to have an effect at low frequencies. However, at the tone frequencies, the SPL increases by as much as of 30 dB, and in the broadband noise these levels are as high 20 dB. It is noted here that the predicted 36 dB increase from the obstructions is not observed and this in part may be due to reflections of the obstruction sound inside the nozzle. The nozzle-exit represents an impedance interface for noise generated inside of rig-plumbing. Figures 3.7 and 3.8 represent typical results, in that similar results are seen at other Mach numbers.

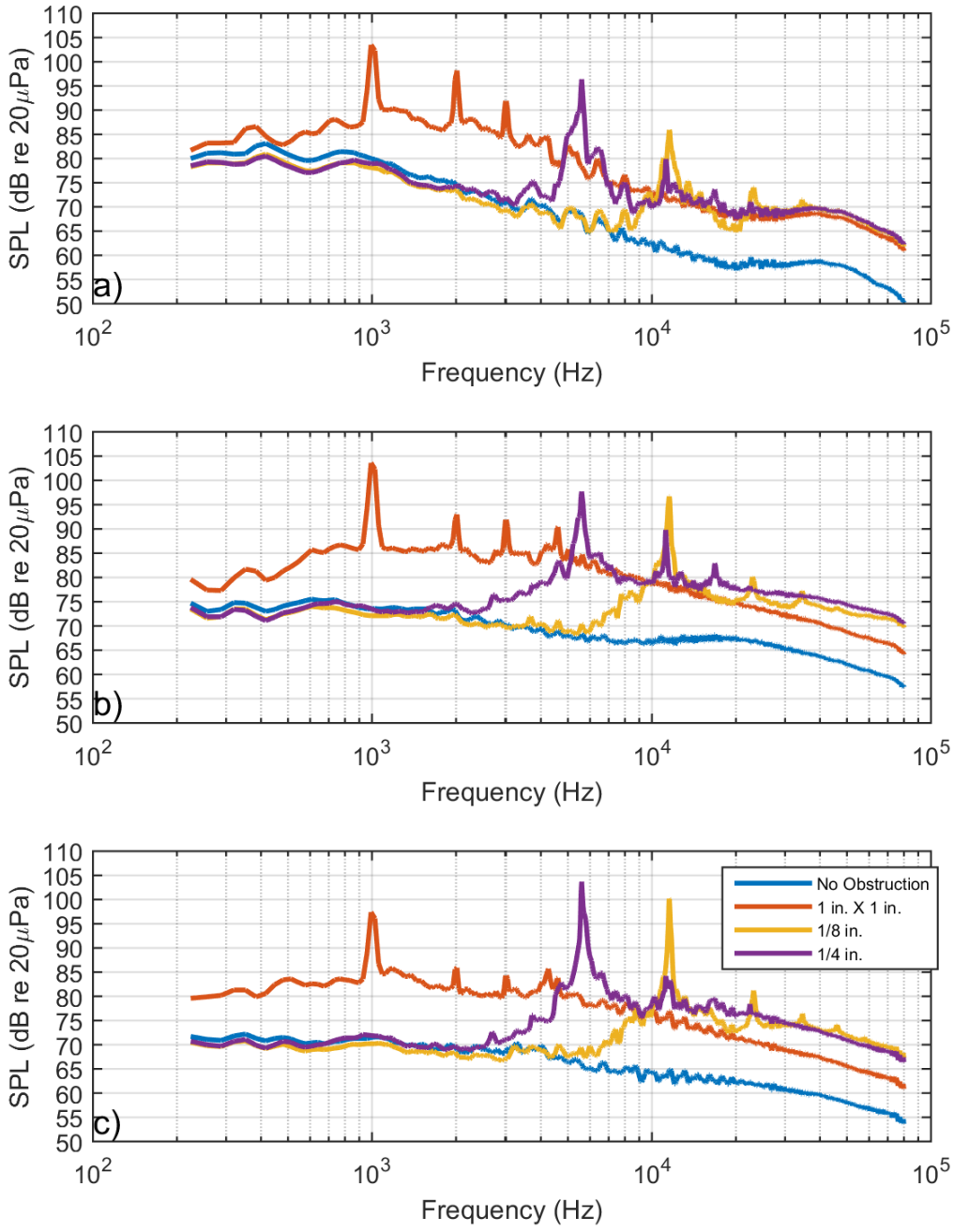

Figure 3.8: Farfield noise with and without obstructions for the four-inch diameter nozzle. a) θ = 30°, b) θ = 60°, and c) θ = 90°. M_j = 0.6, R = 12 ft., D = 2in., Δf = 32 Hz., lossless.

As stated above, the goal of this investigation is to validate the Doubling-Diameter Method of determining if rig-noise maybe contaminating jet noise. The obstructions used are meant to simulate the noise that would be produced from the jet rig. The methodology outlined above assumed that rig-noise behaves as a dipole source that should ideally scale with U_i^6. To this end, Figure 3.9 shows the velocity scaling of the SPL of the tones produced for the 1/8-inch diameter cylindrical obstruction located upstream of the 4-inch diameter nozzle at a polar angle of 90°. The corresponding plot for the 1/4-inch diameter obstruction appears in Figure 3.10. Table 3.5 above contains the internal velocity calculations for these cases. As shown in Figures 3.9 and 3.10, the SPL at the primary vortex shedding frequency for each of the obstructions does scale roughly with the sixth power of the internal velocity. For both 1/8-in. and ¼-in. diameter obstructions, the data points lay at most 2-3 dB away from the ideal U_i^6 line. The exception to this is the highest internal velocity condition. The reason for this is in the spectrum at this condition, the tone all but disappeared. Explaining why the tone disappeared at this condition is well beyond the scope of this study. The fact that a precise sixth power of the internal velocity was not obtained may be related to a number of factors. A sixth power law ideally holds in the absence of duct walls. Additionally, due to the high amplitude of the obstruction tonal noise, part of the tonal energy is lost to higher harmonics during its propagation to the farfield microphone where the tones were measured. Additionally, portions of the energy may be reflected upstream by the nozzle-exit. Similar results are observed for each of the obstructions at polar angles of 30° and 60°.

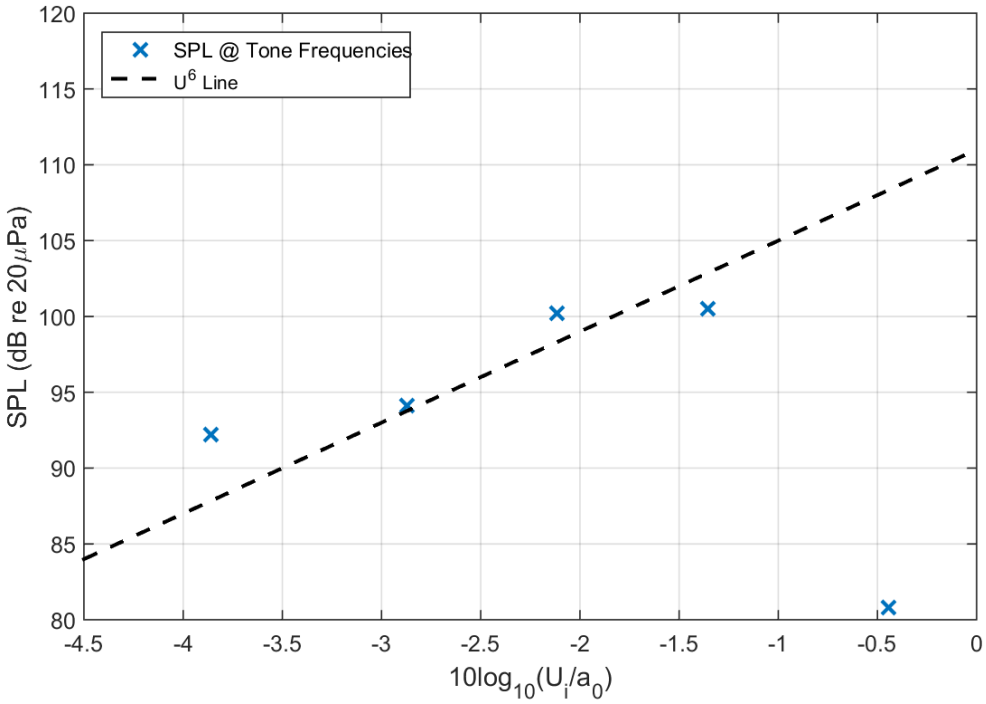

Figure 3.9: Tone SPL scaling with the internal velocity for the 1/8-in. diameter obstruction upstream of the four-inch diameter nozzle. D = 4in., R = 12 ft., θ = 90°, lossless.

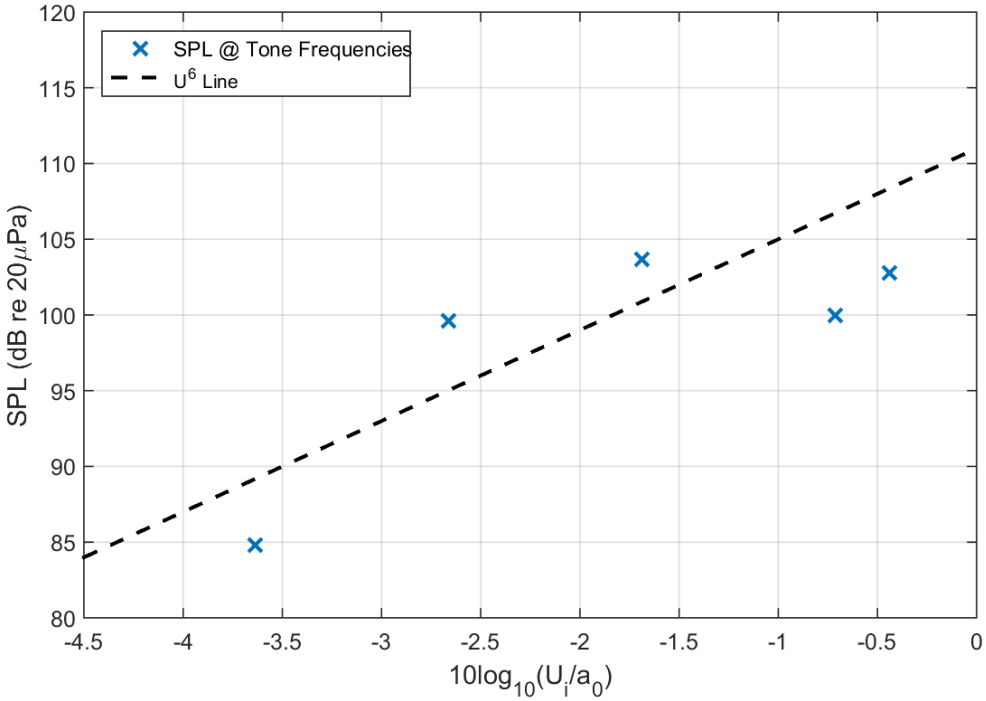

Figure 3.10: Tone SPL scaling with the internal velocity for the 1/4-in. diameter obstruction upstream of the four-inch diameter nozzle. D = 4in., R = 12 ft., θ = 90°, lossless.

It should be noted that for the four-inch diameter nozzle, the presence of the obstruction produced not only obtrusive tones, but also high level broadband noise. To understand how the overall contribution from the obstruction affects the measured farfield noise, OASPLs calculated from the measured lossless spectra were calculated and their variation with internal velocity examined.

Figures 3.11 and 3.12 show the OASPL scaling with the internal velocity for the 1/8-inch diameter and ¼-inch diameter obstructions upstream of the four-inch diameter nozzle, respectively. This is shown because often researchers will use measurements in this form. As seen in Figures 3.11 and 3.12, both the OASPL generated by the four-inch diameter nozzle and each of the two circular obstructions scales with the sixth power of the internal velocity, with a maximum deviation from the mean curve of 2 dB. The exception to this is the case of the 1/8-inch diameter obstruction at a jet Mach number of 0.8 (see Figure 3.10). This was addressed above in the discussion of the SPL at the tone frequencies. If this data point in Figure 3.11, is ignored, the OASPLs for both the 1/8-inch and the ¼-inch diameter can be assumed to be following a sixth power of the internal velocity as assumed in the double diameter methodology and can be used to simulate the rig-noise contamination in the verification process of the Doubling-Diameter Method.

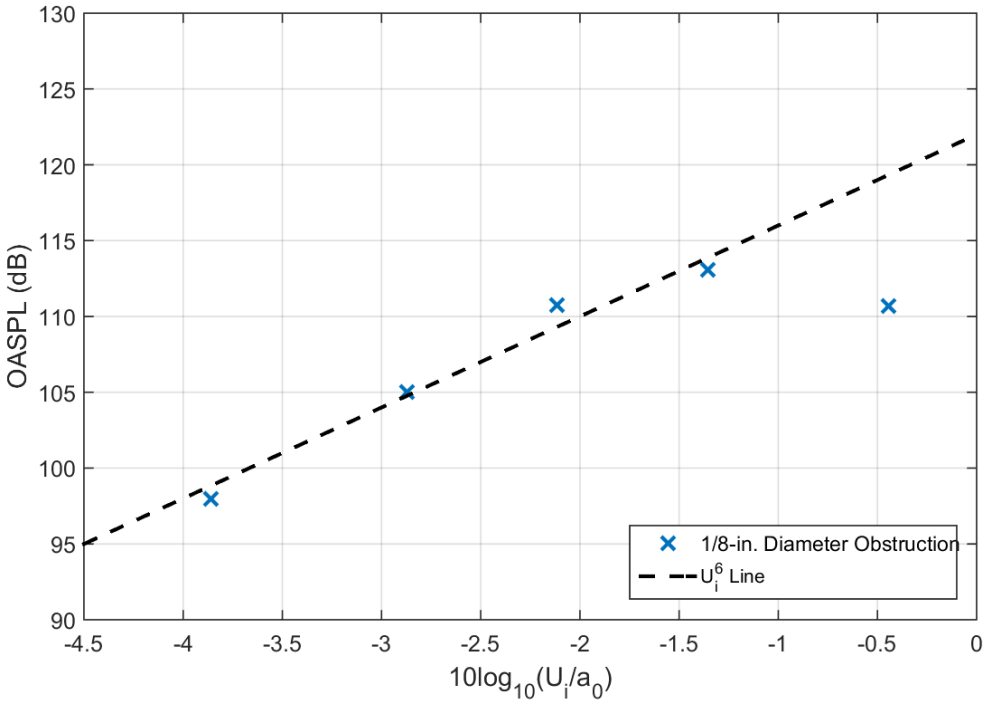

Figure 3.11: OASPL scaling with the internal velocity for the 1/8-in. diameter obstruction upstream of the four-inch diameter nozzle. D = 4in., R = 12 ft., θ = 90°, lossless.

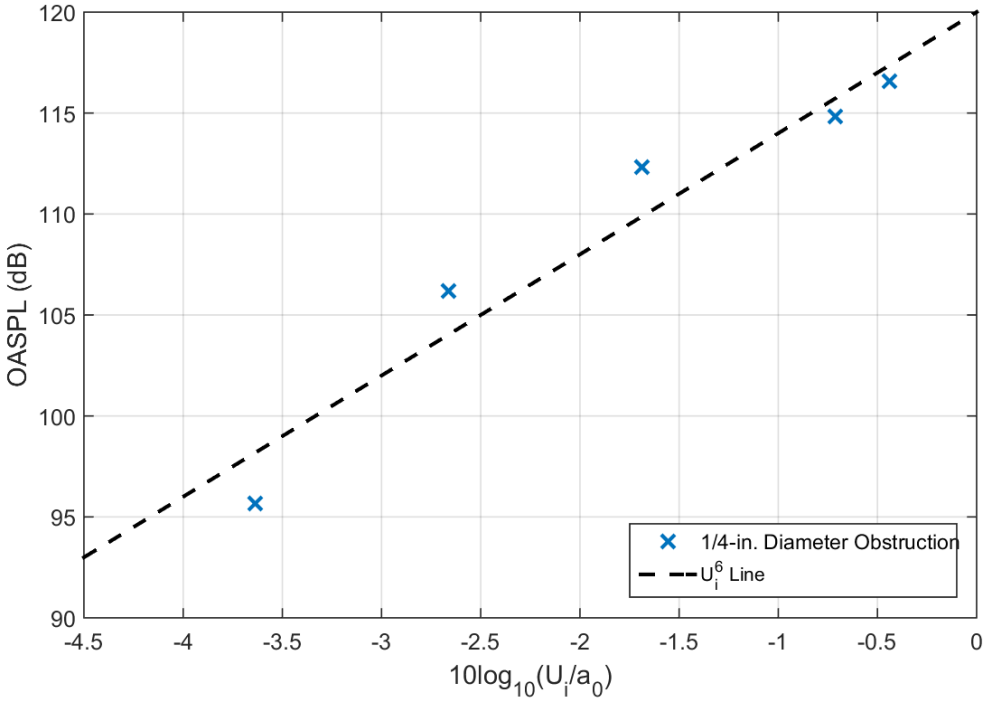

Figure 3.12: OASPL scaling with the internal velocity for the 1/4-in. diameter obstruction upstream of the four-inch diameter nozzle.D = 4in., R = 12 ft., θ = 90°, lossless.

As for the square obstruction, as is shown in Table 3.5, the internal velocity is close to the speed of sound for most of the conditions. This indicates that the square obstruction is likely causing a choked flow condition in the four-inch diameter pipe. In addition, observing the whole dataset, the tones become less prominent and eventually reduce below the level of the jet noise component as the jet velocity increases. But this test configuration also simulates the valve noise for certain conditions where the valve may be operating at a choked condition. The flow field produced from the situation is very complicated and well beyond the scope of the study. The calculated jet velocity and the velocity in the 4-in. diameter pipe section are ultimately determined by the pressure ratio that exists between the stagnation pressure and the ambient pressure in the chamber. Since the velocity is being adjusted by changing the stagnation pressure, there should be some relationship between the velocity in the pipe section and the calculated jet velocity. Figure 3.13 shows the calculated jet velocity scaling with the OASPL produced by the square obstruction and the four-inch nozzle at a polar angle of 90°. As seen in the Figure 3.13, the OASPL scales with the sixth power of the jet velocity. Similar results are seen at θ = 30° and 60°, as well. This is precisely what has been found in earlier studies on excess noise, notably by Bushell[45], where scaling of jet engine data in the presence of upstream noise was found to be proportional to the sixth power of the jet velocity.

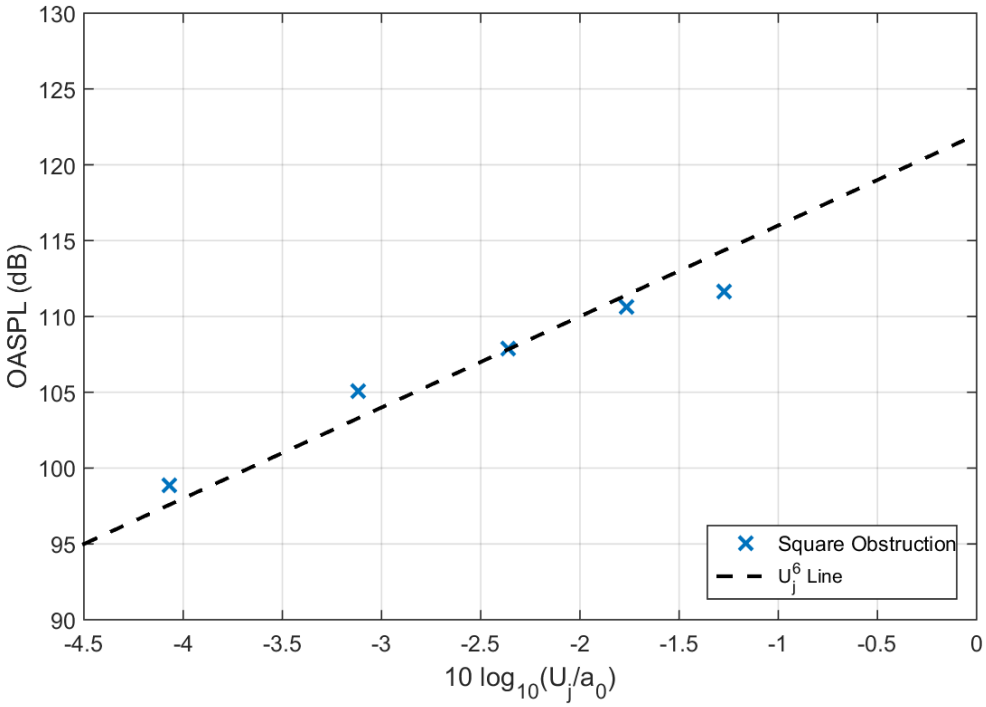

Figure 3.13: OASPL scaling with the internal velocity for the 1-in. square obstruction upstream of the four-inch diameter nozzle. D = 4in., R = 12 ft., θ = 90°, lossless.

Now that it has been established that the noise produced by the two-inch nozzle is unaffected by the obstructions and noise produced by the obstructions is the dominant noise source in the case of the four-inch nozzle, the Doubling-Diameter Method is applied to this dataset as way of verifying the method. Figure 3.14 shows the normalized frequency spectra for the case of 1/8-inch cylindrical obstruction for a jet Mach number of 0.6 at polar angles of 30°, 60°, and 90°. It is noted that similar results are seen for the other Mach numbers. From Figure 3.14, it is seen that spectral collapse is observed for Helmholtz/Strouhal numbers less than 1. This implies at normalized frequencies less than 1, jet noise is the dominant noise source, and at normalized frequencies greater than 1, the noise created by the upstream obstruction is dominant. As can be seen from Figure 3.14, the obstruction creates both a tonal and a broadband component in the four-inch exit case. Based on the total database, the tonal component reaches as high as 45 dB above the levels

of two-inch exit case. The broadband component is on average 20 dB above the two-inch diameter nozzle.

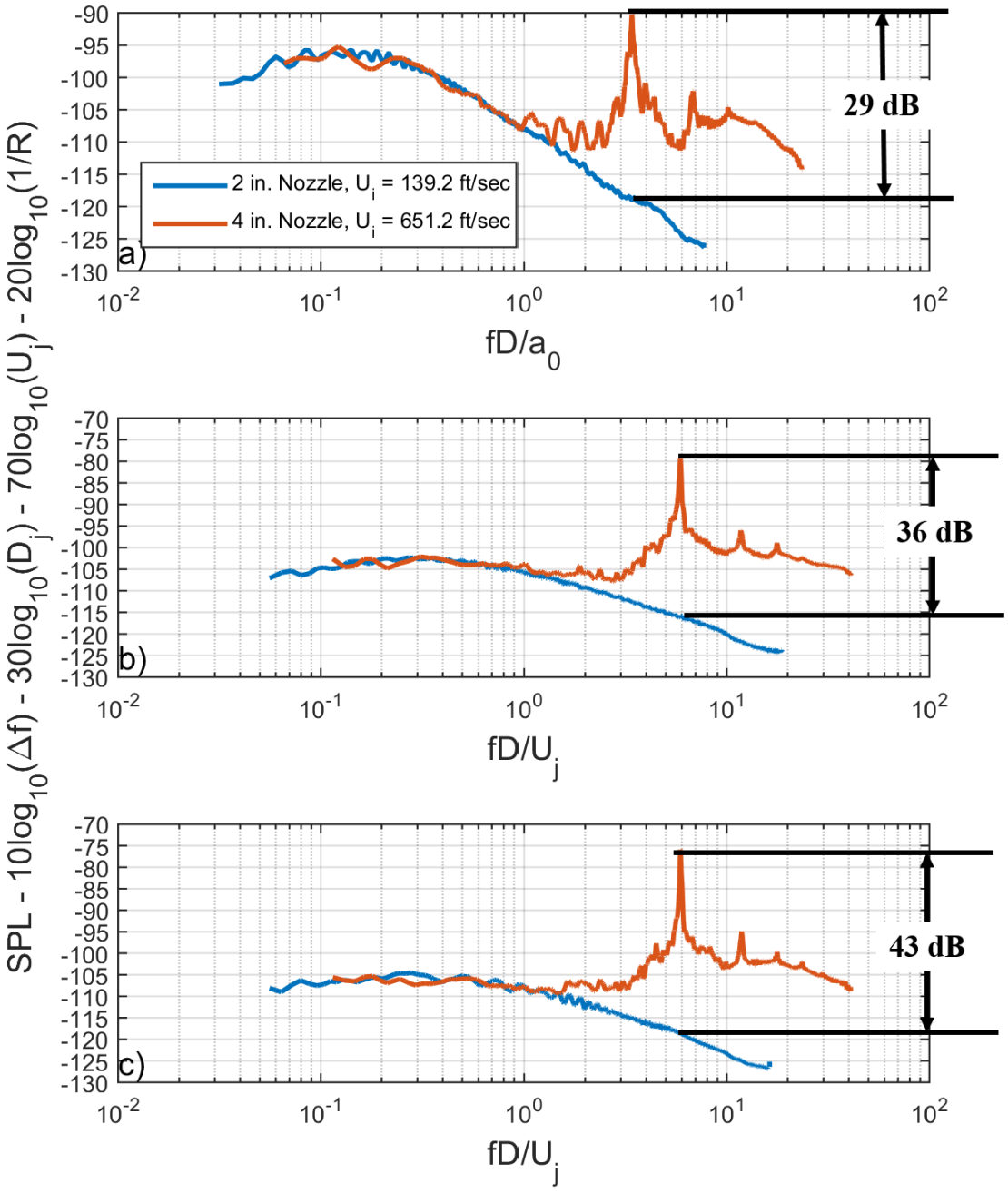

Figure 3.14: Effect of doubling the diameter from the two-inch nozzle to the four-inch nozzle with the 1/8-in. obstruction upstream of the nozzle-exit. a) θ = 30°, b) θ = 60°, and c) θ = 90°. M_j = 0.6, R = 12 ft., Δf= 32 Hz., lossless.

Figure 3.15 shows normalized narrowband frequency spectra (Δf = 32 Hz) for the two and four inch exits with the ¼-inch diameter circular obstruction upstream of the nozzle-exit at polar angles of 30°, 60° and 90° at a Mach number of 0.6. From Figure 3.15 it is seen that spectral collapse is observed for Helmholtz/Strouhal numbers between 0.5 and 1. Just like the 1/8-inch obstruction case, spectral collapse implies jet noise dominance. Obstruction noise dominates when the upstream velocity is high (i.e., in the case of the 4-inch diameter nozzle). In this case, the tonal component reaches as high as 45 dB above the levels of two-inch exit case, and the broadband component is on average 20 dB above that of the two-inch diameter nozzle.

Figure 3.16 shows normalized narrowband frequency spectra for the two and four inch exits with the square obstruction upstream of the nozzle-exit at polar angles of 30°, 60° and 90° at a Mach number 0.6. From Figure 3.16, spectral collapse is not observed at all. This implies that jet noise is not the dominant noise source in the case of the four-inch diameter exit over the whole frequency range. The noise produced by the square obstruction is more broadband and lower frequency than that produced by the circular obstructions. The tonal component in the four-inch diameter exit case is as high as 28 dB above the two-inch exit case, and broadband component ranges from 5-15 dB above the two-inch case. Similar results are observed at the other Mach numbers.

It is worth pointing out that we were expecting an increase of 36 dB on doubling the diameter, but it was not always that value. As alluded to above, this difference can easily be attributed to reflection of the internal noise upstream by the nozzle-exit, non-omnidirectional directivity of the noise radiated from a nozzle in the presence of the flow and non-linear propagation of the high intensity sound from inside of the duct to farfield

and in that process losing tonal energy to harmonics. In some cases, the noise contamination was over 40 dB. While it is above the theoretical 36 dB increase explained above, there is likely some excitation of the jet in those cases to create the so called broadband amplification of jet noise (See Ahuja et al.[64]). In addition, using Helmholtz number and Strouhal number as the normalized frequencies moves the tones into the position where this 40 dB is seen. If the internal velocity or cylinder diameter were to be used as the length and velocity normalizing parameter, the tones in the 4-inch nozzle spectra will shift left compared to the 4-inch nozzle spectra rendering the difference closer to 36 dB. At any rate, it is seen that if not exactly 36 dB, in most cases, comparable levels of increase are noted on doubling the diameter of the nozzle.

This thus validates the Doubling-Diameter Method as a way for detecting or obtaining an indication of the existence of rig-noise contamination. As assumed, the obstructions used as the simulated rig-noise contamination source scale roughly with the sixth power of the internal velocity. The Doubling-Diameter Method was able to show this increase, as well as, the frequencies at which the contamination occurred.

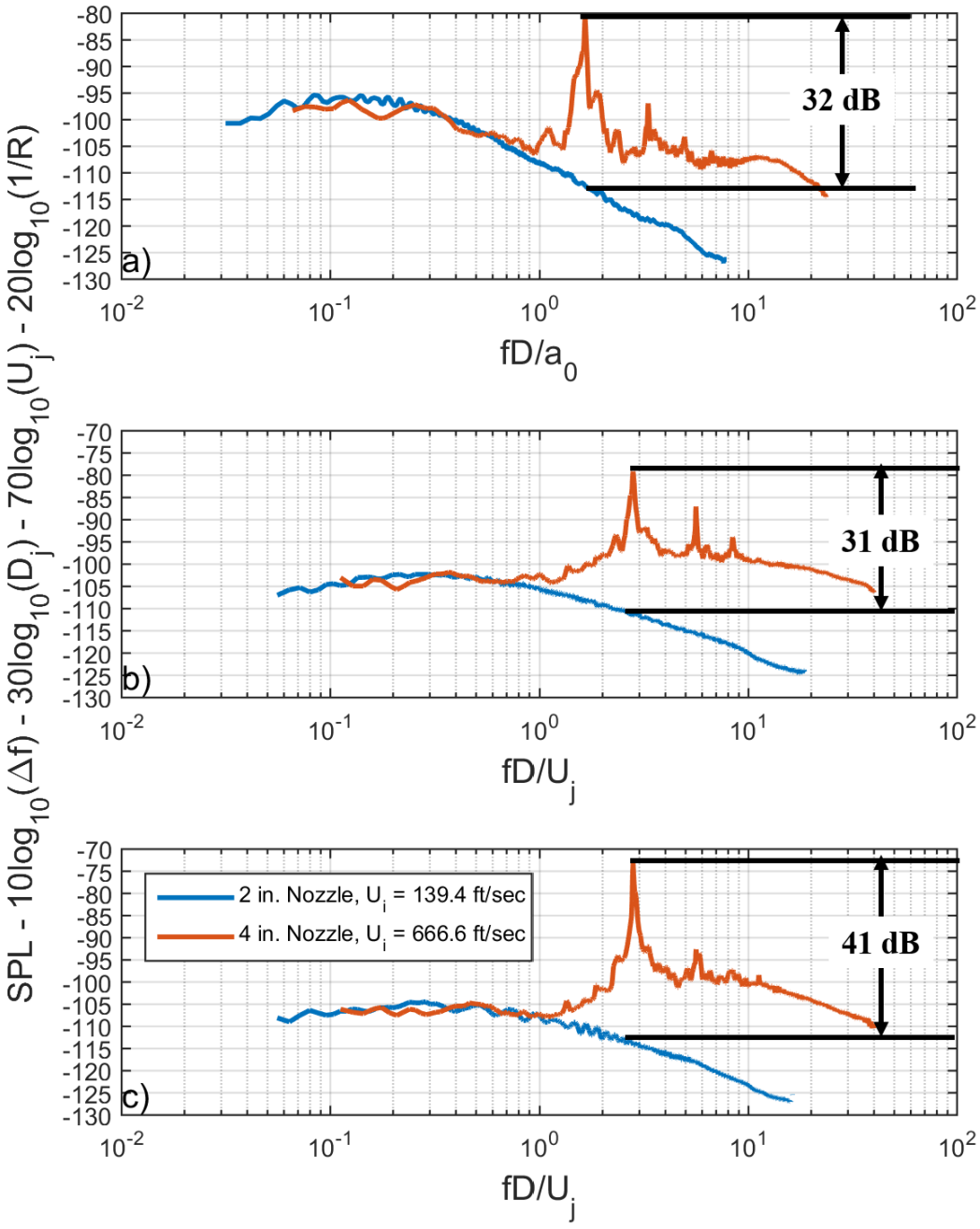

Figure 3.15: Effect of doubling the diameter from the two-inch nozzle to the four-inch nozzle with the ¼-inch obstruction upstream of the nozzle-exit.a) θ = 30°, b) θ = 60°, and c) θ = 90°. M_j = 0.6, R = 12 ft., Δf= 32 Hz., lossless.

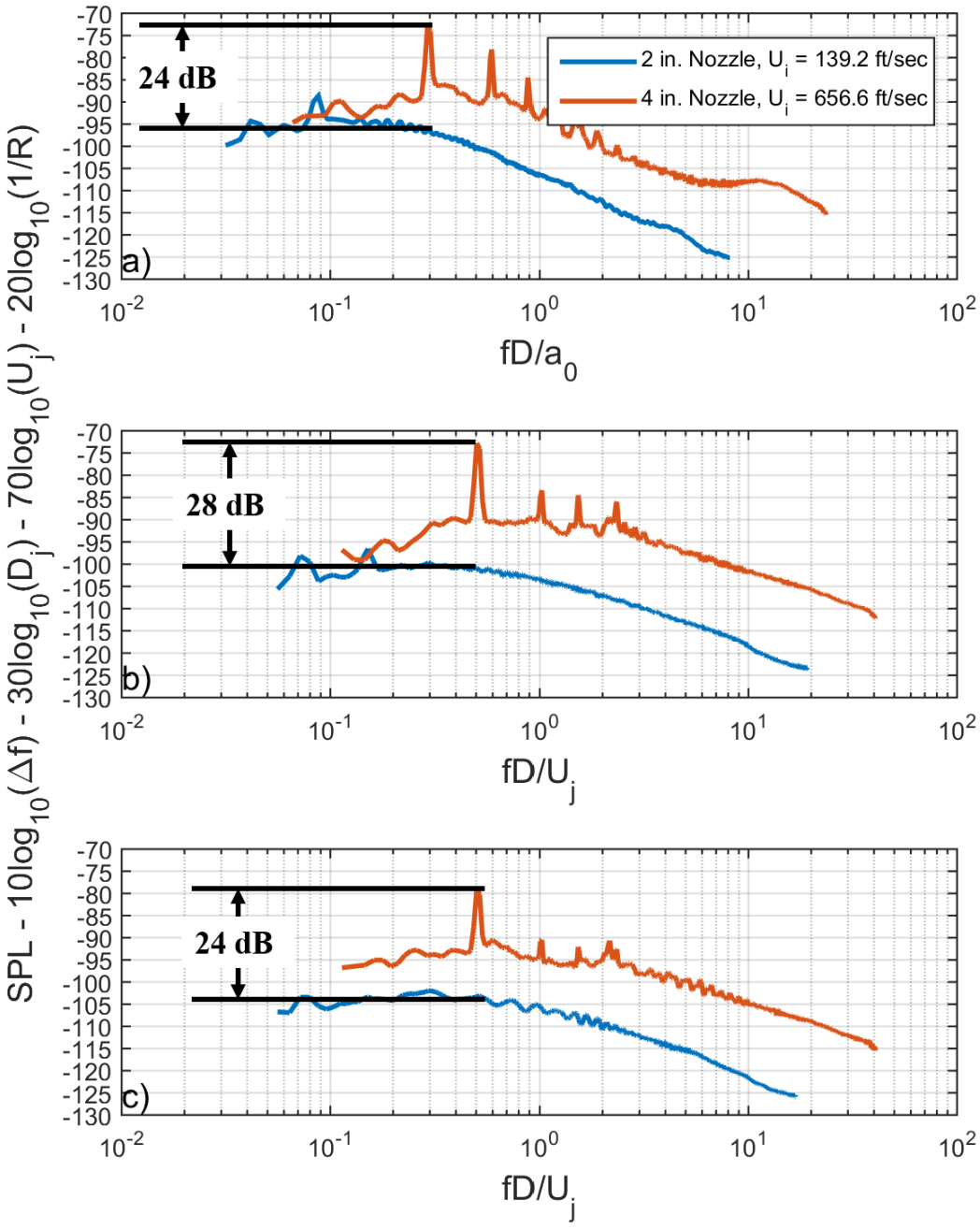

Figure 3.16: Effect of doubling the diameter from the two-inch nozzle to the four-inch nozzle with the square obstruction upstream of the nozzle-exit.a) θ = 30°, b) θ = 60°, and c) θ = 90°. M_j = 0.6, R = 12 ft., Δf= 32 Hz., lossless.

In the test cases discussed above, there was no silencer located downstream of the obstructions that simulated rig noise. But in most good jet noise facilities one employs silencers upstream of the nozzle-exit and downstream of any valves use to control the flow, as indeed in the facility used here. In such a situation, doubling of the nozzle is likely to increase the noise by 36 dB upstream of the silencer, but unless the silencer absorbs all of the rig noise, some rig noise may still show up as rig contamination in the farfield noise measurements, depending upon the rig noise amplitude and the design of the silencer. That was indeed the case in the present facility as discussed below.

Figure 3.17 shows normalized narrowband frequency spectra for the two and four inch exits without an obstruction upstream of the nozzle-exit at polar angles of 30°, 60° and 90° at a Mach number of 0.6. Spectral collapse is observed at Strouhal/ Helmholtz number less than 1, but at the higher frequencies, as much as 11 dB of rig noise appears to be present. Once again, this implies that jet noise is the dominant noise source at normalized frequencies less than one. At normalized frequencies greater than one, all of rig-noise contamination that was not dissipated by the upstream silencers is dominant. (It is for this reason that the jet flow facility used here is not used for testing nozzles much larger than 2-inch diameter.) These high-frequency noise sources are not going to be studied in depth here because that is beyond the scope of this work. This high-frequency noise, which is as high as 11 dB above that produced by a clean jet, is assumed to be rig-noise contamination.

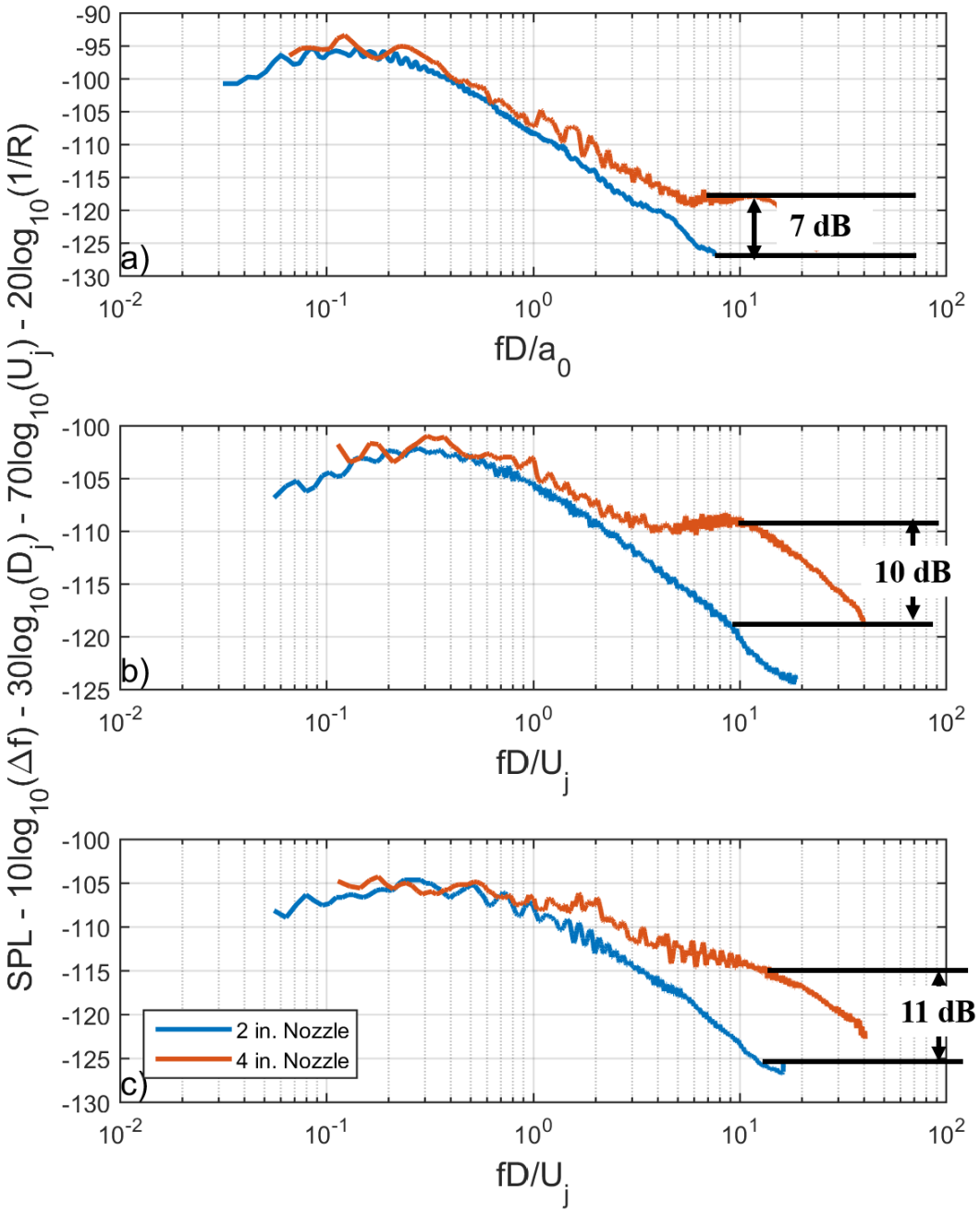

Figure 3.17: Effect of doubling the diameter from the two-inch nozzle to the four-inch nozzle without an obstruction upstream of the nozzle-exit. a) θ = 30°, b) θ = 60°, and c) θ = 90°. M_j = 0.6, R = 12 ft., Δf= 32 Hz., lossless.

3.3.2 Case Study of the GTRI Anechoic Jet-Facility

In this section, the Doubling-Diameter method is used in a case study to show how one can verify that jet noise measurements are free of rig-noise contamination. For this purpose, six nozzles ranging from 0.25 inches to 4 inches in nozzle-exit diameter are used as described above. Figures 3.18 – 3.20 show the normalized narrowband spectra for the six nozzles at Mach numbers of 0.4, 0.6, and 0.8 and at polar angles of 30°, 60°, and 90°. Spectral collapse is observed for most frequencies within ±2 dB for all nozzles except the 4-inch nozzle where considerable deviation is noticed at high frequencies. This case study shows that for the Mach numbers 0.4 – 0.8 and for nozzle diameters from ¼ inches to two inches, if there is no upstream noise downstream of the silencer and if any rig noise is produced from the piping and the valve upstream of the nozzle, it is all absorbed by the silencer. A lack of a precise collapse at all frequencies in the jet spectra for these nozzles is perhaps related to differing nozzle-exit boundary layer (See Bogey et al.[32-37], Karon and Ahuja[65]) and to the simplification of Lighthill's equation to arrive at the scaling used here.

Data up to a Mach number of 0.8 is shown here. Since jet noise is related to seventh power of the jet velocity for narrowband spectra and rig-noise is related to the sixth power of the internal velocity, for a given nozzle diameter the jet noise will become louder as the jet velocity increases. This means that for an appropriate nozzle size, jet noise with a jet Mach number greater than 0.8 will also be free of rig-noise contamination. Rig-noise contamination clearly exists at high-frequencies in the case of the four-inch nozzle, which as high as 15 dB, which most likely would have been higher were the silencer not in place.

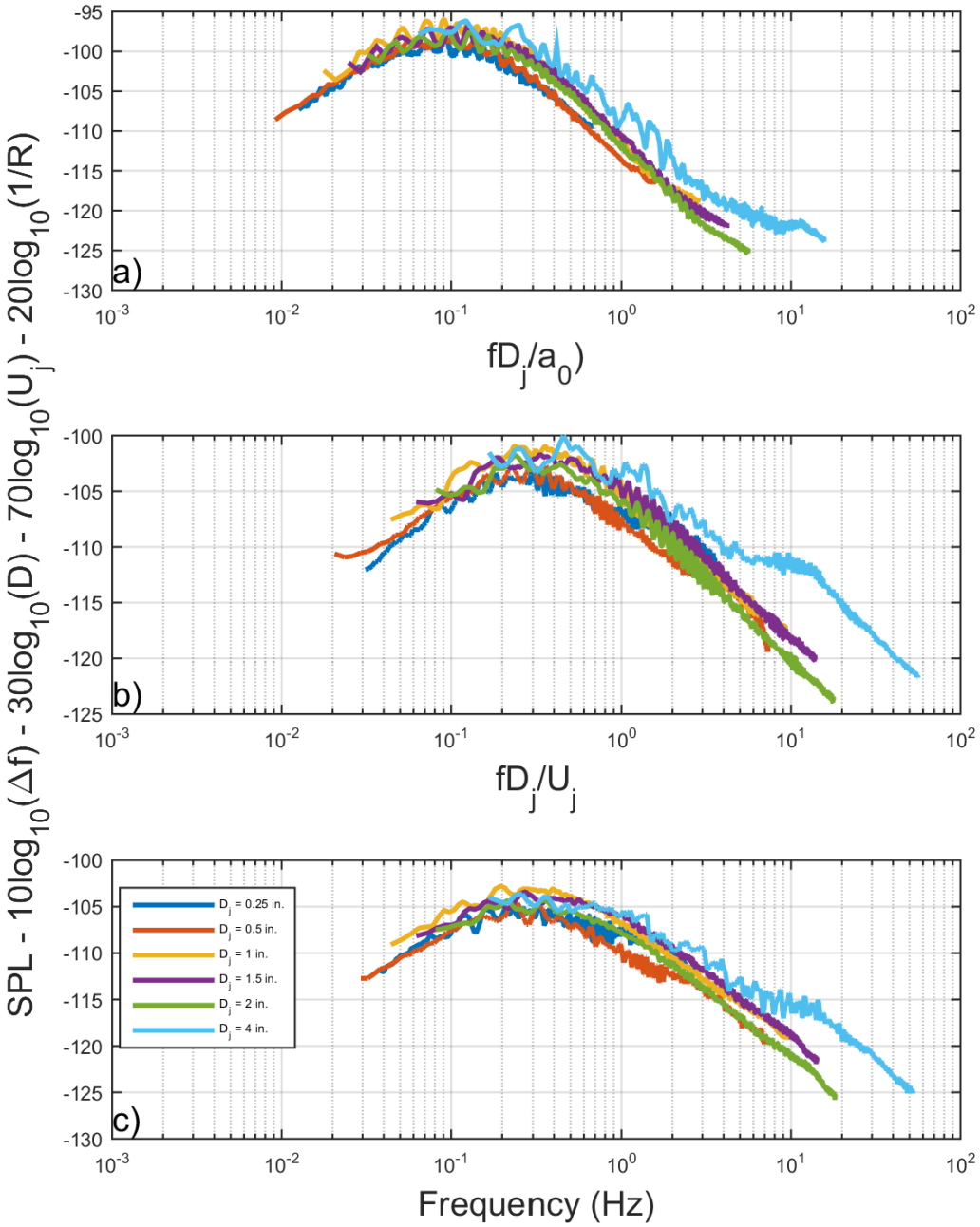

Figure 3.18: Normalized narrowband spectra for nozzles of varying exit diameter at M_j = 0.4. a) θ = 30°, b) θ = 60°, and c) θ = 90°. Δf = 32 Hz, lossless.

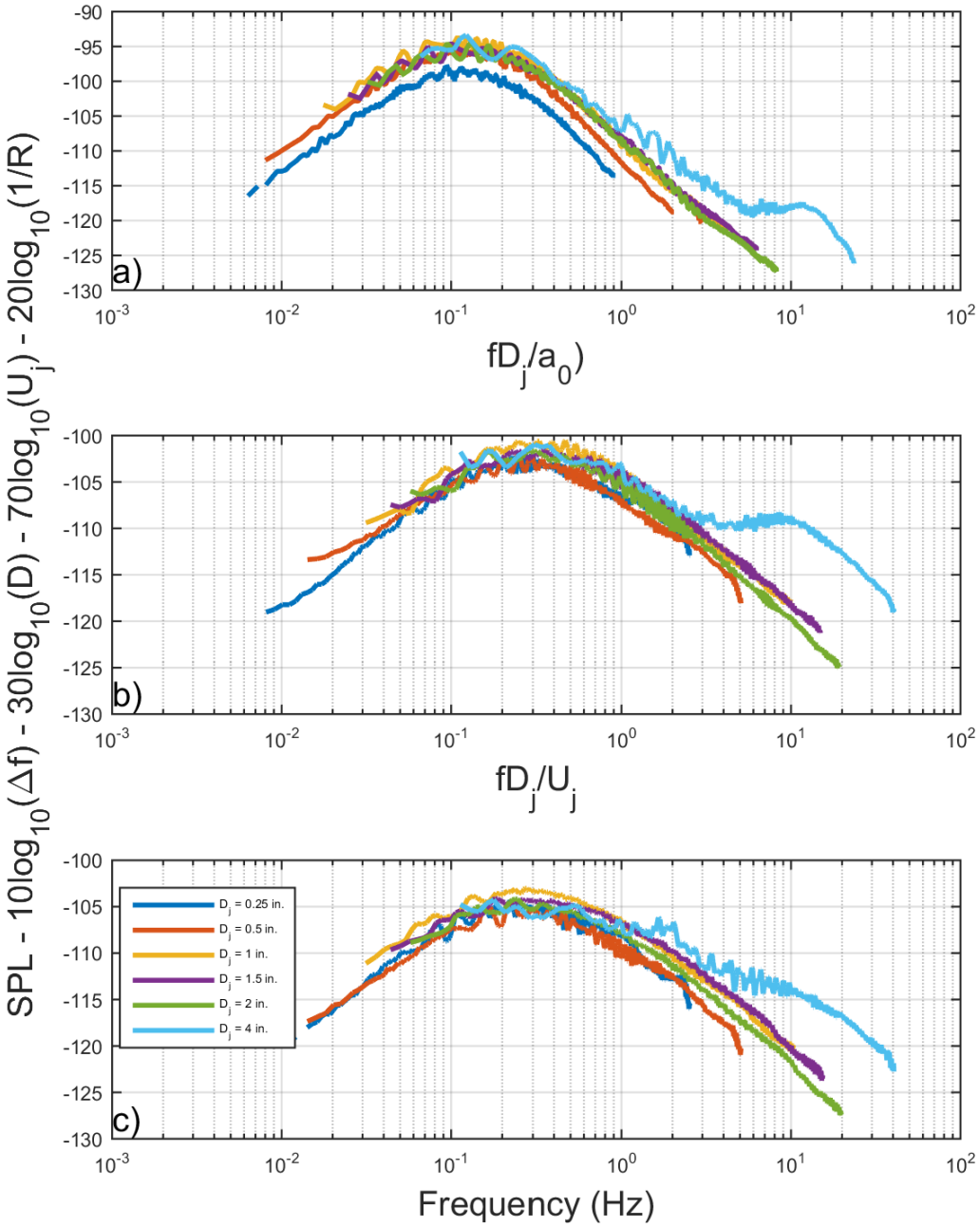

Figure 3.19: Normalized narrowband spectra for nozzles of varying exit diameter at $M_j = 0.6$. a) θ = 30°, b) θ = 60°, and c) θ = 90°. Δf = 32 Hz, lossless.

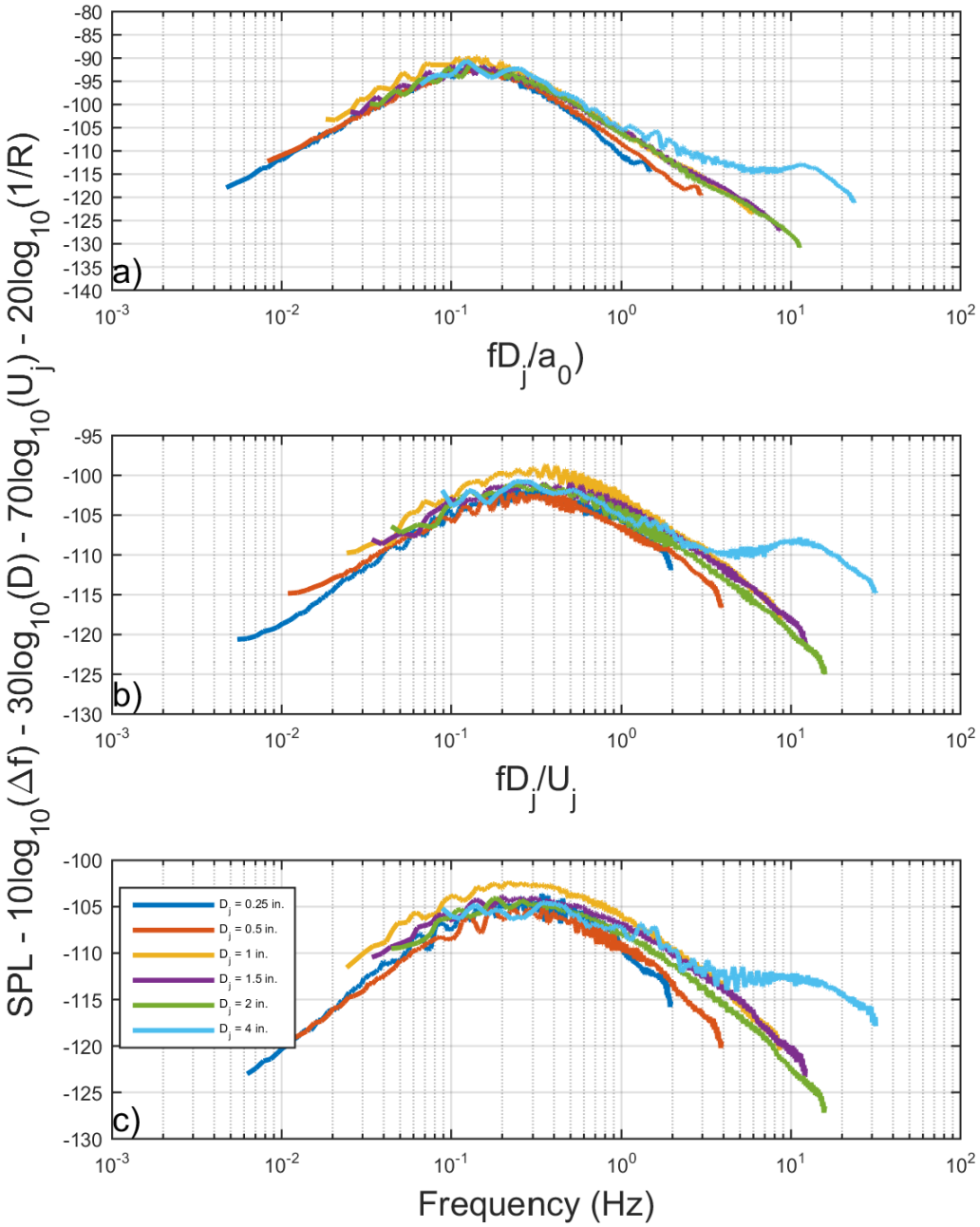

Figure 3.20: Normalized narrowband spectra for nozzles of varying exit diameter at $M_j = 0.8$. a) $\theta = 30°$, b) $\theta = 60°$, and c) $\theta = 90°$. $\Delta f = 32$ Hz, lossless.

3.4 Conclusions

In this study, the Doubling-Diameter Method for detecting rig-noise contamination in jet noise measurements was investigated for its ability to perform this task. The method was found to detect the presence of rig-noise contamination quite well. The case study performed on jet noise measurements acquired in the GTRI Anechoic Jet-Facility verified that jet noise is clean in this facility without any rig-noise contamination for nozzle-exit diameters up to two inches. Larger nozzle-exit diameters are likely to have rig-noise contamination as shown by the four-inch diameter nozzle. This provides confidence in the measurements acquired in this facility for nozzles of up to at least 2 in-diameter for not just the present work but for all future work to be performed in this facility. The experiments in this study were only carried out in the subsonic velocity regime, as supersonic jet noise would likely be loud enough to completely drown any rig-noise as observed by other researchers[43].

CHAPTER 4

EFFECTS OF REYNOLDS NUMBER ON JET NOISE

The Reynolds number and the Mach Number are classical quantities for evaluating the similarity between different aerodynamic flows. The Reynolds number represents the ratio of the inertial effects to the viscous effects of the flow, and the Mach number represents the ratio between the kinetic energy and the internal energy of the flow (Anderson[66]). By matching the Reynolds and Mach numbers of an aerodynamic flow, an experiment can create a flow similar to that encountered in the real world. Traditionally, jet noise measurements from model-scale experimental studies have been extrapolated to full-scale engines using the classical scaling laws, most notably the D^2, U_j^8, and the inverse square laws. The question that remains is: if the properties of the flow measured in an anechoic jet-facility do not match another in terms of both Reynolds and Mach number, can these flows be extrapolated to full-scale jet engines? This study will investigate this very question.

4.1 Previous Work

4.1.1 Review of Jet Noise Scaling Laws

In 1952, the first jet noise theory was developed by Lighthill[1-3] in the form of the acoustic analogy. The results of Lighthill's acoustic analogy take the form of the jet noise intensity scaling relationship:

$$I \sim \frac{\rho_m^2}{\rho_0}\frac{U_j^8}{a_0^5}\frac{D_j^2}{R^2}\,(1 - M_c\cos(\theta))^{-5} \tag{4.1}$$

A scaling/normalization scheme, based on Equation 4.1 is commonly used by the jet noise community (for example, see Ahuja and Bushell[40] and Ahuja[8]). Frequencies are normalized using the Strouhal number:

$$St \equiv \frac{fD_j}{U_j} \tag{4.2}$$

The amplitudes are normalized using the expression:

$$A(St) = SPL - 80\log_{10}(U_j) - 20\log_{10}(D_j) - 20\log_{10}\left(\frac{1}{R}\right) +$$

$$50\log_{10}(1 - M_c\,cos(\theta)) - 20\log_{10}(\rho_m) + 10\log_{10}(\rho_0) + 50\log_{10}(a_0) \tag{4.3}$$

When Equation 4.3 is used, the effects from these parameters are removed and the amplitude of a spectrum at each Strouhal number should be normalized to a constant value. This means theoretically that every jet noise spectrum can be reduced to the same normalized spectrum. Equation 4.3 can be used in reverse to predict jet noise spectra for a jet of any desired parameters. This prediction scheme is still used today. The only change in this scheme in more recent years is that at small angles ($\theta<40°$), the frequencies are normalized to the Helmholtz number as shown in Ahuja[8] and Michel and Ahuja[41], which is defined by the following the expression:

$$He = \frac{fD_j}{a_0} \tag{4.4}$$

Gaeta and Ahuja[42] revisited the scaling scheme that was presented in Equations 4.1 – 4.4. They showed that jet noise presented in 1/3-octave band spectra and narrowband spectra scale differently. They showed that the scaling scheme shown in Equation 4.3 works for 1/3-octave band spectra. For scaling the narrowband spectra, Gaeta and Ahuja[42] derived the following expression:

$$A(St) = SPL - 10\log(\Delta f) - 70\log(U_j) - 30\log(D_j) - 20\log\left(\frac{1}{R}\right) + 50\log(1 - M_c\,cos(\theta)) - 20\log(\rho_m) + 10\log(\rho_0) + 50\log_{10}(a_0)$$

(4.5)

The Δf term in Equation 4.5 adds the requirement of all scaling to be performed in the form of Power Spectral Density (PSD). The extra D_j/U_j comes out of the math, and it is important to mention that Gaeta and Ahuja[42] found that narrowband spectra collapse and scale better using this method. It is noted here that in the study presented by Gaeta and Ahuja[42] only velocity scaling was studied and that they showed that narrowband jet noise spectra scale with D_j^3 and U_j^7.

4.1.2 Previous work Related to the Effects of the Reynolds Number of Jet Noise

The Reynolds Number of a jet flow with respect to the nozzle-exit diameter is defined as[66]:

$$Re_D = \frac{\rho\, U_j\, D_j}{\mu} \tag{4.6}$$

Stromberg et al.[67] investigated the flow features and acoustics from a jet of 7.9 mm exit diameter converging nozzle at a Mach number of 0.9, which had a Reynolds number of 3600. In terms of the flow field, they found low Reynolds number jets develop differently than jet flows of high Reynolds number. The low Reynolds number jet initially develops at a slower rate compared to high Reynolds number jets, making it initially a laminar jet. Further downstream, the turbulence growth rate actually exceeds those of a large Reynolds number jet, resulting in the length of the potential core being the same for both low and

high Reynolds number jets. In terms of the acoustics, they found that the overall sound levels and directivity are similar to those of higher Reynolds number jets.

Long and Arndt[17] performed a comparison of jet noise spectra from jets of different Reynolds numbers. They measured jet noise produced by nozzles that had nozzle-exit diameters of 1.4, 2.4, 4.1, and 7.1 mm, where the change in diameter caused the change in Reynolds number. They then compared their narrowband noise spectra results with noise spectra measured by other experimentalists for nozzles of larger diameters, and thus higher Reynolds numbers. They found that a 7dB difference existed between the low Reynolds number jets they tested and jets of larger Reynolds number tested by others, with all other operating conditions, except Reynolds number, for all the jets kept the same. This comparison is shown in Figure 4.1 where, $\frac{p'^2}{\left(\rho U_j^2\right)^2}\left(\frac{R}{D_j}\right)^2\left(\frac{U_j}{\Delta f D_j}\right)$ is plotted as a function of Strouhal number. As seen in Figure 4.1, the spectra do not collapse to a single spectrum and the high Reynolds number jets produce noise about 7 dB higher than the low Reynolds number jets. Long and Arndt[17] noted that these differences could be caused by a breakdown in the large-scale turbulence structures. The label "This Study" in Figure 4.1 refers to the measurements acquired by Long and Arndt[17]. Hoping to get a better frequency normalization, Long and Arndt[17] plotted $\frac{p'^2}{\left(\rho U_j^2\right)^2}\left(\frac{R}{D_j}\right)^2\left(\frac{a_0}{\Delta f D_j}\right)$ as a function of Helmholtz number. This comparison is shown in Figure 4.2, and just like the comparison in Figure 4.1, there exists a clear 7 dB amplitude difference between the low and high Reynolds number jets. Even though, neither of the normalization schemes shown in Figures 4.1 and 4.2 follows the classical scaling schemes given in Equations. 4.4 and 4.9, since the spectra being compared in Figure 4.1 are at the same velocity and polar angle, in theory the spectra

should collapse to a single spectrum. As seen in Figure 4.1, the spectra do not collapse, which implies that the Reynolds numbers may play an important role in deciding the amplitudes of jet noise.

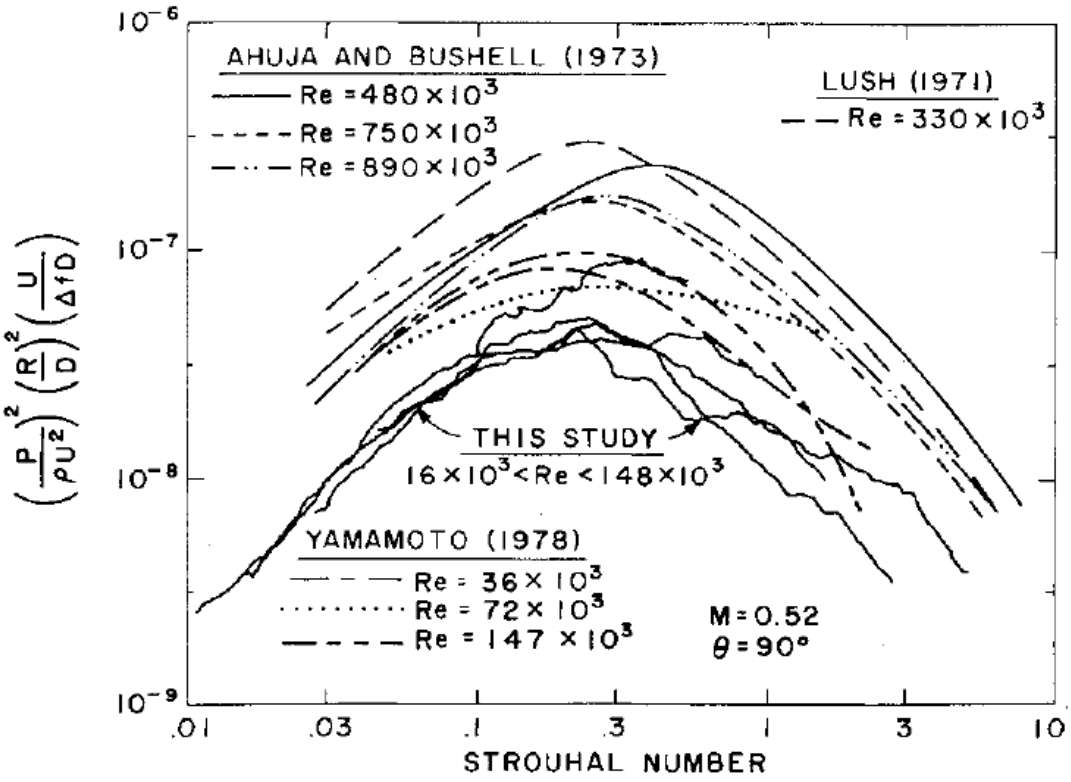

Figure 4.1: Results of the study performed by Long and Arndt[17].

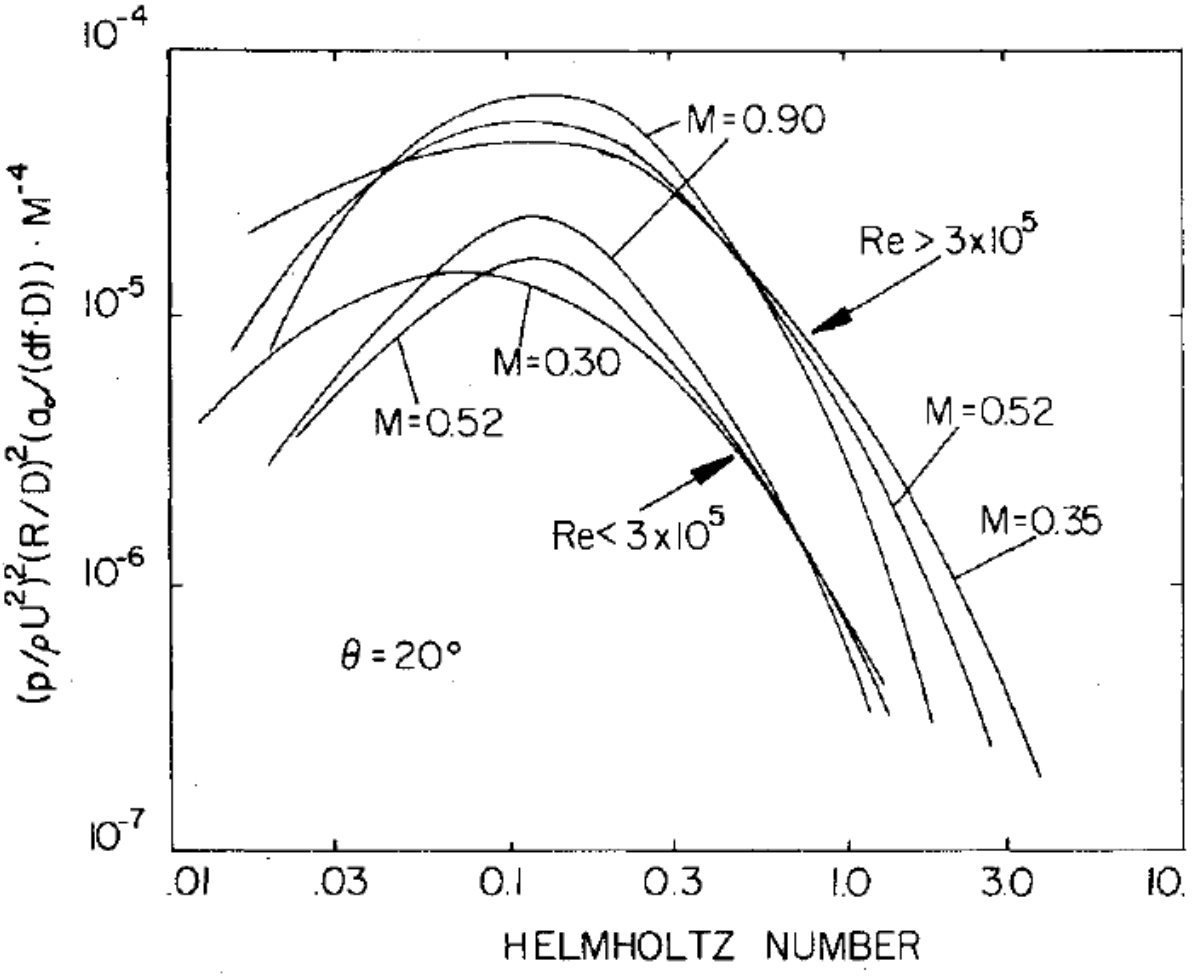

Figure 4.2: Results of the study performed by Long and Arndt[17] with the frequencies normalized to Helmholtz Number.

Kastner et al.[18] compared computational jet noise results of a low Reynolds number jet with the data of a high Reynolds number experimental jet. The comparison is shown in Figure 4.3. They found that at high frequencies, the SPL of the low Reynolds number jet was lower than that of the high Reynolds number jet. This is different from what was found by Long and Arndt[17], who observed a 7 dB difference between the low Reynolds number jets and the high Reynolds number jets at all frequencies. It should be pointed out that the two jets used in the analysis of Kastner et al.[18] had vastly different Reynolds numbers. In this comparison, the low Reynolds number was 3600 and the high Reynolds number was

1060000. The jet velocity and nozzle-exit diameter of the low Reynolds number jet were 288 m/s and 0.0079 m, respectively, while those for the high Reynolds number jet were 385m/s and 0.0254 m, respectively. In addition, the spectra in Figure 4.3 is for a polar angle of 30°. The frequencies of spectra in Figure 4.3 have been normalized to the Strouhal number without normalizing the amplitude. This creates some uncertainty in the conclusions derived from the spectral comparison in Figure 4.3 for the reasons: as stated above, Helmholtz number is the appropriate frequency normalization quantity at low polar angles. In fact, Ahuja and Bushell[40] and Ahuja[8] found that at low angles the higher velocity jets experienced a lower normalized high-frequency noise levels than those of lower velocity jets, when Strouhal number was used as the frequency normalization scheme. Kastner et al.[18] state that their amplitude adjustment scheme is method outlined in Ahuja and Bushell[40], but it is unclear if all the nuances of the scaling for low polar angles was

taken into account. This adds uncertainty to their results as to the effect of Reynolds number given the disparity of the conditions of the two jets as stated above.

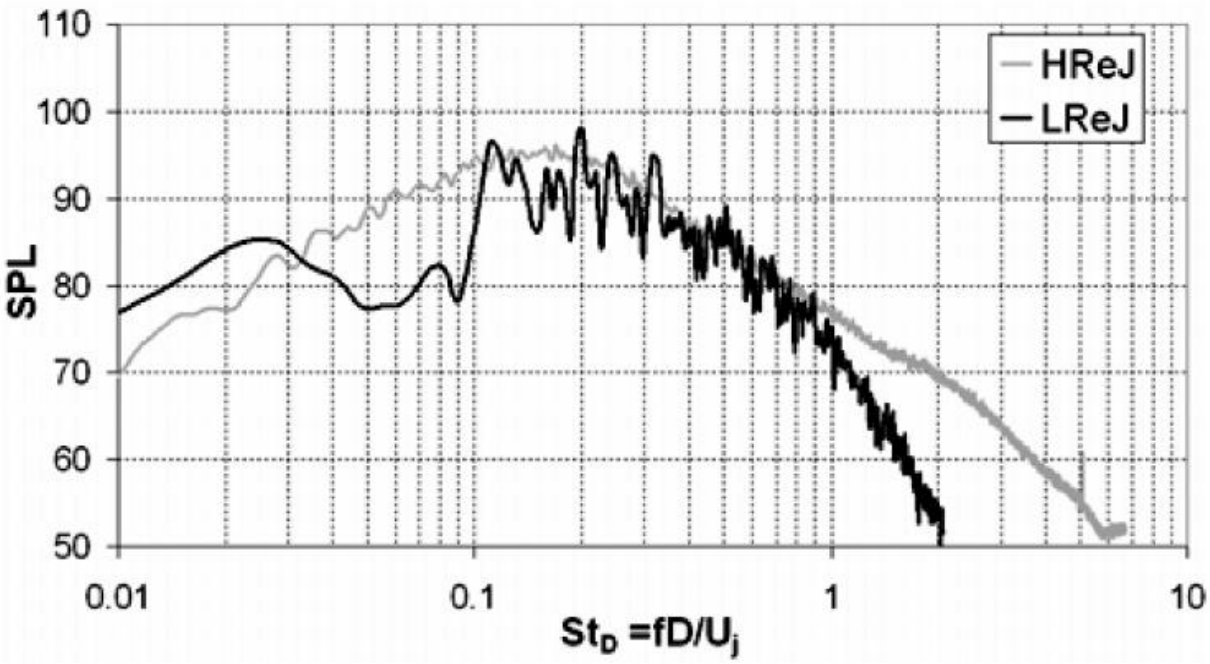

Figure 4.3: Results of the study performed by Kastner et al. [18].

Bhat[19] also examined the effects of Reynolds number on jet noise by comparing the noise measurements of three different nozzle-exit diameters: 1.5 in., 2.46 in., and 3.46 in. The Reynolds numbers were changed by changing the nozzle diameter, but maintaining the same exit velocity. Figures 4.4 and 4.5 illustrate examples of these normalized, narrowband spectra at 90°. These figures show the jet noise spectra of these three nozzles at Mach numbers of 0.6 and 0.7, respectively. He showed that at high frequencies, mostly to the right of the spectral peaks, the jet noise levels increase with increasing Reynolds number. It is interesting to note, that similar to the results of Kastner et al.[18], the effect of the Reynolds number is only seen in the high-frequency region, and not across the whole spectrum like that shown by Long and Arndt[17]. Bhat[19] claims that the reason for this behavior is that large Reynolds number jet-flows contain more fine-scale turbulence than

lower Reynolds number jet-flows, so that would result in more high-frequency noise. This line of thinking is consistent with Long and Arndt[17] and Kastner et al.[18] because a faster rate of large-scale turbulence breakdown would result in more small-scale turbulence, which happens at higher Reynolds numbers compared to lower Reynolds numbers. Bhat[19] also noted that the Reynolds number of the flow can be influenced by the nozzle-exit conditions, and he could not guarantee that the nozzle-exit boundary layer state was consistent for each nozzle.

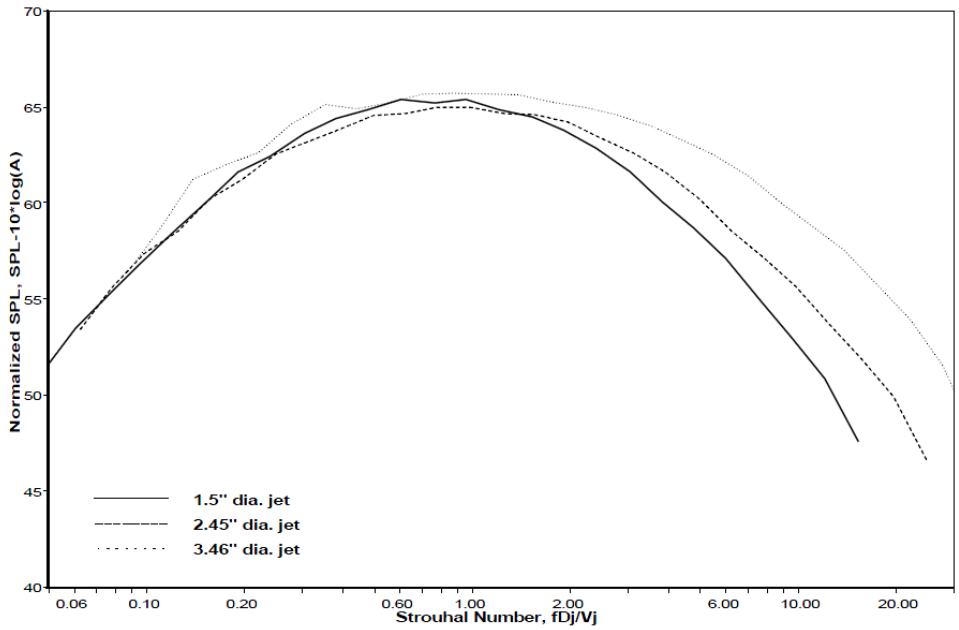

Figure 4.4: Noise of jets of different diameters at Mach 0.6 acquired by Bhat[19].

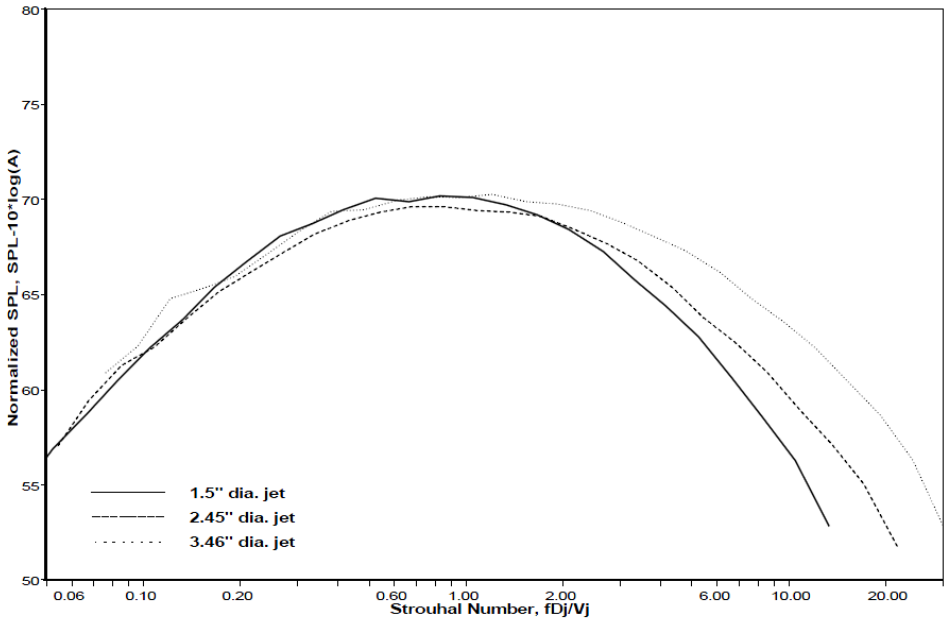

Figure 4.5: Noise of jets of different diameters at Mach 0.7 acquired by Bhat[19].

4.2 Experimental Program

4.2.1 Facility Description

The facility used for this study was the GTRI Anechoic Jet-Facility. These facilities are described in Burrin, Dean and Tanna[59], Burrin and Tanna[60], and Ahuja[10]. The GTRI Anechoic Jet-Facility was setup in two different configurations over the course of this study. The first configuration is shown in Figure 4.6. In this configuration, the jet nozzle was mounted directly to the jet-facility's plenum chamber and microphones used to measure the jet noise were mounted to a circular microphone arc that was centered at the center of the jet-facility. Three farfield microphones were used, which were mounted at polar angles of 30°, 60°, and 90° and at distances of 11 feet, 12 feet, and 10 feet, respectively. The microphones were placed at these distances to place the microphone as far in the farfield as possible within the confines of the anechoic chamber, while being

some distance from the anechoic wedges themselves. The second configuration is shown in Figure 4.7. This second configuration was required for measuring the noise produced by the smaller nozzles, which are described below. It is known that jet noise scales with the size of the nozzle-exit exit diameter. Special attention was paid to ensure that the ambient noise did not contaminate the measured jet noise spectra. In this configuration, a special nozzle, which was designed to have pipe extensions attached to its straight section, was mounted to the plenum in the jet-facility. Four feet of two-inch diameter pipe extensions were attached to this nozzle. The jet nozzle was attached to the end of the pipe extensions. In this configuration, three microphones were used to measure the jet noise. Three microphones were mounted at polar angles of 30°, 60°, and 90° on an existing

microphone traverse shown in Figure 4.7, which in this case just served as a stationary microphone array.

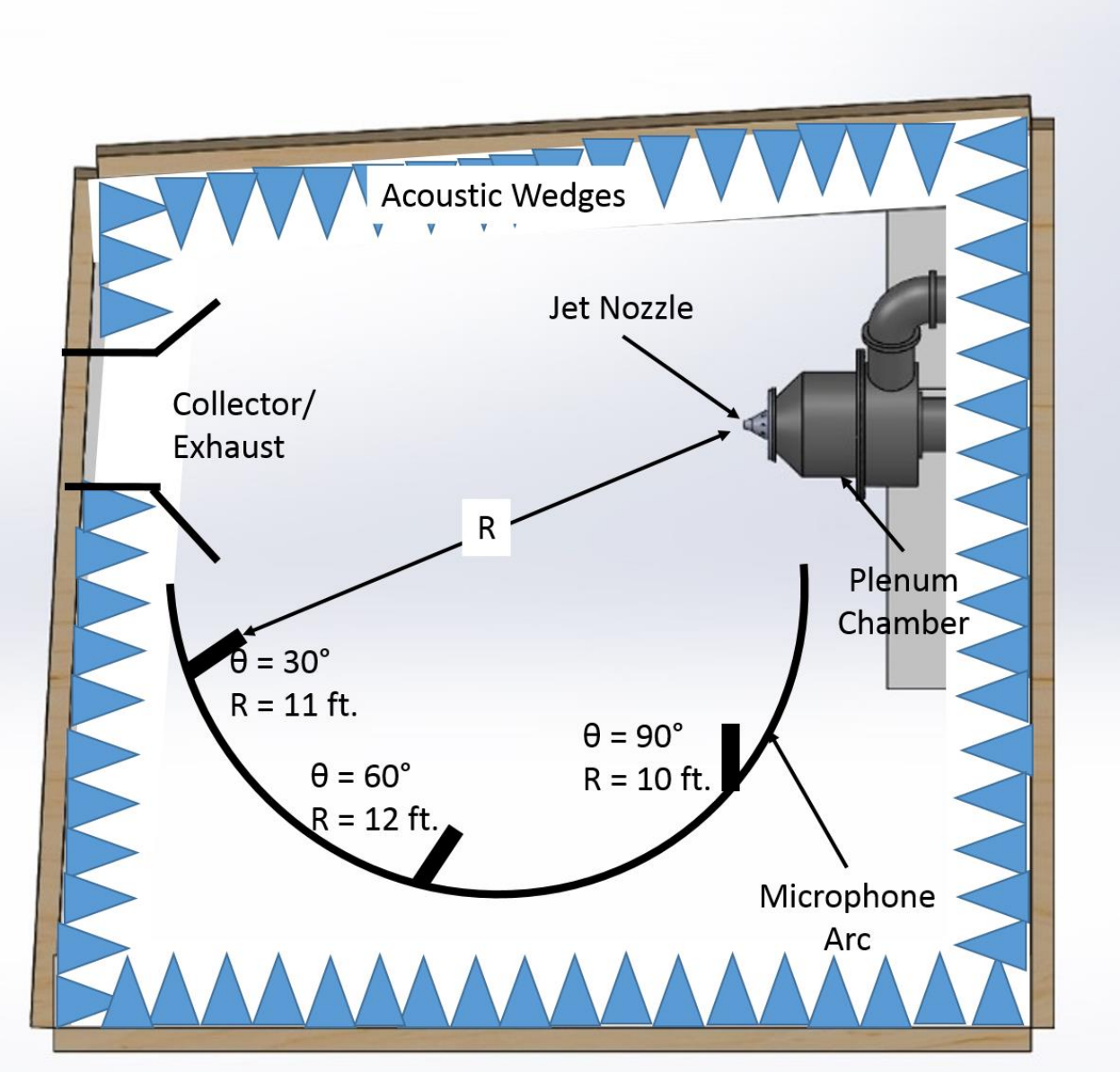

Figure 4.6: Configuration for the first set of experiments.

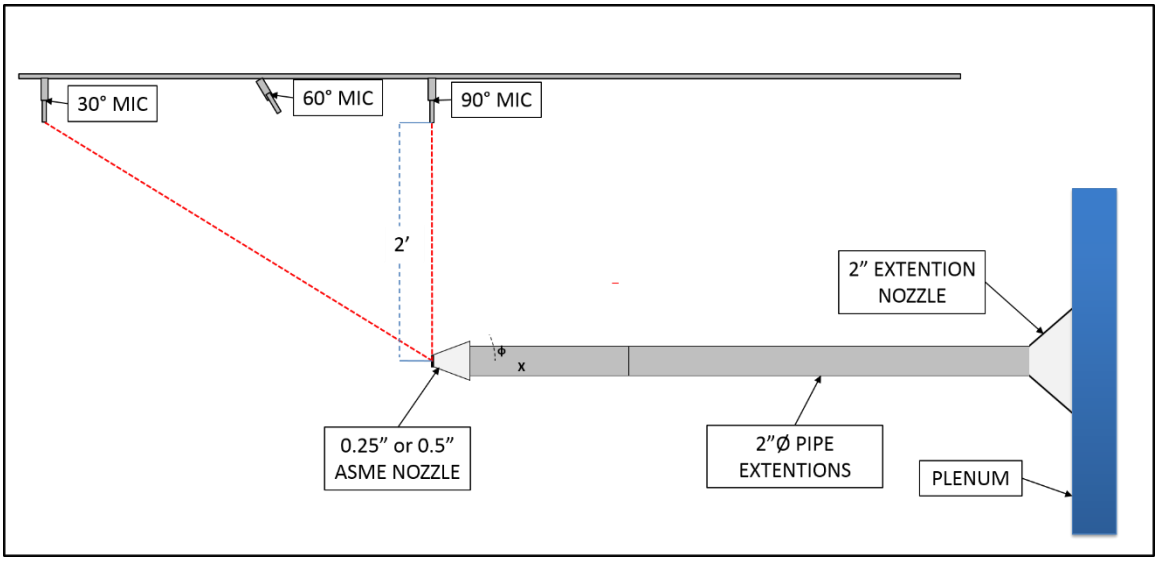

Figure 4.7: The test set-up in the GTRI Anechoic Jet-Facility with the small nozzles.

The acoustic measurements were acquired using 4939 Bruel and Kjear (B&K) ¼-inch free-field microphones, which are attached to 2669 B&K preamplifiers. The 4939 microphones have a frequency range of 4 – 100,000 Hz. The ¼-inch microphone-preamplifier combinations were connected to B&K 2960-A-0S4 Nexus conditioning amplifiers that not only amplify the signal but serve as the microphones' 200 millivolt power supply. The signals were then fed into a National Instruments (NI) PXIe-4499 module inside of an NI PXIe-1073 chassis. The sampling frequency of the PXIe system is a maximum of 204.8 kHz, and this is the frequency at which the microphones are sampled. All the microphone measurements were processed in LabView, the NI programming language.

The pressure signals were processed into averaged frequency spectra. For these experiments, the sampling frequency used with the analyzer was 204.8 kHz; thus 204,800 samples of the acoustic pressure signal were acquired every second. These time signals were processed to provide averaged power spectra using a window size of 6400 samples,

50% overlap, and a Hanning window. This created a Δf of 32 Hz. and a smooth spectral curve. These spectra were then corrected for a variety of conditions, as detailed in Ahuja[10]. The effects of microphone geometry, the microphone protective grid, microphone actuator response, and incidence of the microphone with respect to the source are accounted for as part of the microphone free-field frequency response. This correction, is a function of both frequency and the angle of incidence of the sound wave on the microphone, is lumped together and will be denoted by the variable $A\ (f, \Psi)$. In addition, a foam ball windscreen was used on the $\theta = 30°$ microphone, to prevent hydrodynamic fluctuations from affecting the measurements. The effects of windscreen on a broadband frequency spectrum was determined experimentally and is denoted by the variable $B(f)$. The effect of atmospheric attenuation was accounted for by using the method presented in ANSI S1.26-1995[61]. This atmospheric-attenuation correction methodology contains many equations and is too long to present here, but is shown in Appendix B. This method results in a frequency-dependent attenuation coefficient $\alpha(f)$, which has the units of dB/m. Removing the attenuation effects and applying all of the microphone related corrections described above provides the so-called "lossless spectra," which will be used throughout the analysis. The advantage of this form of the data is that it allows the data from different facilities, different microphones, and acquired on different days to be compared with one another. This also allows the theoretical predictions, which are independent of microphone responses, to be compared with the measured lossless data. Finally, the jet noise measurements are extrapolated to a common distance to help with needed comparisons. This distance was selected to be 72 nozzle diameters and is performed using the inverse square law, which is

part of Equation 4.1. Combining these effects, the free-field and lossless jet noise spectrum is calculated using the equation:

$$SPL(f)_{ree-field,lossless} = SPL_{uncorrected} - A(f,\Psi) + B(f) + \alpha(f)R_1 + 20\log_{10}\left(\frac{R_1}{R_2}\right) \quad (4.7)$$

where R_1 is the distance between the nozzle-exit and the microphone at the time of measurement and R_2 is the extrapolated distance between the microphone and nozzle-exit used in the inverse square law. Corrections for any of the parameters shown in Equation 4.1 are simply done by removing that effect using Equations 4.3 or 4.5 and then adding the effect of the changed parameter back into the spectrum by using the reverse operation. An example of this correction procedure is shown in Appendix A. As an additional level of processing, the uncorrected measurements are compared to the ambient noise measurements. Any data point that is within a ΔSPL of the ambient noise measurements is disregarded due to ambient noise contamination.

The following is a description of the instrumentation used to acquire measurements about the conditions of the jet-flow. The stagnation temperature was measured using a K-type thermocouple located in the jet plenum chamber. This temperature was recorded using one of two devices depending on the availability of the instrumentation: (1) a thermocouple reader box, which outputs a 100 mV/°F DC voltage signal, which was measured using the same PXIe DAQ used for the acoustic measurements or (2) NI SCXI-1112 thermocouple cards inside of a NI SCXI-1001 chassis. The stagnation pressure was measured using a pitot probe located in the jet plenum chamber that is read by a NetScanner Model 9816 pressure reader mounted inside a NetScanner Model 98RK chassis, which also read the chamber's ambient pressure. The chamber's ambient humidity and temperature

were measured using a Newport Electronics ITHP-5-DB9 humidity and temperature probe. The jet properties were then calculated using the isentropic flow relationships. Since the ambient pressure for the jet is also the jet's static pressure, the jet Mach number was calculated using the expression:

$$M_j = \left(\left(\left(\frac{p_t}{p_a} \right)^{\frac{\gamma-1}{\gamma}} - 1 \right) \frac{2}{\gamma-1} \right)^{\frac{1}{2}} \tag{4.8}$$

The jet static temperature, speed of sound in the jet, jet velocity, and ambient speed of sound were then calculated using the equations listed below:

$$\text{The jet static temperature: } T_j = \frac{T_t}{1+\frac{\gamma-1}{2}M_j^2} \tag{4.9}$$

$$\text{The speed of sound in the jet: } a = \sqrt{\gamma R T_j} \tag{4.10}$$

$$\text{The jet velocity: } U_j = M_j a \tag{4.11}$$

$$\text{The ambient speed of sound: } a_0 = \sqrt{\gamma R T_a} \tag{4.12}$$

When setting the jet conditions, the velocity, Mach number or ambient Mach number (U_j/a_0) are used.

4.2.2 Technical Approach

The effect of the Reynolds number on jet noise measurements is examined by varying the nozzle-exit diameter using nozzles of similar design constraints with respect to curvatures of the inner surfaces of the nozzle, contraction ratio, and the distance of the nozzle-exit from an upstream location where the nozzle starts to converge. ASME nozzles, whose design constraints are shown in Figure 4.8, were used. Jet noise measurements were acquired for Mach numbers ranging from 0.4 to 0.8, at polar angles of 30°, 60°, and 90°

with respect to the downstream axis, using the microphone configurations shown earlier in Figures 4.6 and 4.7 for nozzles of exit diameter of 0.25, 0.5, and 2 inches.

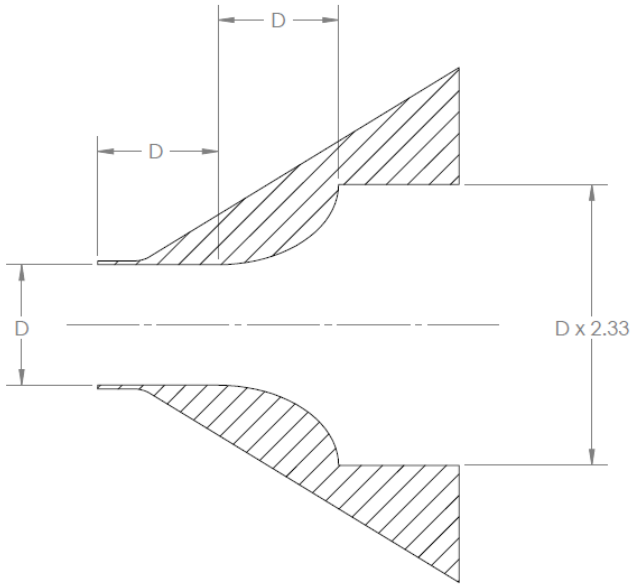

Figure 4.8: Design constraints for an ASME nozzles.

4.3 Results

4.3.1 Typical As-Measured Lossless Spectra as a Function of Reynold Number

Before any of the results are shown, it is noted that a large amount of data was acquired during this study. To avoid needless repetition in the analysis, while the analysis is based on the whole data set, only a small portion of the data is shown in the figures. Figures 4.9 and 4.10 show the jet noise spectra for the 0.25-in., 0.5-in., and the 2-in. nozzle-exit diameter nozzles, at polar angles of 30°, 60°, and 90° and at Mach numbers of 0.4 and 0.8, respectively. The following key observations are made from Figures 4.9 and 4.10. Firstly, it is clearly indicated in Figures 4.9 and 4.10 that as the nozzle-exit diameter is increased from 0.25 in. to 0.5 in. (doubling the nozzle-exit diameter) the noise increases by 9 dB, and

quadrupling the nozzle-exit diameter from 0.5 in. to 2 in. leads to an 18 dB increase. This is consistent with the nozzle-exit diameter scaling with D_j^3 for narrowband spectra, as presented by Gaeta and Ahuja[42]. Secondly, the frequencies of the jet noise spectra shift to lower frequencies as the nozzle-exit diameter is increased. The frequencies are halved as the nozzle-exit diameter is doubled from 0.25 in. to the 0.5 in., and the frequencies are further reduced to an additional fourth as the nozzle-exit diameter is quadrupled from 0.5 in. to 2 in. This is consistent with the fact that the frequencies can be normalized by Strouhal and Helmholtz numbers. Based in Equations 4.2 and 4.4, frequencies are related to the inverse of the nozzle-exit diameter, and the data in Figures 4.9 and 4.10 show this to be consistent. Thirdly, as indicated in the legend of Figures 4.9 and 4.10, with the doubling or quadrupling of the nozzle-exit diameter, the Reynolds number is doubled or quadrupled as well. Jets from the 2-inch nozzle-exit diameter nozzle have a Reynolds number 8 times as large as the Reynolds number from the 0.25-inch nozzle for a given Mach number. Despite this difference, the nozzles scale with the diameter scaling relationship presented by Gaeta and Ahuja[42]. This seems to indicate that in fact that the Reynolds number with respect to diameter does not affect the noise produced by jet in addition to the diameter and velocity effects.

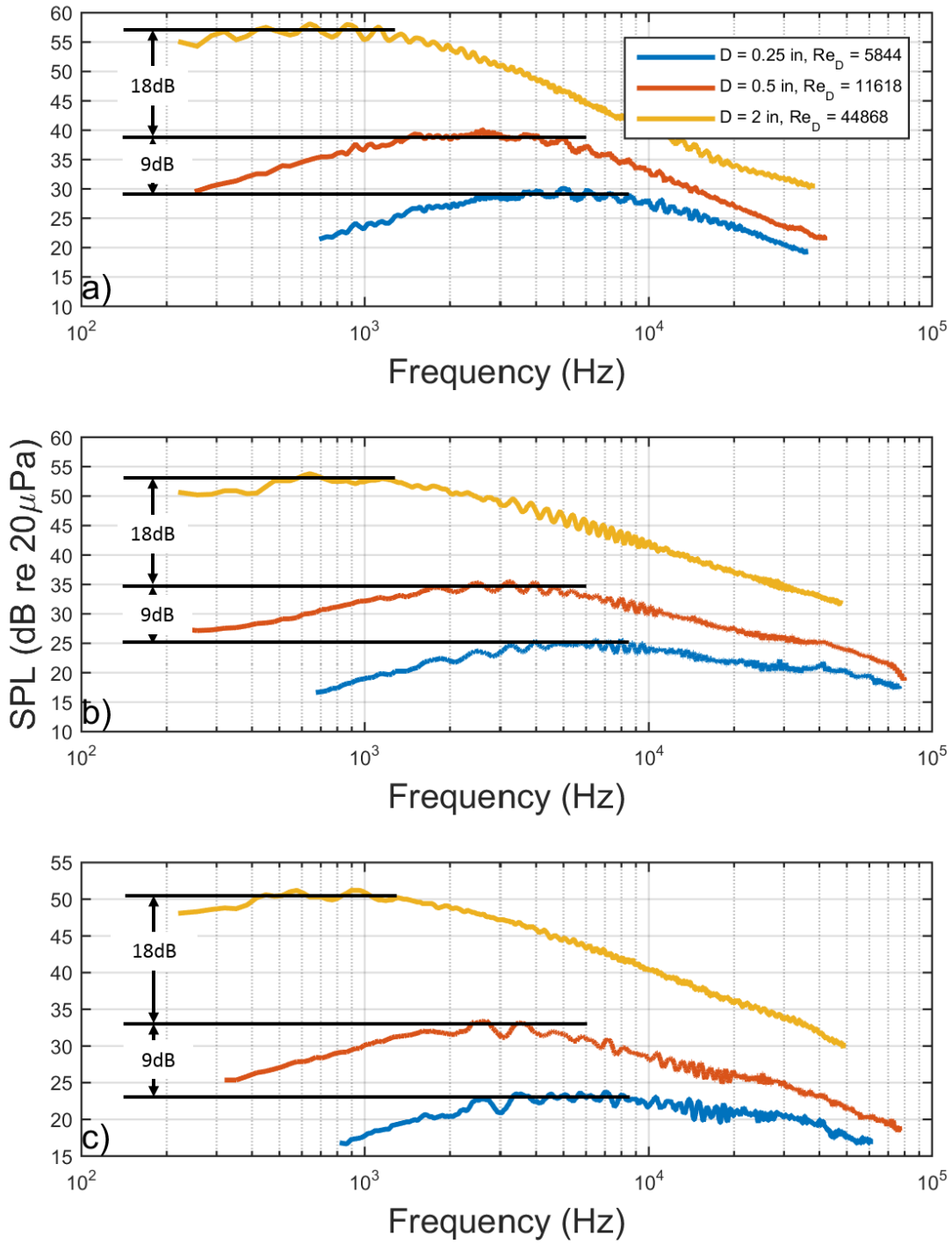

Figure 4.9: Jet noise measurements from the three nozzles used in this experiment at M = 0.4. a) θ = 30°, b) θ = 60°, and c) θ = 90°. R = 12 ft., Δf = 32 Hz, lossless.

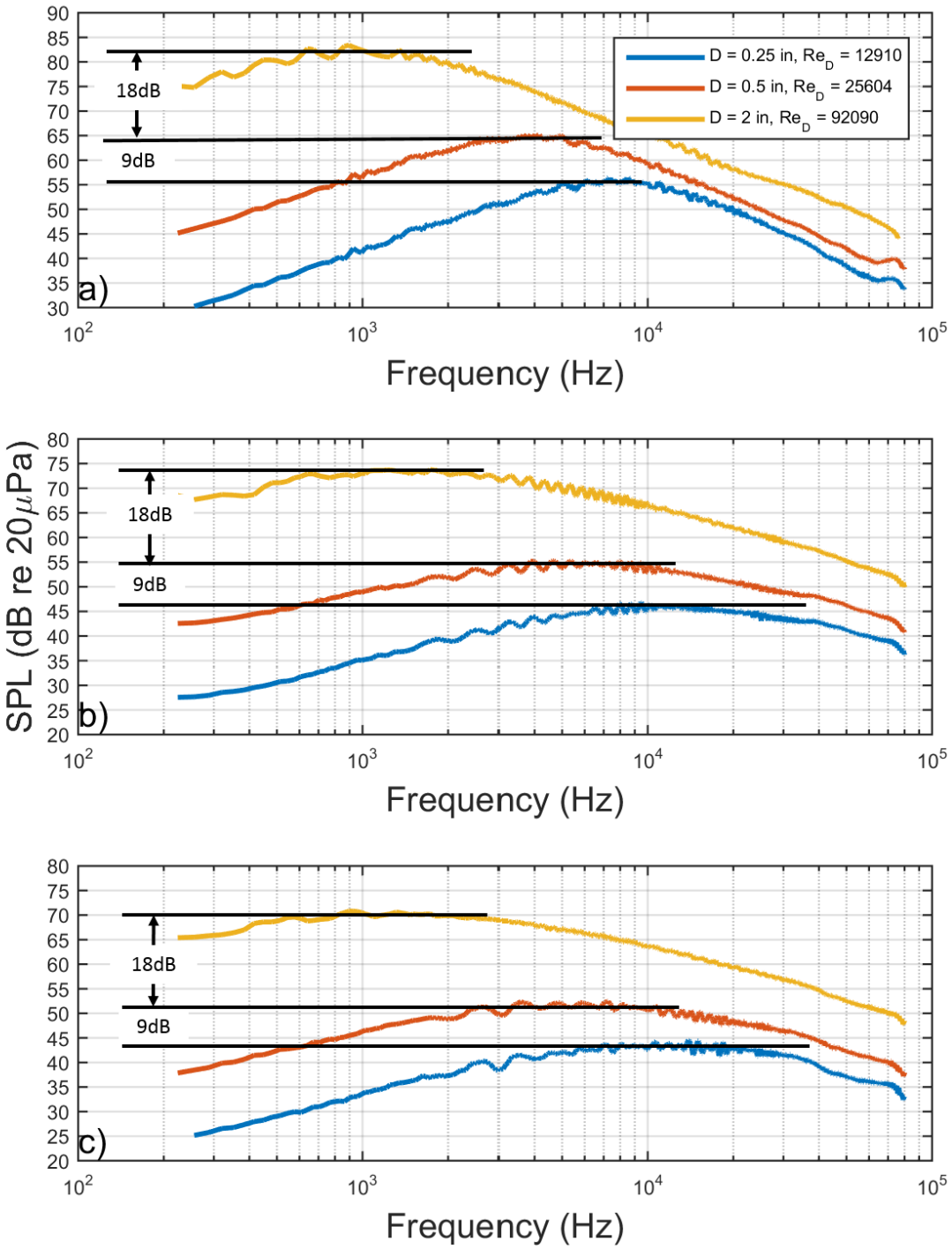

Figure 4.10: Jet noise measurements from the three nozzles used in this experiment at M = 0.8. a) θ = 30°, b) θ = 60°, and c) θ = 90°. R = 12 ft., Δf = 32 Hz, lossless.

4.3.2 Diameter Scaling

Since the Reynolds number in this study is being varied by changing the nozzle-exit diameter and the jet velocity, it is important to show that the assumed scaling relationships holds true. As stated above, there exists two diameter scaling laws: (1) the classical D_j^2 scaling law that is derived from the Lighthill acoustic analogy[1-3] and (2) the D_j^3 scaling law that is derived from the work of Gaeta and Ahuja[42]. Also, as stated above, the D_j^2 scaling law is used for 1/3-octave spectra and OASPL, while the D_j^3 scaling law is used in cases of narrowband spectra.

Figures 4.11 – 4.13 show the diameter scaling of the OASPL, 1/3-octave spectrum peak SPL, and narrowband spectrum peak SPL, respectively, for Mach numbers 0.4, 0.5, 0.6, 0.7, and 0.8, and at a polar of 90°. In Figures 4.11 and 4.12, the measurements are shown alongside the ideal D_j^2 line, while the peak narrowband SPL measurements in Figure 4.13 are shown with the ideal D_j^3 line. In each of the figures, the measurements do not deviate from the ideal line by more than 1 dB. Similar results are seen at polar angles of 30° and 60° as well. This validates the use of the D_j^2 scaling relationship for scaling OASPL and 1/3-octave band spectra and the D_j^3 scaling relationship for narrowband spectra, which was investigated by Gaeta and Ahuja[42].

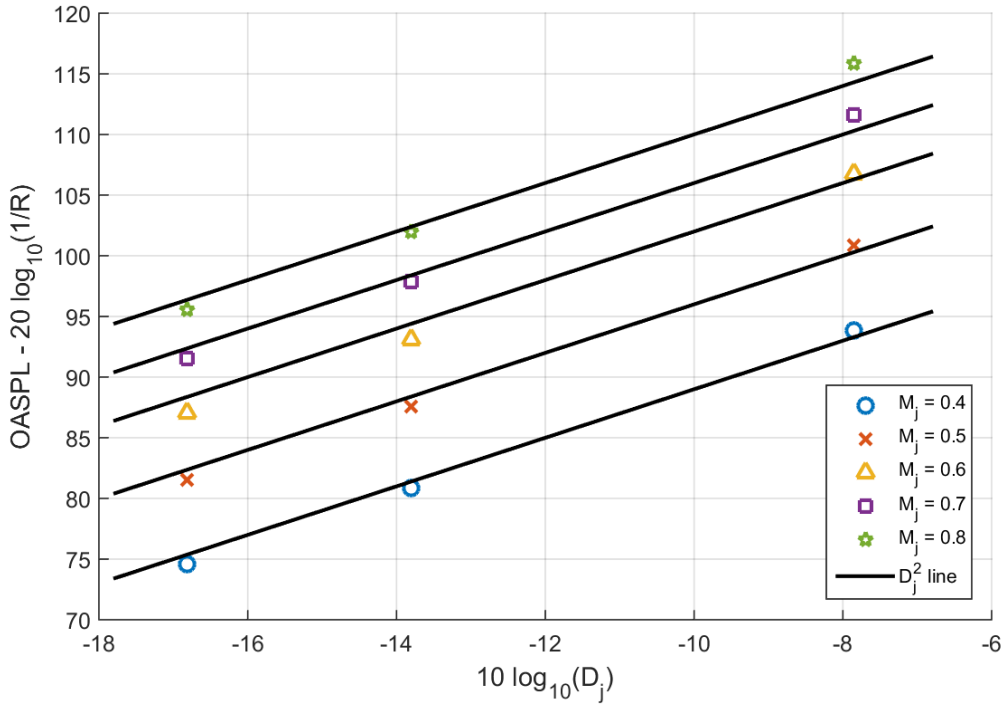

Figure 4.11: OASPL diameter scaling. θ = 90°, lossless.

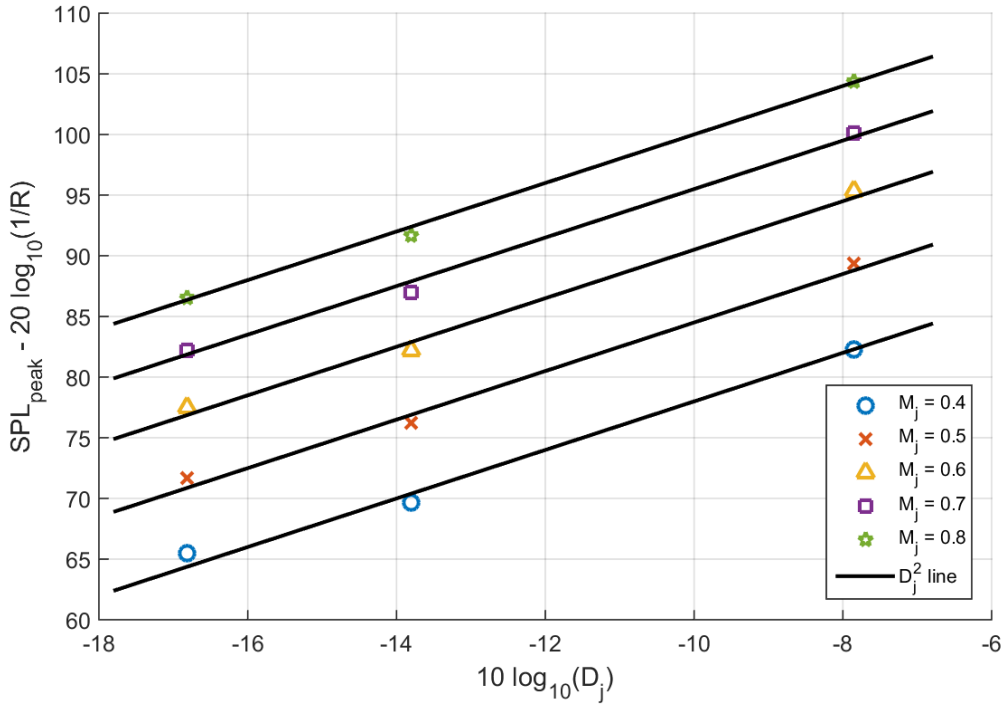

Figure 4.12: 1/3-octave band spectra peak SPL diameter scaling. θ = 90°, lossless.

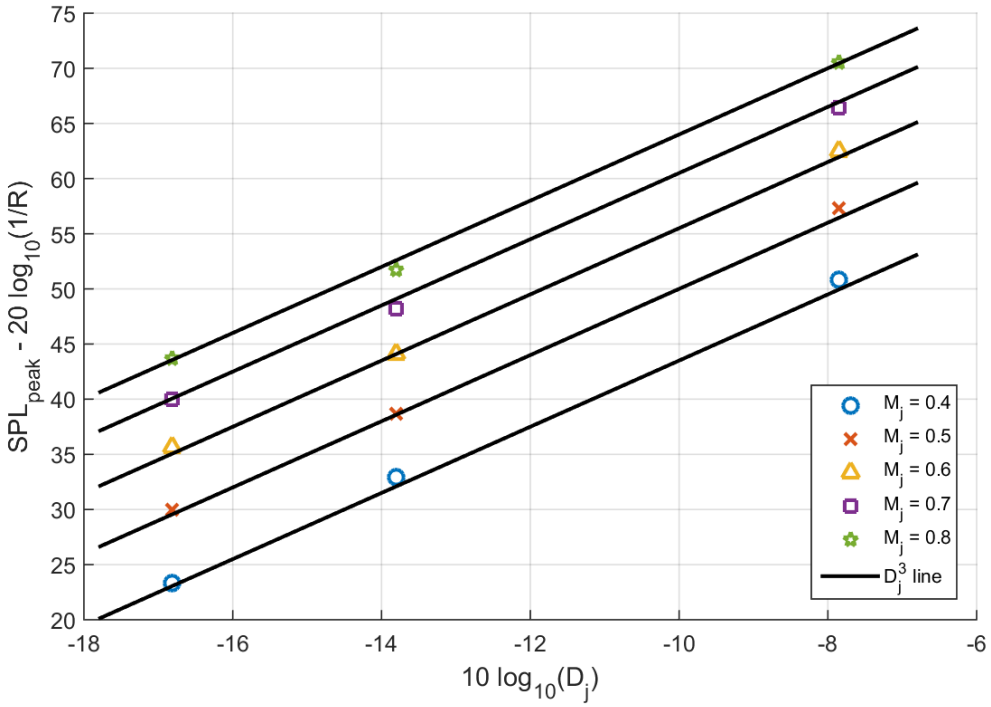

Figure 4.13: Narrowband spectra peak SPL diameter scaling. θ = 90°, lossless.

4.3.3 Velocity Scaling

Since the Reynolds number with respect to diameter (Equation 4.6) will be varied using the jet velocity, the velocity scaling of the data needed to be verified. Figures 4.14 – 4.16 show the velocity scaling of the OASPL, peak 1/3-octave band SPL, and the peak narrowband SPL, respectively. In these figures, the velocity scaling is shown for each of the 3 nozzle-exit diameters and at a polar angle of 90°. Figures 4.14 and 4.15 show the OASPL and peak 1/3-octave SPL measurements, respectively, alongside the ideal U_j^8 line, and Figure 4.16 show the peak narrowband SPL measurements alongside the ideal U_j^7 line. In Figures 4.14 – 4.16, the deviations of the measurements from the ideal lines are negligible, with the exception of the peak 1/3-octave SPL at the lowest velocity with a nozzle-exit diameter of 0.25 in., which deviates from the ideal by less than 1 dB. Similar results were observed at θ = 60°. The θ = 30° data was not studied for velocity scaling.

Bushell and Ahuja[40] and Ahuja[8] showed that at low polar angles the velocity scaling relationship break down and the low and high frequency ranges scale differently. To avoid the confusion between these effects and actual effects of the Reynolds number with respect to diameter, for the remainder of this study normalization with respect to velocity is not shown for $\theta = 30°$. This shows that the velocity scaling relationships studied by Gaeta and Ahuja[42] are valid for the range of the diameter studied in this work. In addition, the validity of both the diameter and velocity scaling relationships for the range of nozzle-exit diameters and jet velocities studied indicated that there is not additional effect of the Reynolds number with respect to diameter. Additionally, for the remainder of this study, the D_j^2 and U_j^8 scaling laws will be used with OASPL and 1/3-octave band spectra, and the D_j^3 and U_j^7 scaling laws will be used with narrowband spectra without additional comment.

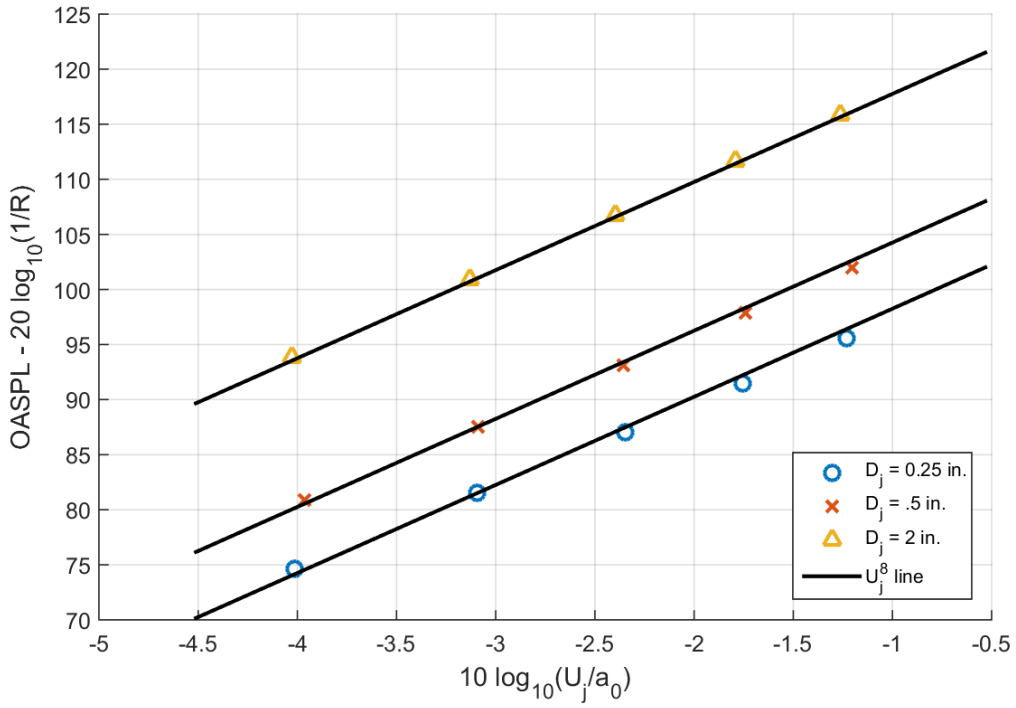

Figure 4.14: OASPL velocity scaling. θ = 90°, lossless.

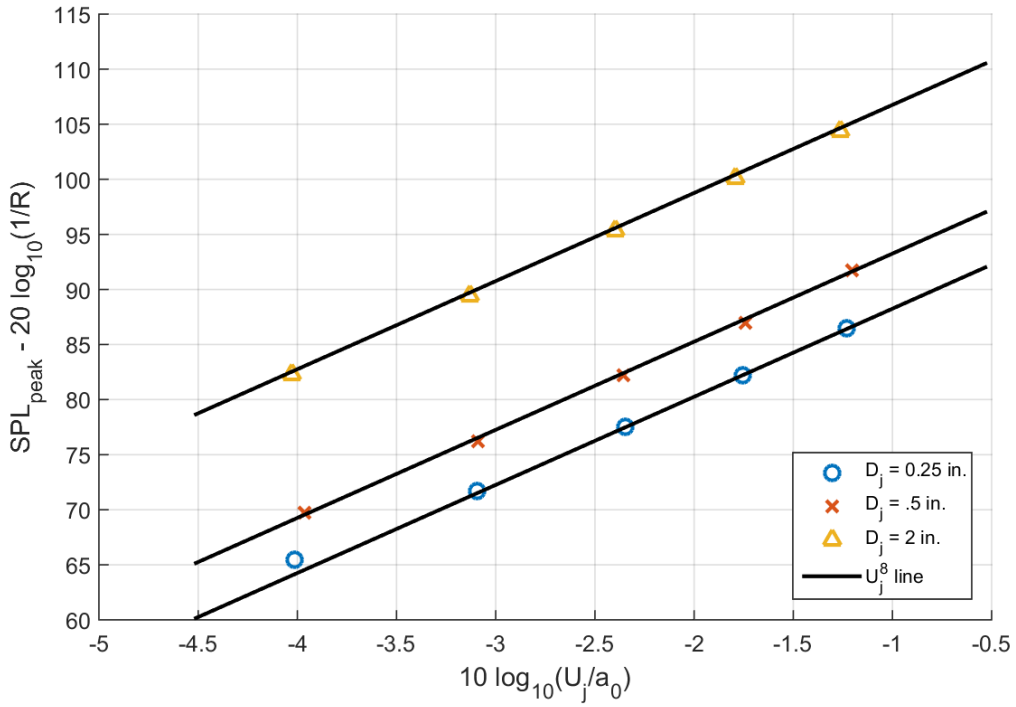

Figure 4.15: 1/3-octave spectra peak SPL velocity scaling. θ = 90°, lossless.

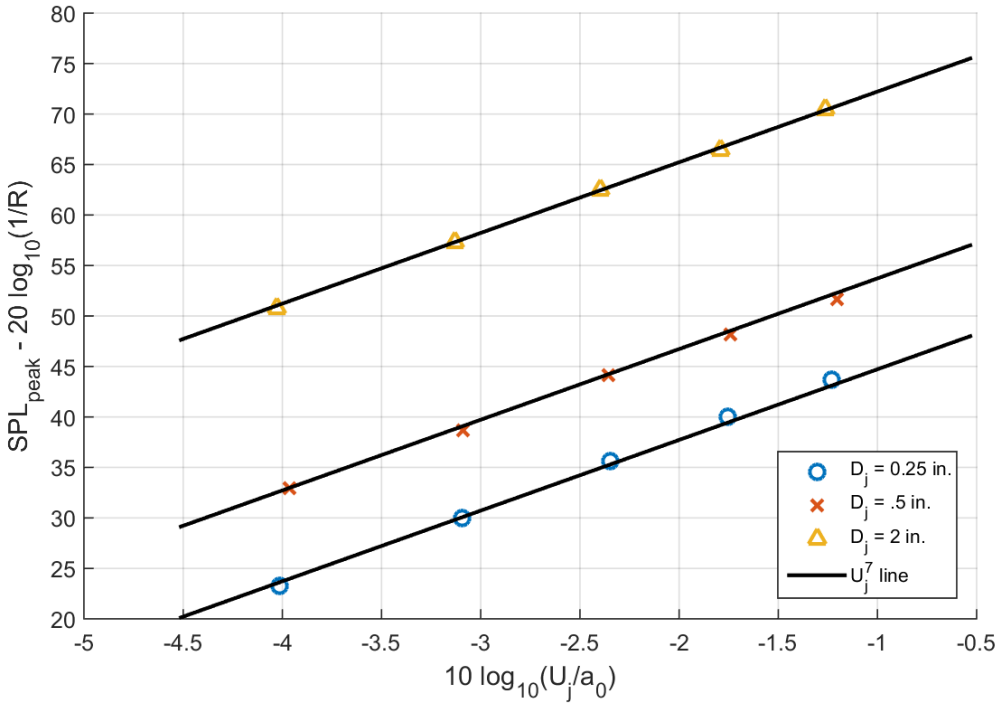

Figure 4.16: Narrowband spectra peak SPL velocity scaling. θ = 90°, lossless.

4.3.4 Directivity

The directivity of the of the noise measurements are shown in Figures 4.17 and 4.18 for Mach numbers of 0.4 and 0.8, respectively. Due to the fact that measurements were acquired at only three polar angles, these directivities are shown as bar graphs. In Figures 4.17 and 4.18, the OASPL is normalized using the diameter scaling relationship. First of all, Figures 4.17 and 4.18 show the expected directivity trend of subsonic jets. As the polar angle increases, the OASPL decreases. Secondly, in Figures 4.17 and 4.18 the OASPLs are normalized for the effects of diameter. For a given Mach number and polar angle, the OASPL collapse within ±1 dB on average, even though there are cases where that range is closer to ±1.5 dB. This shows that even though the Reynolds number is doubled as the nozzle-exit diameter is increased from 0.25 inches to 0.5 inches and then quadrupled as the nozzle-exit diameter is increased from 0.5 inches to 2 inches, relatively good normalization is observed. This continues to show that the Reynolds number with respect to diameter does not have any additional effect on jet noise.

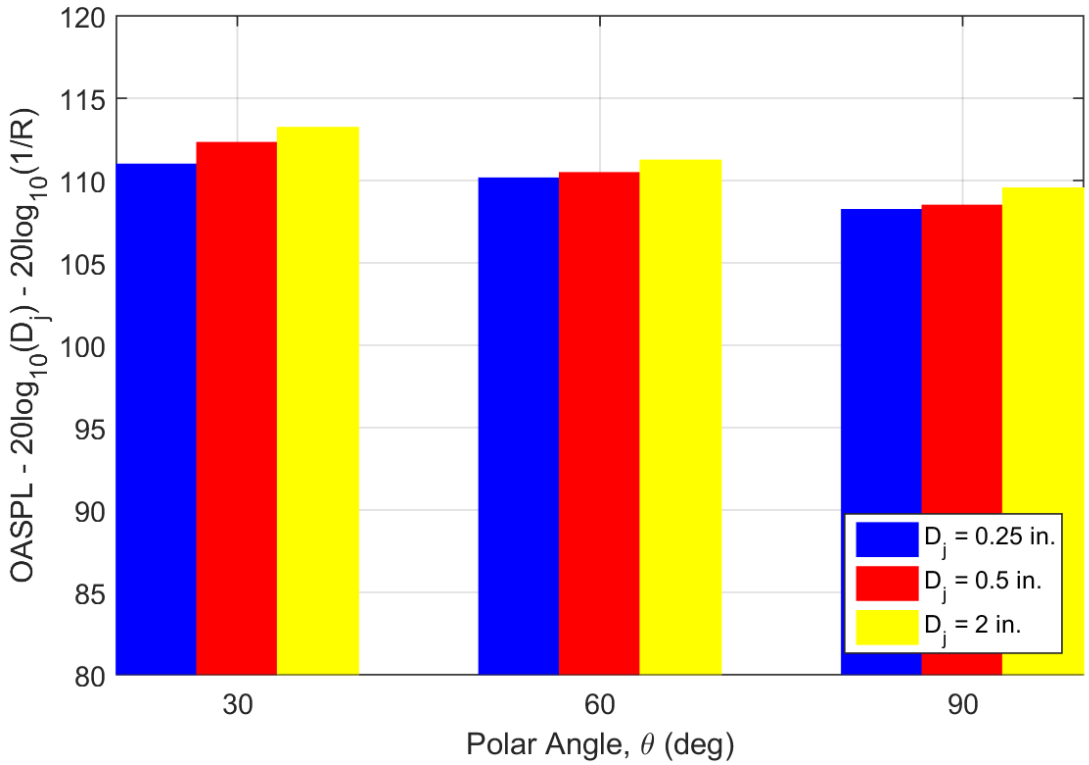

Figure 4.17: OASPL directivity at M_j = 0.4. Lossless.

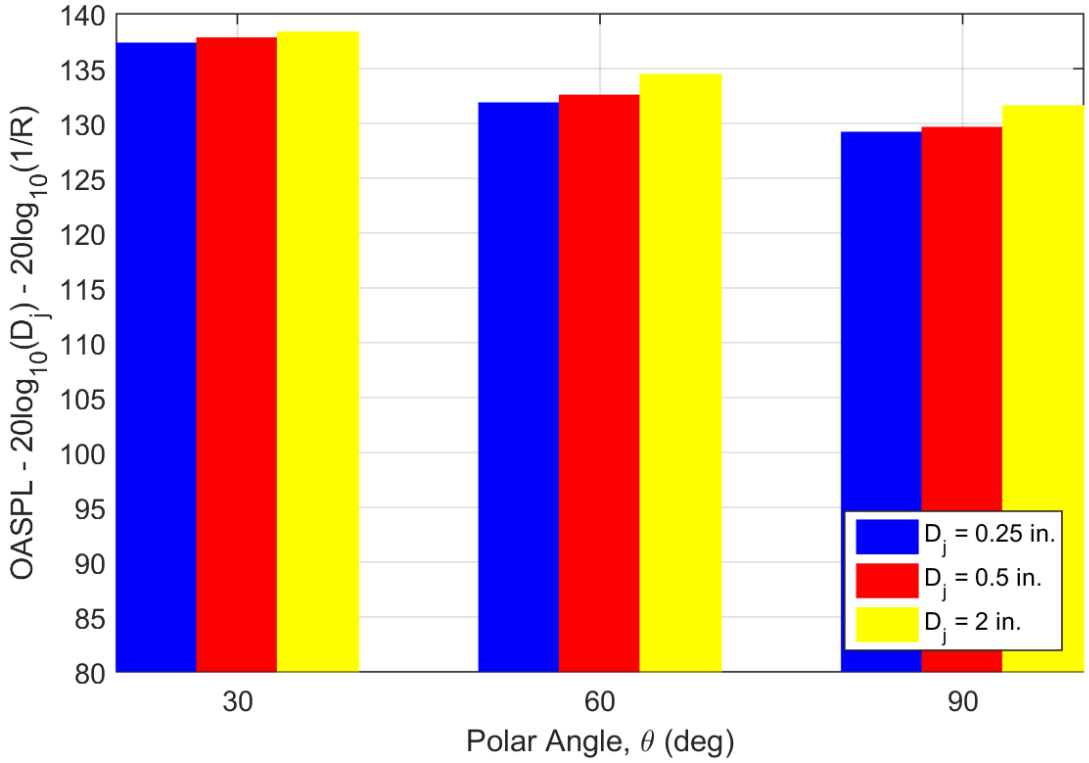

Figure 4.18: OASPL directivity at M_j = 0.8. Lossless.

4.3.5 Increasing the Reynolds number by Varying the Nozzle Diameter for Fixed Jet Velocities

In order to confirm, that Reynolds number with respect to does not impact the noise produced by a jet, outside of the previously established scaling laws, spectral normalization by the nozzle-exit diameter of the jet is performed for a given jet velocity or Mach number. To this end, the jet noise spectra shown in Figures 4.19 and 4.20 are normalized by the using the diameter scaling relationship as shown in Equation 4.5.

Figures 4.19 and 4.20 show these comparisons, where the nozzle-exit diameter of the nozzles is increased from 0.25 inches to 2 inches, and the spectra are shown for polar angles of 30°, 60°, and 90°, at Mach numbers of 0.4 and 0.8, respectively. As the nozzle-exit diameter is increased from 0.25 inches to 0.5 inches the Reynolds number is doubled, and as the nozzle-exit diameter is increased from 0.5 inches to 2 inches the Reynolds number is quadrupled. With these large increases in Reynolds number, spectral collapse is observed here within ±1 dB. This further proves that the Reynolds number with respect to diameter does not add an extra effect to the noise produced by a jet.

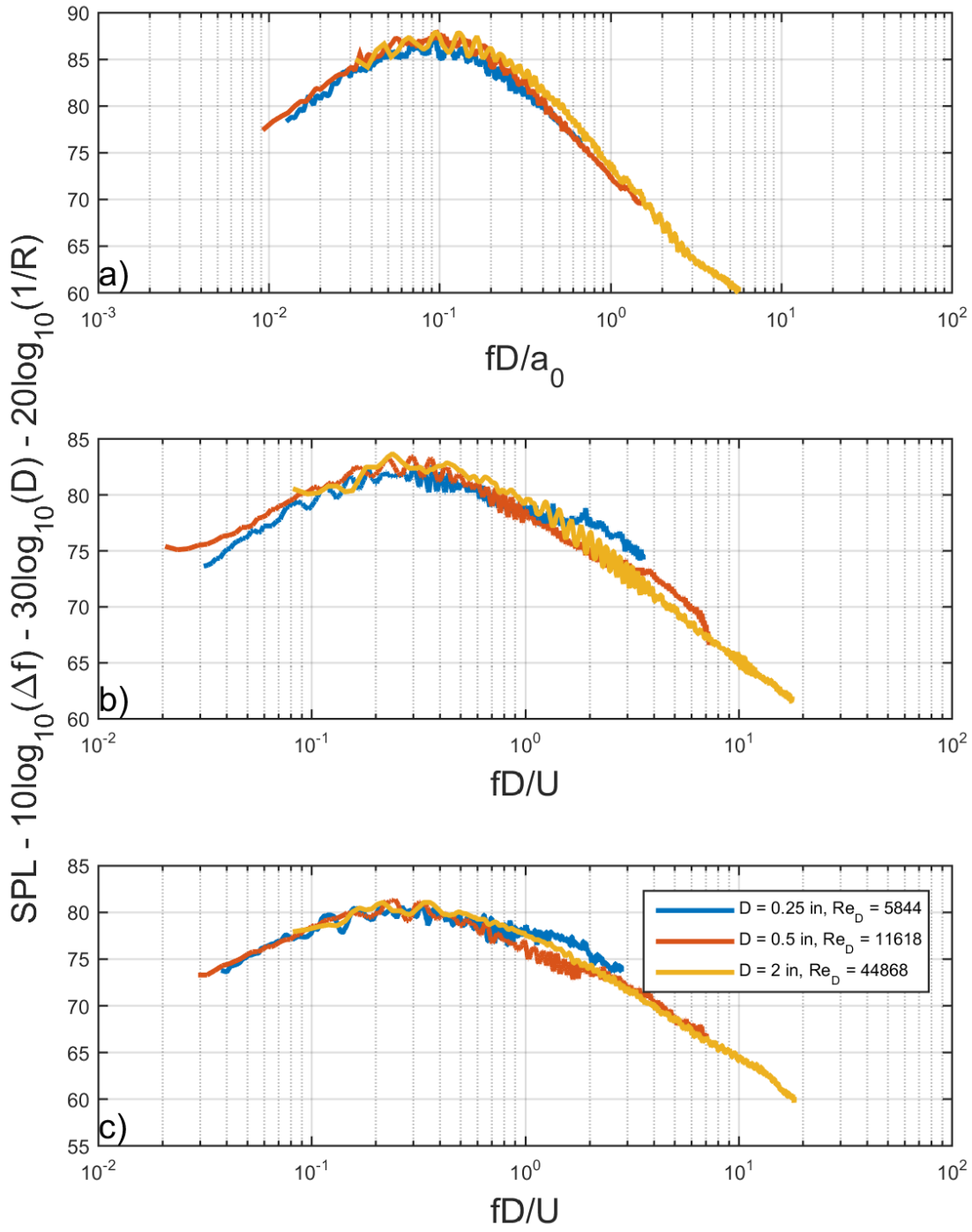

Figure 4.19: Jet noise measurements from the three nozzles for a Mach number 0.4. a) θ = 30°, b) θ = 60°, and c) θ = 90°. R = 12 ft., Δf = 32 Hz, lossless.

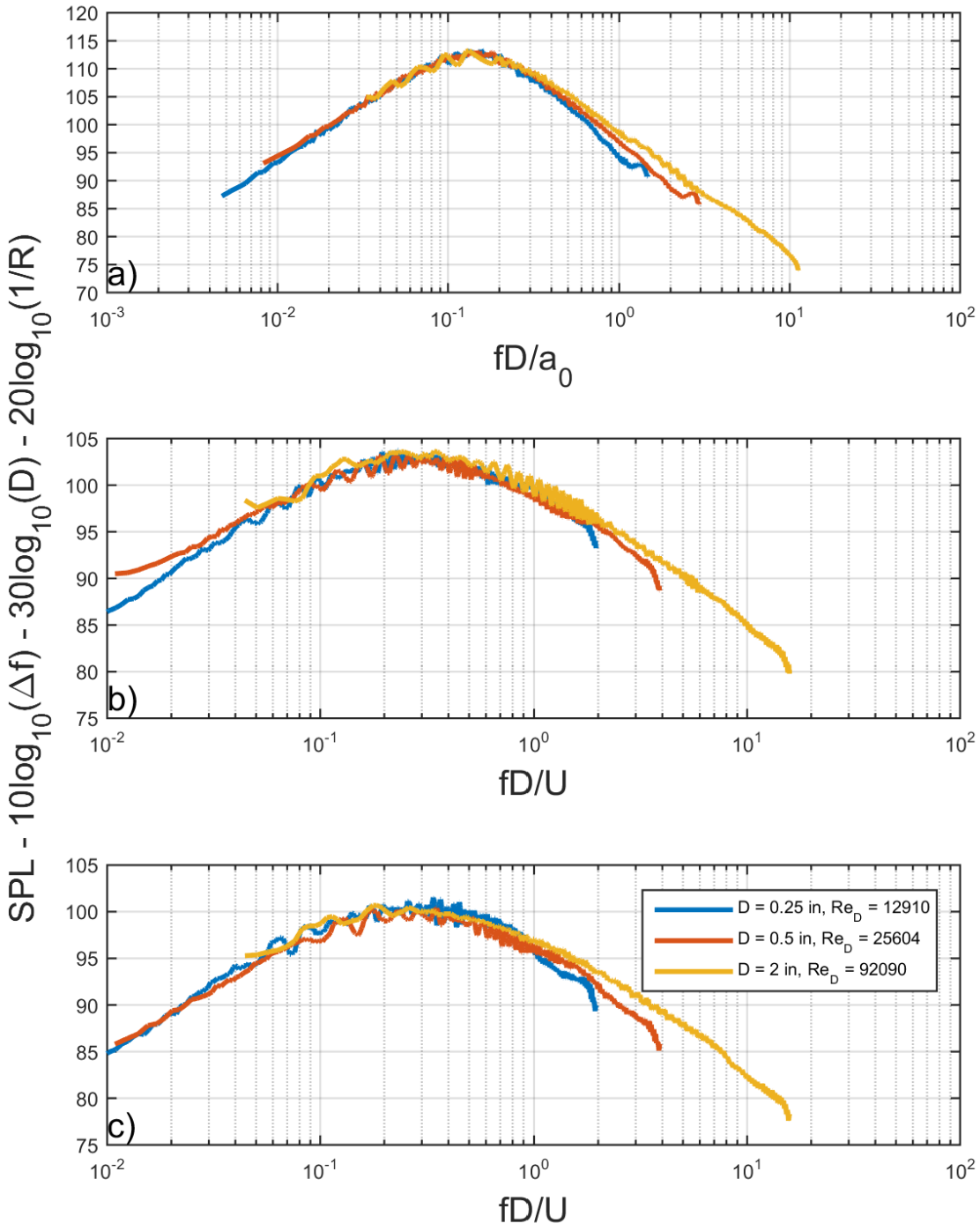

Figure 4.20: Jet noise measurements from the three nozzles for a Mach number 0.4. a) θ = 30°, b) θ = 60°, and c) θ = 90°. R = 12 ft., Δf = 32 Hz, lossless.

4.3.6 Increasing the Reynolds by Varying the Jet Velocity for a Given Nozzle-Exit Diameter

As shown in Equation 4.6, the Reynolds number with respect to diameter can be varied by changing the jet velocity. Figures 4.21 – 4.23 show the comparisons of the normalized spectra of the 0.25-in., the 0.5-in., and the 2-in. nozzle-exit diameter jets, respectively, at jet Mach numbers of 0.4 – 0.8 at polar angles of 60° and 90°. As shown in Figures 4.21 – 4.23, spectral collapse occurs within ±0.5 dB over most of the frequency ranges for the three nozzles. In Figures 4.21 and 4.22, which refer to the 0.25-in. and 0.5-in. nozzles, respectively, spectral collapse stops at high frequencies. The author does not believe that this an effect of the Reynolds number since the jet noise shown in Figures 4.21 – 4.23 represent only a doubling of Reynolds number, where the spectra in Figures 4.19 and 4.20 represent an 8 times increase in Reynolds number. Figures 4.19 and 4.20 do not have this type of high frequency reduction where the higher Reynolds number has lower high-frequency levels. The author believes this is some other effect of the nozzles that is beyond the scope of this study. As shown in Figure 4.23, the 2-inch nozzle does show spectral collapse over the whole frequency range. This shows that outside of the effects associated with the jet velocity, the Reynolds number with respect to diameter does not have an impact on jet noise.

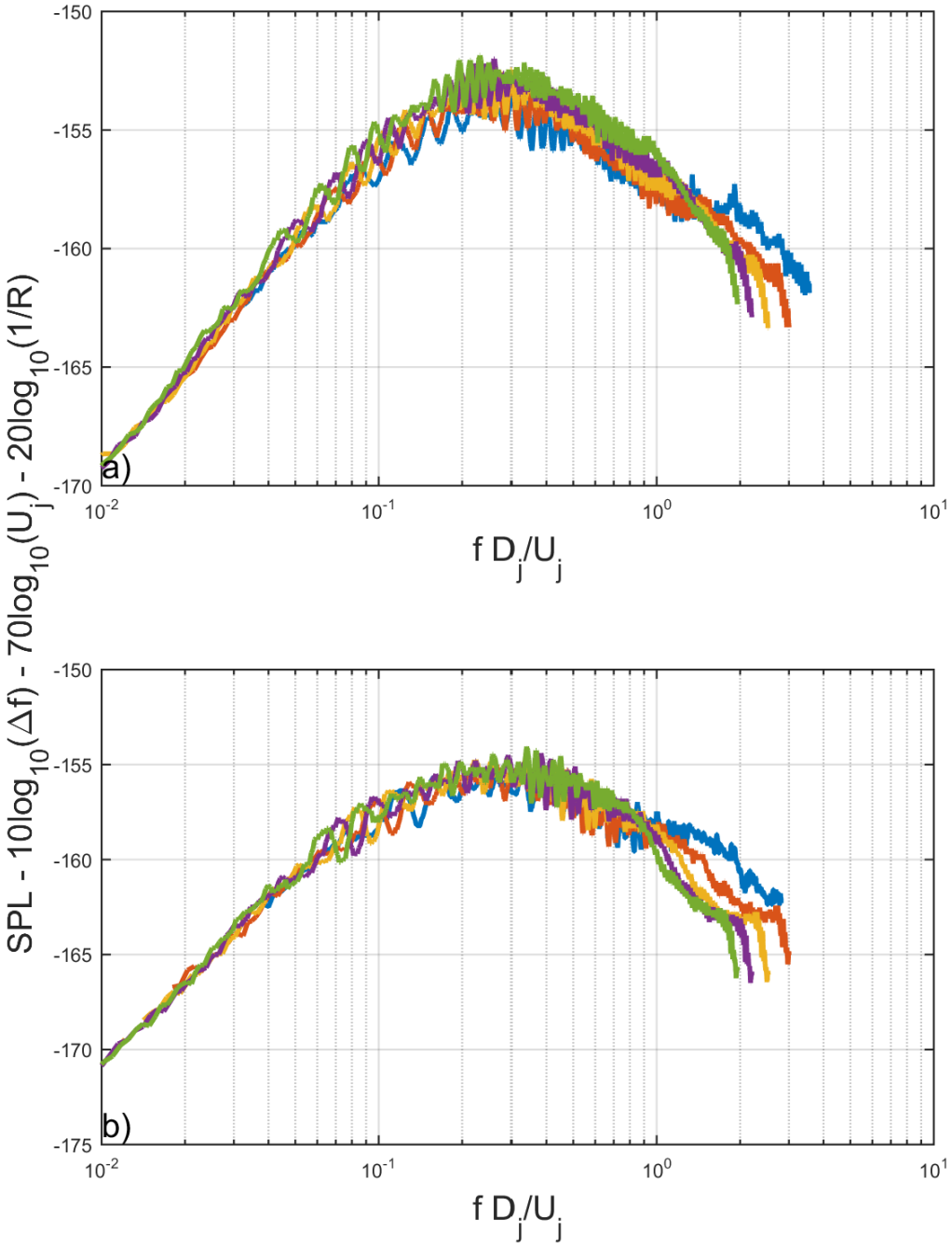

Figure 4.21: Normalized jet noise measurements from the 0.25-in. nozzle for a Mach numbers 0.4-0.8. a) θ = 60°, and b) θ = 90°. R = 12 ft., Δf = 32 Hz, lossless.

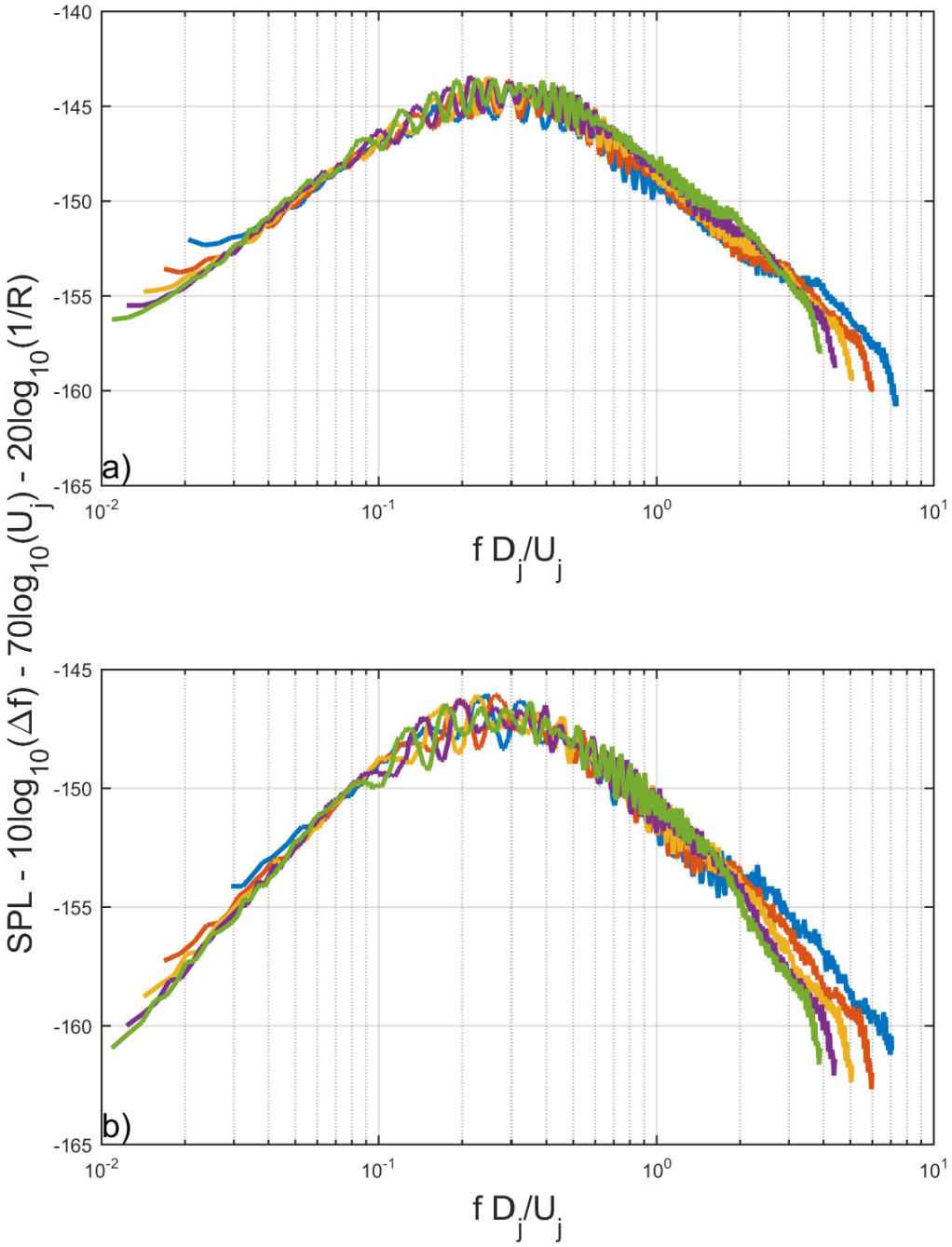

Figure 4.22: Normalized jet noise measurements from the 0.5-in. nozzle for a Mach numbers 0.4 – 0.8. a) θ = 60°, and b) θ = 90°. R = 12 ft., Δf = 32 Hz, lossless.

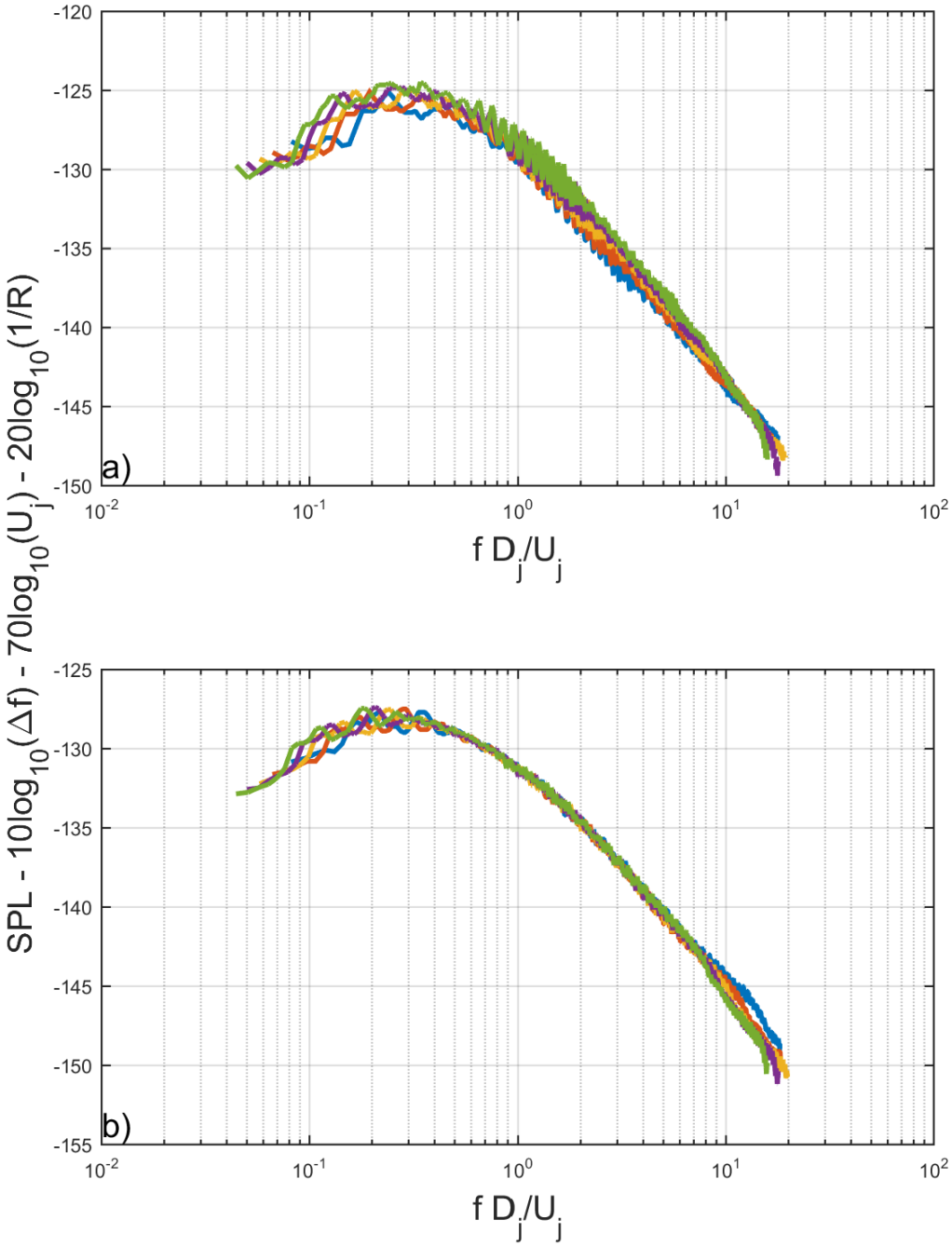

Figure 4.23: Normalized jet noise measurements from the 2-in. nozzle for a Mach numbers 0.4 – 0.8. a) θ = 60°, and b) θ = 90°. R = 12 ft.,

4.3.7 Comparison of the Lowest and Highest Reynolds Number Jets

To show that the Reynolds number with respect to diameter does not have an additional effect on jet noise outside of the parameters shown in the Lighthill Acoustic Analogy[1-3] (see Equation 4.1) ad nauseam, the noise produced by the smallest Reynolds jet is compared to that produced by the largest Reynolds number jet. This comparison of normalized narrowband spectra for a polar angle of 90° is shown in Figure 4.24. As can be seen in Figure 4.24, spectral collapse within ±0.5 dB is observed at Strouhal numbers less than 1, and within ±1 at Strouhal numbers greater than 1. It should be pointed that the high Reynolds number case has a Reynolds number more than 15 times that of the lower Reynolds number case. Even with this large difference in the Reynolds number of these jets, relatively good spectral collapse is observed. This once again shows that the Reynolds number with respect to diameter does not have an additional impact on jet noise.

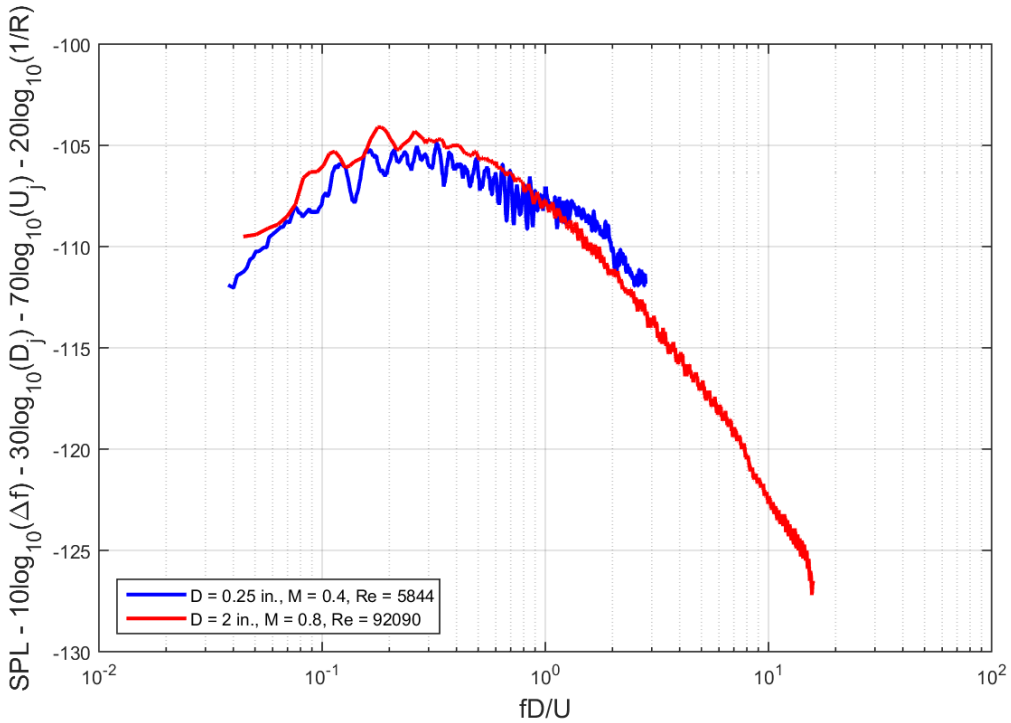

Figure 4.24: Comparison of the smallest and largest Reynolds number jets at a polar angle of 90°. Δf = 32 Hz, lossless.

4.4 Conclusions

It is clear from the results presented above that changing the Reynolds number with respect to diameter has no impact on the normalized jet noise. Thus one should be able to extrapolate the jet noise obtained from as small as ¼-inch diameter nozzle to larger nozzles. In addition, the use of the D_j^2 scaling relationship for OASPL and 1/3-octave band spectra and the D_j^3 for narrowband spectra, as was derived by Gaeta and Ahuja[42] was not backed-up with measurements, was proven. In future, the measurements used in this study will be compared to noise from nozzles larger than 2 inches. This could not be done as part of this study since as shown in Chapter 3, the GTRI Anechoic Jet-Facility cannot produce clean jet noise for jets much larger than 2 inches. These measurements would have to come from a facility capable of producing clean jet noise for larger nozzles.

It is important to mention that the Reynolds number and boundary layer are linked. This link is weakest by using the Reynolds number with respect to the diameter as scaling parameter because nozzles with vastly different design specification can have the same Reynolds number, as is pointed out in the next chapter. Bogey[34] criticized using this parameter for this very reason. A better parameter may be the Reynolds number with respect to the boundary layer displacement thickness, momentum thickness, or the length of the nozzle. This would more closely link the Reynolds number quantity to the boundary layer, which contain the viscous effects of the jet.

The nozzles used in this study are all model-scale nozzles. In the future, comparing the jet noise produced by nozzles even smaller (e.g., a nozzle-exit diameter on the order of 1 mm) and much larger (e.g., a nozzle on the order of a typical full-scale jet nozzle) than those used here would reveal if truly even the smallest model-scale nozzles can be scaled

to the full-size nozzles. In addition, testing these nozzles at supersonic speeds could reveal possible effects of the Reynolds number with respect to the nozzle-exit diameter on shock-associated noise, a topic that to the author's knowledge has never been studied.

CHAPTER 5

EFFECTS OF THE NOZZLE-EXIT BOUNDARY LAYER ON JET NOISE

It was stated in Chapter 1 that differences exist between university-style and industrial-style anechoic jet-facilities. As was explained in Chapter 1, Harper-Bourne[12] points out that differences seen in the jet noise produced by university and industrial anechoic jet-facilities similar to those shown by Viswanathan[4, 5], could be a result of different nozzle-exit conditions. Different nozzle-exit conditions refers to different boundary layer thickness and different initial turbulence level which is a function of the plenum chamber's contraction ratio and the nozzle choice. Large contraction ratios combined with aerodynamically favorable nozzles, such as the ASME nozzle, which will be discussed below, result in jet flows with low initial turbulence, and this is typical of many university anechoic jet-facilities. On the other hand, industrial jet-facilities tend to produce flows with more turbulence. This issue will be investigated in this Chapter.

5.1 Previous Work

The state of a boundary layer is typically described using four properties: the boundary layer thickness (δ), the displacement thickness (δ^*), the momentum thickness (θ^*), and the shape factor (H). The boundary layer thickness is defined as the distance between the wall (zero-velocity point) and where the velocity in the boundary layer reaches 99% of the edge velocity. The displacement thickness is representative of the missing mass

flow from an inviscid fluid flow due to the presence of the boundary layer[66], and is defined by the equation:

$$\delta^* \equiv \int_0^{y_1} \left(1 - \frac{\rho u}{\rho_e u_e}\right) dy \tag{5.1}$$

where the radial distance from nozzle center can be described as *½ - r*. Here the subscript "e" refers to the edge properties, which are the flow properties unaffected by the presence of the boundary layer, and the properties without the subscript refer to the properties inside the boundary layer. In the case of a jet flow, the edge properties are equivalent to the flow properties in the jet's potential core. Similarly, the momentum thickness is a measure of the momentum loss from an inviscid fluid flow due to the presence of the boundary layer[66], and is defined by the equation:

$$\theta^* \equiv \int_0^{y_1} \frac{\rho u}{\rho_e u_e}\left(1 - \frac{u}{u_e}\right) dy \tag{5.2}$$

The shape factor is defined as:

$$H \equiv \frac{\delta^*}{\theta^*} \tag{5.3}$$

The shape factor is normalized parameter that is used to determine the state of the boundary layer. Based on classical boundary layer theory[68], the Blasius profile, which is the ideal laminar boundary layer profile, has shape factor of 2.59. Based on classical experimental data[68], a turbulent boundary layer profile has a shape factor around 1.4. Obviously, attaining either of these two precise states experimentally is unlikely. Zaman[69] suggests, based on the work of Hussain[70], there exist several transition states that can be broadly categorized as either nominally laminar or nominally turbulent. Taking a variety of cases shown in Schlichting[68] into account, a nominally laminar boundary layer can be assumed

to have a shape factor between 2 and 3, while nominally turbulent boundary layers will have a shape factor between 1.4 and 2.

Bogey and Marsden[37] provided a brief review of the theory behind the impact of the nozzle-exit boundary layer profile on jet noise. They investigated the influence of the nozzle-exit boundary-layer profile on high-subsonic round jets by performing compressible large-eddy simulations using low dissipation numerical schemes. They examined boundary layer profiles with four separate shape factors equal to 1.68, 1.77, 2.01, and 2.36 and showed that the noise results from the fourth case with a laminar velocity profile differed significantly from those from the three first cases with transitional profiles. They identified the clear trend that when the shape of the exit boundary-layer profile changes from laminar to turbulent, higher azimuthal modes and higher Strouhal numbers are found to predominate at the pipe exit close to the wall and early on in the mixing layers. It is now known that the growth rate of large-scale structures in thicker or turbulent boundary layers is slowed down. This can lead to a longer potential core, and weaker velocity fluctuations are obtained in the shear layers and on the jet axis. This can thus generate lower noise levels as indeed found in the work of Bogey and Marsden[37].

Based on work by those such as Hill et al.[71], Browand and Latigo[72], Hussain and Zedan[73], and Husain and Hussain[74], it has been demonstrated that downstream of the nozzle-exit the turbulence intensity grows rapidly to a peak value in the case of the laminar nozzle-exit boundary layer and increases monotonically in the case of the turbulent nozzle-exit boundary layer. In addition, based on the results of Hill et al.[71], Raman et al.[75, 76], Russ and Strykowski[77], and Xu and Antonia[78], the jet flow development is faster in the case of the laminar nozzle-exit boundary layer, which leads to a shorter potential core and faster

centerline velocity decay. The faster jet growth rates associated with jets with a laminar nozzle-exit boundary layer translates into high noise levels, which will be illustrated in the following studies. In addition, from the work of those such as Bridges and Hussain[79], the additional noise that is produced by laminar jets is the result of vortex ring pairing. The vortex structures in jets are in the form of vortex rings, and it has been found that in the case of the laminar nozzle-exit boundary layer, vortex rings of opposite rotation can combine adding extra noise.

In 1954, Powell[13] experimentally investigated the effect of the velocity profile on the noise generation from a jet. He compared the noise from a jet with a square exit velocity profile, which typically has thin laminar boundary layers, to that of, as he denoted, a fully-developed pipe flow, which is a fully turbulent flow. A fully-developed pipe flow has the largest "boundary layer" possible, as it takes up the whole radius of the nozzle-exit. Both jets had a nozzle-exit diameter of 2 inches. The results of his study are shown in Figure 5.1, which shows octave-band frequency spectra of the noise produced by these two jets at polar angles of 30° and 90° with jet velocities of 708 ft/sec and 990 ft/sec. As can be seen in Figure 5.1, the noise from the fully developed pipe flow has lower noise than the jet with the square exit-velocity profile at both polar angles. At lower frequencies, the noise level differences appear almost constant (2-3 dB). Alternatively, at higher frequencies these differences actually increase with frequency. These differences are as high 7 dB at the highest frequency shown in Figure 5.1. This work shows that the conditions at the nozzle-

exit have an impact on the noise produced by the jet, and show the trends associated with this effect.

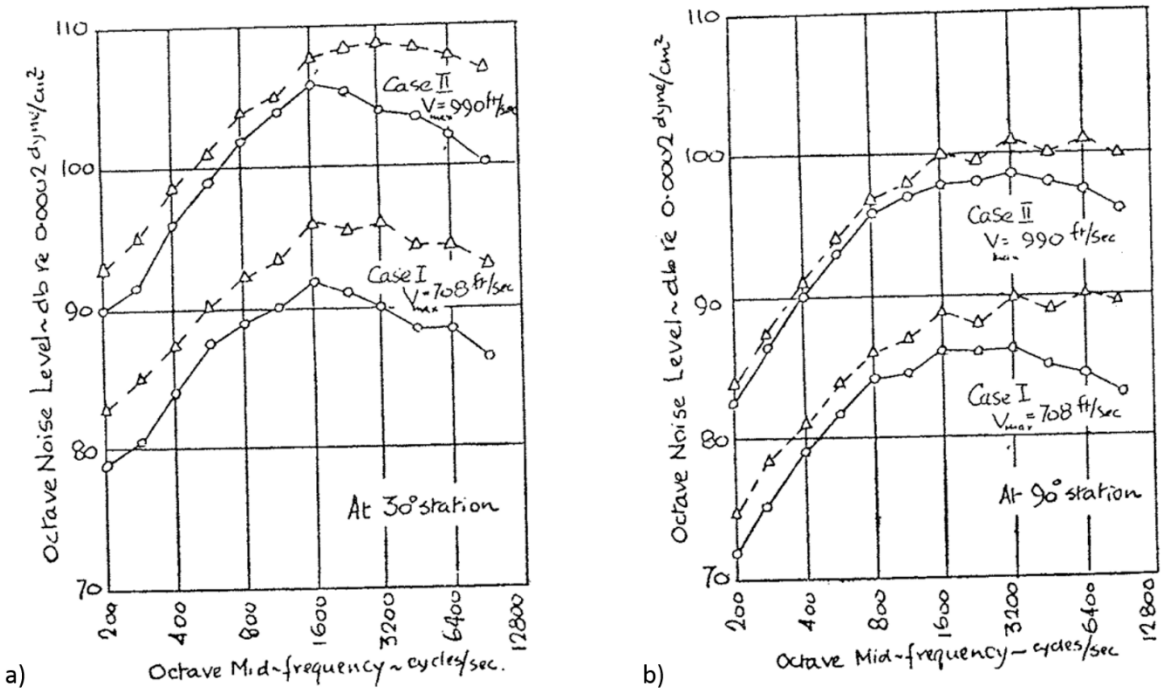

Figure 5.1: Results of the investigation by Powell[13] on the noise produced by a jet with a square velocity profile (Δ) and that produced by full developed flow (○), a) θ = 30° and b) θ = 90°.

Ahuja[31] conducted experiments on the effect of the boundary layer on the jet noise by adding extensions to the straight section of a nozzle in order to develop the boundary layer over a distance rather than changing the surface roughness or using a trip ring. The advantage of increasing the boundary layer thickness over a distance rather than using a trip ring or changing the surface roughness is that one has more control over the development of the boundary layer. Holding the operating pressure ratio condition of the jet constant, Ahuja[31] increased the straight section of a 2.8-inch nozzle-exit diameter jet from 3.8 inches to 24 inches and then to 36 inches. Figure 5.2 shows results from this study. Figure 5.2 shows 1/3-octave-band spectra for the three nozzle straight section lengths at polar angles of 30° and 90°. As one can see from Figure 5.2, the jet noise

decreases with the increased length, and therefore with more the developed boundary layer. Ahuja[31] explains these results as a reduction in the jet velocity due to a pressure drop inside the extensions. The experiments performed by both Ahuja[31] and Powell[13] followed similar principles in that the velocity profile or boundary layer state was changed by developing the flow.

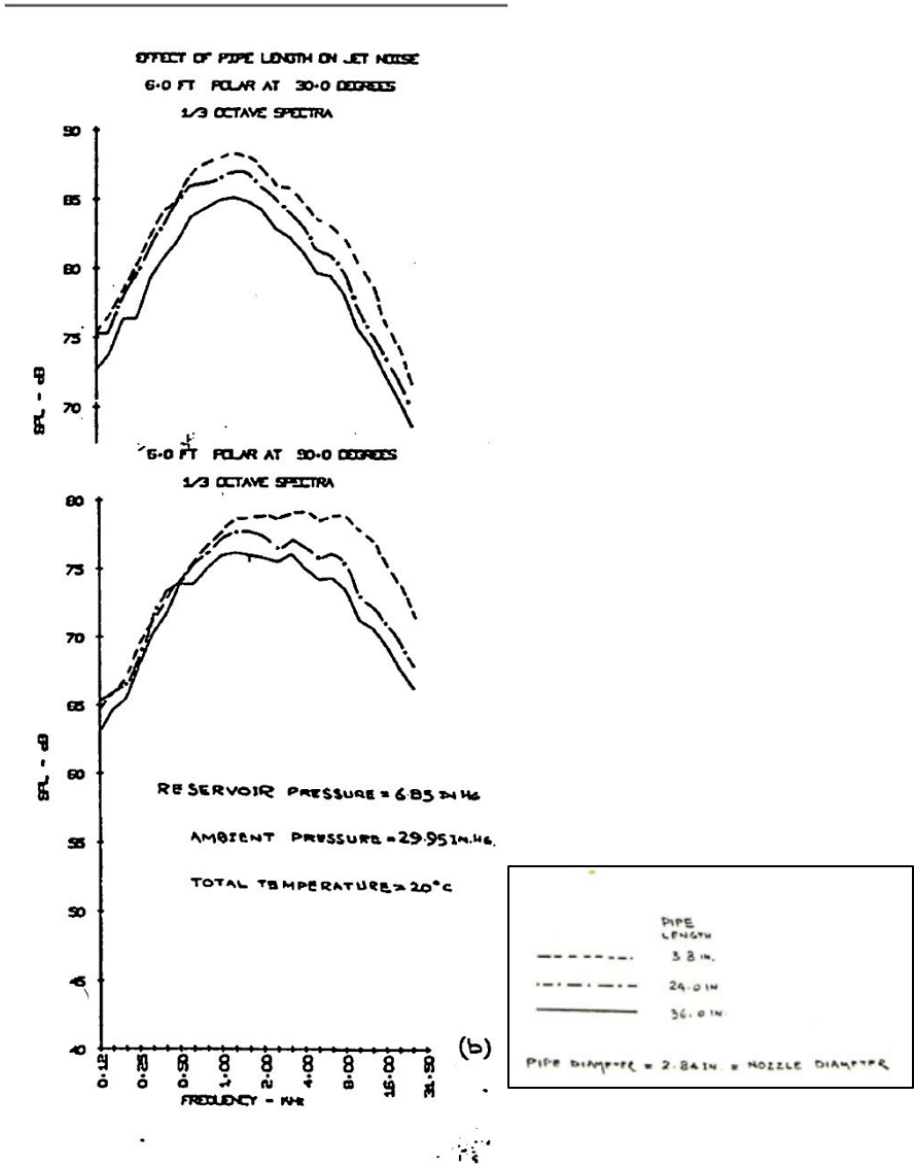

Figure 5.2: Results from the study on the nozzle-exit boundary layer conducted by Ahuja[31].

Viswanathan and Clark[15] and Zaman[16, 69] conducted similar but independent experiments on the role of nozzle-exit boundary layer states on jet noise. Viswanathan and Clark[15] and Zaman[16] changed the nozzle-exit boundary layer by changing the internal geometry of the nozzle, but keeping the other conditions of the jet flows constant. This was done by comparing ASME nozzles and conical nozzles. The exact design specifications of these types of nozzles will be described below, but it is well known that the aerodynamically favorable geometry of the ASME nozzle causes laminar nozzle-exit boundary layers, while the conical nozzle produces more developed nozzle-exit boundary layers. Figures 5.3 and 5.4 show comparisons of the jet noise spectra from the two different types of nozzles for the same jet conditions as acquired by Viswanathan and Clark[15] and Zaman[16], respectively. Figure 5.3 shows the comparison conducted by Viswanathan and Clark[15] of jet noise between three nozzles, a conical nozzle, an ASME nozzle, and a cubic nozzle, at polar angles of 130°, 90° and 35° at a Mach number of 1.0. From Figure 5.3, it is seen that the ASME nozzle produced more high-frequency noise than the conical nozzle in the forward arc and the sideline direction. These differences become smaller in the rear arc.

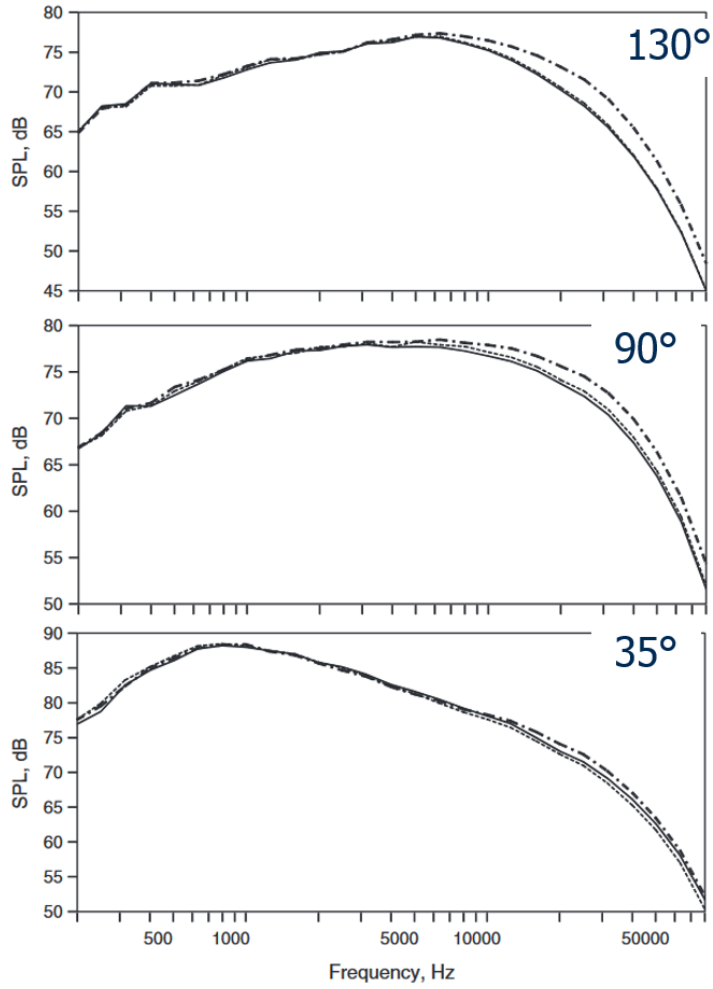

Figure 5.3: Spectral comparisons from the study by Viswanathan and Clark[15]. M=1.0, T_r/T_a=1.0. Solid: conic; dashed: cubic; dotted: ASME.

Figure 5.4 shows the comparison performed by Zaman[16], where he compared jet noise produced by a ASME nozzle and a conical nozzle at a polar angle of 75°, 60°, and 25° at a Mach number of 0.9. Figure 5.4 once again shows that the conical nozzle produces lower noise at high frequencies than the ASME nozzle. In addition, Figure 5.4, also shows how these boundary layer effects change with the polar angle of the microphone. Such effects are not as prominent at lower polar angles, similar to the results of Viswanathan and Clark[15] shown in Figure 5.3. In addition, it is interesting to note that for a more developed nozzle-exit boundary layer, Powell[13] and Ahuja[14] observed noise reductions

across the whole spectrum, whereas Viswanathan and Clark[15] and Zaman[16] observed such reductions only at the high frequencies.

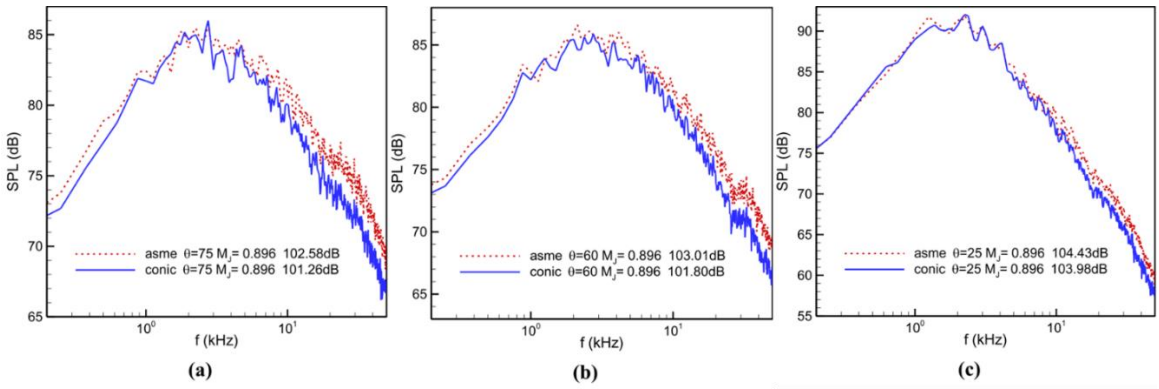

Figure 5.4: Results from the study from Zaman[16]; a) θ = 75°, b) θ = 60°, and c) θ = 25°.

In their recent computational modeling, Bogey et al.[32-37, 80] found that a more developed flow, in the form of either a thicker boundary layer or as a jet transition from laminar to turbulent produces less noise. One example of these results can be seen in Figure 5.5. Figure 5.5 shows the noise spectra for computational jets with shape factors of 2.55, 1.88, and 1.52 at polar angles of θ = 40° and 90°. As can be seen from Figures 5.5, similar trends were observed by Viswanathan and Clark[15] and Zaman[16] as described above. The

shape factors for the jets varied from 2.55 to 1.40. The greatest reductions are seen at θ = 90° and high frequencies. At the θ = 40° almost no effect is seen.

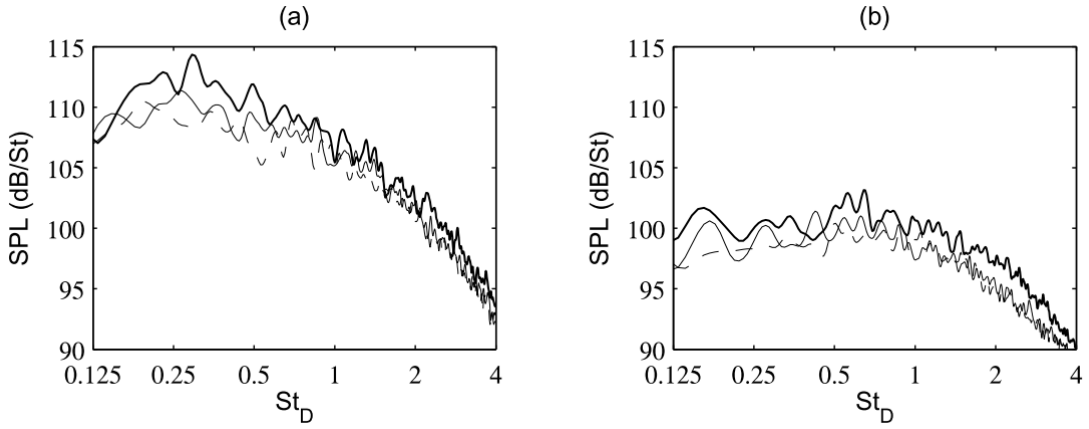

Figure 5.5: Comparison of computationally created laminar and turbulent jets by Bogey and Marsden [37]: a) θ = 40° and b) θ = 90°. Thick black line, H = 2.55; thick black line, H = 1.88; dashed line, H = 1.52; dotted line, H = 1.40.

The above studies show that nozzle-exit boundary layer state can significantly influence the noise produced by a jet. These observations are further confirmed in the current investigation where detailed boundary layer profiles have been measured. An empirical method has also been developed for predicting the SPL changes as a function of the nozzle-exit boundary layer shape factor.

5.2 Experimental Program

5.2.1 Facilities Description

The experiments that were performed as part of this study were conducted in the GTRI Anechoic Jet-Facility and the GTRI Flow Diagnostic Facility. These facilities are described in Burrin, Dean, and Tanna[59], Burrin and Tanna[60], and Ahuja[10]. The GTRI Anechoic Jet-Facility was setup using the configuration shown in Figure 5.6. The jet nozzles were mounted on the plenum chamber and the microphones were mounted on a circular arc that was centered about the center of the anechoic chamber. The microphones

were mounted at polar angles of 30°, 60°, and 90° and at distances of 11 feet, 12 feet, and 10 feet, respectively. This ensured that all the microphones were in the geometric far-field, removing any near-field effects from the frequency spectra. The microphones were not placed at a common distance due to the limitation of the size of the room and the position of the microphone arc. Bruel and Kjaer (B&K) 4939, ¼-inch free-field microphones attached to 2669 preamplifiers. These microphone-preamplifier combinations were connected to B&K 2690-A-0S4 Nexus conditioning amplifier, which serve to amplify the microphone signals, and power and polarize the microphones. The outputs from the conditioning amplifier are recorded using NI PXIe-4499 acquisition cards inside of a PXIe-1073 chassis. This hardware configuration is capable to sampling 48 channels independently at a sampling frequency up to 204.8 kHz. The signals were recorded using this Data Acquisition System (DAQ) for 100-120 seconds.

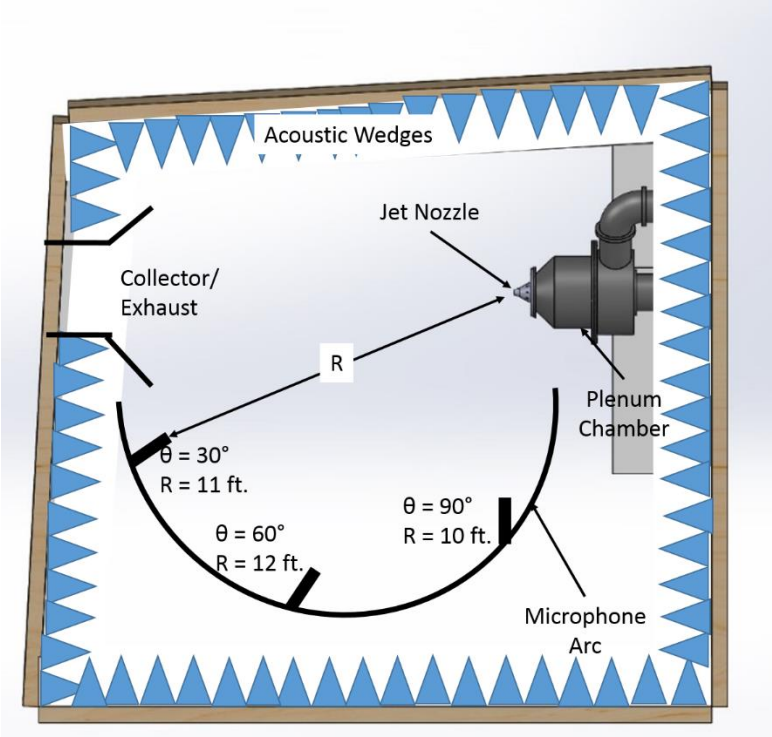

Figure 5.6: Set-up used in the GTRI Anechoic Jet-Facility for this experiment.

The acoustic pressure time histories were then processed into average power spectra using NI LABVIEW, using a Hanning window, with a window length of 6400 samples, and 50% overlap; this led to on average 7500 averages in the power spectra and Δf of 32 Hz. These spectra were then corrected for a variety of conditions, as detailed in Ahuja[10]. The effects of microphone geometry, the microphone protective grid, microphone actuator response, and incidence of the microphone with respect to the source are accounted for as part of the microphone free-field frequency response. This correction, is a function of both frequency and the angle of incidence of the sound wave on the microphone, is lumped together and will be denoted by the variable $A(f,\Psi)$. In addition, a foam ball windscreen was used on the $\theta = 30°$ microphone, to prevent hydrodynamic fluctuations from affecting the measurements. The effect of windscreen on the broadband frequency spectrum was determined experimentally and is denoted by the variable $B(f)$. The effect of atmospheric attenuation was accounted for by using the method presented in ANSI S1.26-1995[61]. This atmospheric-attenuation correction methodology contains many equations and is too long to present here, but is shown in Appendix B. This method results in a frequency-dependent attenuation coefficient $\alpha(f)$, which has the units of dB/m. Removing the attenuation effects and applying all of the microphone related corrections described above provides the so-called "lossless spectra," which will be used throughout the analysis. The advantage of this form of the data is that it allows the data from different facilities, different microphones, and acquired on different days to be compared with one another. This also allows the theoretical predictions, which are independent of microphone responses, to be compared with the measured lossless data. Finally, the jet noise measurements are extrapolated to a common distance to help with needed comparisons. This distance was

selected to be 72 nozzle diameters and is performed using the inverse square law. Combining these effects, the free-field and lossless jet noise spectrum is calculated using the equation:

$$SPL(f)_{free-field,lossless} = SPL_{uncorrected} - A(f,\Psi) + B(f) + \alpha(f)R_1 + 20\log_{10}\left(\frac{R_1}{R_2}\right) \quad (5.4)$$

An example of this correction procedure is shown in Appendix A.

The second facility used in this study is the GTRI Flow Diagnostic Facility and is described in detail in Burrin and Tanna[60]. This facility is shown in Figure 5.7. This facility can create jet flow identical to those produced in the GTRI Anechoic Jet-Facility. This facility was used for the flow measurement even though it is a non-anechoic facility and smaller than the GTRI Anechoic Jet-Facility, because with the traversing table right under the jet, it was far easier to mount traverses, pitot probes and other equipment in this facility.

Figure 5.7: The GTRI Flow Diagnostic Facility set up for boundary layer measurements.

A number of nozzles were used over the course of the experimental program. These fall in two categories: (1) ASME nozzles and (2) conical nozzles. ASME nozzles have a curved converging section that follows the contour of a quarter of an ellipse with a ratio of post-converging diameter to pre-converging diameter of 3/7, as shown in Figure 5.8a. Conical nozzles used have a straight taper converging section, with a range of taper angles. Figure 5.8b shows a generalized diagram of a conical nozzle. Since the conical nozzle has more free design constraints, two conical nozzles with the same inlet and exit diameters

can have different contraction angles, potentially providing nozzle exit boundary layers of different thicknesses and turbulence intensities.

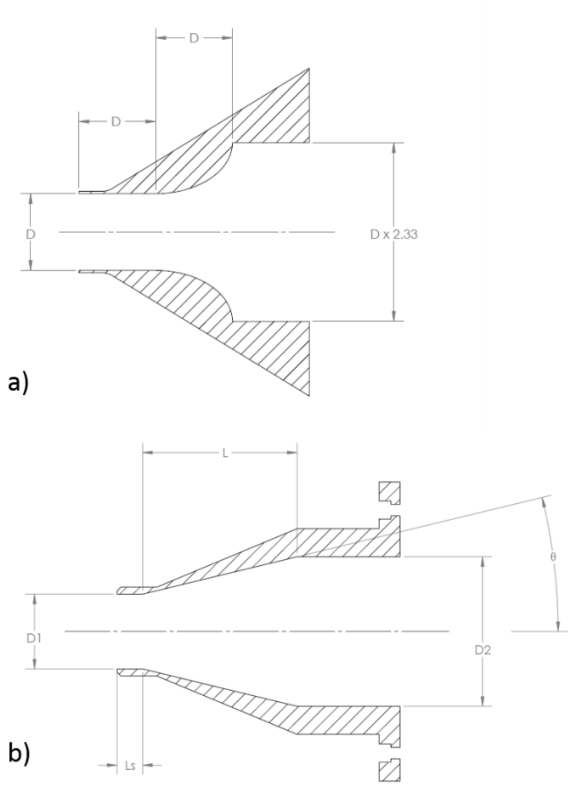

Figure 5.8: ASME and Conical design specifications. a) ASME nozzles and b) conical nozzles.

For this study, a 1.54-inch ASME, 1.6-inch conical, a 2-inch ASME and a 2-inch conical nozzle were used to generate the jets. The ASME nozzles were designed using the ASME standards listed above, while the conical nozzles had different design constraints.

Table 5.1: Specifications of the two conical nozzles used in this study.

	2" Conical Nozzle	1.6 " Conical Nozzle
Diameter (in.)	2	1.6
Total Length (in.)	7.875	13.5
Straight Section (in.)	1	1
Converging Section (in.)	4.175	9.75
Taper Angle (deg)	13	5.9

Table 5.1 shows the design constraints for the two the conical nozzles based on Figure 5.8b. The 2-inch conical nozzle was designed to be identical to the 2-inch ASME nozzle with the exception of the type of convergence, i.e., a straight taper rather than a quarter ellipse convergence. This resulted in the taper angle being much larger for the 2-inch conical nozzle compared to the 1.6-inch conical nozzle. It should be added that the 2-inch conical nozzle was designed to have NPT threads on the outside of the converging section, allowing attachment of PVC pipe extensions of various lengths to the nozzle-exit. This enabled testing jets with nozzle-exit boundary layers of varying thicknesses. The extension lengths used were 8 inches (4 diameters) and 16 inches (8 diameters).

5.2.2 Experimental Program Description

Both jet mixing noise and jet exit flow properties were measured for the jets produced by the ASME and conical nozzles described above for Mach numbers ranging from 0.4 to 0.8. The acoustic measurements were made in the GTRI Anechoic Jet-Facility and the flow measurements were made in the GTRI Flow Diagnostic Facility.

The boundary layer velocity profile was measured using a United sensor BA -025-12-C-11-650 boundary layer pitot probe connected to an Omega PX409-030D pressure transducer. The stagnation pressure of the jet was measured in the plenum chamber using an Omega PX302-200GV pressure transducer. The ambient pressure in the jet-facility, which is the also the static pressure of the jet and the boundary layer was measured using a NetScanner 9032 absolute pressure transducer. The Mach number in the boundary layer or Mach number of the jet was calculated using the equation:

$$M = \left(\left(\left(\frac{p_t}{p_a} \right)^{\frac{\gamma-1}{\gamma}} - 1 \right) \frac{2}{\gamma-1} \right)^{\frac{1}{2}} \tag{5.5}$$

The stagnation temperature was measured using a K-type thermocouple. The jet static temperature can then be calculated using the equation:

$$T = \frac{T_t}{1+\frac{\gamma-1}{2}M^2} \tag{5.6}$$

The speed of sound in the jet can be calculated using the expression:

$$a = \sqrt{\gamma RT} \tag{5.7}$$

The jet velocity can now be calculated:

$$U = Ma \tag{5.8}$$

The displacement thickness, momentum thickness and shape factor were calculated using Equations 5.1 – 5.3, which were stated above. The density that is required for these calculations is found using:

$$\rho = \frac{P}{RT} \tag{5.9}$$

These measurements were acquired for Mach numbers ranging from 0.4 to 0.8. The integration operations required for the displacement and momentum thicknesses was performed using the trapezoidal numerical integration technique. Laminar boundary layers have shape factors greater than two, while for turbulent boundary layers the shape factor less than two[68]. Far-field acoustic measurements were acquired for the same Mach numbers for which the boundary layer measurements were made. These acoustic measurements were made at polar angles of 30°, 60°, and 90° with respect to the downstream axis. Both sets of measurement helped determine the effect of the nozzle-exit boundary layer state on the jet noise.

As referenced above, Viswanathan[15] and Zaman[16] have had success at adjusting the nozzle-exit boundary for nozzles of the same exit diameter by using nozzles of different

internal geometry, mainly the ASME nozzles versus the conical nozzles. This same strategy was used in this study, with the exception that two conical nozzles of very different designs were used. In addition, duct extensions were added to the end of the 2-inch diameter conical nozzle. In order to avoid fully-developed flow at the nozzle-exit, the extensions used in this experiment were limited to 10 diameters.

5.3 Results

Before any of the data is presented, it is noted that over the course of this study a large amount data was acquired. Acoustic and boundary layer velocity profile measurements were made for the 30 configurations described above (6 nozzle configuration and 5 Mach numbers). In the interest of brevity, only a small percentage of spectra and velocity profiles are shown, but all the data was used in the analysis and to draw the conclusions.

Figures 5.9 and 5.10 compare the jet noise spectra for the 1.5-inch ASME nozzle and 1.6-inch conical nozzle at polar angles of 30°, 60°, and 90°, for Mach numbers of 0.4 and 0.8, respectively. As shown in Figures 5.9a and 5.10a, at a polar angle of 30°, there is not much difference in the noise produced by the two nozzle types. As the polar angle increases, the noise to the right of the spectral peak produced by the conical nozzle appears to be lower than that produced by the ASME nozzle at frequencies on the right of the spectral peak. These differences are as high as 4 dB. In addition, these differences in the noise decrease as the jet velocity increases. Included in the legends of Figures 5.9 and 5.10 are the calculated boundary layer thicknesses, δ, and boundary layer shape factors, H, based the measured velocity profiles. The noise levels decrease as the boundary layer thickens and becomes more developed (as is indicated by the decrease in the shape factor). This gives credibility to the claim that as a jet's nozzle-exit boundary layer becomes thicker and

more developed, the jet noise gets reduced. These results are consistent with those seen Viswanathan and Clark[15] and Zaman[16] and with the explanations provided above in section 5.1 with respect to the computational work of Bogey and Marsden[37].

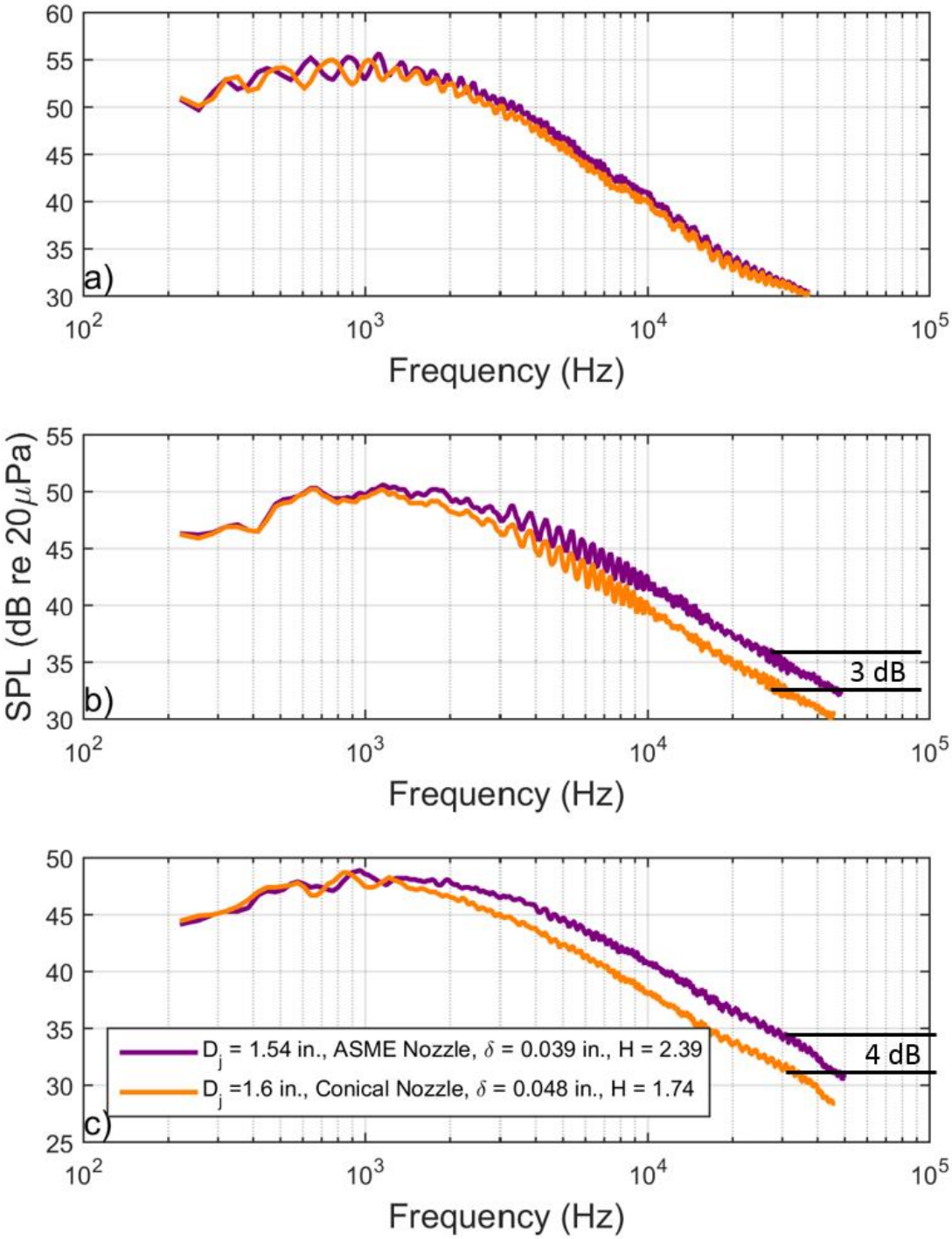

Figure 5.9: Comparison on the noise produced by the 1.54-inch ASME nozzle and the 1.6-inch conical nozzle. a) θ = 30°, b) θ = 60°, and θ = 90°. R = 12ft., M_j = 0.4, Δf = 32 Hz., lossless.

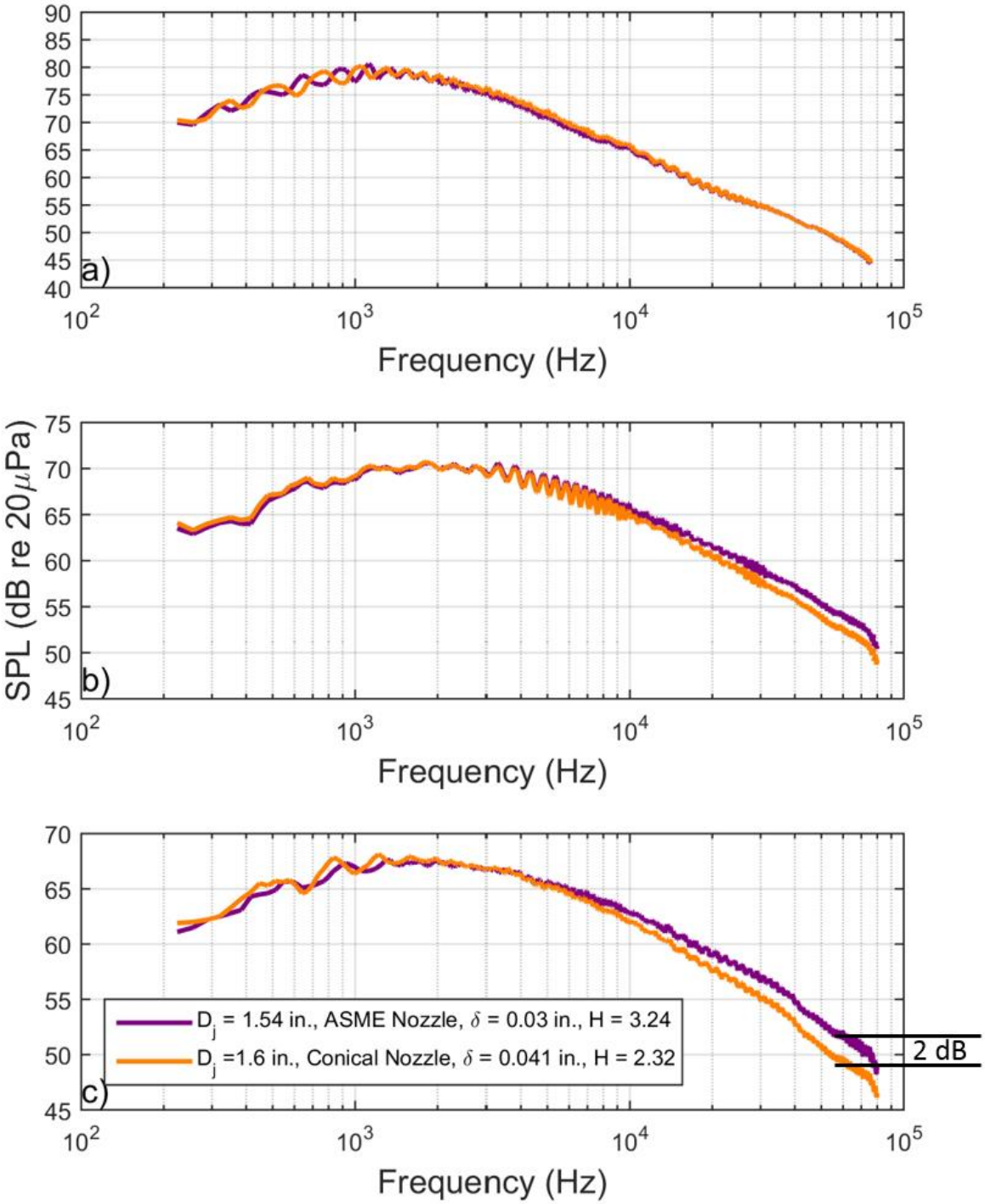

Figure 5.10: Comparison on the noise produced by the 1.54-inch ASME nozzle and the 1.6-inch conical nozzle. a) θ = 30°, b) θ = 60°, and θ = 90°. R = 12ft., M_j = 0.8, Δf = 32 Hz., lossless.

Figures 5.11 and 5.12 show the differences between the 2-inch conical and ASME nozzles as well as the effect of the straight section extensions on the jet noise at polar angles of 30°, 60°, and 90°, for Mach number of 0.4 and 0.8, respectively. Included in Figures 5.11 and 5.12 are nozzle-exit boundary layer thicknesses and shape factors. In these figures, the uppermost two spectra (in red and blue) are for the nozzles with no extensions. There is a tendency for the ASME nozzle to be a bit noisier than the conical nozzle for all polar angles and Mach numbers. This is also accompanied by an increase in the boundary layer thickness and a corresponding decrease in the shape factor. On adding the extensions to the straight section of the nozzle, considerable additional reduction in noise is observed at all frequencies but more so at the higher frequencies as the boundary layer has thickened with the addition of duct extensions. For example, in Figure 5.11, the boundary layer thickness (δ) for the conical nozzle increases from 0.084 in. to 0.344 in. by adding a 4D long duct extension and to 0.40 in. by adding an 8D long extension. The corresponding shape factor values (H) are 2.12, 1.45 and 1.38 respectively. These numbers were observed for a jet exit Mach number of 0.4. The trend is very similar for a jet Mach number of 0.8 as shown in Figure 5.12 where the value of δ changed from 0.056 in. to 0.32 in. and then to 0.42 in. by adding duct extensions. The corresponding values for H were 2.68, 1.59, and 1.55. These noise differences are the lowest at a θ = 30° and increase as the polar angle increases. Noise reductions shown in Figures 5.11 and 5.12 are as high as 4-5 dB.

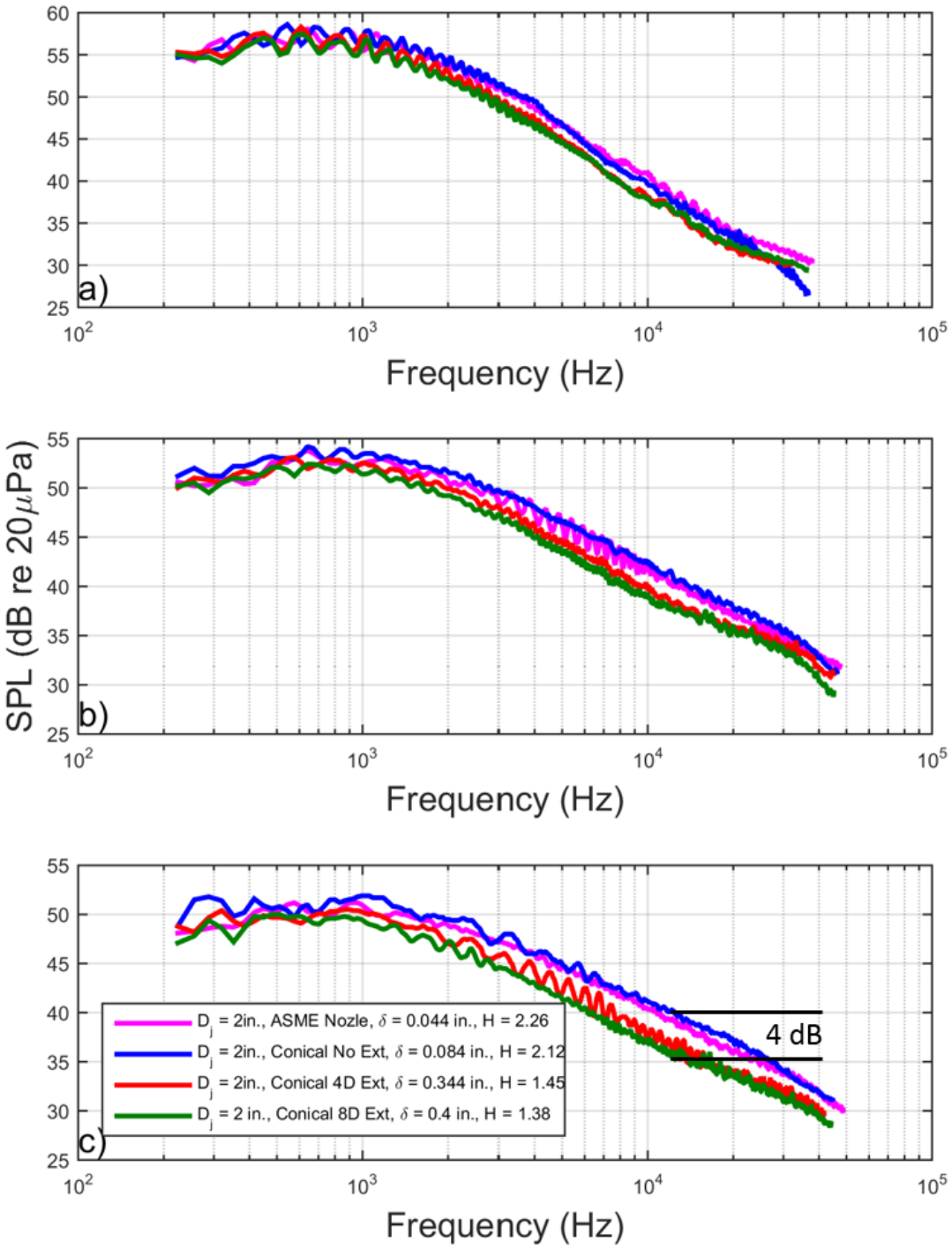

Figure 5.11: Comparison on the noise produced by the four 2-inch nozzle configurations. a) θ = 30°, b) θ = 60°, and θ = 90°. R = 12ft., M_j = 0.4, Δf = 32 Hz., lossless.

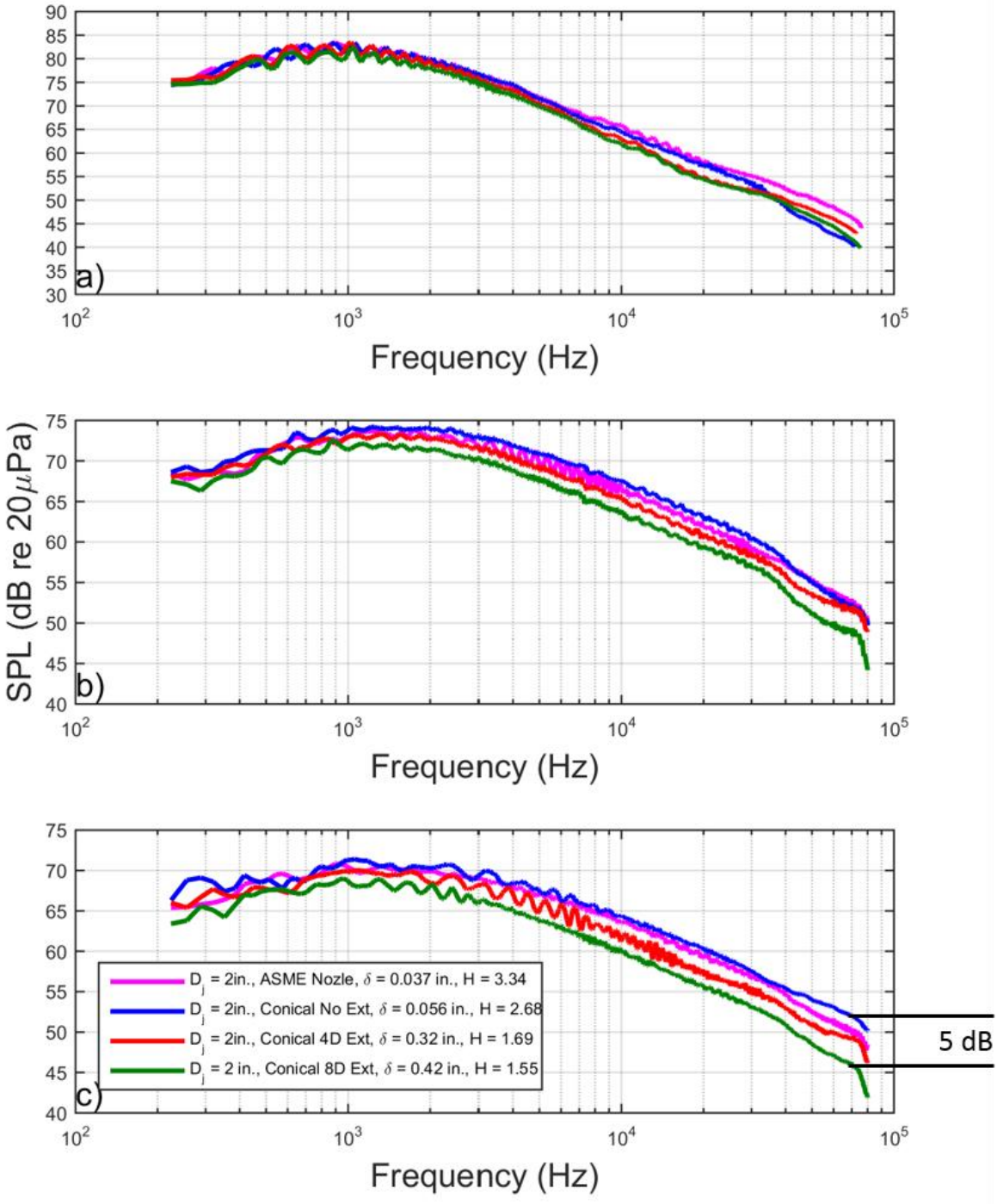

Figure 5.12: Comparison on the noise produced by the four 2-inch nozzle configurations. a) θ = 30°, b) θ = 60°, and θ = 90°. R = 12ft., M_j = 0.8, Δf = 32 Hz., lossless.

The normalized boundary layer velocity profiles for the 2-in. diameter conical nozzle with and without the 4D and 8D duct extensions for a jet exit Mach number of 0.8 are shown in Figure 5.13. These velocity profiles are presented alongside the Blasius boundary layer profile. The velocity profiles in Figure 5.14 are normalized in the following manner: (1) the velocity values are normalized by the jet exit velocity and (2) the distance into the boundary layer is normalized by the boundary layer thickness. The legend in Figure 5.1 also contains the boundary layer thickness and shape factor values for each test condition. As can been seen Figure 5.13, the 2-in. conical nozzle without any duct extension produces a boundary layer profile that is most similar to the Blasius profile indicating that it is quite thin and laminar. On the other hand, the 2-in. conical nozzle with the duct extensions have thicker boundary layers, lower shape factors, and have the most turbulent-looking velocity profiles. Table 5.2 shows the boundary layer thickness, displacement thickness, momentum thickness, and shape factor for each nozzle at each condition.

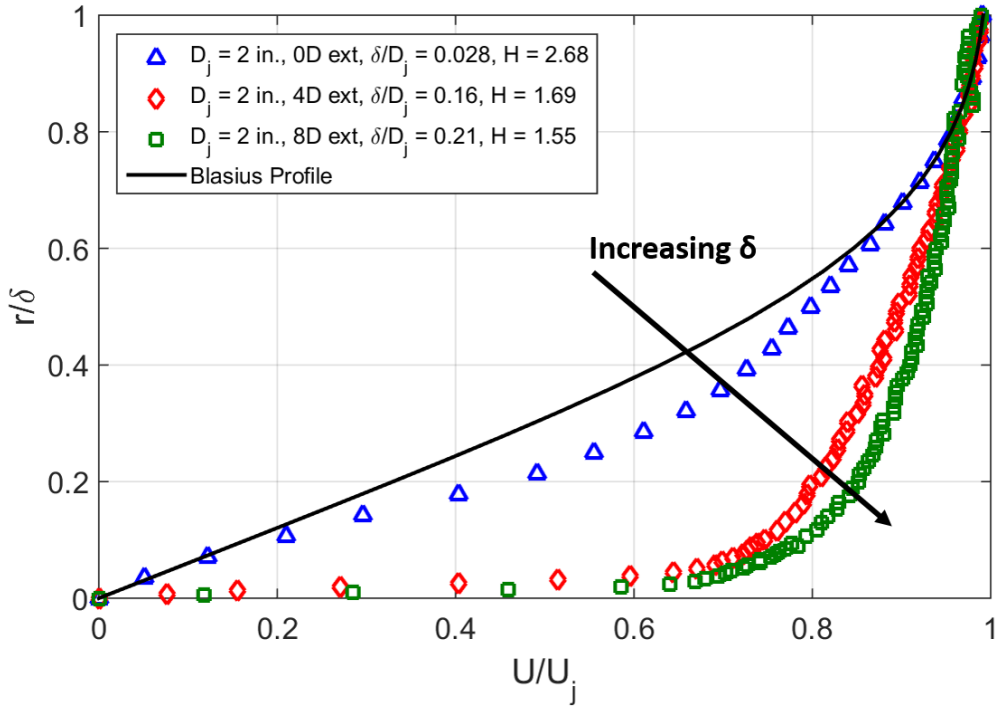

Figure 5.13: Boundary layer velocity profiles for the 2-in. conical nozzle with and without the duct extensions at M_j = 0.8.

Figure 5.14 shows the normalized boundary layer profiles for the 1.54-in. ASME nozzle and 1.6-in. conical nozzle at a jet exit Mach number of 0.8. The normalization scheme used for Figure 5.13 is used for Figure 5.14 as well. Based on the boundary layer thickness and shape factor shown in the legend of this figure, the conical nozzle has the thicker and more developed boundary layer. The peculiar feature of these plots is that for a normalized distance r/δ (y-axis of Figure 5.14) of less than 0.4, ASME nozzle flow appears to be less developed than the conical nozzle flow and is quite close to the Blasius profile. This implies that the ASME nozzle is producing a less developed laminar nozzle-exit boundary layer up to this value of r/δ. On the other hand, for r/δ greater than the 0.4, the ASME nozzle's boundary layer profile is farther from the Blasius profile than that for the conical nozzle, which would imply a more developed and maybe even turbulent boundary layer.

This type of "overlapping" behavior of boundary layer profiles was shown by Schubauer and Klebanoff[81] and elaborated on by Schlichting[68] to be a transitional boundary layer. As a boundary layer transitions from laminar to turbulent, there is point in its development that it switches between laminar and turbulent states. This is quantified as the intermittency factor, where the higher value of intermittency means that the boundary layer is closer to being turbulent. This could mean that either the ASME nozzle, the conical nozzle, or both are in transitional state.

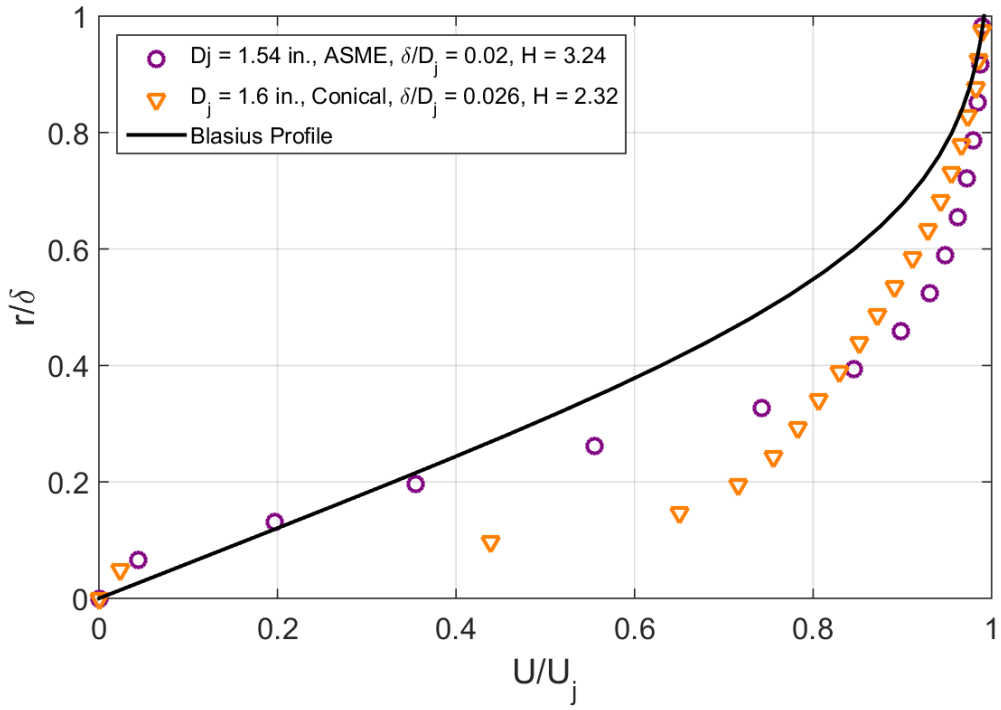

Figure 5.14: Boundary layer velocity profiles for the 1.54-in. ASME nozzle and the 1.6-in. conical nozzle at M_j = 0.8.

The normalized boundary layer velocity profiles for all 6 nozzles used in this study at a jet exit Mach number of 0.8 are shown in Figure 5.15. The first observation is that, with exception of the two ASME nozzles, all test nozzles demonstrate that as the shape factor decreases the velocity profiles shift from a laminar profile (similar to the Blasius profile) to a turbulent profile. The two ASME nozzles have the transitional velocity profile

appearance described above. These are also the boundary layers with shape factors greater than 3, which is typically not seen in the published literature. In the case of flow over a flat plate, a shape factor greater than 3 usually implies flow separation. But the boundary layer profiles described here were measured just outside of the nozzle-exit, implying that the flow does not have a surface from which to separate. Such detailed boundary layer profiles at the nozzle-exits have typically not been obtained by other investigators. It is possible that, for these nozzle-exit boundary layers, a shape factor greater than 3 implies that the boundary layer is in a state of transition.

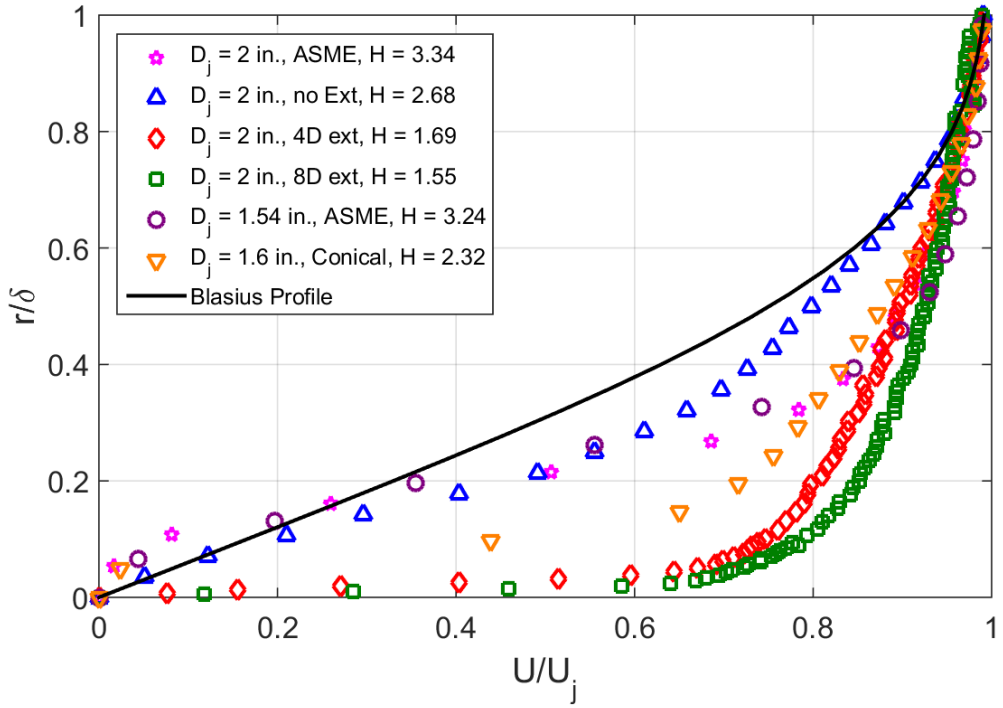

Figure 5.15: Boundary layer velocity profiles for all the nozzles studied at M_j = 0.8.

Table 5.2: Boundary layer state data for all the nozzles and conditions examined in this study.

		M = 0.4	M = 0.5	M = 0.6	M = 0.7	M = 0.8
2 in. ASME	δ(in.)	0.044	0.049	0.041	0.038	0.037
	δ*(in.)	0.0093	0.0116	0.0101	0.0102	0.0107
	θ*(in.)	0.0041	0.0041	0.0036	0.0033	0.0032
	H	2.26	2.85	2.78	3.11	3.34
2 in. Conical 0D extension	δ (in.)	0.084	0.068	0.0209	0.065	0.056
	δ*(in.)	0.0222	0.0211	0.061	0.0210	0.0184
	θ*(in.)	0.0104	0.0088	0.0081	0.0076	0.0068
	H	2.12	2.40	2.57	2.75	2.68
2 in. Conical 4D extension	δ (in.)	0.344	0.312	0.0327	0.356	0.321
	δ*(in.)	0.0498	0.0514	0.0528	0.0537	0.0505
	θ*(in.)	0.0342	0.0323	0.0331	0.0331	0.0299
	H	1.46	1.59	1.60	1.62	1.69
2 in. Conical 8D extension	δ (in.)	0.402	0.351	0.371	0.374	0.425
	δ*(in.)	0.0476	0.0491	0.0470	0.0493	0.0533
	θ*(in.)	0.0345	0.0326	0.0314	0.0321	0.0345
	H	1.38	1.51	1.50	1.54	1.55
1.54 in. ASME	δ(in.)	0.039	0.034	0.03	0.029	0.03
	δ*(in.)	0.0081	0.0089	0.0081	0.0075	0.0087
	θ*(in.)	0.0034	0.0031	0.0029	0.0028	0.0027
	H	2.39	2.87	2.76	2.67	3.24
1.6 in. Conical	δ(in.)	0.048	0.048	0.045	0.042	0.041
	δ*(in.)	0.0088	0.0089	0.0098	0.0081	0.0094
	θ*(in.)	0.0051	0.0050	0.0047	0.0043	0.0040
	H	1.74	1.78	2.09	1.89	2.32

Figure 5.16 shows the variation of the normalized nozzle-exit boundary layer thickness with the shape factor. Figure 5.16 shows that as the boundary layer gets thicker, the boundary layer becomes more developed and the shape factor decreases. Based on this

trend for the remainder of this analysis the decreasing boundary layer shape factor will be used as the condition to show a thicker and more developed boundary layer.

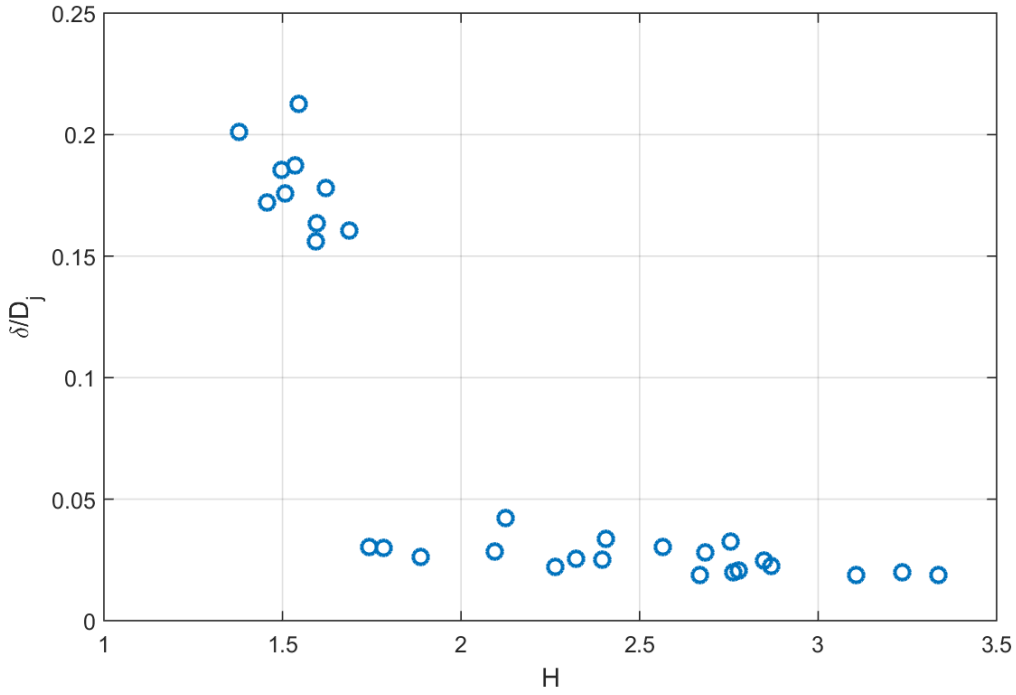

Figure 5.16: Variation of the nozzle-exit boundary layer shape factor with the normalized boundary layer thickness.

Figures 5.17 and 5.18 show the normalized jet noise spectra corresponding to the spectra shown in Figures 5.9 – 5.12. Since only narrowband spectra are presented here, the normalization follows the methodology spelled out in Gaeta and Ahuja[42]. It is assumed that if the spectra of different jet velocities and diameters and boundary layer thicknesses, followed the scaling laws discussed earlier in Chapters 3 and 4 where boundary layer effects were not accounted for, all spectra will collapse. But if they do not collapse, it is reasonable to attribute the spectral regions where they do not collapse to the effect of boundary layer. In Figures 5.17 and 5.18, spectral collapse is observed mostly at low-frequencies but not at the higher frequencies to the right of the spectral peak. This indicates

that the spectral normalization shown in Gaeta and Ahuja[42] continues to work at low frequencies even for jets with large nozzle-exit boundary layers, but the additional high-frequency reductions are a result of the varying nozzle-exit boundary layer states. This allows for the use of the normalizing scheme used in Figures 5.17 and 5.18 for the analysis that follows to be based on all 30 cases acquired as part of this study and not just the data from a single nozzle.

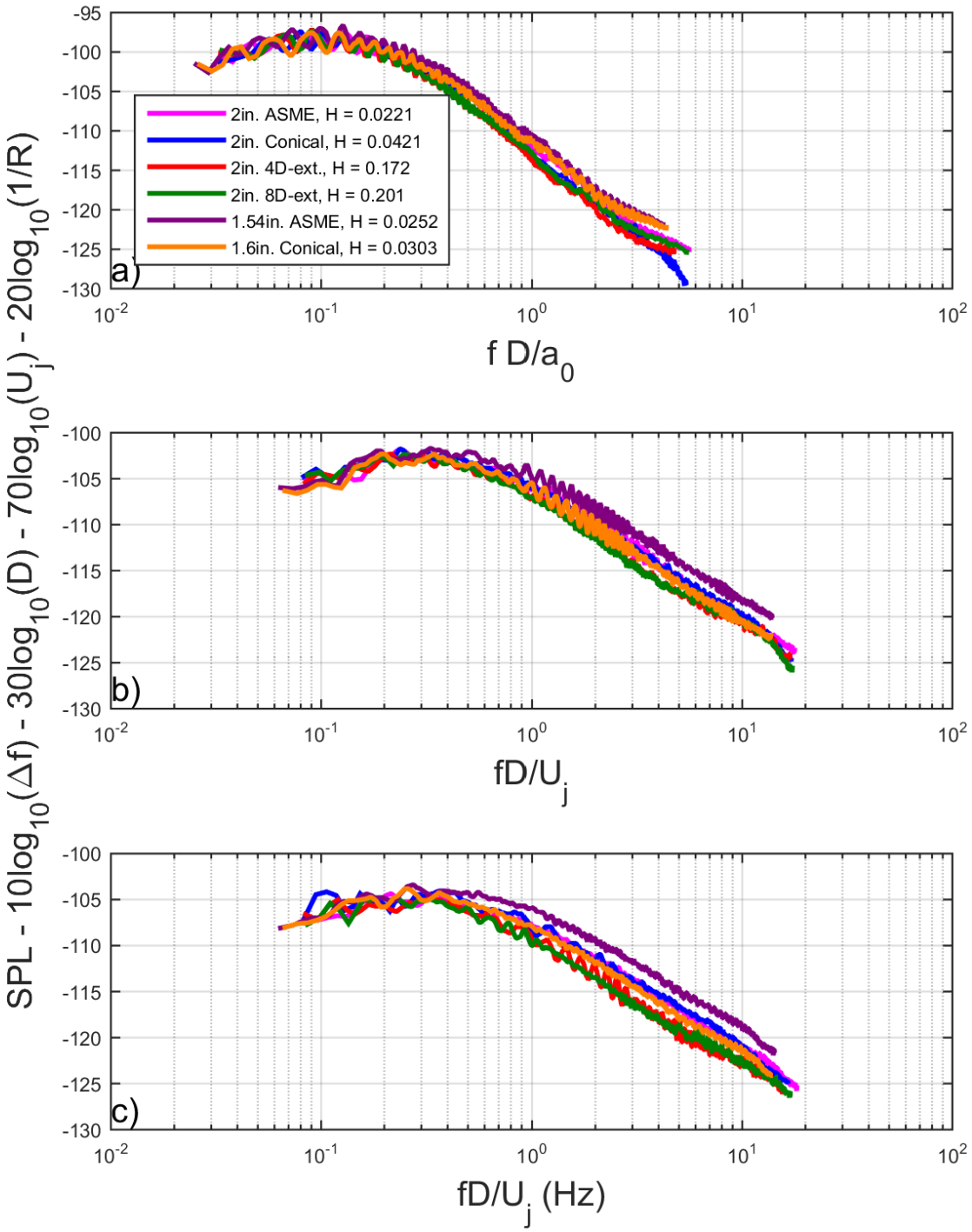

Figure 5.17: Normalized spectra of the six nozzle configurations at $M_j = 0.4$. a) θ = 30°, b) θ = 60°, and θ = 90°. R = 12ft., Δf = 32 Hz., lossless.

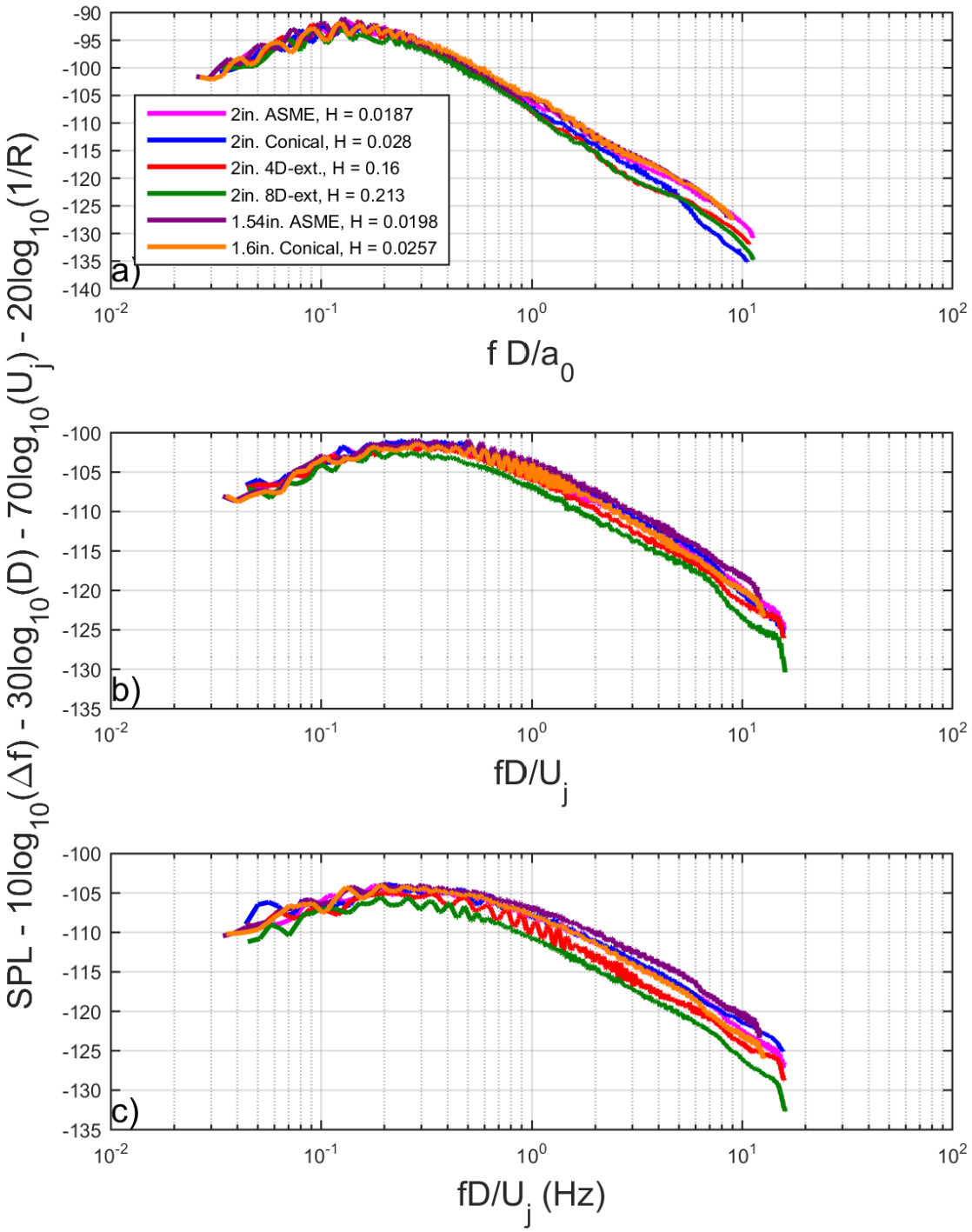

Figure 5.18: Normalized spectra of the six nozzle configurations at M_j = 0.8. a) θ = 30°, b) θ = 60°, and θ = 90°. R = 12ft., Δf = 32 Hz., lossless.

The large reductions across the whole spectral range that were observed by Powell[13] and Ahuja[31] are not observed in the above measurements. The author suggests that the reason for this is the following. Even the case of the 8-diameter extension, the jet flow never became fully developed. Powell[13] compared the case of a jet with a laminar nozzle-exit boundary layer to the case of a fully developed flow. Since the above data shows that jet noise is reduced with a more developed nozzle-exit boundary layer, it is not outside the realm of possibility that since the fully developed jet flow used in Powell[13] is more developed than the boundary layers in this study, those large reductions occur in extreme case of the fully developed flow. Similarly, Ahuja[31] added 18 diameters worth of extensions to his nozzle. This would cause the flow to develop much more than any of measured jets in this study. This implies that Ahuja[31] would see larger reductions than observed in the current study.

5.3.1 Variation of OASPLs with the Boundary Layer Shape Factor

The variation of the OASPLs with the boundary layer shape factor will now be discussed. Figure 5.19 shows this variation for polar angles of 30°, 60°, and 90°. A regression curve is drawn through the measured data. As shown in Figure 5.19a, at θ = 30°, there is not any clear relationship between the shape factor and the OASPL. This is contradictory to Figures 5.16 and 5.17 that does show high-frequency reductions at θ = 30°, even though this reduction at this angle begins at a higher frequency than at the other two polar angles. A lack of clear relationship of the OASPL with the shape factor at θ = 30° can be attributed to the fact that the reductions at this angle occur at frequencies where the spectral levels are rather low and the OASPL is dominated by the SPL levels associated

with the spectral peak, which show spectral collapse at $\theta = 30°$. This was not the case at other polar angles for which a better curve fit was obtained as discussed below.

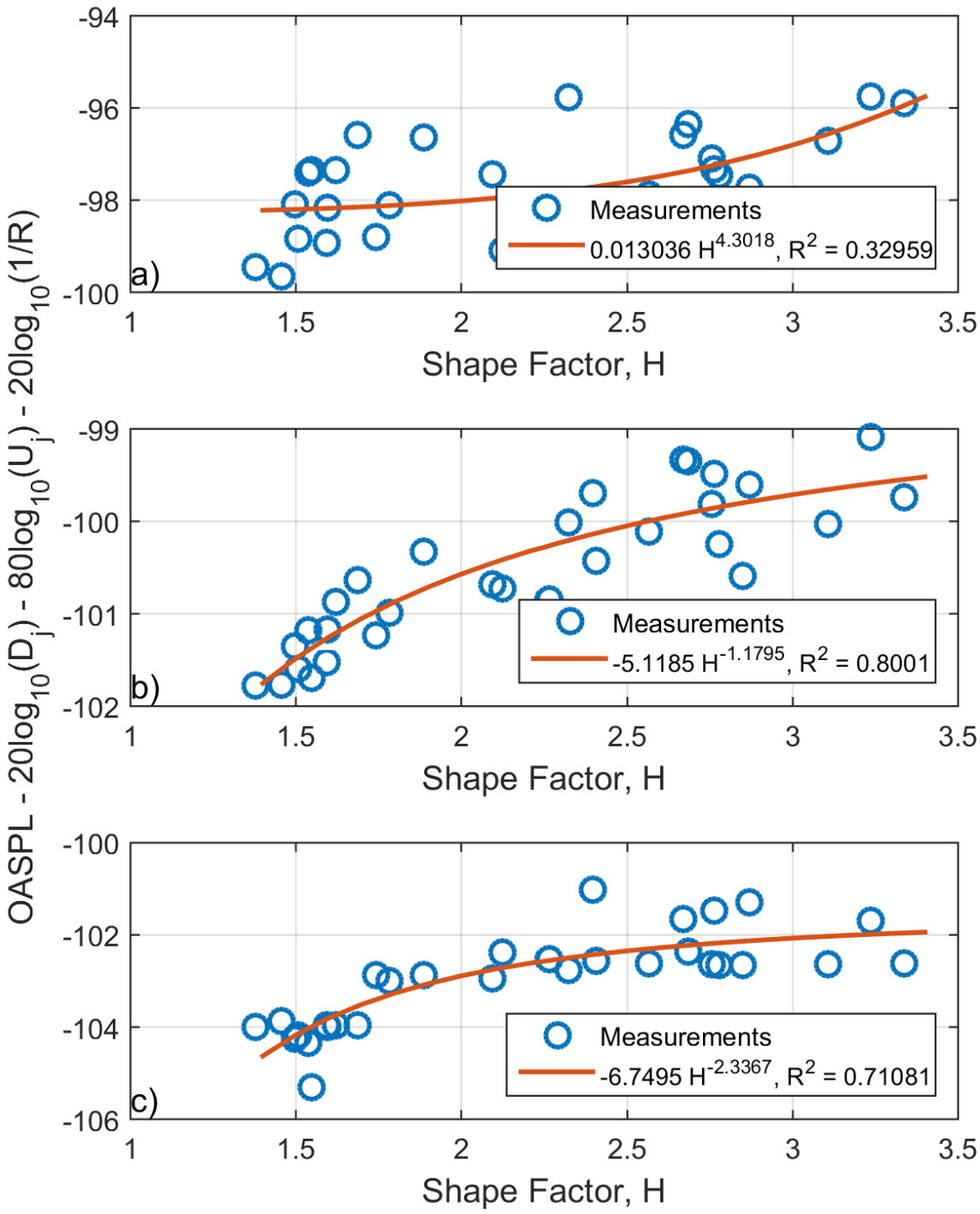

Figure 5.19: Normalized OASPL variation with boundary layer shape factor. a) θ = 30°, b) θ = 60°, and θ = 90°.

For spectra where the high-frequency reduction contributed to the OASPLs, the relationship between the boundary layer shape factor and the OASPL followed the following empirical relationship:

$$OASPL \propto \Gamma H^{\Omega} \tag{5.9}$$

This is depicted in Figures 5.19b and 5.19c. Note that both curves level off at a value of H just larger than 3.5. The legends in each part of 5.19 contain the equations of the curve fits, as well as the R^2 goodness factors associated with the curve fit. While, the goodness factors even for the measurements at polar angles of 60° and 90° are not as high as would be desired, these values still show that there is a reasonable trend of OASOLs increasing with increasing shape factor (or with decreasing boundary layer thickness). Part of the reason for these lower R^2 values can be the scatter in the $H = 2.5 – 3$ region. In comparison, the $\theta = 30°$ has such a low goodness factor that the data does not seem to have any defined relationship. As a laminar boundary layer develops, it will transition to a turbulent boundary layer passing through the nominally laminar and nominally turbulent boundary layer states[69], which result in a steady decrease in the shape factor. The curves indicate that at as the boundary layer becomes more laminar, the effect of the jet noise reaches an asymptote. On the other hand, at the turbulent end of the curve where the shape factor values are low, a small decrease in the shape factor can lead to large reductions in noise as seen in the OASPL variation shown in Figure 5.19. This further reconciles the works of Powell[13] and Ahuja[31], who observed larger noise reduction, but with much more developed boundary layer. It is noted here that no other researcher has conducted this type of analysis before.

As shown in Figures 5.16 and 5.17 above, the effect of the boundary layer on the jet noise is also frequency dependent. Due to this fact, Figures 5.20 and 5.21 are presented, which show the variation of the normalized noise at specific Strouhal number with boundary layer shape factor. To construct Figures 5.20 and 5.21 the normalized narrowband spectra above were interpolated to acquire the normalized SPL at specific Strouhal number for each of the six nozzle configurations and five Mach numbers.

Figures 5.20 and 5.21 show the variation of normalized SPL with the nozzle-exit boundary layer shape factor for Strouhal numbers of 0.5 and 14. In both figures, this variation is shown for polar angles of 60° and 90°. These polar angles were used because based on Figures 5.16 and 5.17, the high-frequency reductions are larger in magnitude and occur over a larger portion of the spectra. As can be seen from Figures 5.20 and 5.21, the general relationship shown in Equation 5.9 holds. Because these trends are of the same form as those shown in Figure 5.19, the comments made for the OASPL variation with the shape factor hold true here as well. Based on this data, there does not seem to be a specific trend between the parameters Γ and Ω of Equation 5.9 and the Strouhal number. Similar results were shown for the variation of normalized SPL with the boundary shape factor at other Strouhal numbers between 0.5 and 14. Even though, the R^2 values are low for these curve fits, which the author believes are related to the scatter associated with the data points, the trends are still captured.

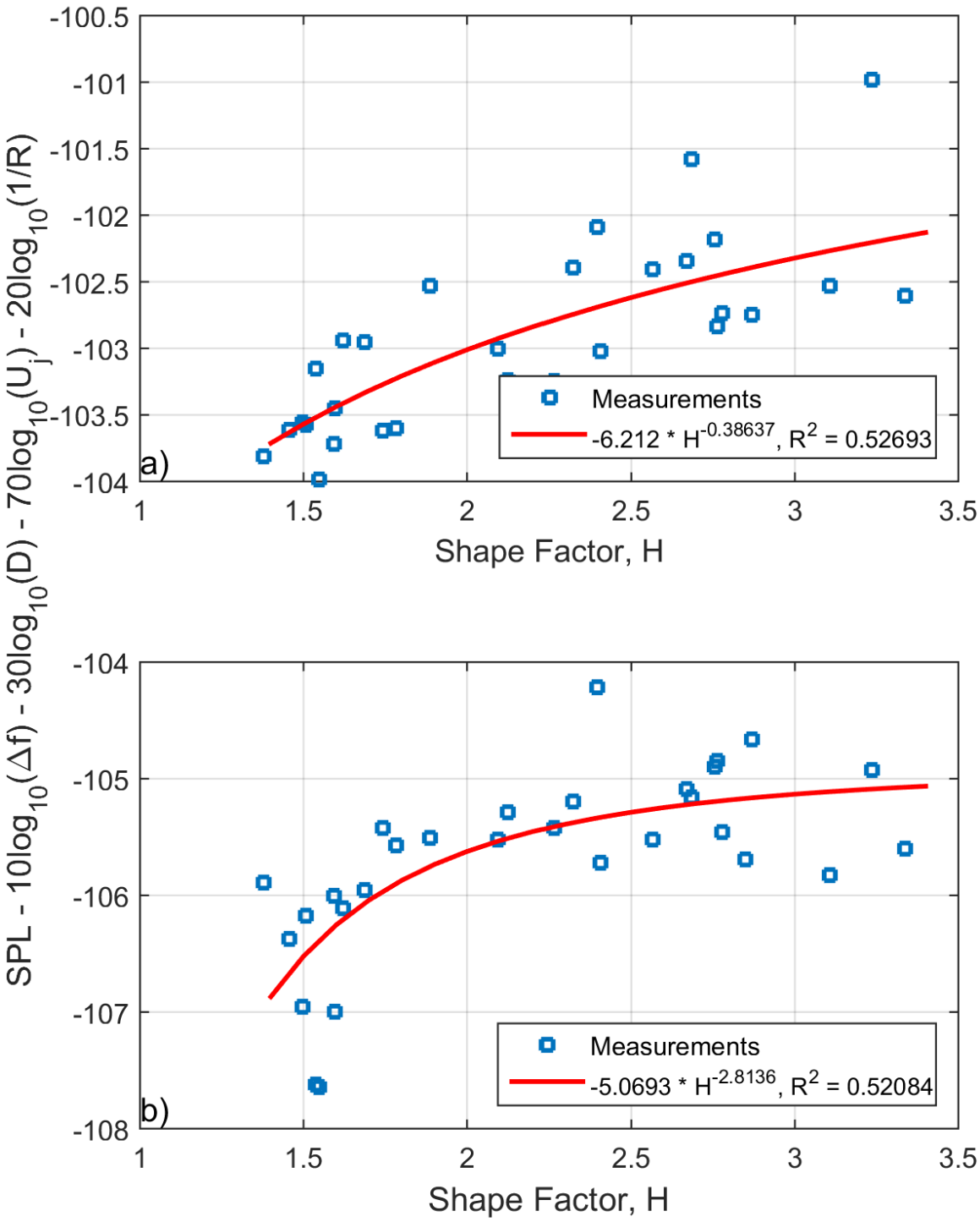

Figure 5.20: Normalized SPL variation with boundary layer shape factor for a Strouhal number of 0.5. a) θ = 60° and b) θ = 90°.

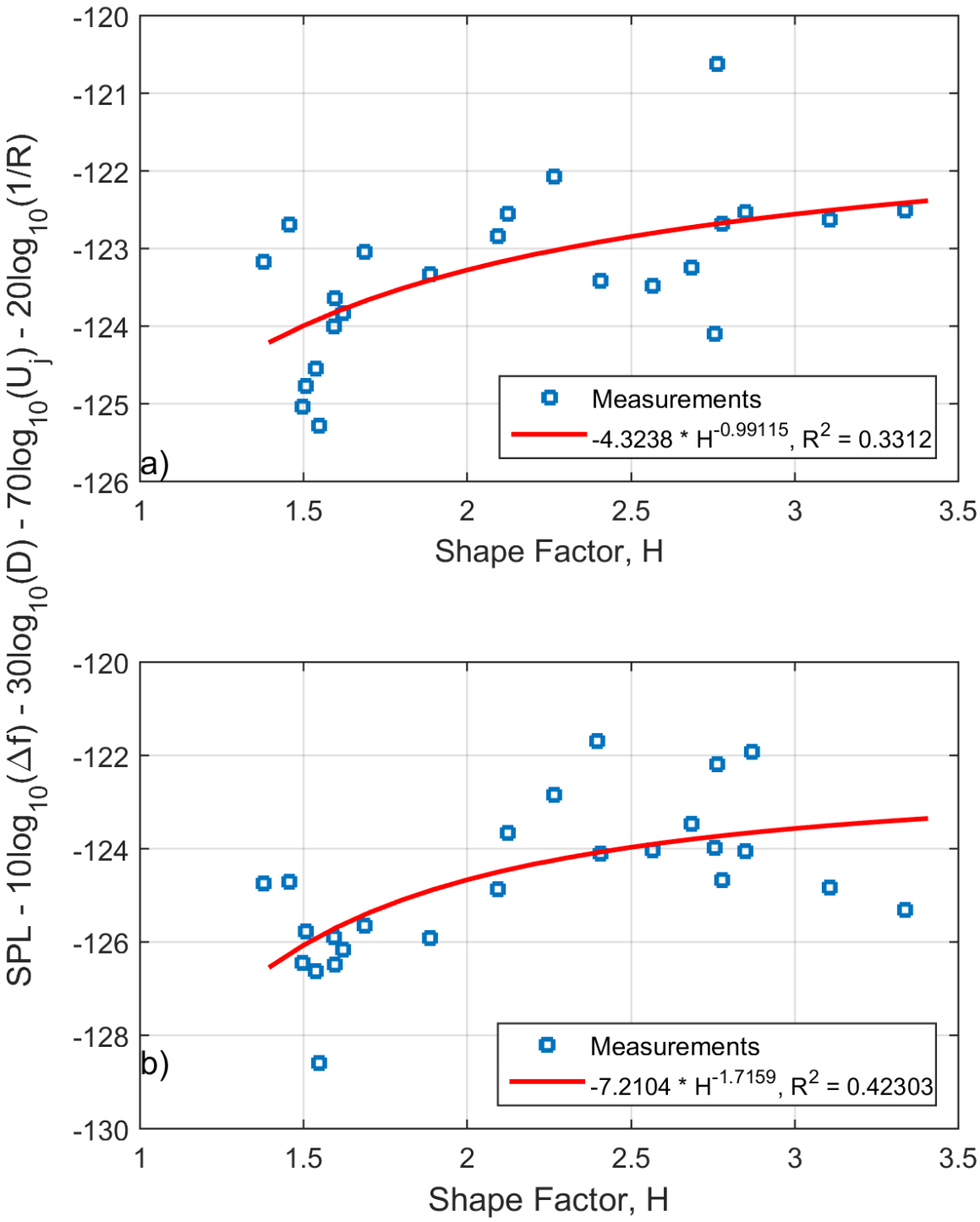

Figure 5.21: Normalized SPL variation with boundary layer shape factor for a Strouhal number 14. a) θ = 60° and b) θ = 90°.

It is clear from the equations derived for the curve fits of the data shown in Figures 5.20 and 5.21 that they follow the trend indicated by Equation 5.9, but the values of the coefficients Γ and Ω of Equation 5.9 vary with Strouhal number. It turns out that both coefficients can be empirically derived as a function of Strouhal number. This relationship is shown in Figure 5.22. For simplicity, only the 90° polar angle relationship is shown. As seen in Figure 5.22, the variation of both Γ and Ω when plotted against the Strouhal number can be modeled as polynomials. These polynomials are:

$$\Gamma = (4.355 \times 10^{-5}\, H^6) - (0.002144\, H^5) + (0.04356\, H^4) - (0.4718 H^3) + (2.822\, H^2) - (7.941 H) - 2.386 \quad (5.10)$$

$$\Omega = (3.829 \times 10^{-5}\, H^5) - (0.001559\, H^4) + (0.02313\, H^3) - (0.1617 H^2) + (0.6682\, H) - 3.37 \quad (5.11)$$

The data and curve fits shown in Figure 5.22 are only for Strouhal numbers of 0.25 to 15. The R^2 values are shown in the plot legends. This is done because based on the normalized spectra shown in Figures 5.16 and 5.17, the reductions in levels due to the nozzle-exit boundary layer state begin at a Strouhal number of 0.25 at $\theta = 90°$. A Strouhal number of 15 is used as the upper limit of these plots as is the largest Strouhal number in which data is available for all 6 nozzle configurations at all 5 Mach numbers tested. The curves shown in Figure 5.22 are now used to calculate the coefficients in Equation 5.9 and used to correct jet noise spectra for the effect of the nozzle-exit boundary layer.

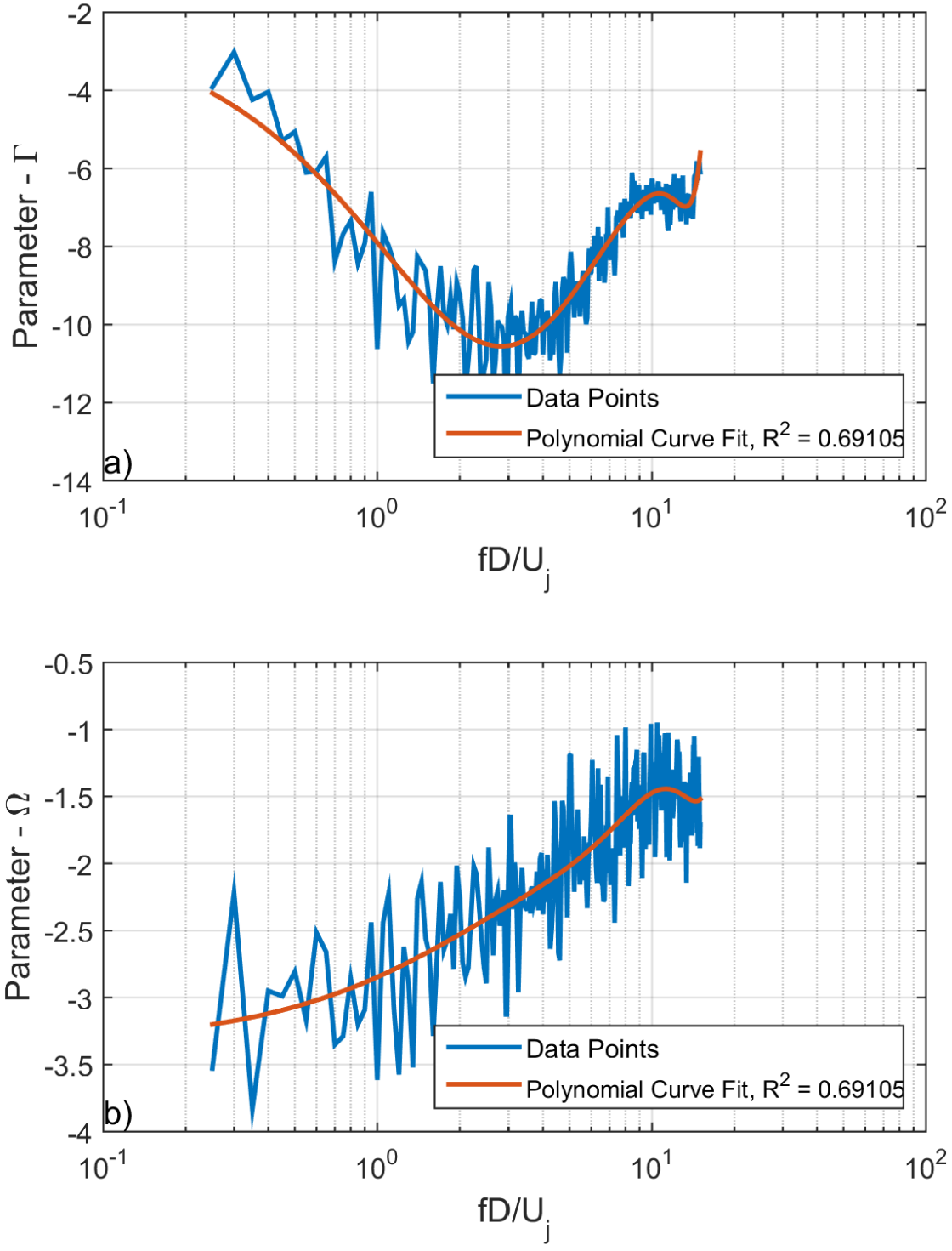

Figure 5.22: Empirically derived curve fits for the Ω and Γ parameters in the ΓH^{Ω} function.

Given this information, spectra in Figures 5.16 and 5.17 along with the remainder of the dataset not shown in those figures are normalized using this relationship. The results of this normalization are shown in Figure 5.23. All of the nozzle configurations and Mach number cases are plotted on the same axes. In addition, the curves are cut off at a Strouhal number of 15, since that was the extent of the curve fits used to generate the nozzle-exit boundary layer correction. As shown in Figure 5.23, the spectra collapse to within ±1.75 dB. Based on Figures 5.19 and 5.20 that show the variation of normalized SPL with nozzle-exit boundary layer shape factor at specific Strouhal numbers, there are outlying points that do not sit close to curve fit. Considering this, the collapse can be considered quite reasonable.

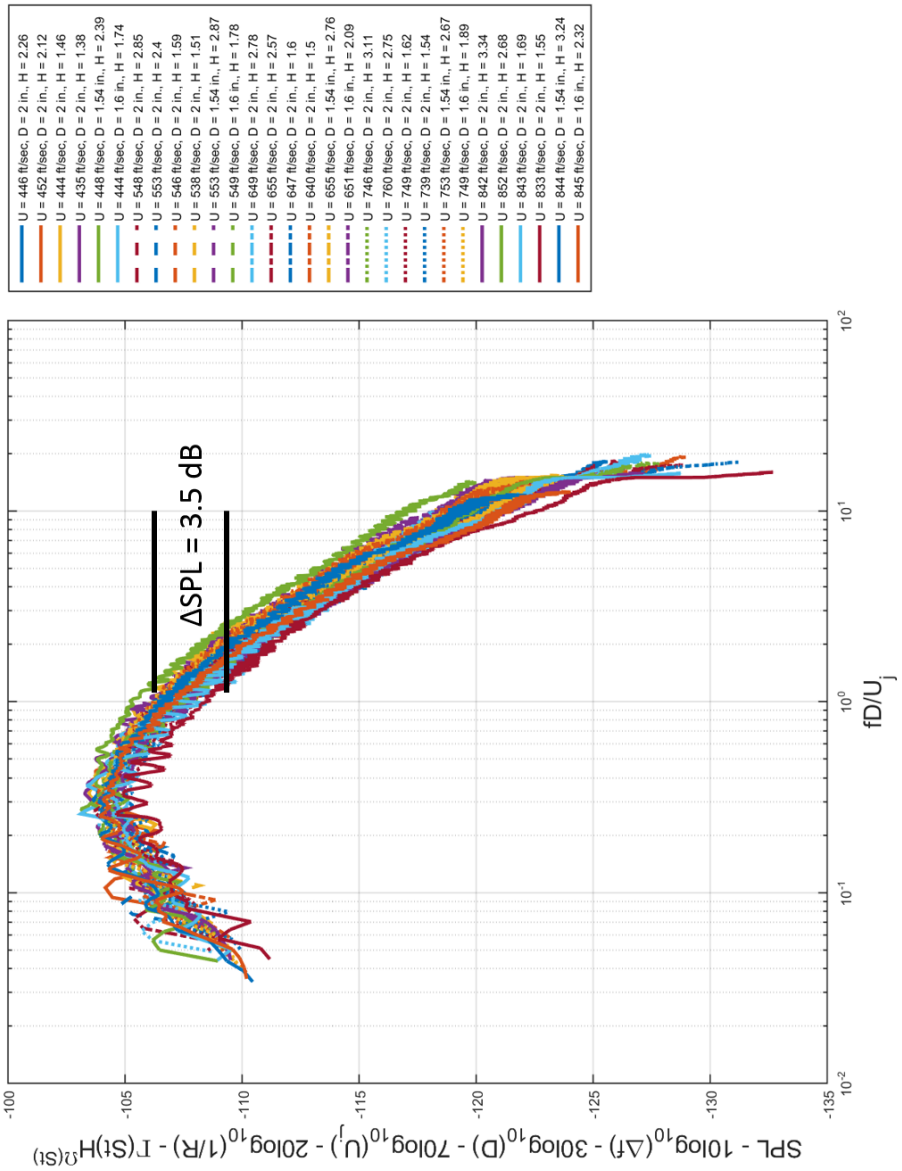

Figure 5.23: Full normalization of all 30 cases used in this study including the correction for the nozzle-exit boundary layer at θ =90°.

5.4 Conclusions

This study confirms that the nozzle-exit boundary state can have a major effect on the measured jet noise. It was shown that as the nozzle-exit boundary layer develops and transitions from laminar to turbulent, the high frequency jet noise decreases. In addition,

these reductions vary with frequency. In particular, larger higher reductions are observed at higher frequencies. An empirical relationship was derived between the jet noise and the boundary layer shape factor. The methodology developed here should be further verified against well-controlled experiments involving detailed noise and nozzle-exit boundary layer measurements in the future. The data presented here should also prove valuable for validating future theoretical and computational formulations.

The most important conclusion of this study is that if the lossless jet noise data presented by different authors acquired in different facilities (no matter how clean) does not match after allowing for known velocity, temperature, distance, angle, and nozzle area scaling laws, a good the reason can be a difference in the nozzle-exit boundary layer. It is therefore recommended that when jet noise measurements are acquired, the accompanying boundary layer measurements should also be acquired as a matter of routine.

There are four important tasks for future work in this area: (1) validating the empirically derived correction on measurements outside of the database presented in this work, (2) deriving and validating a purely theoretical expression relating the boundary layer state and the jet noise produced by the jet, (3) making similar noise and nozzle boundary layer measurements for a full-scale engine, and (4) conducting these same tests at supersonic speeds to observe the effects on shock noise and extend the correction to that velocity regime.

CHAPTER 6

EFFECT OF NOZZLE'S PROXIMITY TO PLENUM CHAMBERS AND SUPPLY DUCTS ON MEASURED JET NOISE

In Chapter 3, the Doubling-Diameter method for detecting rig-noise contamination in an anechoic jet-facility was discussed and used for the investigation of the existence of rig-noise contamination in the GTRI Anechoic Jet-Facility. It was shown that if a jet noise facility designed for testing smaller diameter nozzles is used for testing larger diameter nozzles, the jet noise may become contaminated by rig noise and one must establish if this is the case before using the facility for larger nozzles. Besides rig noise, the proximity of nozzle's proximity to plenum chambers and supply ducts can produce inaccuracies in jet noise measurements via associated reflections and shielding. These effects need to be taken into account when the anechoic jet-facility and an experimental set-up are designed. Many of the spectra in previous were thought to have contamination due to reflections to their wavy appearance. The role of such reflections and shielding within an anechoic jet-facility are investigated in this chapter.

6.1 Previous Work

Over the last 60 years, many jet noise measurements have been made in many different facilities for varying jet operating conditions, nozzle geometries. A standard practice in making jet noise measurements is to use a plenum chamber upstream of the nozzle as shown in Figure 6.1. Ahuja[10] outlines a procedure for designing clean anechoic jet-

facilities and points out that the jet plenum chamber can often block a microphone's direct line-of-sight to the nozzle-exit of the jet at larger polar angles with respect to the jet's downstream axis. He suggested that enough room should be left between the plenum and the collector to allow extending the nozzle/nozzle-exit such that the microphones at large angles can "see" the nozzle-exit. In addition, if proper acoustic treatment is not provided on the plenum chamber, the front of the plenum, on which the nozzle attaches, can act as a reflector and may cause cancellation and/or amplification of different frequencies in the jet noise spectrum in the rear arc depending upon the distance of the microphone from the jet noise sources.

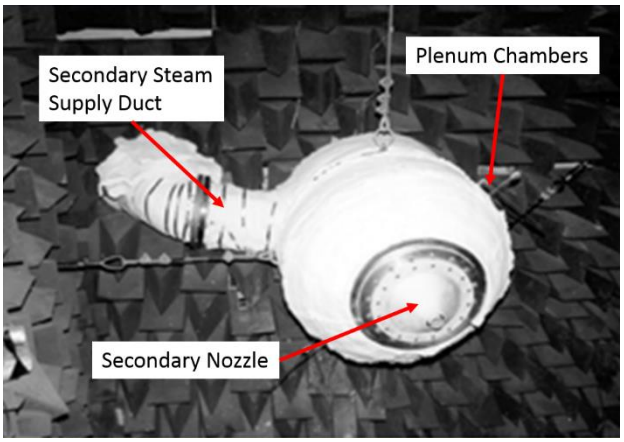

Figure 6.1: Plenum chamber in the GTRI Anechoic Jet-Facility, reproduced from Ahuja[10].

The problem of reflection contamination in jet noise spectra is illustrated in Figure 6.2. A reflection from a surface within an anechoic chamber can interfere with the incident sound signal at the microphone and depending on the phase difference between the reflected and incident wave signals of a given frequency of jet noise, cancellation or amplification can occur. In Figure 6.2, the phases of the incident and reflected waves are denoted as β_1 and β_3, respectively. At a given frequency, when the phase difference between the incident and reflected waves is 0°, the greatest amplification occurs. On the

other hand, for a given frequency, when the phase difference between the incident and reflected waves is 180° the greatest cancellation occurs. Between a phase differences of 0° and 180°, partial amplification or cancellation will occur, with amplification occurring closer to 0° and cancellation occurring closer to 180°. Since, it is a reflected wave interfering with the incident wave, the phase difference is a function of the path length difference between the incident and reflected waves. The phase of the signal of a given frequency is related to distance that signal has traveled through the wave number, *k(f)*. The wave number is the sound wave's spatial frequency, and is defined by the equation:

$$k(f) = \frac{2\,\pi\,f}{a} \tag{6.1}$$

Each frequency component of the broadband jet noise spectrum will experience a different phase difference and therefore different constructive or destructive interference effects at the microphone location. Each frequency will, thus, experience a different amount of amplification or cancellation, which gives the broadband spectrum a "wavy" appearance. It is noted here when the distance traveled by the incident and reflected waves is large, these reflection effects will become smaller or even negligible, because of the inverse square law and atmospheric attenuation causing the levels of the reflected signal to be so much lower than the incident signal. This would cause the incident signal to completely mask the reflected signal.

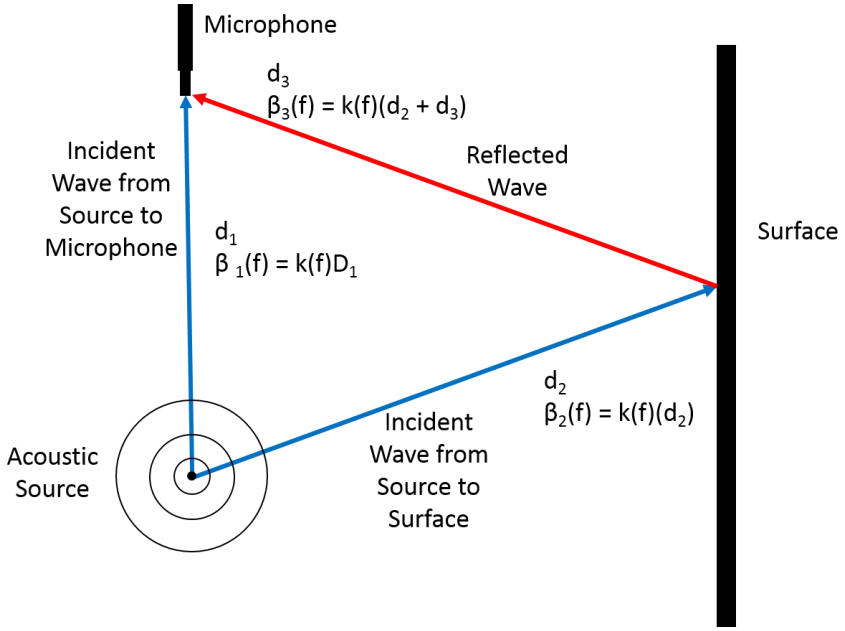

Figure 6.2: The mechanism behind reflection contamination in broadband spectra.

In addition to the reflection effects, the presence of plenum chambers and large flanges on air supply ducts can often produce changes in the observed jet noise via shielding of the sound from reaching the microphone. The physical mechanisms behind shielding are described here and illustrated in Figure 6.3. There are four main mechanisms behind shielding: (1) transmission loss, (2) refraction, (3) scattering, and (4) diffraction[82]. As shown in Figure 6.3, when a sound wave is incident on a hard-surface shield, the wave is reflected back from the shield. Not all of the sound power is reflected away from the shield, some of the sound power will transmit through the shield, depending upon the material properties of the shield and the amplitude and frequency of the sound incident on the shield. The difference in the level of the incident signal and the part of the signal that is transmitted through the shield is typically referred to as the transmission loss. In addition, this transmitted component may not travel in the exact same direction after it is transmitted through the shield. This is commonly referred to as refraction. These two effects contribute to shielding as follows: transmission loss causes lower levels to reach the

microphone when the shield is present and the refraction can cause the wave to not even reach the microphone at all. In addition, sound can move around the shield. This effect is most likely not present in facilities used for jet noise measurements where the duct structure and plenum flanges are typically quite massive. As the sound is incident on the edge of the shield, it can scatter in all directions. This will change the amount of the sound that will actually reach the microphone. In addition, as the sound signal moves over this edge and behind the shield, the different frequency components will travel differently, i.e. diffract. This causes the frequencies in a broadband spectrum to reach the microphone in varying amounts, causing these effects to be highly dependent on frequency.

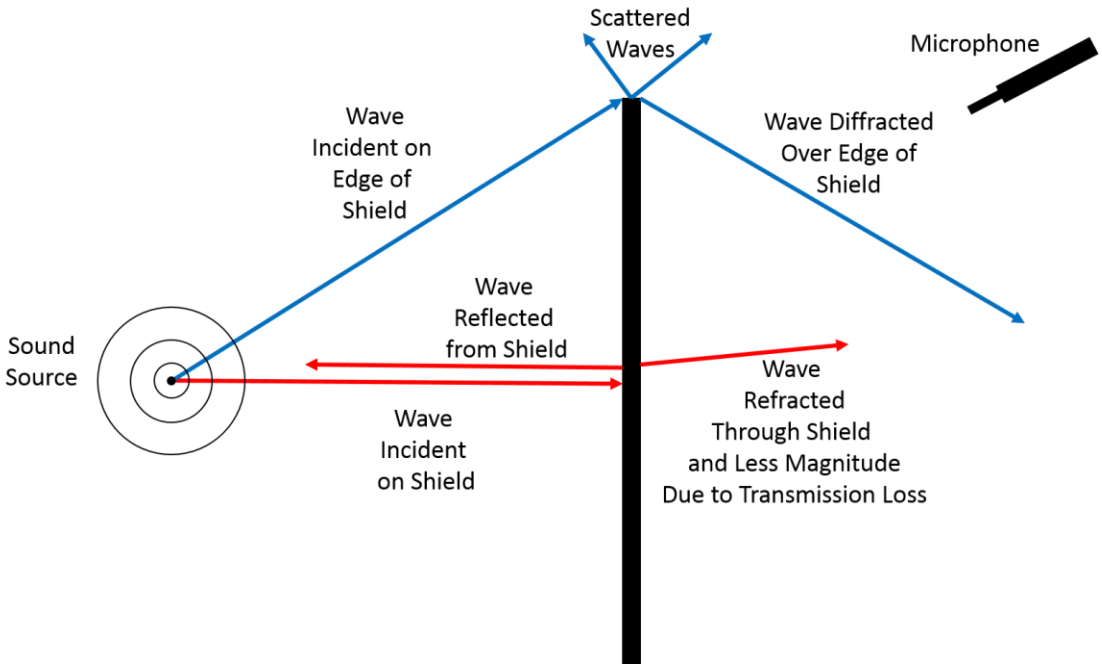

Figure 6.3: Physical mechanisms behind acoustic shielding.

As explained above, reflections can cause reductions and amplifications at specific frequencies within a jet noise spectrum giving the spectrum a "wavy" appearance. Inside of an anechoic jet-facility, the cause of this is twofold: (1) anechoic jet-facilities are not anechoic at all frequencies, so there exists a lower frequency limit where a chamber can be

considered anechoic, and (2) surfaces inside the chamber associated with the microphone arc, the jet plenum, and jet rig's supporting structure, and other mounting devices are often either not acoustically treated for reflections appropriately or at all. The effect of reflections from non-absorbing surfaces manifests itself as peaks and valleys in the measured noise spectrum resulting from the above-described constructive or destructive interference between the incident and reflected acoustic waves, depending on their phase relationship, as explained above. In order for this interference to be significant enough to affect the jet noise spectrum, the reflected and incident acoustic waves must be of similar level. The only way that can happen is: (1) if the reflection takes place from a surface near the microphone so the SPL of the reflected wave is comparable with that incident on the microphone, or (2) if the reflection is from a surface near the jet noise source so the two waves interfere at the microphone after traveling along the same propagation path, where the wave from the source and reflected wave started with comparable levels. Thus, the reflecting surfaces near the jet or near the microphone are most likely to produce inaccuracies in the measured jet noise data.

The problems described above warrant particular scrutiny if the jet-facility is equipped with a large plenum. Having a large plenum has the advantage of creating a clean flow, as the air is moving very slow in the plenum, there is minimal turbulence. One can also have a large plenum if one is working with multiple-stream jets, for example coannular jets. The additional streams need a plenum of their own for a pressure source. These are typically placed coaxially around the primary plenum, increasing the size of the overall structure, as done in the GTRI facility shown in Figure 6.1. Additionally, even if the plenum chamber were not an issue, the secondary nozzle itself can shield part of the primary jet noise in the

forward arc. How well the outer nozzle shields the noise of the inner nozzle needs to be understood. Also, if one assumes the noise measured in the forward arc with such configurations to be pure jet mixing noise, the comparison with established analytical models of jet noise can potentially provide inaccurate comparisons. This problem can become more complicated if the inner nozzle of a two or a three stream nozzle is offset.

Figure 6.1 shows a picture of the plenum chamber inside of the GTRI Anechoic Jet-Facility. The plenum structure in Figure 6.1 contains a primary and a secondary plenum chamber to allow for coannular jet flows. The front face of the plenum and an acoustically untreated secondary nozzle could potentially cause reflections. In addition, since the plenum structure, especially its flange, is large, microphones in the forward arc could potentially suffer from shielding especially for noise sources close to the nozzle-exit. This potential shielding zone in the GTRI Anechoic Jet-Facility is illustrated in Figure 6.4 to the right of the red line shown in the figure. In addition, if the microphone arc or plenum chamber are not properly treated with acoustic lining, reflections from these surfaces could affect the microphone measurements, especially in the rear arc.

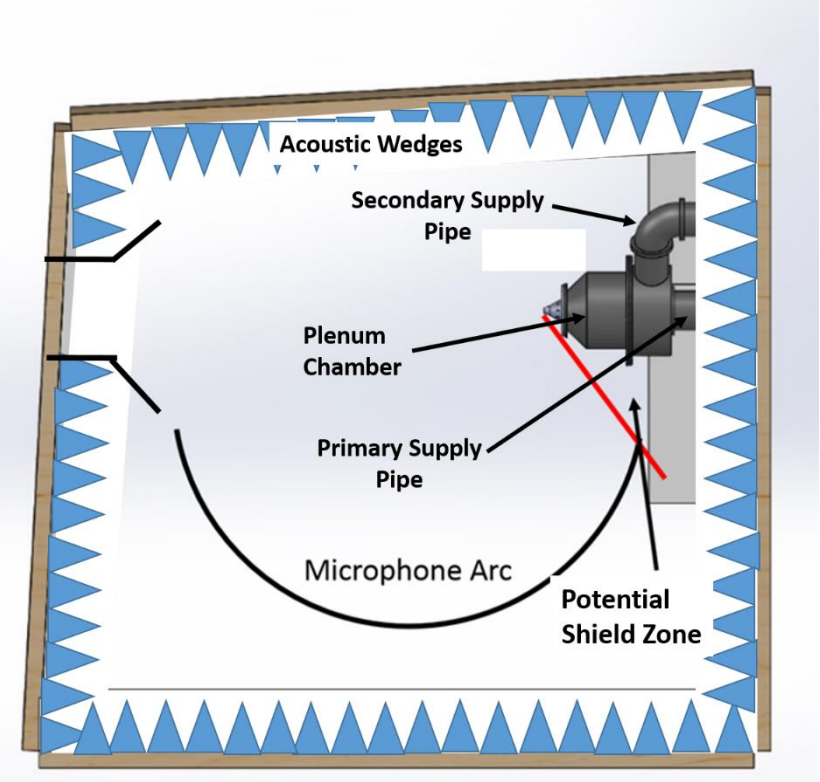

Figure 6.4: The GTRI Anechoic Jet-Facility.

Figures 6.5 – 6.7 show diagrams of other anechoic jet-facilities, in which published data has been acquired and where the plenum could potentially cause shielding effects in the forward arc or reflections in the rear arc. Figure 6.5 shows the GE Cell 41 test facility[83]. The red line in Figure 5 indicates the largest angle before shielding could occur on microphones in the forward arc by the jet rig structure. Based on Figure 6.5, the jet noise measured by the microphone at about 45° could potentially be affected by shielding. Also from Figure 6.5 it can be seen that microphones in the rear arc, especially angles 140° to 155°, could receive reflections from the rig structure.

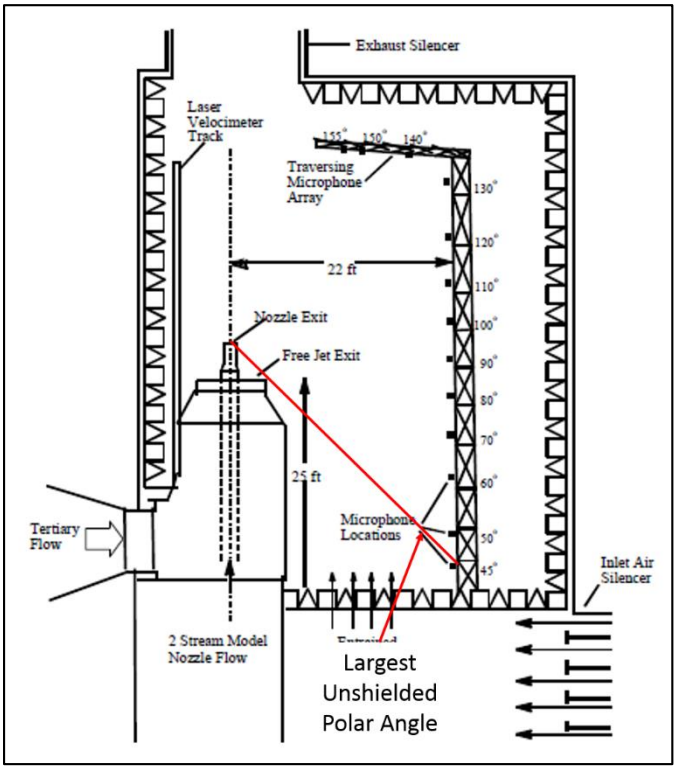

Figure 6.5: GE Cell 41 Facility[83].

Figure 6.6 shows the Penn State High Speed Jet Noise Facility[84], and while the facility has a primary jet stream and a free jet stream, the microphone arc does not appear to be in a position where shielding would happen, but if proper acoustic treatment is not applied to

the jet rig, jet noise measured at microphones in the rear arc could suffer from contamination from reflections.

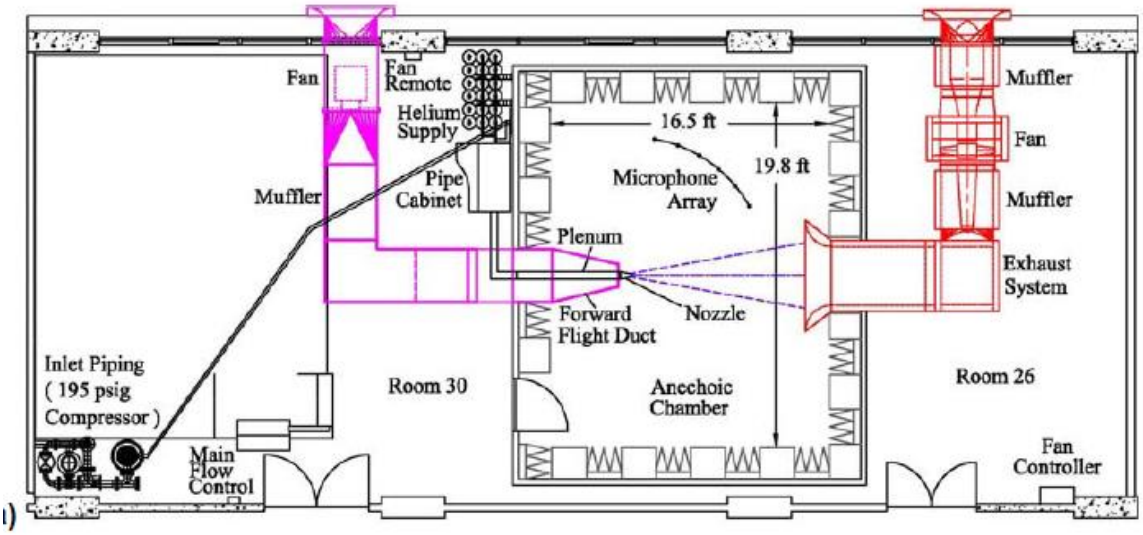

Figure 6.6: The Penn State anechoic high speed jet noise facility[84].

Figure 6.7 shows the Boeing Low Speed Aeroacoustic Facility. As seen in Figure 6.7b this facility does not have a large plenum chamber to supply the jet flows. Therefore, even though it is a coaxial flow facility, the compact nature of the rig will likely not cause

shielding in the forward arc, but like all jet-facilities if there is poor acoustic treatment of the surfaces inside the chamber, reflection contamination is still possible.

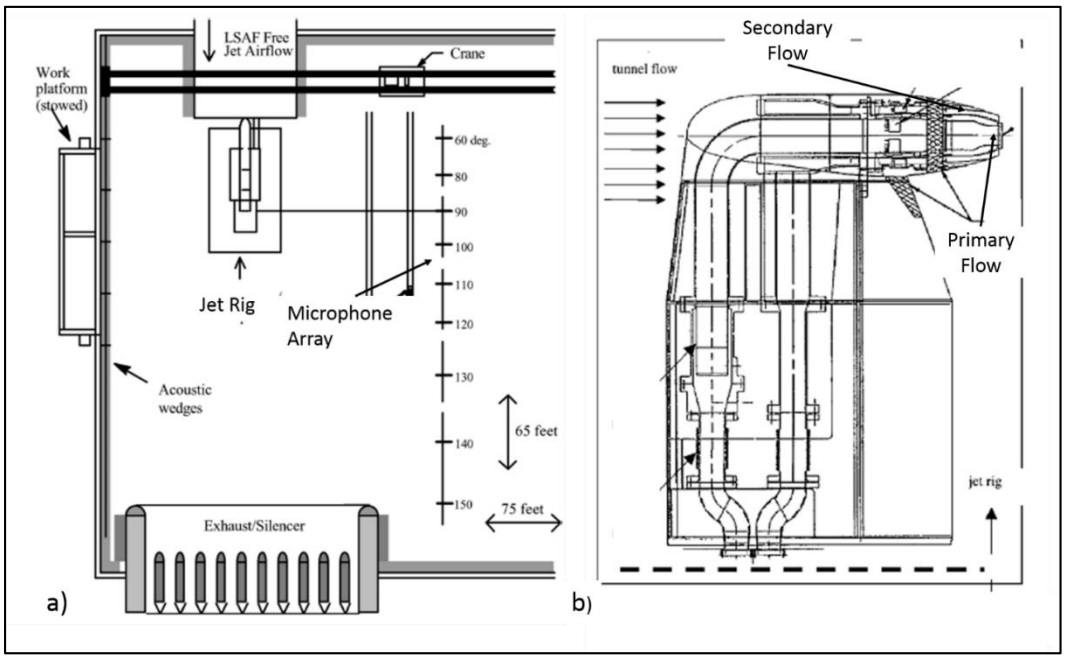

Figure 6.7: The Boeing Low Speed Aeroacoustic Facility[85], a) the configuration of the facility, b) a close up of the jet rig.

It is worth pointing out that the comments made above are purely based upon the diagrams available in the open literature and are pure conjectures. The operators of these facilities might have taken adequate precautions to reduce the effects discussed here.

Based on the reviewed literature, no research has been performed on the shielding effects of plenum chambers. Most of the research pertains to jet noise shielding by wings, aft-decks or the fuselage of an aircraft. Most researchers simply assume that the jet nozzle and the microphones in the forward arc are clear of any obstructions.

Ahuja[10] and Viswanathan [38] both point out the importance of mitigating reflections inside of an anechoic jet-facility and present some strategies for treating surfaces. Both authors also point out that removing all reflection sources is nearly impossible, especially at the low frequencies. The published jet noise spectra of many jet noise researchers seem

to be marred with reflections. A small sample of such spectra along with the facilities in which the noise measurements were acquired is presented here. The comments here are based solely on the spectra and published figures/pictures of the facilities in which the spectra were acquired. If the presented spectra were actually acquired in conditions of improved acoustical treatment than shown in the provided pictures, then this highlights how difficult of a problem reflections can be. It is also noted that the comments made here are not meant to criticize the results of the authors cited here, but just to show that reflection contamination is an ongoing problem that jet noise researchers must address as part of their continuing work. In a 2011 conference paper, Zaman[16] presented many jet noise spectra for his investigation of the effect of nozzle-exit conditions on jet noise. One such spectrum is shown in Figure 6.8a. While the issue of measurement contamination by reflections is not discussed by Zaman[16], the current author believes that the waviness in the spectrum is attributable to reflections. The picture of the facility, which is supplied in the paper, is shown in Figure 6.8b. From Figure 6.8b, it is seen that there are many surfaces near the

jet nozzle that are not acoustically treated, and may lead to reflections if not adequately treated with sound-absorbing lining.

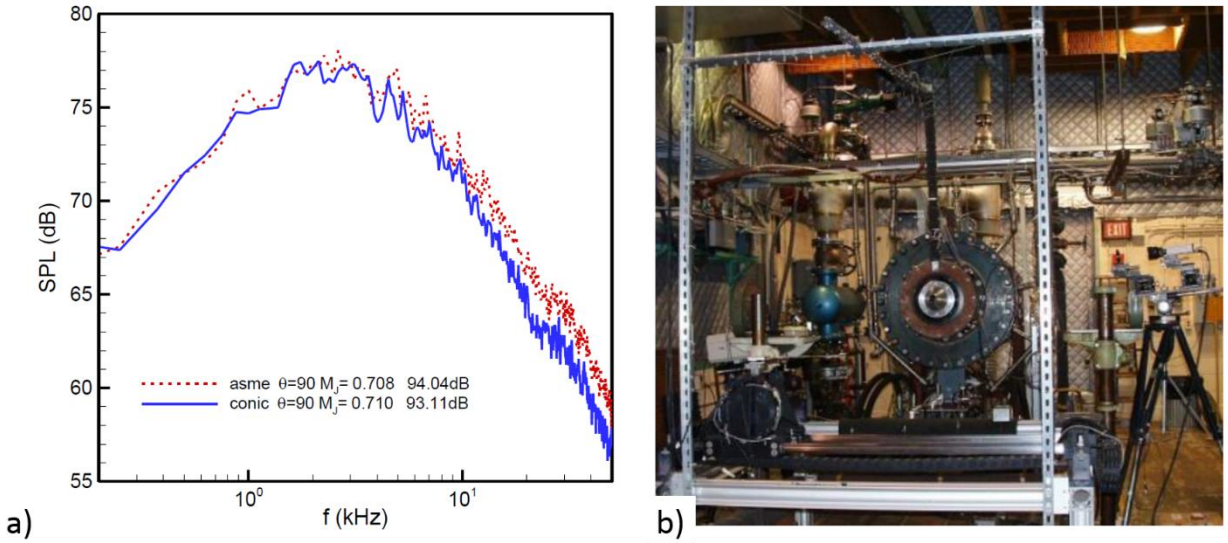

Figure 6.8: (a) Example of jet noise spectra acquired by Zaman[16] and (b) the facility used to acquire the data. (The facility might have been treated for acquiring the acoustic data.)

In a recent paper by Morris et al.[84], the jet noise spectrum shown in Figure 6.9a was presented. Figure 6.9a shows measurements from a baseline nozzle and two fluidic insert nozzles. Figure 6.9b shows a picture of the facility where this data was acquired. This facility seems to have many acoustically untreated surfaces and thus potential sources of reflections. The waviness in each of the measured spectra indicates possible contamination

by reflections. (Note that waviness may not appear perceptibly large and is due to the SPL-scale being quite compact compared to similar plots shown here from other authors.)

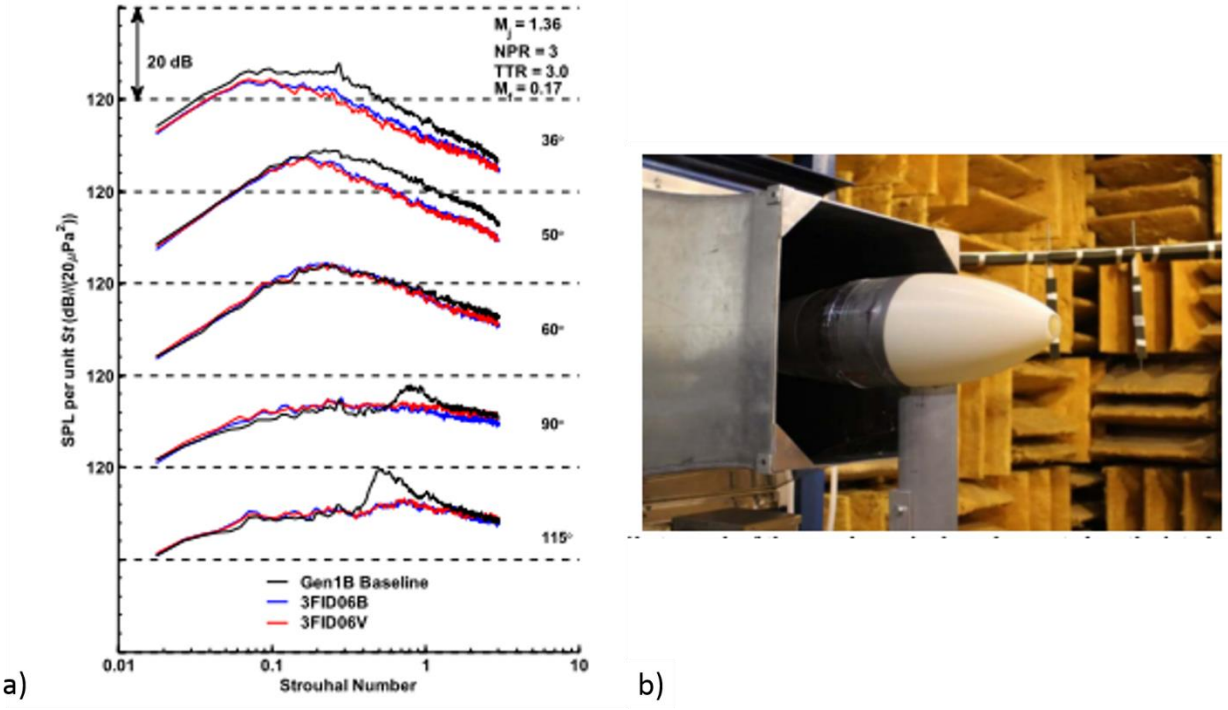

Figure 6.9: (a) Example of jet noise spectra acquired by Morris et al.[84] and (b) the facility used to acquire it.

In 2010, Henderson and Bridges[86] presented the data reproduced here in Figure 6.10a. Figure 10a shows jet noise measurements from nozzles with various chevron configurations. As one can see, this data is full of waviness typical of the result of reflections. The experimental facility used by Henderson and Bridges[86] is shown in Figure 6.10b. Although there is excellent wedge treatment near the jet nozzle, the microphone

array support in the figure appears to be largely untreated and the acoustic reflection from these surfaces maybe the cause of the peaks and valleys shown in Figure 6.10b.

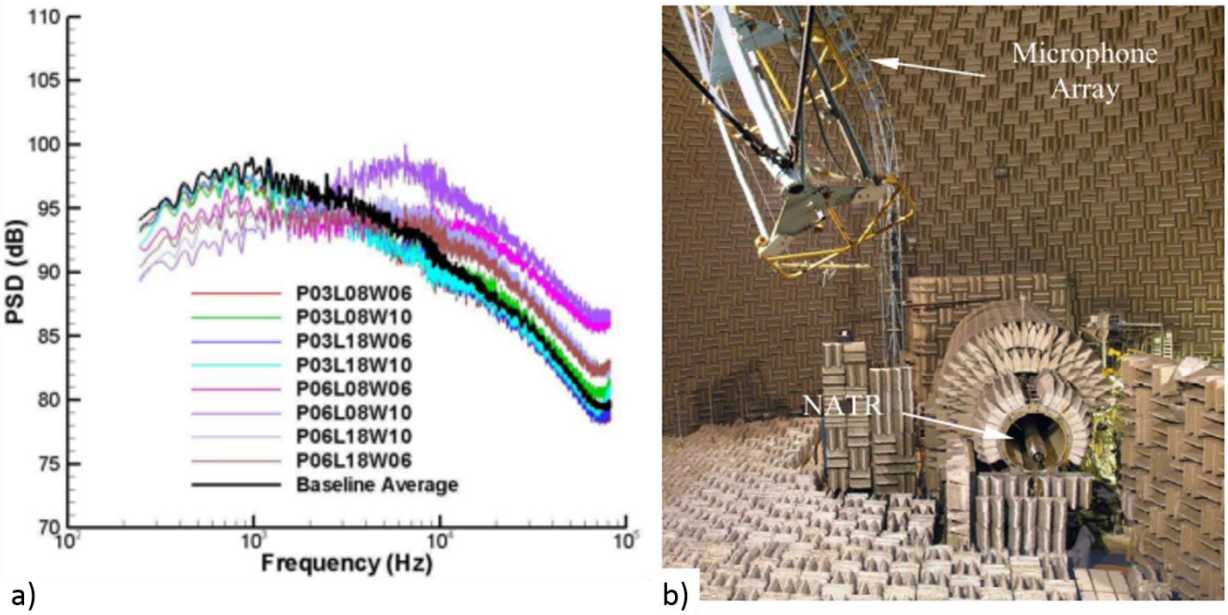

Figure 6.10: (a) Example of jet noise spectra acquired by Henderson et al.[86] and (b) the facility used to acquire it.

The examples given above from experienced jet noise experimentalists show that reflection effects in jet noise spectra are a major concern and best treatment possible needs to be taken to ensure that the cleanest jet noise data possible is measured.

6.1.1 A note on Jet Noise Source Location and Possibility of Larger Shielding of High Frequency Jet Noise in most Jet Noise Facilities

Knowledge of the location of the sound generators can help improve the models used to predict jet noise. Glegg[57] provided a review of this topic. Laufer et al[55], Chu et al[54], Fisher et al[56], and Ahuja et al.[58] all used varying techniques to locate the position of the jet noise sources for each frequency inside of the jet. A compilation of their results on a plot relating fD/U_j to x/D along with the curve fit was shown in Breen and Ahuja[53] and is reproduced here in Figure 6.11a. Breen and Ahuja[53] showed that the jet noise sources move

downstream as the Reynolds number of the jet is reduced and this has an impact on how the source frequency varies with source location. Figure 6.11b shows a reproduction of their data that shows this trend.

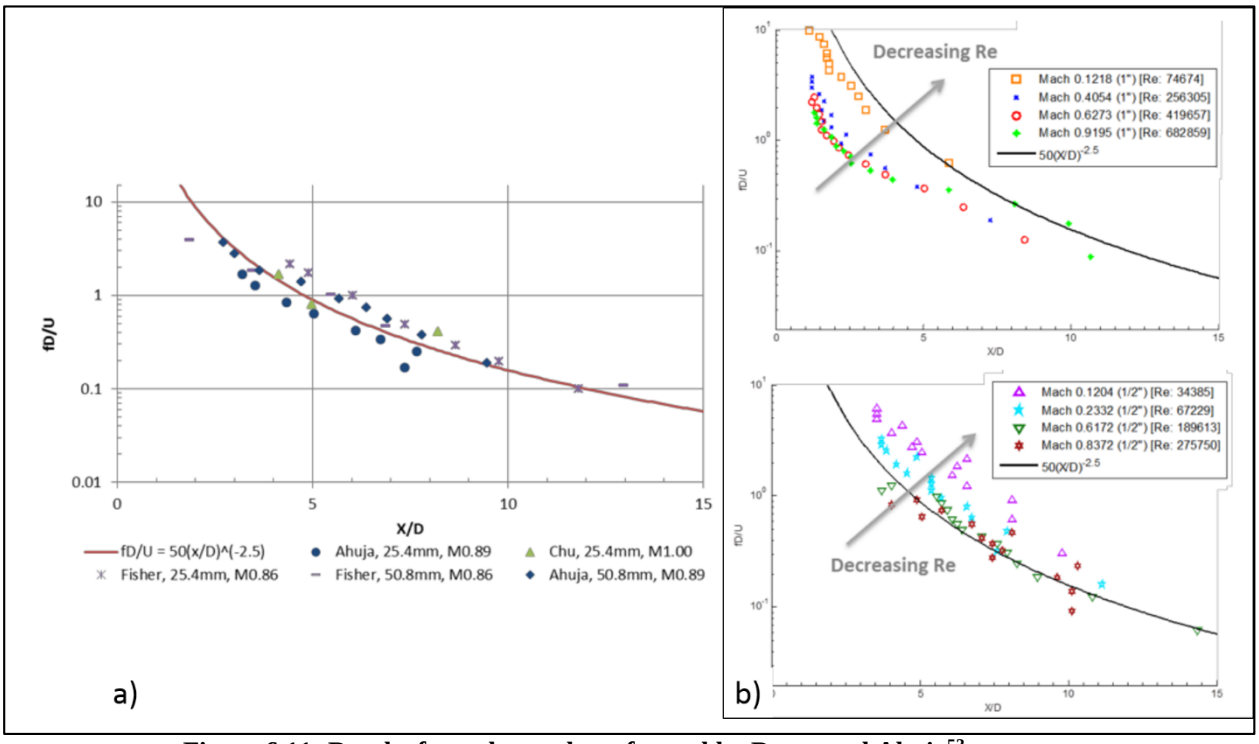

Figure 6.11: Results from the work performed by Breen and Ahuja[53].

These results clearly indicate that irrespective of whether the jet is operated at low Reynolds number or high Reynolds number, the high frequency sources are located close to the nozzle-exit. It is thus quite likely that the high frequency sources will most likely be in a non-line-of-sight at microphones in the forward arc and will undergo shielding depending upon the size of the shielding obstruction or the plenum chamber as appropriate. Low frequency sources, which appear to be located downstream of the nozzle may not suffer shielding in the forward arc unless the plenum chamber and supporting flanges are extremely large in diameter. They may, however, be affected by the proximity of an untreated jet collector, a common feature of most jet noise facilities.

6.1.2 Prior Work on Shielding

Much work has been performed on the problem of acoustic shielding from the effects of diffraction, refraction, and scattering. In the aeroacoustics field, much of the shielding research has been focused on how the wings and fuselage of an aircraft can shield selected noise sources from the community[87-90]. Considerable research on shielding of aeroacoustics sources has been funded by NASA's Environmentally Responsible Aviation (ERA) program and large amounts of noise have been shown for both model open rotors and high bypass ratio turbofans when integrated with shielding surfaces of Hybrid Wing Bodies (HWB)[89].

Ahyte and McCulley[39] conducted a rigorous review of these early contributions. Some of the early developments of shielding of a noise included Primakoff, Klein, Keller and Carstensen[91] who looked at the shielding effects of a point source from a circular disk where the point source was on the axis of symmetry and the measurement points were near this axis as well. Leitner[92] investigated a similar situation where instead of a spherical wave from a point source, plane waves were incident on the circular disk. Davis and Gabrielson[93] examined the shielding effects of a point source by rectangular plate. The three cases above all make use of the Kirchoff assumptions that require that pressure goes to zero in the shadow side of the shield. All cases also require numerical integration, which is computationally quite demanding. Ahtye and McCulley[39], following the example of Bowman, Senior and Uslenghi[94], developed a computational scheme that uses approximations for the shielding. Ahtye and McCulley[39] used the results for the shielding of half-plane and extended it to the quadrilateral shield. This scheme was used to perform some initial approximations for the shielding effects from a wing or fuselage. This scheme

is reduced to the shielding of a point source of either a tone or broadband noise from the rectangular or a cylindrical shield. Turkdogru[95] used this same code to calculate the shielding effects of flat solid walls on rotors.

Nark, Burley, Tinetti, and Rawls[96] developed a code, which they named the Fast Scattering Code (FSC) that is meant to replace the noise scattering function in the Aircraft NOise Prediction Program (ANOPP). Without getting into fine details, in the original ANOPP program, one can either adjust the directivity of the source or adjust the noise propagated to the observer. The FSC uses a source, which is the superposition of time-harmonic monopoles, dipoles, and quadrupoles, and shields it using an arbitrary shield.

Papamoschou[97] designed his own code for predicting the shielding effects of a wing or a hard surface on jet noise. This code, similar to the FSC, is supposed to be an improvement to the predictions calculated from ANOPP. Papamoschou[97] used a wave packet model that was combined with a monopole, and a Boundary Element Method was used to compute the shielding from a rectangular plate. He found agreement with available experimental data, but concedes that the method is limited as it requires modeling a random process with deterministic signals.

From the above, it is clear that whereas shielding can be useful in as the name implies shielding an observer from the noise source, this effect can be detrimental when one is trying to measure jet noise that unfortunately is being shielded by parts of the facilities from which it is issuing. The shielding effects by the plenum in the forward arc are a topic for which there is not any prior research. Studying this very effect, along with potential effect of reflections as outlined above, forms the backbone of the current experimental study that is described below. This study is divided into three parts:

1) An experimental investigation of the reflection and shielding effects of a plenum chamber
2) Computational investigation of the shielding effects of a plenum chamber
3) Shielding effects on a primary nozzle by a secondary nozzle

In this chapter, the experiments related to each of these studies will be described and the results of the study will follow immediately after that description.

6.2 Experimental Investigation of the Reflection and Shielding Effects of a Plenum Chamber

6.2.1 Experimental Set-up

The experiments were performed in the GTRI Anechoic Jet-Facility, which is described in detail in Burrin and Tanna[60] and Ahuja[10]. A special nozzle set-up was used as shown in Figure 6.12 where the nozzle-exit could be placed at a selected distance from a simulated shielding surface to emulate a plenum flange. The distance between the jet exit and the shielding surface, referred to here as a baffle, was varied by employing pipe extensions. Figure 6.13 shows a diagram of this configuration. In this case, the nozzle was attached at the end of a six-foot-long pipe extension, which positioned the nozzle roughly in the middle of the chamber. The pipe had a diameter of two inches. A small ½ inch diameter ASME nozzle was used as the jet source for this experiment. This small nozzle size was selected to facilitate simulation, via the baffle shown in Figures 6.12 and 6.13, of different sizes of plenum chamber blockages in a way that, by varying the distance between the nozzle-exit and the baffle, a range of forward microphone angles could be used within the constraints of the room geometry and dimensions. A square 9.75 inches by 9.75 inches baffle was created out of plywood to serve as a scaled replica of the frontal projection of the GTRI Anechoic Jet-Facility plenum in the sense that the area of the nozzle-exit and the area of

the baffle were in proportion of a nominal two-inch diameter nozzle normally used in the GTRI facility and the largest existing frontal surface area of the plenum chamber behind the nozzle. Acoustic measurements were made with microphones at polar angles (θ) of 30°, 60°, 90°, and 150° with respect to the downstream jet axis, using Bruel and Kjaer 4939, ¼ inch free-field microphones, which are attached to 2669 B&K preamplifiers. The 4939 microphones have a frequency range of 4 – 100,000 Hz. The ¼-inch microphone-preamplifier combinations were connected to B&K 2960-A-0S4 Nexus conditioning amplifiers that not only amplify the signal but serve as the microphones' 200 millivolt power supply.

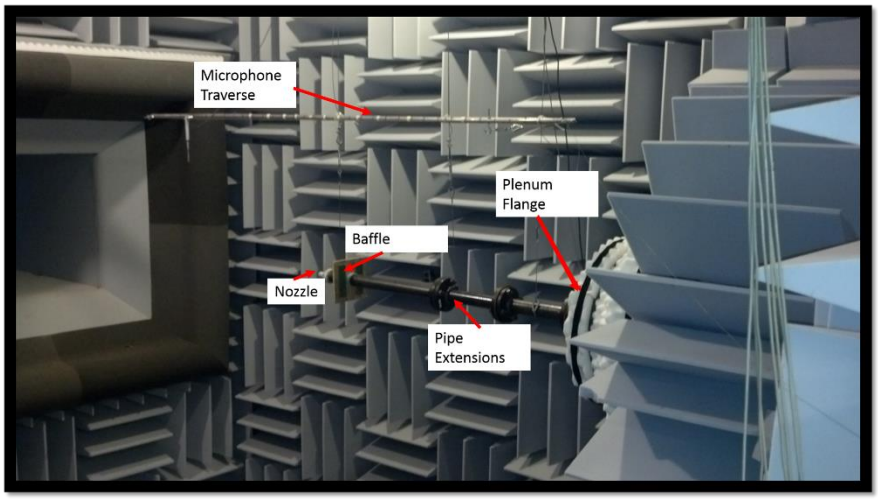

Figure 6.12: The GTRI Anechoic Jet-Facility setup for the small nozzle experiments.

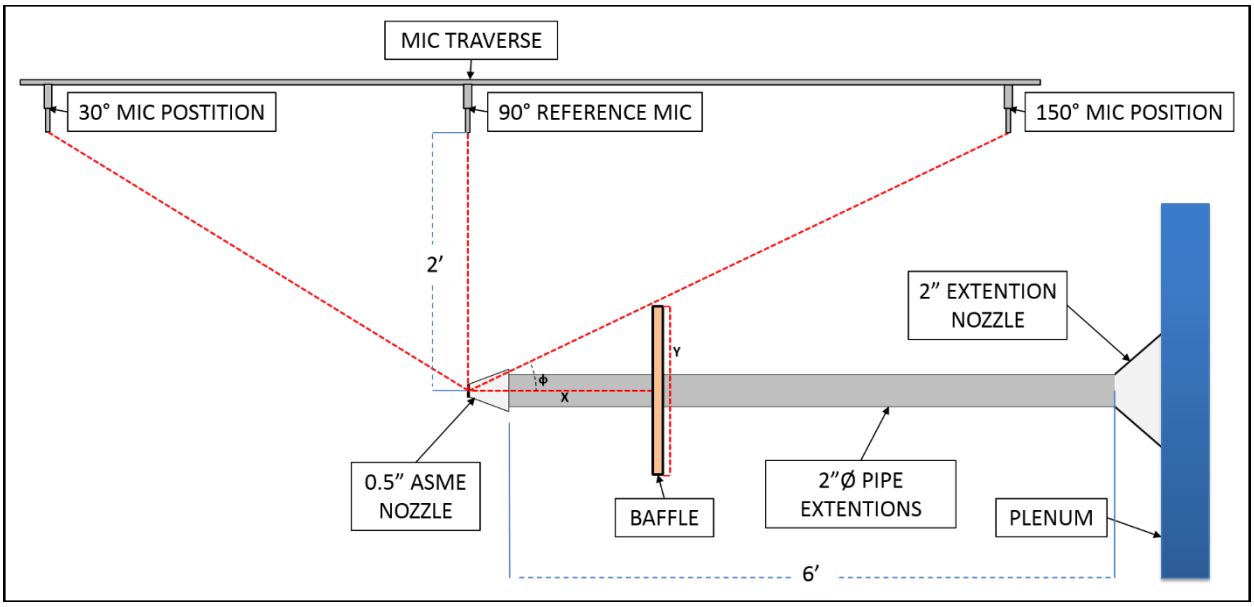

Figure 6.13: Set-up for the small nozzle tests inside the GTRI Anechoic Jet-Facility.

The θ = 30° and 150° measurements were acquired by the same microphone mounted on a linear traverse shown in Figures 6.12 and 6.13 mounted at a distance of two feet from the nozzle center line. All data was extrapolated to a distance of three feet using the inverse square law. The three-foot distance was chosen because this is a distance of 72 nozzle diameters, which is a typical distance used in jet noise measurements in the GTRI facility. Figures 6.13 and 6.14 illustrate the experimental set-up of the cases studied. The distance between the nozzle-exit and baffle was varied such that: (1) there was a clear line-of-sight between the nozzle-exit and 150° microphone as shown in Figure 6.14a (this case is referred to as "Clears"), (2) the baffle just interferes with the line-of-sight between the nozzle-exit and the 150° microphone at the edge of the baffle as shown in Figure 6.14b (this cases is referred to as "Tangent"), (3) the baffle blocks-the-line of sight between the nozzle-exit and the 150°microphone as shown in Figure 6.14c (this case is referred to as "Blocks"), and (4) a scaled replication of line-of-sight between the nozzle-exit and the 150° microphone as would be seen in the GTRI Anechoic Jet-Facility as shown in Figure 6.14d (this case is referred to as "GTRI" implying correspondence of this configuration with the

two inch diameter nozzle mounted in the GTRI facility in Figure 6.1). The distance between the nozzle-exit and the baffle and the angle that the baffle makes with the jet axis are provided in Figure 6.14. Jet noise data was acquired for all of the four configurations shown in Figure 6.14 for both subsonic and supersonic jet-operating conditions, specifically for fully expanded Mach numbers of 0.6, 0.8, 1.2, and 1.4. Supersonic jet noise was used in addition to the subsonic jet noise as broadband shock noise is known to be dominant in the upstream direction. Additionally, the primary screech tone is typically dominant in the upstream direction and the first harmonic is dominant at a polar angle of 90° (see Norum[98]). The lossless jet noise spectrum of each situation normalized to a distance of three feet is compared to investigate the effect of this baffle on the microphones at different angles, with emphasis provided to the microphone located in the extreme forward angle of 150°.

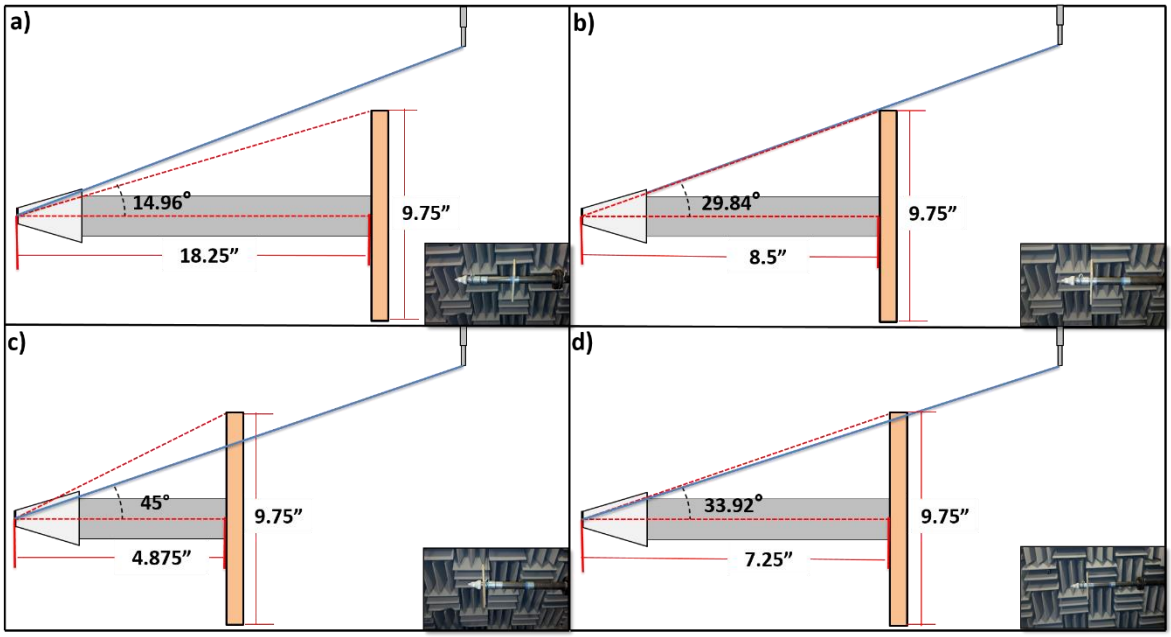

Figure 6.14: The four cases studied using the small nozzle set-up: a) “Clears”, b) “Tangent”, c) “Blocks” and d) “GTRI”.

The pressure signals from the microphones were processed into averaged frequency spectra. For these experiments, the sampling frequency used with the analyzer was 204.8 kHz; thus 204,800 samples of the acoustic pressure signal were acquired every second. These time signals were processed to provide averaged power spectra using a window size of 6400 samples, 50% overlap, and a Hanning window. This created a Δf of 32 Hz. and a smooth spectral curve. These spectra were then corrected for a variety of conditions, as detailed in Ahuja [10]. The effects of microphone geometry, the microphone protective grid, microphone actuator response, and incidence of the microphone with respect to the source are accounted for as part of the microphone free-field frequency response. This correction, is a function of both frequency and the angle of incidence of the sound wave on the microphone, is lumped together and will be denoted by the variable $A\ (f, \Psi)$. The effect of atmospheric attenuation was accounted for by using the method presented in ANSI S1.26-1995[61]. This atmospheric-attenuation correction methodology contains many equations and is too long to present here, but presented in Appendix B. This method results in a frequency-dependent attenuation coefficient $\alpha(f)$, which has the units of dB/m. Removing the attenuation effects and applying all of the microphone related corrections described above provides the so-called "lossless spectra," which will be used throughout the analysis. The advantage of this form of the data is that it allows the data from different facilities, different microphones and acquired on different days to be compared with one another. This also allows the theoretical predictions, which are independent of microphone responses, to be compared with the measured lossless data. Finally, the jet noise measurements are extrapolated to a common distance to help with needed comparisons. This distance was selected to be 72 nozzle diameters and is performed using the inverse

square law, which is part of Equation 3.1. Combining these effects, the free-field and lossless jet noise spectrum is calculated using the equation:

$$SPL(f)_{free-field,lossless} = SPL_{uncorrected} - A(f,\Psi) + B(f) + \alpha(f)R_1 + 20\log_{10}\left(\frac{R_1}{R_2}\right) \quad (6.2)$$

where R_1 is the distance between the nozzle-exit and the microphone at the time of measurement and R_2 is the extrapolated distance between the microphone and nozzle-exit used in the inverse square law. Corrections for any of the parameters shown in Equation 1 are simply done by removing that effect using Equations 3 or 5 and then adding the effect of the changed parameter back into the spectrum by using the reverse operation. An example of this correction procedure is shown in Appendix A. As an additional level of processing, the uncorrected measurements are compared to the ambient noise measurements.

6.2.2 Results

The results of the experimental study of the four baffle-nozzle configurations shown in Figure 6.14 are presented in this section. Each case is assigned a color in Figures 6.15 – 6.18: the "Clears" case is the blue line, the "Tangent" case is the green-dashed line, the "GTRI" case is the orange dashed-dotted-line, and the "Blocks" case is the red dotted-line. Figures 6.15 and 6.16 illustrate the effect of the baffle on subsonic jet noise at angles of 30°, 60°, 90° and 150° for M_j = 0.6 and M_j = 0.8, respectively. In terms of reflections, there are clearly some reflections at all of measured angles as evident by the peaks and valleys in the measured spectra. However, because these peaks and valleys do not move along the frequency axis as the baffle is moved, the baffle is not the cause of these reflections. It is believed that these reflections are caused by the untreated support structure

of the microphone traverse as seen in Figures 6.12 and 6.13. The microphone traverse and its supporting structure could not be adequately treated for reflections, because acoustic foam would have interfered with the traversing mechanism. Reflections caused by the microphone arc and similar untreated structures are not discussed in this study.

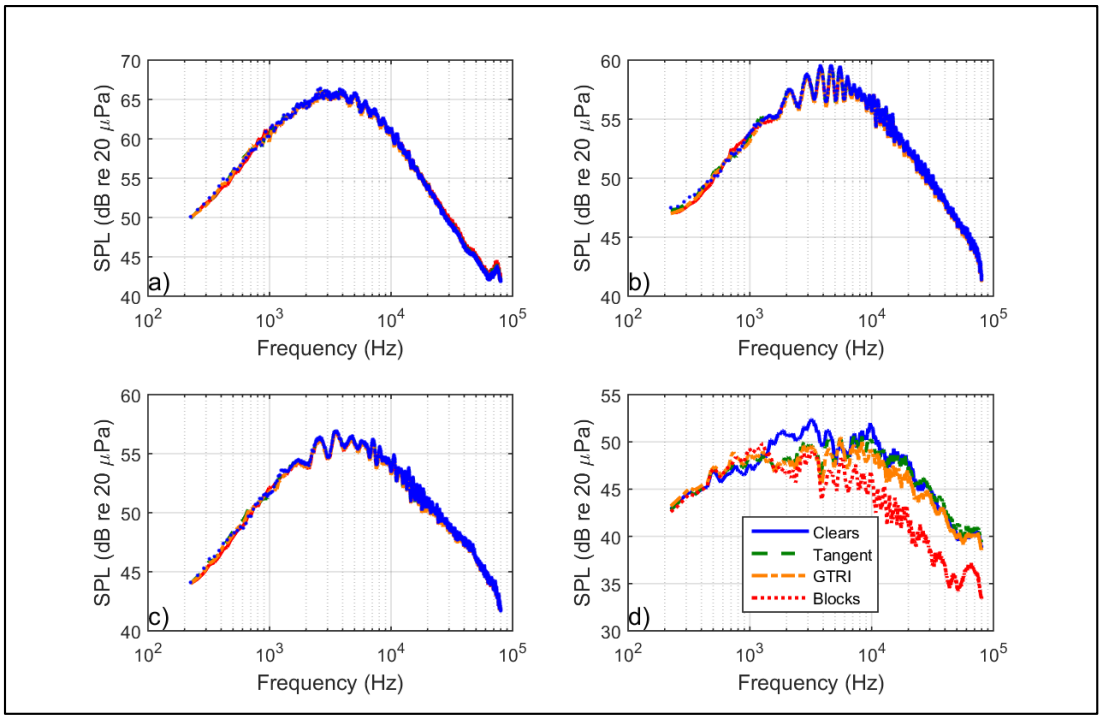

Figure 6.15: Effect of the baffle configuration on the jet noise. a) θ = 30°, b) θ = 60°, c) θ = 90°, and d) θ = 150°. Δf = 32 Hz, M_j = 0.6, R = 3 ft., D = 0.5 in., Lossless.

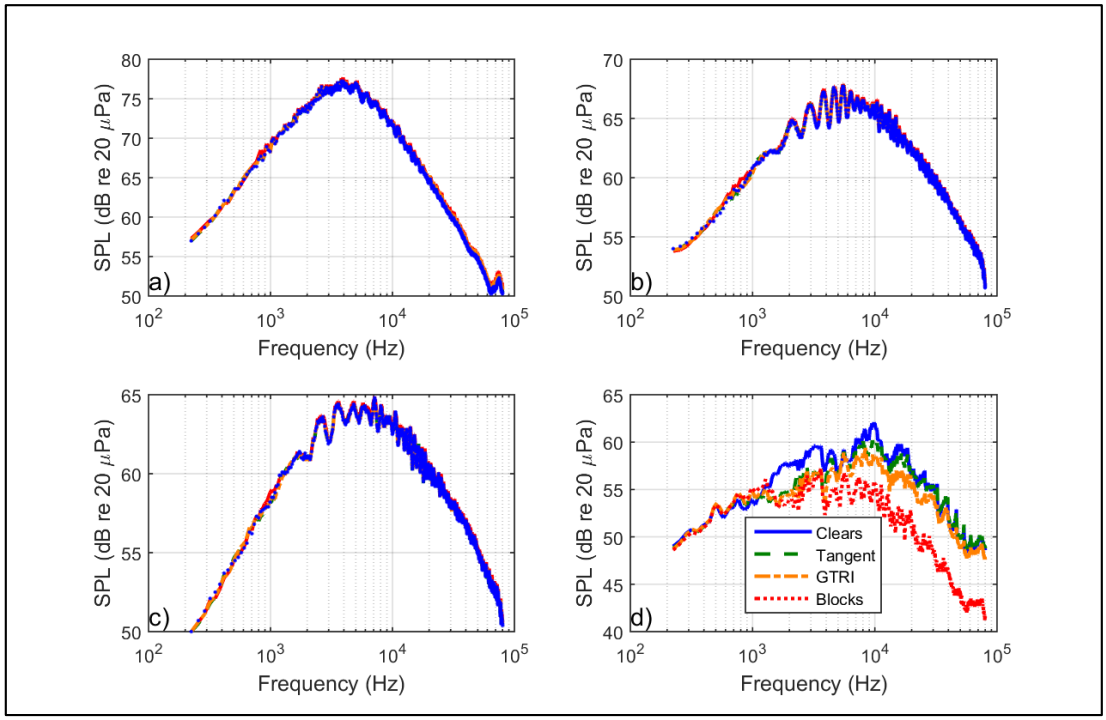

Figure 6.16: Effect of the baffle configuration on the jet noise. a) θ = 30°, b) θ = 60°, c) θ = 90°, and d) θ = 150°. Δf = 32Hz, M_j = 0.8, R = 3 ft., D = 0.5 in., Lossless.

In terms of shielding, as seen in the 150° angle in Figures 6.15 and 6.16, shielding effects begin to show up even when the line-of-sight between the nozzle and microphone is tangent to the baffle edge, presumably due to the edge diffraction effects discussed earlier. When the baffle's edge is tangent to the line-of-sight between the nozzle and the microphone, which is earliest opportunity for shielding effects to be apparent, lower frequencies in the range of 1000 Hz to 4000 Hz show the greatest reductions due to the baffle. These reductions due to the shielding effect are of the order of 2-3 dB. As the non-line-of-sight between the microphone and the nozzle-exit becomes more substantial, additional reductions in the SPL occur at all frequencies above 1000 Hz and are of the order of 5-6 dB at all frequencies to the right of the spectral peak.

Figures 16.7 and 6.18 show the effect of baffle position on shock-containing supersonic jet noise for underexpanded jets operated at M_j = 1.2 and 1.4, respectively. As done for

the last two figures, spectral comparisons are provided for both the rear arc and the forward arc at polar angles of 30°, 60°, 90°, and 150°. There seems to be some reflection effects caused by the baffle, but exclusively of the screech and part of the high frequency noise, as evidenced by an increase in noise by "blocks" configuration. These effects are particularly clear at θ = 30°. Since screech noise is dominant in the forward arc and the high frequency noise is produced close to the nozzle-exit and hence close to the reflecting surface of the hard baffle it makes sense that as this noise on propagating in the direction of the forward arc would reflect off the baffle and travel in the downstream direction. This will also apply to the broadband shock associated noise which predominantly propagates in the forward direction and upon reflection at the baffle may show up at the downstream direction. Spectra at θ = 30°, in Figure 6.17 shows clear evidence of increased shock associated noise for "Block" case. This is further confirmed by the ray tracing performed below. For instance, at 30° the screech tone amplitude is increased by as much as 10 dB due to reflections from the baffle and possibly from other pipe surfaces. This indicates that reflection from a hard surface located upstream of the nozzle could potentially provide a larger screech tone in the rear arc. At the same time, since the shock noise is dominant in the forward arc, when the baffle does interfere with the line-of-sight between the nozzle and the 150° microphone, this noise would experience the greatest shielding effects. From the spectra of the noise at the 150° microphone as seen in Figures 6.17 and 6.18, the portion of the spectra that is dominated by pure jet mixing noise (to the left of the screech frequency), the shielding follows the same trend as seen above for the subsonic case. Alternatively, in the shock noise portion of the spectra, the shielding effects do not occur until the baffle significantly blocks the line-of-sight between the microphone and nozzle.

But the reductions seen in the shock containing noise cases also is similar to that observed for the subsonic case, which is of the order of 5-6 dB. It was found that the screech amplitudes were also reduced by as much as 10 dB for the full-non-line-of-sight case.

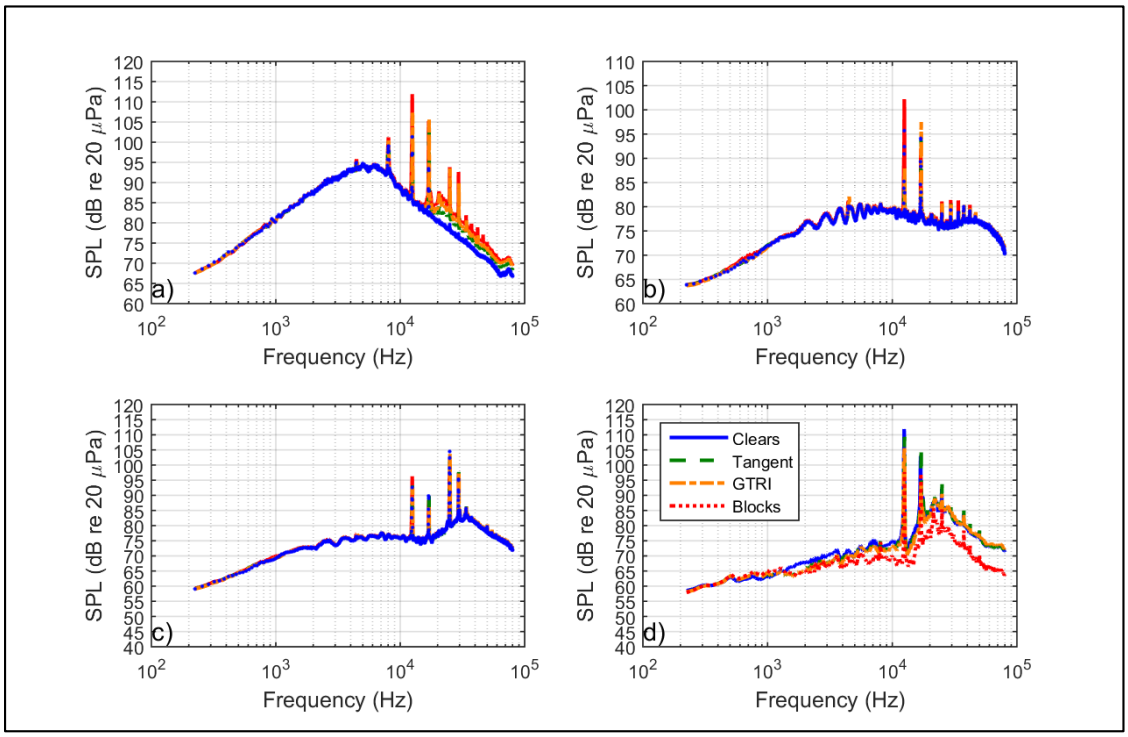

Figure 6.17: Effect of the baffle configuration on the jet noise. a) θ = 30°, b) θ = 60°, c) θ = 90°, and d) θ = 150°. Δf = 32Hz, M_j = 1.2, R = 3 ft., D = 0.5 in., Lossless.

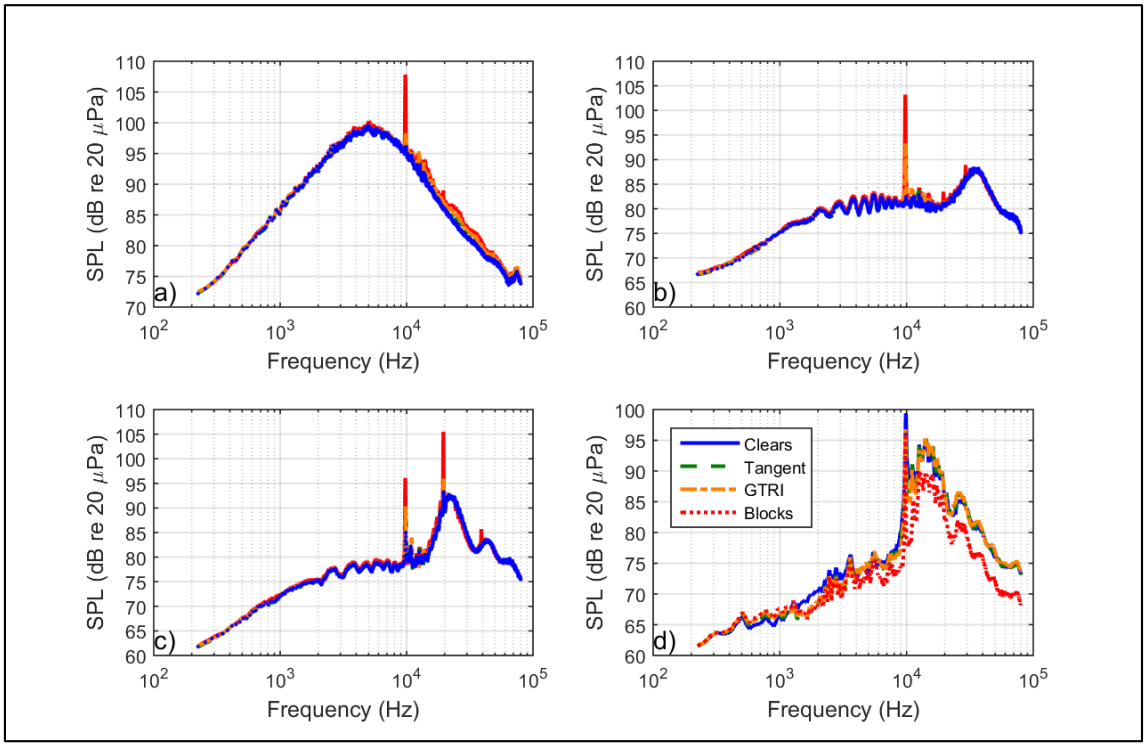

Figure 6.18: Effect of the baffle configuration on the jet noise. a) θ = 30°, b) θ = 60°, c) θ = 90°, and d) θ = 150°. Δf = 32Hz, M_j = 1.4, R = 3 ft., D = 0.5 in., Lossless.

As a sanity check for the experimental data, ray tracing was performed to locate the angles that are theoretically affected by the reflection and shielding effects of the baffle. This exercise is summarized in Figure 6.19 and Table 6.1. Figure 6.19 shows the geometry use for the ray tracing. Referring to Figure 6.19, the angle σ is the angle that the nozzle-exit makes with the top edge of the baffle, L_{NB} is the distance between the nozzle-exit and the baffle, L_{DS} is the distance downstream of the nozzle-exit where the ray reflected from the top edge of the baffle intersects with the microphone traverse line. The initial polar angle where shielding occurs is calculated using the equation:

$$\theta_s = 180° - \sigma \tag{6.3}$$

The largest polar angle where reflection effects will occur is calculated using the equation:

$$\theta_r = \tan^{-1}\left(\frac{24}{L_{DS}}\right) \tag{6.4}$$

Table 6.1 summarized the results of the ray tracing. Based on these results, it is confirmed that all the microphones in the "Clears" case are unaffected by reflections or shielding. The shielding effects seen in the rest of cases makes sense as the 150° microphone is in the shielding zone for each of these cases. As for the reflections, since broadband shock noise prominently propagates in the upstream direction, it makes sense that if reflected by the baffle, it will mostly be seen at the shallower angles in the rear arc. And indeed it is seen to be dominant at the 30° microphone as seen in Figures 6.17 and 6.18. Effect of reflection of the screech tones in the rear arc is also evident at the shallower angles for the "blocks" case.

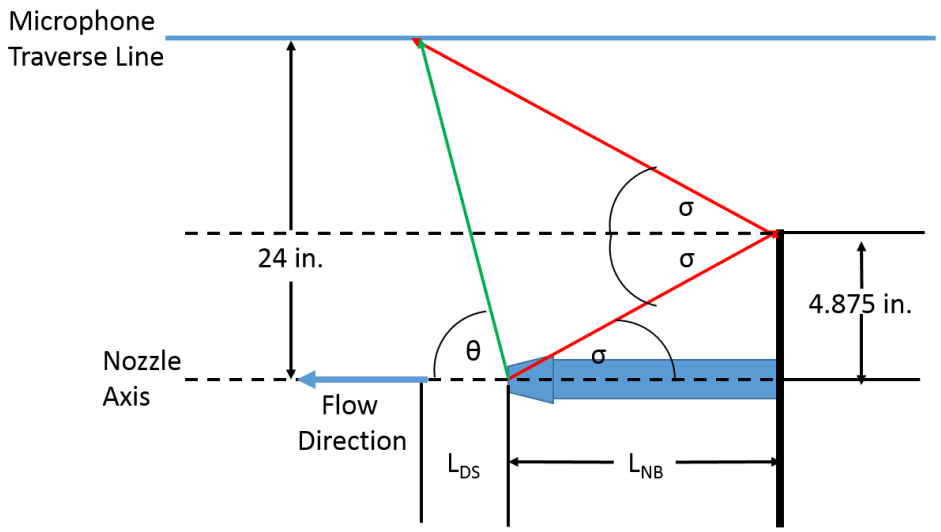

Figure 6.19: Ray tracing to show the polar where shielding and reflection effects are likely to occur.

The present findings indicate that microphone placed in the forward arc in the non-line-of-sight region are likely to provide considerably inaccurate jet noise measurements and

Table 6.1: Listing of the polar angles where shielding and reflection effects are likely to occur for each of the four cases studied

Case	σ	L_{NB} (in.)	L_{DS} (in.)	θ_r	θ_s
"Clears"	14.96°	18.25	53.33	24.2°	165.04°
"Tangent"	29.84°	8.5	24.84	44.0°	150.16°
"Blocks"	45°	4.875	14.25	59.3°	135°
"GTRI"	33.92°	7.25	21.19	48.6°	146.08°

those in the rear arc are likely to be affected by reflections, and more so by noise that would normally be propagating upstream towards an untreated surface such as screech.

6.3 Computational Investigation of the Shielding Effects of a Plenum Chamber

6.3.1 Computational Program Set-up

The computational program developed by Ahtye and McCulley[39] is used for this study. This choice is motivated by the simplicity and availability of the code. For additional details of the computational code and the MATLAB code that was used for this study can be seen in Appendix C, but the reader is referred to Ahtye and McCulley[39] for the finer details. Figure 6.20 shows a diagram of the set-up for the computational code. The source frequency and location along the jet axis is determined by the curve fit shown in Figure 6.11a, which was reproduced from Breen and Ahuja[53]. As mentioned above, since Breen and Ahuja[53] found that there is a Reynolds Number dependence on this curve, only jets with a Mach number 0.8 will be considered, as the experimental data, on which the curve fit is based, was valid in this range. In addition, based on the work from Breen and Ahuja[53] as shown in Figure 6.11b, using the 0.5 in. nozzle at a Mach number of 0.8, the source distribution seems to lie directly on this curve fit. The distance of the source of a given frequency from the nozzle-exit as derived from this curve fit when added to the distance between the nozzle-exit and baffle provides L_{NB} shown in Figure 6.20 and is needed in the

computer code. The microphone is positioned at a distance, *R*, of 3.5 feet from the nozzle-exit, in order to be consistent with the experiments of the configuration shown in Figure 6.14. The distance between the baffle on the microphone plane, L_{BM}, is given by the equation:

$$L_{BM} = R\cos(180 - \theta) - L_{NB} \tag{6.5}$$

The angle, ϕ, which is an angle defined in the computational code, is related to the distances and polar angles shown in Figure 6.20 by the equation:

$$\phi = \tan^{-1}\left(\frac{\sin(180-\theta)}{L_{BM}}\right) \tag{6.6}$$

The code developed by Ahyte and McCulley[39], was used to predict the shielding effects of each of the configuration shown in Figure 6.14. The effects of baffle on jet noise are shown in Figure 6.14 for a polar angle of 150°. The shielding spectra predicted from these simulations will be compared with the experimental results both for the narrowband data and the 1/3-octave band data.

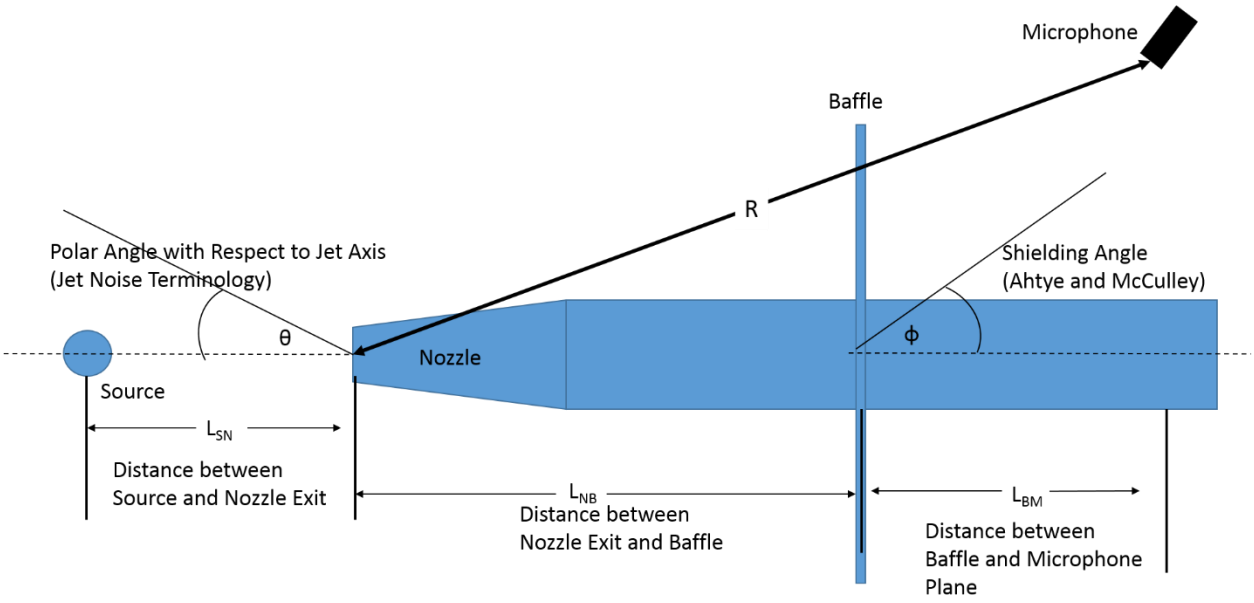

Figure 6.20: The configuration used for the computational code.

6.3.2 Results

Figures 6.21 – 6.23 compare the measured shielding with that predicted by simulations for the "Tangent", "GTRI", and the "Blocked" cases, respectively, as defined above. Narrowband data (Δf of 1 Hz) is shown on the left and the 1/3-octave band data is shown on the right of each figure. The experimental data and computational data do not agree completely, but the trends are similar. This is indicated by the initial dip and then rise of the shielding effects with increasing frequency. As the computational code is based on the shielding of tones and not broadband noise; the computed dips are deeper than the experimental data. It is also noticed that the computational spectra are somewhat shifted with respect to frequencies compared to the experimental data. Examining Figure 6.21, which is the results for the "Tangent" case configuration in Figure 6.14 above, the simulation actually shows amplification due to the baffle, where experimental data shows very minimal effects due to the baffle. Both the experiments and simulation show a hump at low frequencies, which is followed by a large drop leading to 4 to 5 dB of shielding. Both the simulation and experiments show amplification and shielding as the frequency increases, but any of the effects from the baffle become minimal at high frequencies.

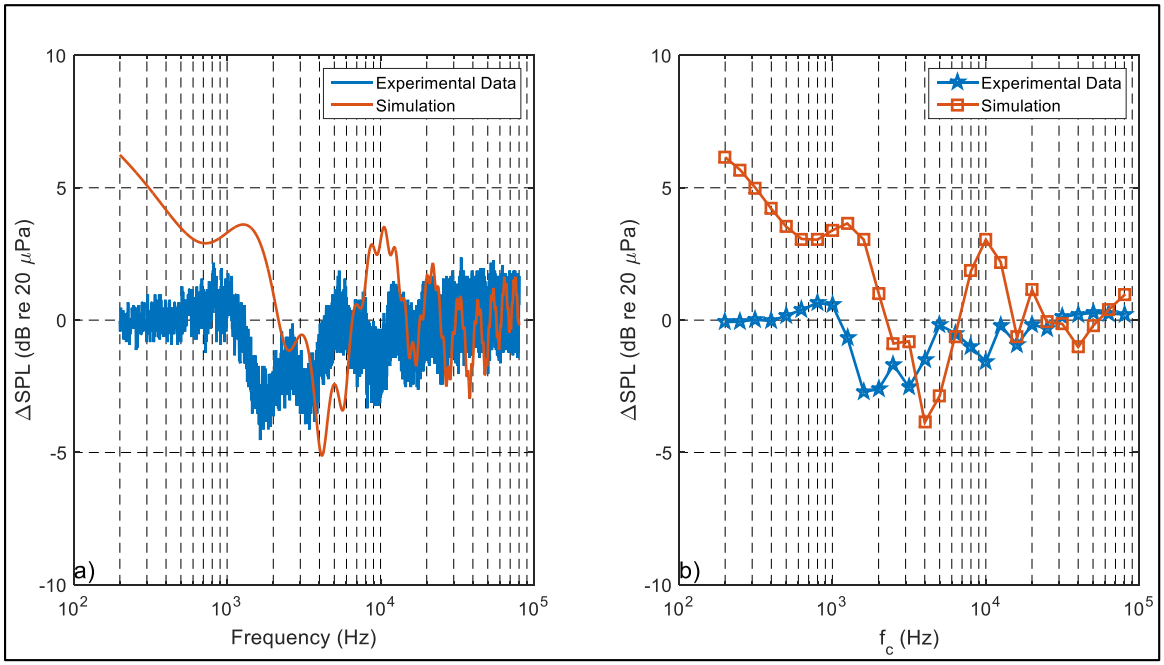

Figure 6.21: Experimental vs Computation Shielding Effects for the "Tangent" Shielding Case. a) Narrowband with a Δf = 1 Hz, b) 1/3-octave bands. Experimental Data: Δf for Narrowband Spectra = 1 Hz, D = 0.5 in., M_j = 0.8, R = 3 ft., θ = 150°, Lossless.

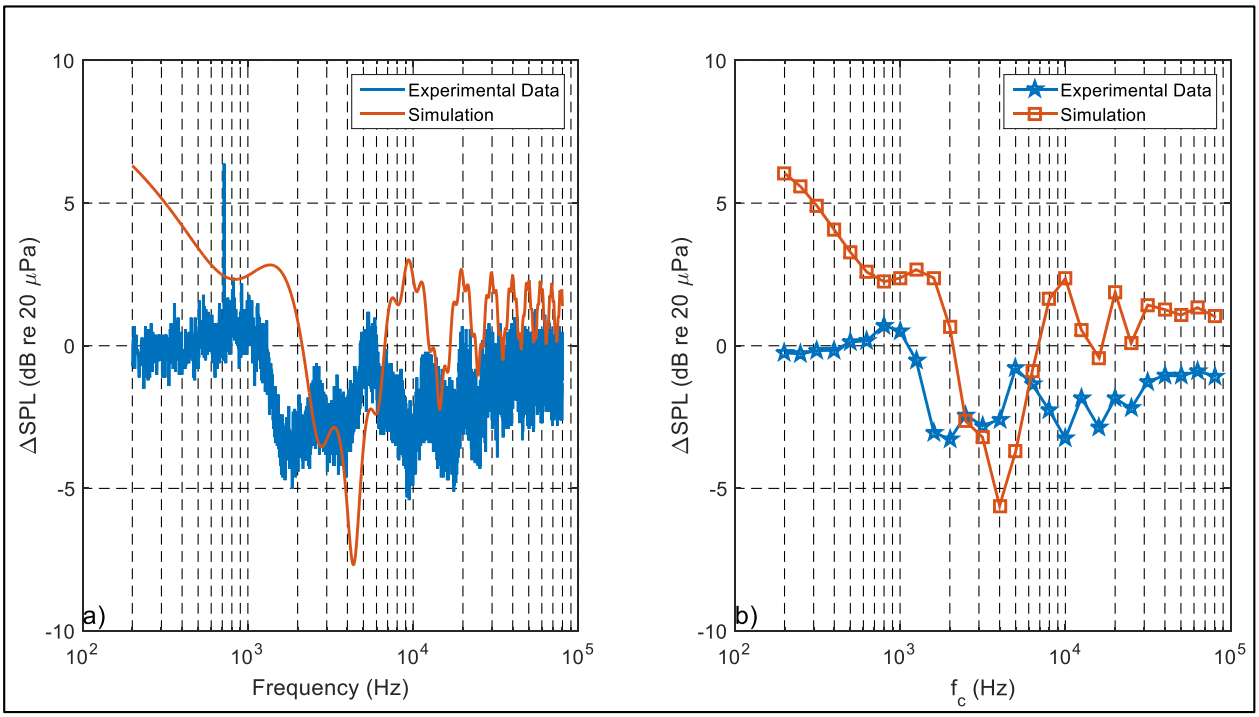

Figure 6.22: Experimental vs Computation Shielding Effects for the "GTRI" Shielding Case. a) Narrowband with a Δf = 1 Hz, b) 1/3-octave bands. (D = 0.5 in., M_j = 0.8, R = 3 ft., θ = 150°, Lossless).

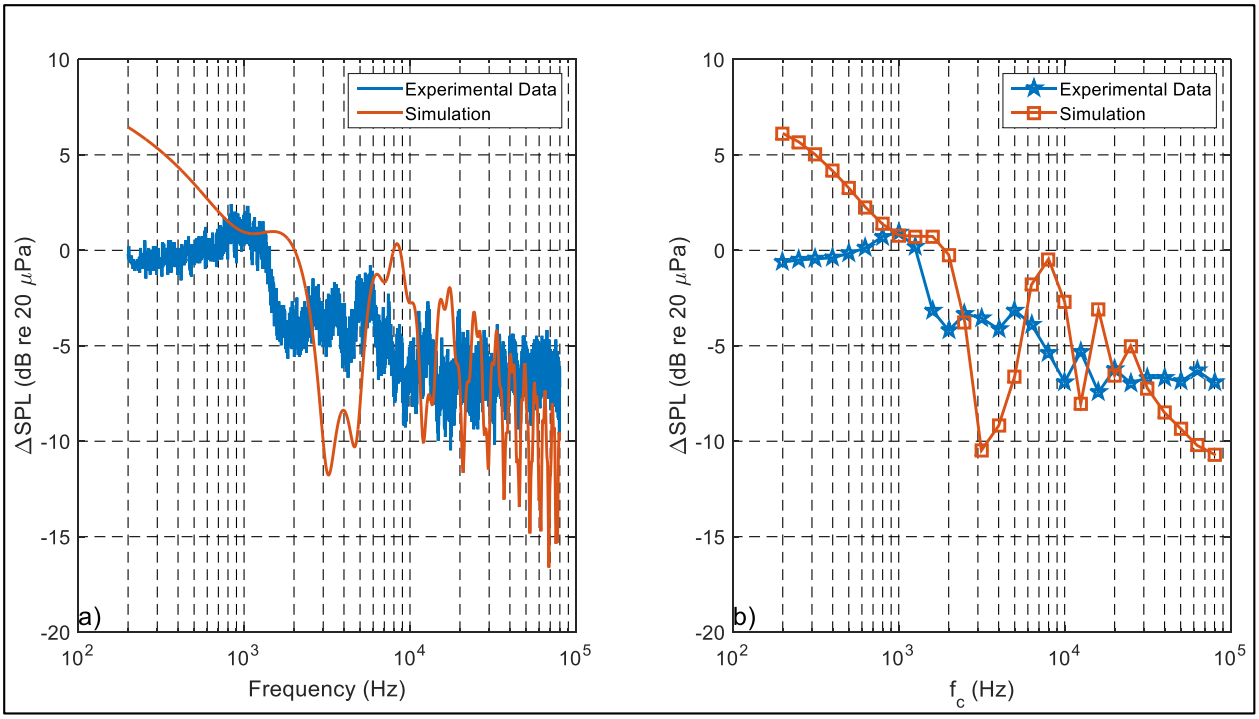

Figure 6.23: Experimental vs Computation Shielding Effects for the "Blocked" Shielding Case. a) Narrowband with a Δf = 1 Hz, b) 1/3-octave bands (D = 0.5 in., M_j = 0.8, R = 3 ft., θ = 150°, Lossless).

Figure 6.22 shows the results of the experiments and simulation for the "GTRI" case shown in Figure 6.14. Like in the "Tangent" case, the simulation over predicts shielding at the mid frequencies and shows amplification at frequencies where shielding should occur. Although, while the amplitudes are can be very different, the up-and-down trends that are seen in Figure 6.22 are seen in both the experiments and simulation. This leads to similar trends, while the exact amplitude and frequencies of these trends are different, the overall trends are the similar.

Figure 6.23 shows the results of the experiments and simulation for the "Blocked" case shown in Figure 6.23. The simulation follows the trends of the experiments a lot closer. Like the previous cases, the frequencies appear shifted along the trend. At the high frequencies, the simulation over predicts the shielding effects, but actually shows noise

reduction at these frequencies unlike in the "Tangent" and "GTRI" case shown in Figures 6.21 and 6.22 respectively.

6.4 Shielding of the Primary Jet Noise by a Secondary Nozzle for a Round Coannular Nozzle Arrangement

6.4.1 Experimental Set-up

In addition to the small nozzle tests mounted on a pipe extension as described above, jet noise data for a coannular nozzle (both nozzles of equivalent diameter = 2 in.) mounted directly on the plenum chamber was acquired with the specific purpose of understanding shielding of noise of the inner jet by the secondary nozzle in a coannular nozzle configuration.

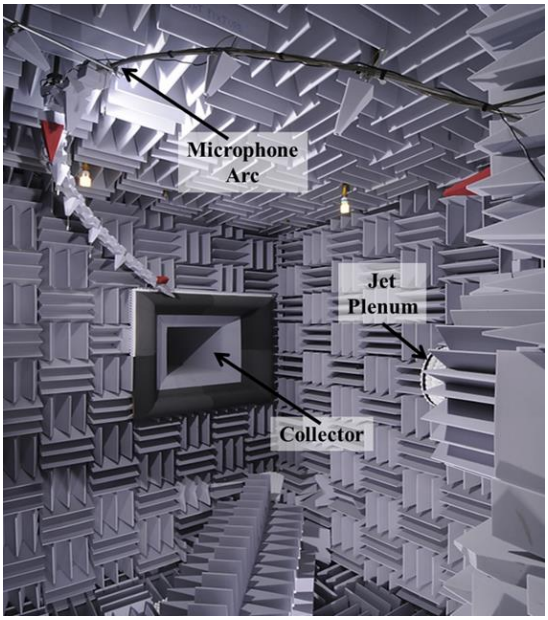

Figure 6.24: Far-field microphone arc in the GTRI Anechoic Jet-Facility.

The configuration of the microphones mounted on a microphone arc is shown in Figure 6.24. The microphone types and data processing scheme is identical to scheme presented above. The microphones in this far-field array were placed at least 10 feet (60 primary nozzle diameters) from the center of the primary nozzle, to ensure that the microphones were located in the geometric far-field. The frequency spectra from these microphones

were extrapolated to a distance of 12 feet (72 primary nozzle diameters) using the inverse square law. In this case, selected measurements from a linear near-field array shown in Figure 6.25 were also acquired. The microphones in this nearfield array are located 28 inches (14 primary nozzle diameters) from the primary jet axis. The spectra from these microphones were not extrapolated to any distances as the inverse square law does not work for nearfield acoustic data for all frequencies. Two configurations were used. In the first configuration, the primary nozzle protruded out from the secondary nozzle (Figure 6.26a). In the second configuration, the primary nozzle and secondary nozzle exits were coplanar (Figure 6.26b). These configurations are shown in Figure 6.26. An ASME converging nozzle was used for the configuration in Figure 6.26a and a converging-diverging nozzle (C-D nozzle) with a design Mach number of 1.4 was used in the configuration shown in Figure 6.26b. These nozzles were chosen for convenience as these were available at the time of experimentation.

Figure 6.25: The near-field array in the GTRI Anechoic Jet-Facility.

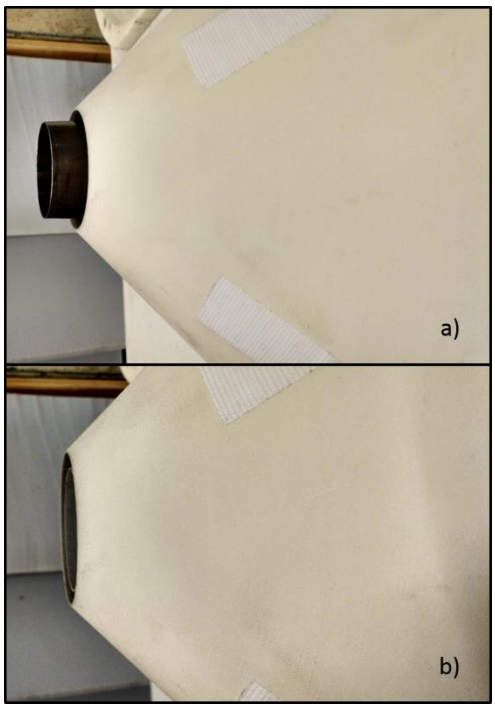

Figure 6.26: Test configurations for the secondary nozzle shielding study: a) primary nozzle extends out of the secondary nozzle; b) primary nozzle is coplanar with the secondary nozzle.

6.4.2 Results

The shielding of the jet noise from the primary nozzle by the physical presence of secondary nozzle were found to be insignificant and are shown in Figures 6.27 – 6.29. Figure 6.27 shows the comparison of jet noise with and without the presence of the secondary nozzle shown in Figure 6.26a, for a two-inch converging primary nozzle operated at $M_j = 0.8$. The data is shown for a polar angle of 120°. Figures 6.28 and 6.29 show jet noise using a C-D nozzle with a design Mach number of 1.4 at a perfectly expanded Mach number of 0.8 at polar angles of 120° and 110°, respectively, when the secondary nozzle in Figure 6.26b is and is not present. As seen in Figure 6.27, with the primary nozzle-exit sticking out past the secondary nozzle-exit, no shielding occurs at microphones in the forward arc. On the other hand, when the primary and secondary nozzle-exits are coplanar some shielding can theoretically occur. Figures 6.28 and 6.29 shows the effect of the secondary nozzle on the sound measured at polar angles of 120°

and 110° respectively. It is necessary to show both, because when the measurements were taken for the first configuration shown in Figure 6.27, the plenum chamber did not have foam on it and as such, it did not block the line-of-sight from the nozzles to the 120° microphone. As shown on Figures 6.27 – 6.29 any shielding effects from the secondary nozzle on the jet noise in the forward arc is insignificant. There are some frequencies that shown increases or reduction in jet by less than one dB. These small increases or reductions in jet noise could be the result of edge diffraction of sources located close to the nozzle-exit caused by the secondary nozzle similar to what was observed in in the first study above. This seems to indicate, at least for model-scale jets, secondary nozzles do not produce significant shielding effects on jet measured in the forward arc up to a polar angle of 120°, the upper limit of the data acquired here.

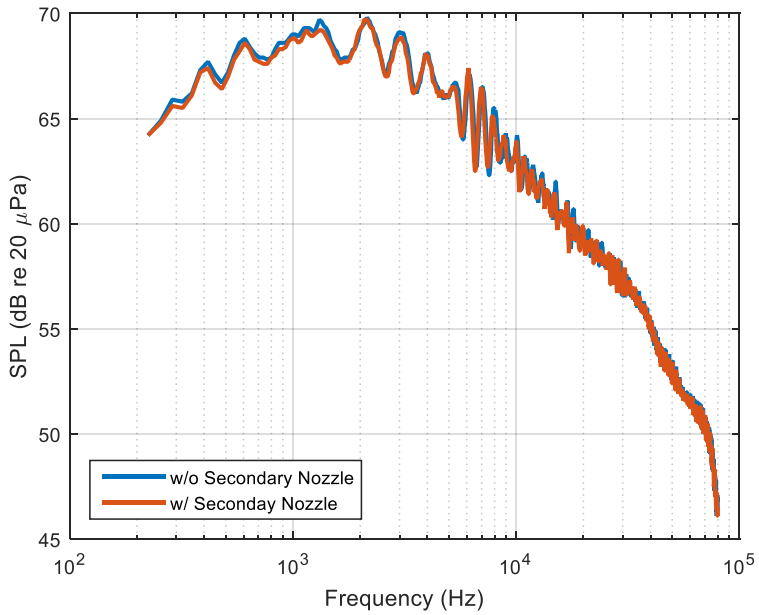

Figure 6.27: Shielding Effects using the configuration in Fig. 4.26a. Δf = 32 Hz, M_j = 0.8, D = 2 in., R = 12 ft., θ = 120°, lossless, ASME converging nozzle.

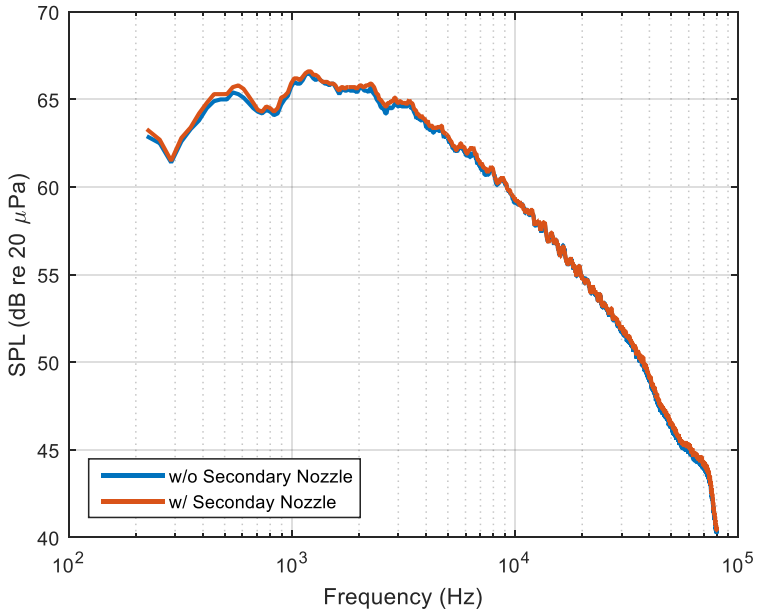

Figure 6.28: Shielding Effects on using the configuration in Fig. 4.26b. Δf = 32 Hz, M_j = 0.8, D = 2 in., R = 12 ft., θ = 120°, lossless, C-D nozzle with M_D = 1.4.

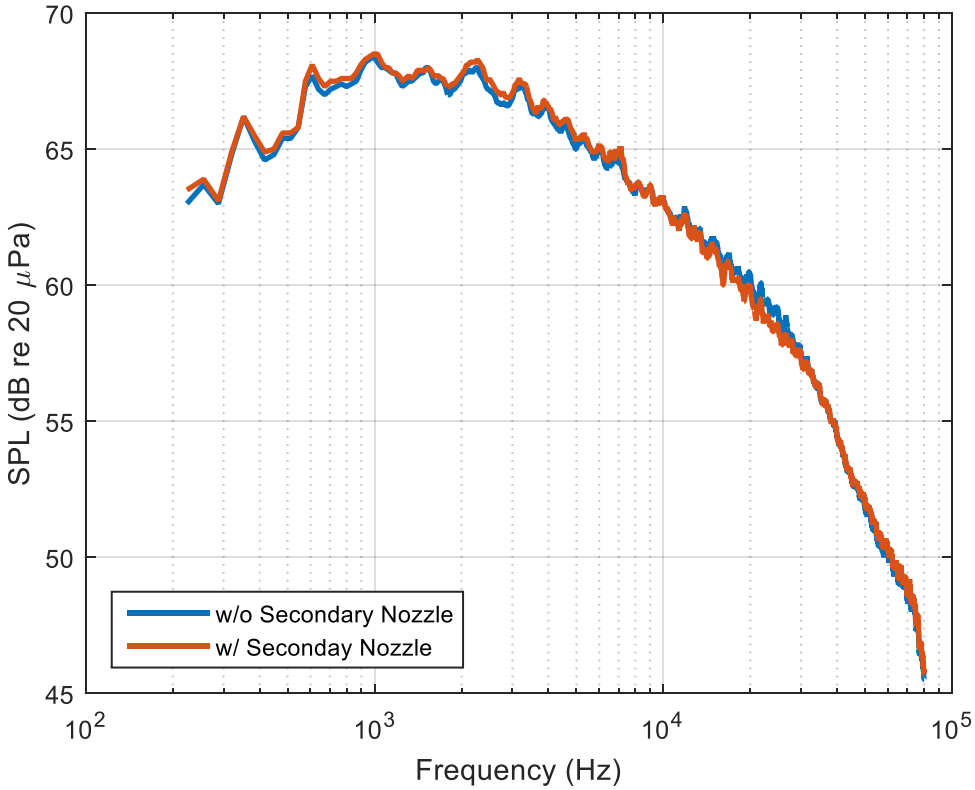

Figure 6.29: Shielding effects for the configuration in Fig. 4.26b. Δf = 32 Hz, M_j = 0.8, D = 2 in., R = 12 ft., θ = 120°, lossless, C-D nozzle with M_D = 1.4.

6.5 Conclusions

The study presented in this paper shows that even the best anechoic jet-facilities have the potential to produce measurements that are affected by reflections and shielding. In terms of shielding, it is shown that a jet-facility's plenum chamber has the potential to act as a shield for microphone in the forward arc and can produce as much as 5 dB reductions in broadband noise and as much as 10 dB in screech of supersonic shock containing jets. In addition, jet-facilities plenum chamber can produce reflections of the shock noise producing contamination in the rear arc. In our tests, up to 10 dB increase in screech tone SPLs was obtained in the rear arc.

The shielding computational code created by Ahyte and McCulley[39] produced similar shielding trends as the experimental measurements but not the same values. It is believed that the differences are attributable to not knowing precisely where the sources of different frequencies are located. Additionally, jet noise is a broadband phenomenon while the computational code is based on the tonal shielding. Even using the best approximations, tonal noise will behave differently than broadband noise given its coherent nature. This being said, the computational code can produce the general trends reasonably well, if the sources of jet noise of different frequencies are known precisely.

A secondary coannular nozzle was shown to not affect the measurements of the noise produced by a primary jet in any significant fashion. This is fortunate that microphones in the forward are not easily influenced by the addition of this secondary nozzle.

This study only investigated the reflection and shielding effects of the plenum chamber and surfaces close to it. As explained above, reflections close to the microphones can cause contamination of the measurements acquired in an anechoic jet-facility. This effect needs to be studied in a methodical fashion, and from this study, recommendations for reducing

the effects of the reflections from the microphone mounts can be made. In addition, a more sophisticated computational code could be used to simulate the effects of the baffle, which was the topic of the first two studies of this article.

CHAPTER 7

UNCERTAINTY ANALYSIS

In this chapter, uncertainty of the measurements presented in the previous chapters is analyzed to give confidence in the results. Various factors and measurements will be handled separately. First, the general methodology for the analysis will be discussed. Next, the uncertainty with respect to measuring the jet conditions will be analyzed. Next, the uncertainty in positioning the microphones at a given distance and angle will be discussed. Following this, the uncertainty of the acoustic measurements will be analyzed. Next, the uncertainty related to the three microphone method, which was used in Chapter 3 will be discussed. Then, uncertainty related to the hotwire anemometer measurements will be discussed. Finally, the uncertainty related to the boundary layer measurements with the boundary layer probe will be discussed.

7.1 Uncertainty Analysis Methodology

The methodology used in this analysis is taken from the AIAA standards[99, 100] and Coleman and Steele[101]. In this scheme, an equation that uses measured quantities or variables calculated from measured quantities can be expressed in the form:

$$r = r(X_1, X_2, \ldots, X_J) \tag{7.1}$$

where, r is the result of the calculation using J variables, X_i. The large sample 95% confidence uncertainty analysis equation is:

$$U_r = \sqrt{B_r^2 + R_r^2} \tag{7.2}$$

where, B_r is the systematic uncertainty and R_r is the random uncertainty associated with the with r. B_r and R_r are determine using the equations:

$$B_r^2 = \sum_{i=1}^{J} \left(\frac{\partial r}{\partial X_i} B_i \right)^2 + 2 \sum_{i=1}^{J-1} \sum_{k=i+1}^{J} \frac{\partial r}{\partial X_i} \frac{\partial r}{\partial X_k} B_i B_k \tag{7.3}$$

$$R_r^2 = \sum_{i=1}^{J} \left(\frac{\partial r}{\partial X_i} R_i \right)^2 \tag{7.4}$$

where, B_i's and R_i's are the systematic and random uncertainties of each variable used to calculate r. It is noted here, that the second term in Equation 7.3 is used when the error between the measuring devices is correlated. As stated in the AIAA standard[99, 100] this typically happens when the same measuring device is used for measuring a number of different measurements, or when the devices are calibrated against the same standard. For each calculation, the above procedure is used to calculate the overall uncertainty. Because of the large number of measurement types used in this study, each group of measurements will be handled in different sections of this chapter.

7.2 Effect of Round-off Errors

Round-off error occurs when the resolution of the A/D conversion of a measurement is not fine enough to resolve the voltage output of the measurement device accurately. In this particular study the following NI A/D cards were used: PCI-6035E, PXIe-4499, PCIe-6351, PCI-6034e, and PXie-6052e. Each of these cards is at a minimum of a 16 bit A/D card. This means even for a card that reads a 10-volt range and a 16-bit card, the card resolves 0.15 mV. Since the transducers used in this study resolve resolves on the order of 0.5 mV, these A/D cards adequately resolve the measurements.

7.3 Uncertainty of Jet Conditions

Since this study is about jet noise, the acoustics are the main focus of the study. In order to study jet noise properly, the uncertainty of setting the jet to the correct condition is required and how that will affect the jet noise produced. To this end, first the uncertainty of the jet velocity and how that will in turn will affect the uncertainty of jet noise spectrum is studied.

As shown in previous chapters, three measurements are used to determine the jet velocity: (1) stagnation pressure, (2) ambient pressure, and (3) stagnation temperature. The ambient pressure is measured using a NetScanner 9032 pressure reader. The stagnation pressure is measured using a NetScanner 9816 module inside of a NetScanner 98RK chassis. The stagnation temperature is measured using a K-type thermocouple, which was read using NI SCXI-1112 module inside of a SCXI-1001 module and digitized using a PCI-6035e A/D card. Since these measurement devices are uncorrelated, the second term in Equation 7.3 can be neglected. With this assumption and substituting Equation 7.3 and 7.4 into Equation 7.2, the uncertainty equation becomes:

$$U_r = \sqrt{\sum_{i=1}^{J}\left(\frac{\partial r}{\partial X_i}\,B_i\right)^2 + \sum_{i=1}^{J}\left(\frac{\partial r}{\partial X_i}\,R_i\right)^2} \tag{7.5}$$

Rearranging Equation 7.5:

$$U_r = \sqrt{\sum_{i=1}^{J}\left(\frac{\partial r}{\partial X_i}\right)^2 (B_i^2 + R_i^2)} \tag{7.6}$$

Using the definition of total uncertainty, as shown in Equation 7.2:

$$U_r = \sqrt{\sum_{i=1}^{J}\left(\frac{\partial r}{\partial X_i}\right)^2 U_i^2} \tag{7.7}$$

where, U_i is the combined random and systematic uncertainty of variable i

The Mach number is calculated using the equation:

$$M = \left(\left(\left(\frac{p_0}{p_a} + 1 \right)^{\frac{\gamma-1}{\gamma}} - 1 \right) \left(\frac{2}{\gamma-1} \right) \right)^{\frac{1}{2}} \tag{7.8}$$

where, p_0 is the pressure measured by the transducer for measuring the stagnation pressure (NetScanner 98RK-9816), p_a is the ambient pressure reading (NetScanner 9032), and γ is the ratio of the specific heats, which is 1.4 for air. Typically, the stagnation pressure measurement is the sum of the pressure measured with the NetScanner 98RK-9816 and the ambient pressure measured with the NetScanner 9032 because the NetScanner 9816 is a differential pressure transducer. In order to keep the measurements uncorrelated, in Equation 7.3 everything separated out. In order to use Equation 7.7 to calculate the uncertainty associated with the Mach number calculation, the derivatives of Equation 7.8 with respect to p_0 and p_a are required:

$$\frac{\partial M}{\partial p_0} = \left(\left(\left(\frac{p_0}{p_a} + 1 \right)^{\frac{\gamma-1}{\gamma}} - 1 \right) \left(\frac{2}{\gamma-1} \right) \right)^{-\frac{1}{2}} \left(\frac{1}{\gamma} \right) \left(\frac{p_0}{p_a} + 1 \right)^{-\frac{1}{\gamma}} \left(\frac{1}{p_a} \right) \tag{7.9}$$

$$\frac{\partial M}{\partial p_a} = \left(\left(\left(\frac{p_0}{p_a} + 1 \right)^{\frac{\gamma-1}{\gamma}} - 1 \right) \left(\frac{2}{\gamma-1} \right) \right)^{-\frac{1}{2}} \left(-\frac{1}{\gamma} \right) \left(\frac{p_0}{p_a} + 1 \right)^{-\frac{1}{\gamma}} \left(\frac{p_0}{p_a^2} \right) \tag{7.10}$$

To calculate the velocity of jet, the speed of sound of the flow is required so therefore, the static temperature of the jet must be calculated from the stagnation temperature measurement. This operation is performed using the following equation:

$$T_s = \frac{T_0}{1+\frac{\gamma-1}{2}M^2} \tag{7.11}$$

Just as with the Mach number uncertainty calculation, the derivatives of the Equation 7.11 with respect to stagnation temperature and Mach number are required to use Equation 7.7 for uncertainty calculations, and these are:

$$\frac{\partial T_s}{\partial T_0} = \frac{1}{1+\frac{\gamma-1}{2}M^2} \tag{7.12}$$

$$\frac{\partial T_s}{\partial M} = \frac{-T_0\, M\,(\gamma-1)}{\left(1+\frac{\gamma-1}{2}M^2\right)^2} \tag{7.13}$$

Now, the speed of sound for the jet flow is calculated using the equation:

$$a = \sqrt{\gamma\, \tilde{R}\, T_s} \tag{7.14}$$

where $\tilde{R}$ is the specific gas constant for air, 1716 ft-lb slugs^{-1} °R^{-1}. The only measured quantity in Equation 7.14 is the static temperature, so the derivative of Equation 7.14 with respect to static temperature is:

$$\frac{\partial a}{\partial T_s} = \frac{1}{2}\sqrt{\frac{\gamma\, R}{T_s}} \tag{7.15}$$

The jet velocity is calculated using the equation:

$$U_j = Ma \tag{7.16}$$

The derivatives needed for uncertainty analysis for this quantity are:

$$\frac{\partial U_j}{\partial M} = a \tag{7.17}$$

$$\frac{\partial U_j}{\partial a} = M \tag{7.18}$$

Finally, relating the uncertainty of the velocity calculation to the uncertainty of SPL produced by the jet with respect to the uncertainty of the jet velocity is found using the following equation

$$\pm SPL_{U,M} = 80\ \log_{10}\left(\frac{U_j \pm U_U}{U_j}\right) - 50\log_{10}\left(\frac{1-0.65\ (M \pm U_M)\cos(\theta)}{1-0.65\ M\cos(\theta)}\right) \qquad (7.19)$$

It should be noted that Equation 7.19 is based on the jet noise scaling laws used in previous chapters. The use of Equation 7.19 is an attempt to estimate how the SPL changes when there is uncertainty in the jet velocity measurement and Mach number, since the SPL is measured with microphones rather than calculated from the jet conditions. The significance of this uncertainty of the SPL should be compared to the uncertainty of the actual microphone measurements to see if any effects are real. The uncertainty associated with the microphones used in this study is ±0.2 dB.

Table 7.1 shows the uncertainty for each of the quantities discussed above. The uncertainties associated with the two pressure measurements are the uncertainties provided by the manufacturer. The uncertainty for the temperature measurement is that presented in Nakos[102], since the study was very thorough and the NI DAQ used in the study was identical to the DAQ for the temperature measurements used in the current study. The calculations shown above where performed for conditions that related to the Mach numbers 0.4, 0.5, 0.6, 0.7 and 0.8. From Table 7.1 it can be seen that the worst uncertainty associated with Mach number and jet velocity is 0.2% and 0.3%, respectively. While the uncertainty trends down with the increasing stagnation pressure, it is not a significant change.

Table 7.1: Uncertainty analysis of the variables used to calculate the jet velocity

		p_0	p_a	T_0	M	T_s	a	U_j
M=0.4	**Value**	1.71 psig	14.07 psia	527.23 °R	0.41	510.24 °R	1107.16 ft/s	451.79 ft/s
	Uncertainty	±0.005 psig	±0.0225 psia	±2.1°R	±0.0007	±2.03 °R	±2.21 ft/s	±1.15 ft/s
	Uncertainty (%)	0.3	0.2	0.4	0.2	0.4	0.2	0.3
M=0.5	**Value**	2.63 psig	14.07 psia	526.18 °R	0.50	501.07 °R	1097.16 ft/s	549.26 ft/s
	Uncertainty	±0.005 psig	±0.0225 psia	±2.1°R	±0.0006	±2.00 °R	±2.19 ft/s	±1.27 ft/s
	Uncertainty (%)	0.2	0.2	0.4	0.1	0.4	0.2	0.2
M=0.6	**Value**	3.91 psig	14.07 psia	525.47 °R	0.60	489.90 °R	1084.87 ft/s	653.66 ft/s
	Uncertainty	±0.005 psig	±0.0225 psia	±2.1 °R	±0.0006	±1.96 °R	±2.17 ft/s	±1.44 ft/s
	Uncertainty (%)	0.1	0.2	0.4	0.1	0.4	0.2	0.2
M=0.7	**Value**	5.50 psig	14.07 psia	524.23 °R	0.70	477.10 °R	1070.60 ft/s	752.43 ft/s
	Uncertainty	±0.005 psig	±0.0225 psia	±2.1°R	±0.0006	±1.91 °R	±2.15 ft/s	±1.63 ft/s
	Uncertainty (%)	0.1	0.2	0.4	0.1	0.4	0.2	0.2
M=0.8	**Value**	7.49 psig	14.07 psia	523.09 °R	0.80	463.07 °R	1054.75 ft/s	849.07 ft/s
	Uncertainty	±0.005 psig	±0.0225 psia	±2.1 °R	±0.0006	±1.86 °R	±2.12 ft/s	±1.82 ft/s
	Uncertainty (%)	0.1	0.2	0.4	0.1	0.4	0.2	0.2

Table 7.2: Uncertainty analysis of the SPL due jet velocity and Mach number

	M= 0.4	M= 0.5	M= 0.6	M= 0.7	M= 0.8
$U_{SPL,UM}$ (θ = 30°)	±0.10 dB	±0.09 dB	±0.09 dB	±0.09 dB	±0.09 dB
$U_{SPL,UM}$ (θ = 60°)	±0.09 dB	±0.08 dB	±0.08 dB	±0.08 dB	±0.08 dB
$U_{SPL,UM}$ (θ = 90°)	±0.09 dB	±0.08 dB	±0.08 dB	±0.07 dB	±0.07 dB

Table 7.2 shows the effect of the velocity and Mach number uncertainty on the jet noise. The first thing to note is that the all the uncertainties shown in Table 7.2 is insignificant compared to the ±0.2 dB uncertainty from the microphone measurements. This means that even with the worst uncertainties at ±0.1 dB, ±0.09 dB and ±0.09 dB for the polar angles of 30°, 60° and 90°, respectively, the uncertainties of the microphone measurements are controlling uncertainties. The uncertainties trend down with larger polar angles and velocities and Mach numbers. From this analysis, it is shown that the jet velocity and Mach number can be set accurately, and any errors associated with this jet setting does not create any uncertainties in the jet noise.

The above analysis pertains to the measurement of the Mach number and jet velocity of jet. Unfortunately, setting this Mach number and jet velocity consistently is not an easy task. As stated in earlier chapters a two-inch control valve was used to control the jet flow. A Valtek Mark 1 control valve that is outfitted with a StarPak Logix 2000 unit for digital control is used as the control valve. The valve was used in its digital control mode through an RS232 connection. The specifications for the digital control indicate that the uncertainty of the valve to open to a certain position is less than 0.035% of full scale. Also, it is noted that there exists a less than 0.03% of full scale dead band. This means there is a small amount of command in which the valve will not move. While, the valve behaves in an accurate and consistent manner, often other factors such as the pressure in

high pressure tanks, the temperature of the air in the tanks, the ambient humidity, can cause a given valve opening to cause slightly different jet flows. In addition, the valve cannot always make the small adjustment required to throttle the jet to a consistent condition. Even though these flow differences can happen, based on the above analysis, small changes in the jet velocity does not affect the sound produced. As a final note on the ability to set a certain jet Mach number and velocity, as the jet flow is created, the high pressure air stored in the pressure tanks get drained and will cause an air compressor to turn on the refill the tanks. This can often cause fluctuations in the Mach number on the order of ±0.005, which is not significant.

7.4 Uncertainty in Microphone Placement

In addition to the properly setting and measuring the jet flow, the microphones need to be placed at the correct polar angles and distances from the jet. The polar angle of jet was measured using a protractor with a string with a weight at the end attached. The protractor is oriented at the nozzle-exit such that the body of the protractor is coplanar with the microphone arc. The string is extended from the protractor, slung over the microphone arc and held in that position using the weight at the end of the string. The protractor has 1° divisions along it, and the polar angle is determined by the angle over which the string lays on the protractor. The error in this method is all human error, but given the distances at which the microphones are mounted the uncertainty of the polar angle is approximately ±1°

As for the distance of the microphone from the nozzle-exit, this was measured was performed using a tape measure. Given resolution on a standard tape measure, the only

error in this method is human error is reading the tape measure. For this reason, the uncertainty associated with this measurement is approximated at ±0.5 in.

Just as was performed above, using the jet noise scaling relationships, the effect on the jet noise produced by the uncertainties of the polar angles and distance of the microphone from nozzle-exit can be approximated using the equations:

$$\pm SPL_\theta = -50 \log_{10}\left(\frac{1-0.65\,M\cos(\theta \pm U_\theta)}{1-0.65\,M\cos(\theta)}\right) \tag{7.20}$$

$$\pm SPL_R = 20 \log_{10}\left(\frac{R}{R \pm U_R}\right) \tag{7.21}$$

Equation 7.20 can be used separately from the Equation 7.19 because the uncertainty of the Mach number and velocity is not coupled with the uncertainty of the polar angle. Based on Equation 7.20, the uncertainty of the SPL from this factor is a function of the Mach number. Table 7.3 shows the results of this analysis. One can see from Table 7.3 that the uncertainty associated with increases with Mach number and peaks at a polar angle of 60°. The worst uncertainty is at the same uncertainty level as that reported from B&K on the microphones, which is ±0.2 dB. This is an uncertainty to be paid attention. As stated in earlier chapter the distances of the microphone measurements for polar angles of 30°, 60°, and 90° for the large nozzle set-ups were 12 ft, 11 ft, and 10 ft respectively. Applying the uncertainty of ±0.5 in to Equation 7.21 leads to uncertainties of ±0.03 dB, ±0.03 dB, and

Table 7.3: Uncertainty analysis of the polar angles of the microphones

	M= 0.4	**M= 0.5**	**M= 0.6**	**M= 0.7**	**M= 0.8**
$U_{SPL,\theta}$ **(θ = 30°)**	±0.06 dB	±0.08 dB	±0.11 dB	±0.14 dB	±0.18 dB
$U_{SPL,\theta}$ **(θ = 60°)**	±0.10 dB	±0.13 dB	±0.16 dB	±0.19 dB	±0.23 dB
$U_{SPL,\theta}$ **(θ = 90°)**	±0.10 dB	±0.12 dB	±0.15 dB	±0.17 dB	±0.20 dB

±0.04 dB, for polar angles of 30°, 60°, and 90°, respectively. These uncertainties are insignificant with respect to the uncertainty of the microphone measurements themselves.

7.5 Uncertainty in the Jet Noise

The total uncertainty of the SPL based on the Mach number, jet velocity, microphone polar angles and microphone distance from the nozzle-exit is approximated using the equation:

$$U_{SPL} = \sqrt{\left(\pm SPL_{M,U}\right)^2 + (\pm SPL_{\theta})^2 + (\pm SPL_{R})^2} \qquad (7.22)$$

The results of the approximation of the uncertainty of SPL with respect to the jet setting and microphone placement are shown in Table 7.4. The worst uncertainties, which occur at a Mach number of 0.8 and a polar angle of 60°. These uncertainties are on the order of the uncertainties associated with the microphone measurements as published by the manufacturer, which ±0.2 dB. Because of this, these uncertainties should be taken into account when the overall uncertainties of the microphone measurements are considered.

Table 7.4: Uncertainty analysis of the microphone measurements based on the uncertainty of the jet settings and microphone placements

	M= 0.4	**M= 0.5**	**M= 0.6**	**M= 0.7**	**M= 0.8**
U_{SPL} (θ = 30°)	±0.12 dB	±0.13 dB	±0.15 dB	±0.17 dB	±0.20 dB
U_{SPL} (θ = 60°)	±0.14 dB	±0.15 dB	±0.18 dB	±0.21 dB	±0.25 dB
U_{SPL} (θ = 90°)	±0.14 dB	±0.15 dB	±0.17 dB	±0.19 dB	±0.21 dB

7.6 Uncertainty in the Acoustic Measurements

The analysis performed in this and following section is based in the uncertainty analysis performed by Nance[52]. As mentioned in previous chapters the acoustic

measurements acquired in this study were acquired using B&K 4939 microphones which were read using NI 4499 acquisition cards. B&K lists the uncertainty of measurements acquired with these microphones as ±0.2 dB.

$$\frac{B_{G_{xx}}}{G_{xx}} = \frac{\ln(10)}{10} B_{SPL} \tag{7.23}$$

$$\frac{R_{G_{xx}}}{G_{xx}} = \frac{1}{\sqrt{n_d}} \tag{7.24}$$

where, B_{SPL} is the uncertainty of the microphone measurement as provided by the manufacturer and n_d is the number of averages used in the processing the frequency spectrum. Given that the frequency spectra used in this study are averaged with typically 7500 averages, the systematic and random uncertainties of the microphone measurements in this study are ±0.05dB and ±0.01dB, respectively. These uncertainties combine to gives a total uncertainty for the microphone measurements of ±0.05 dB.

7.7 Uncertainty in the Boundary Layer Probe Measurements

The instrumentation used to track the Mach number and jet velocity of the jets in the GTRI Flow Diagnostic Facility are identical to those used in the GTRI Anechoic Jet-Facility. Therefore, the uncertainty analysis performed for that facility can be applied to this facility as well. The uncertainty of the boundary layer probe measurements themselves are now analyzed. In terms of the calculations, the uncertainty of the velocity at a point in the boundary layer is calculated using Equations 7.7 – 7.18 above.

The stagnation pressure at each location in the boundary was measured using a United Sensor BA-025-12-C-11-650 boundary layer probe or a made-in-lab boundary layer probe of the same specifications in conjunction with an Omega PX409-030DDU5V pressure transducer. This pressure transducer has an uncertainty of ±0.024 psid. The

ambient pressure is measured by the NetScanner 9032 absolute pressure transducer with an uncertainty of ±0.005 psia. Finally, the stagnation temperature is measured by a K-type thermocouple using an NI DAQ system similar to that used in the GTRI Anechoic Jet-Facility. This gives these pressure measurements a ±2.2°C uncertainty. Ultimately, the velocity profiles are used to calculate the boundary layer shape factor, which is the ratio of the displacement thickness to the momentum thickness. Both the displacement thickness and momentum thickness are integrated quantities, which makes calculating the uncertainty of these quantities complicated. It is noted that the uncertainty in the velocity measurements is highest at low velocities, as these are calculated from small stagnation pressure readings. The author was unable to find a satisfactory method for calculating the uncertainty for the integrated quantities, so will not attempt to make these calculations and have them be potentially inaccurate.

CHAPTER 8

CONCLUSIONS AND FUTURE WORK

The above study looked to answer the question: why do jet noise measurements of jets that are presumed to be at the same conditions sometimes measure very different? This was done using a four-part approach: (1) investigating rig-noise detection methods, (2) investigating the effect of the jet's Reynolds number on jet noise, (3) investigating the effects of the nozzle-exit boundary layer on jet noise measurements, and (4) investigating the effects of reflections and shielding on jet noise measurements. The conclusions of this four-part investigation as well as the potential areas for future work are summarized here.

8.1 Conclusions

The Doubling-Diameter Method was found to detect the simulated rig-noise that was produced using cylinder obstruction upstream of the nozzle-exit. This method was also used in the case study looking into rig-noise contamination in the GTRI Anechoic Jet-Facility. The results of this study were that rig-noise is does not exist in the jet-facility for nozzles ranging in nozzle-exit diameter from 0.25 inches to 2 inches and at Mach number ranging from 0.4 to 0.8. This proves that the jet noise produced in the GTRI Anechoic Jet-Facility from nozzles of an appropriate are clean without contamination. This also disproves the claim from Viswanathan[4, 5] that rig-noise contamination is the reason for the differences between his measurements and those in Tanna Jet Noise Database[6].

The Reynolds number with respect to diameter was found to have no effect on the noise produced by the jets. The Reynolds number was varied between 5000 and 100000.

This indicates that jet noise from model-scale test should be able to be scaled up to the jet noise produced by full-scale jet engines.

The nozzle-exit boundary layer does effect the noise produced by a jet. This effect was found to follow the power fit equation, and this fit was seen both with the normalized OASPL and the normalized noise at a given Strouhal number. Best fits were found for this effect and a potential correction was created. It is suggested in the future that jet noise researchers present the boundary layer state parameters alongside their jet noise spectra.

With respect to the reflections and shielding effects of surfaces surrounding the nozzle, it was found that the plenum chamber will act as both a reflector and a shield and can have considerable effects on the jet noise. The shielding effects occur at all conditions once the line-of-sight between the nozzle-exit and a microphone in the forward arc is broken by the nozzle. These effects increase with frequency for the reasons explained in Chapter 6. The plenum acting a reflector has the greatest effects on the screech produced by a supersonic jet. On the other hand, the secondary nozzle has negligible effects on the jet noise produced by a primary nozzle. The simple computation simulation used to predict the shielding effects, could not match the experimental results, but this probably has more to do with the simplicity of the model and complexity of jet noise as a noise source.

This study was motivated in part by the claims made by Viswanathan[4] from his comparisons of his data with the Tanna Jet Noise Database. To remind the reader, Viswanathan[4] found that compared to his own data the Tanna Jet Noise Database had higher high frequency levels. His comparison is seen in Figure 1.1. These differences look strikingly similar to the effect of the nozzle-exit boundary layer on jet noise. In truth, Viswanathan used a long conical nozzle in his study compared, while the Tanna Jet Noise

Database was measured using an ASME type nozzle. It is possible that the differences shown are in fact the result of boundary layer differences between the two nozzles. But, without the velocity profiles of the jets this cannot be concluded.

As stated in Chapter 1, Viswanathan[4, 5] saw high-frequency differences between his data and the data acquired by others, including the Tanna Jet Noise Database, as rig-noise contamination. In this study, not only has a method for detecting rig-noise been validated, but the GTRI Anechoic Jet-Facility (where the Tanna Jet Noise Database was acquired) has been verified to be free of rig-noise contamination. In addition, it has been shown that the nozzle-exit boundary layer state can have a large impact on the noise. The author would like to suggest that this is in fact the differences seen by Viswanathan[4, 5]. The data acquired by Viswanathan, was measured in the Boeing Low Speed Aeroacoustic Facility, which does not have a plenum chamber, and a conical nozzle was used. Based on the statements of Harper-Bourne[12], these jets should have a turbulent nozzle-exit boundary layer. Alternatively, the Tanna Jet Noise Database, was measured in a facility with a plenum chamber that has a contraction ratio of 36 using an ASME nozzle. These jets should have a laminar nozzle-exit boundary layer. This differences would cause the Tanna Jet Noise Database to have higher levels at and to the right of the spectral peak.

8.2 Future Work

8.2.1 Rig Noise

On the subject of rig-noise contamination of jet noise measurements, exploring more sophisticated methods of rig-noise contamination would be helpful. One such method is the three-microphone method that was developed by Chung[103] and applied to jet

noise applications by Nance et al.[49-52]. This method would in theory only require one set of measurements instead of the two or more required by the Doubling-Diameter Method.

8.2.2 Reynolds Number Effects

It is recommended that additional work be carried out on the effects of the Reynolds number on jet noise with respect to a length scale, at least in three categories as listed below:

(1) Examine jet noise of much smaller and much larger nozzle sizes than those used in the present study.

(2) Investigate Reynolds number effects on jet noise with respect to length scales that change with the physics of the jet itself not just the nozzle diameter, such as the boundary layer displacement and momentum thickness, as suggested by Bogey34.

(3) Investigate the effects of the Reynolds number with respect to diameter on supersonic jet noise.

8.2.3 Boundary Layer Effects

It is recommended that the effects of the nozzle-exit boundary layer on jet noise be further examined in the following manner.

(4) Validate the empirical correction developed in this work with measurements from a larger dataset acquired in various facilities.

(5) Develop a theoretical or computational model that relates the jet noise to the nozzle-exit boundary layer state for both subsonic and supersonic jets.

(6) Acquire boundary layer data in full-scale engine noise data and attempt to relate the jet noise to the exit boundary layer state.

(7) Extend the current work to supersonic jets.

8.2.4 Facility Reflections and Shielding Effects on Jet noise

While, this study showed some of the potential sources of reflections and shielding experimentally, an advanced shielding model (such as that developed at NASA by Nark[96]) should be employed for improved design of the jet rig and placement of microphones in anechoic chambers especially in the forward arc. In addition, one could argue that more reflections would come from the surfaces associated with the microphone mounting structure than the plenum chamber as they are typically not lined with adequate sound absorbing material. A detailed computational and experimental study of the potential reflections from typical microphone mounting structures should be conducted as a function of mounting arrangements. Additionally, ways of mitigation of the reflections from these mounting structures should be studied. This could include the effect of distance of the microphone grid from the arc supporting the microphones and distance of the microphone grid from the anechoic walls.

APPENDIX A

EXAMPLE OF CORRECTING JET NOISE SPECTRA TO LOSSLESS

This appendix shows how microphone corrections are applied to frequency spectra to change them to as if the measurements were acquired by a perfect, omnidirectional transducer in a freefield. Microphones do not measure sound perfectly at every frequency and every incidence angle. These imperfections in the microphone measurements can be corrected using a series of corrections. These corrections are described and are applied in an example below. These corrections are described in Ahuja[10].

The pressure signals are processed into averaged frequency spectra using a Fast Fourier Transform (FFT) technique. In these techniques, a sound signal is divided into smaller segments and the FFT of each segment is calculated. These FFTs are then averaged in order to reduce the uncertainty associated with the calculations. For the experiments in this study, the sampling frequency used with the analyzer is 204.8 kHz, i.e., 204,800 samples of the acoustic pressure signal are acquired every second. Acoustic pressure time signals are recorded using these sampling settings. These time signals are processed into averaged power spectra using a window size of 6400 samples, 50% overlap and a Hanning window. This creates a Δf of 32 Hz and a smooth spectral curve.

The example spectrum is a jet noise spectrum. The noise was generated by a jet created by a two-inch diameter converging nozzle, with a jet Mach number of 0.8. The microphone used in the measurement is a B&K 4939 microphone, placed 11 feet from the nozzle-exit at a polar angle of 30°. Since the microphone was pointed at the nozzle-exit at the time of the measurement, the incidence angle is 0°. In addition, due to the shallow

polar angle hydrodynamic noise contaminated the low frequency measurements, so a foam ball windscreen was used to attenuate these effects. At the time of the measurement, the ambient pressure was 14.07 psia, the ambient temperature was 69.26°F, and the relative humidity was 80.5%.

The effects of microphone geometry, the microphone protective grid, microphone actuator response, and incidence of the microphone with respect to the assumed sound incidence angle are accounted for as part of the microphone free-field frequency response. This correction is lumped together and will be given the variable *A(f, Ψ)*, because this correction is a function of both frequency and the angle of incidence, Ψ, of the sound wave on the microphone. The definition of the microphone incidence angle is shown in Figure A.1. The correction is usually provided by the microphone manufacture.

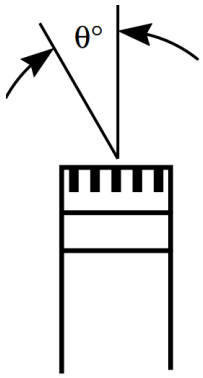

Figure A.1: Definition of the incidence angle of a microphone, reproduced from the B&K Microphone Handbook[104].

The correction due to the freefield response is applied using the equation:

$$SPL_{freefield}(f) = SPL(f) - A(f, \psi) \quad \text{(A.1)}$$

Figure A.2 shows this correction being applied to the example uncorrected spectrum. Figure A.2a shows the uncorrected spectrum that was created by using the FFT parameters described above. Figure A.2b shows the freefield response, *A(f, Ψ)*, for the microphone

used in the measurement as provided by B&K. Figure A.2c shows the freefield corrected frequency spectrum, which is calculated using Equation A.1.

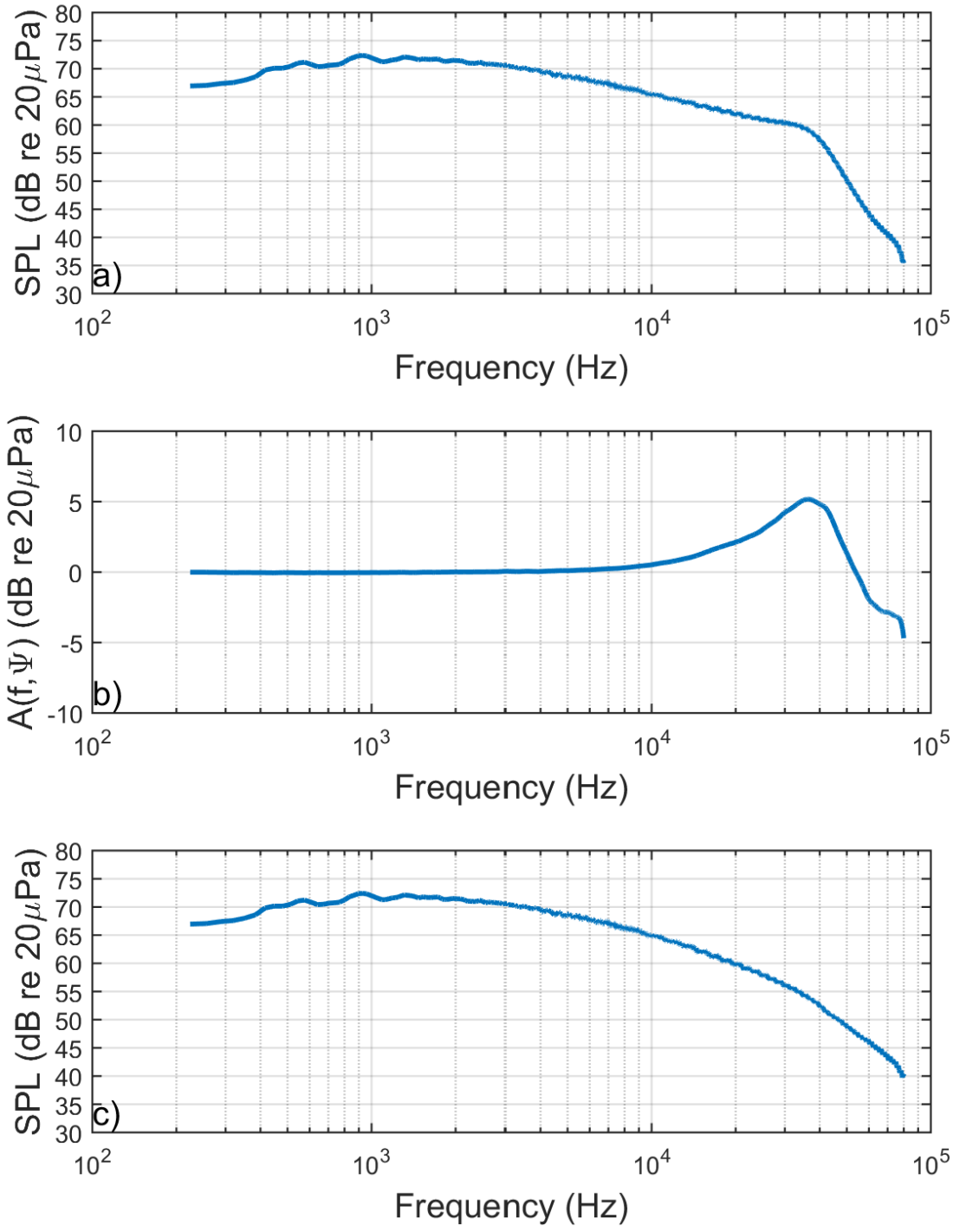

Figure A.2: Example spectrum having the freefield response correction applied. a) base spectrum, b) the freefield response of the microphone, and c) the freefield response corrected spectrum.

The effect of atmospheric attenuation is accounted for by using the method presented in ANSI S1.26-1995[61]. This correction contains many equations and is too long to present here and but is presented in Appendix B. The method results in a value *α(f)*, which has the units of dB/m. This value is the attenuation coefficient and varies with frequency. Removing the freefield response and attenuation effects provides the spectra in a form known as "lossless," which will be used throughout the analysis. The advantage of this form of the data is that it allows the losses to the acoustic signal, which are caused by atmospheric attenuation, to be added back into the spectrum at each frequency and comparisons to any other jet noise measurements can be made without concern for differences due to day-to-day ambient conditions. This correction is applied using the equation:

$$SPL(f)_{lossless} = SPL_{freefield} + \alpha(f)R_1 \qquad \text{(A.2)}$$

where R_1 is the distance of the microphone from the nozzle at the time of measurement. The attenuation coefficient as calculated using the method outlined in outlined in Appendix B is shown in Figure A.3. Figure A.4 shows atmospheric attenuation correction being applied to the freefield corrected spectrum. Figure A.4a shows the freefield corrected spectrum, which is the same spectrum as shown on Figure A.2c. Figure A.4b shows the SPL lost due to the atmospheric attenuation for each frequency. Figure A.4c shows the spectrum corrected for the effects of atmospheric attenuation using Equation A.2. This spectrum is now considered lossless.

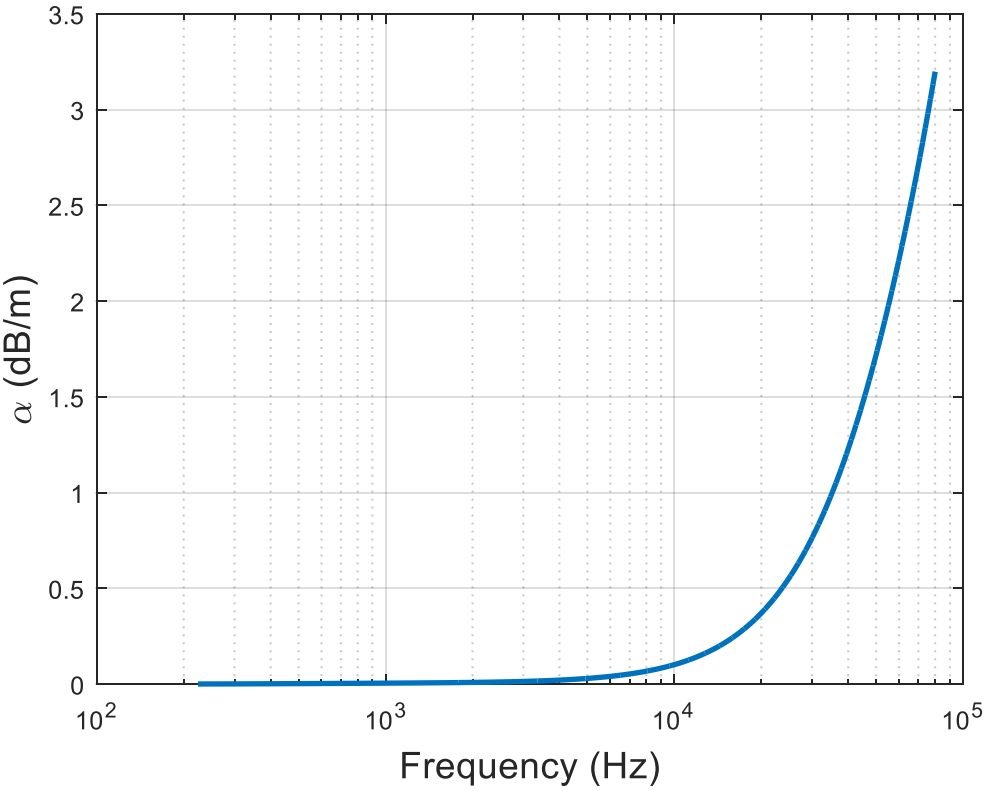

Figure A.3: Attenuation coefficient as a function of frequency calculated using the method of ANSI S1.26-1995[61] for the atmospheric conditions stated above.

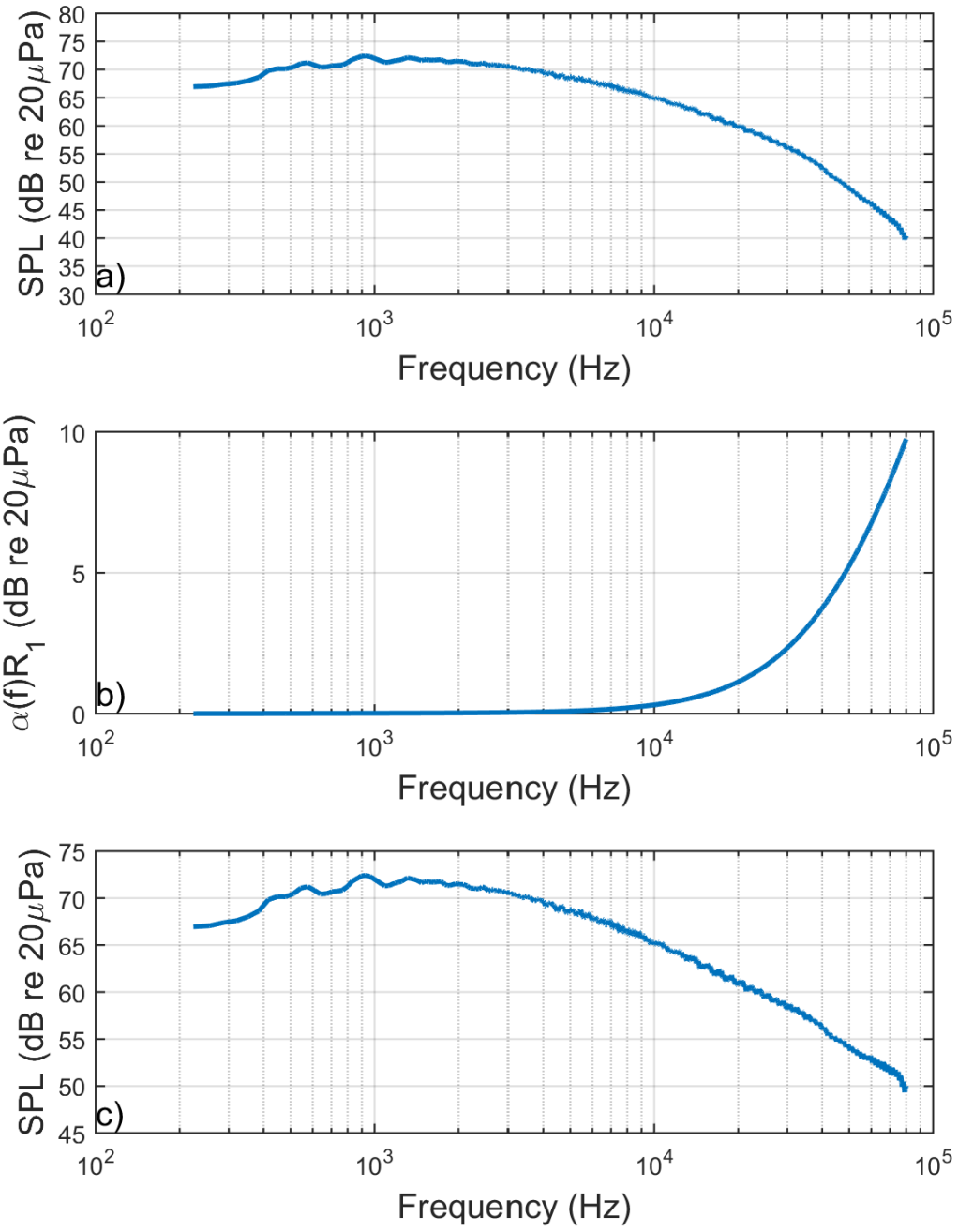

Figure A.4: Application of the atmospheric attenuation correction. a) freefield response corrected spectrum, b) losses due to atmospheric attenuation, and c) lossless spectrum.

Next, the jet noise measurements are extrapolated to a common distance to help with needed comparisons. This operation is performed using the equation:

$$SPL(f)_{lossless,R_1} = SPL_{lossless,R_2} + 20\log_{10}\left(\frac{R_1}{R_2}\right) \quad \text{(A.3)}$$

where R_2 is the corrected distance. The second term in Equation A.3 is the application of the inverse-square law, which is used to account for the SPL changes as the intensity generated by the jet is spread over a distance. Figure A.5 shows this correction being applied. Figure A.5a shows the same spectrum as was shown in Figure A.4c, which is corrected for both the freefield response and losses due to atmospheric attenuation. Figure A.5b shows the SPL change due to the microphone distance extrapolation. Because the assumption used is that the microphone is the acoustic and geometric farfield, the jet is assumed to be a point source located at the nozzle-exit. Based on this assumption and as shown in Figure A.5b, the SPL change is constant over the entire frequency range. Figure A.5c shows the distance correction applied using Equation A.3. It is important to note, that the distance correction shown in Equation A.3 is used in this example because the jet noise is assumed to follow the inverse-square law for distances in the acoustic and geometric farfield, i.e., the jet is viewed as point source. If one is measuring a sound source that obeys different power "spreading" laws those should be used in place of the Equation A.3. For example, the sound source creates cylindrical waves, the SPL will vary with *1/R* rather than $1/R^2$. In addition, with a distributed source, such as a jet in the nearfield, the atmospheric attenuation distance corrections will need to be applied with knowledge of the

source distribution. This means that the distance R_1 will vary based on how far each source is from the microphone. For more information about this see Ahuja[10, 105].

The final correction applied in this example is the correction applied since a foam ball was used on the microphone, to prevent hydrodynamic fluctuations from affecting the measurements. The effect of the windscreen on a broadband frequency spectrum was determined experimentally and is given the variable *B(f)*. The experiment performed to create this correction conducted in the GTRI Anechoic Jet-Facility. A ½-inch diameter nozzle attached to jet plenum. This nozzle was used because it can generate high-frequency nozzle and can without a doubt be assumed to act as point source in the geometric and acoustic farfield, due to the small diameter. Jet noise measurement were acquired at polar angles of 30° and 90° with and without the windscreen placed on the microphone. The jet noise spectrum without the windscreen was subtracted from the jet noise spectrum with the windscreen, and the varying SPL change with frequency is used as the correction in variable *B(f)*. Applying this correction uses the equation:

$$SPL_{corrected}(f) = SPL_{windscreen}(f) - B(f) \tag{A.4}$$

Figure A.6 shows how these corrections are applied. Figure A.6a shows the same jet noise spectrum shown in Figure A.5c. Figure A.6b shows the parameter *B(f)* and how it varies with frequency. Figure A.6c shows the spectrum with the windscreen correction applied.

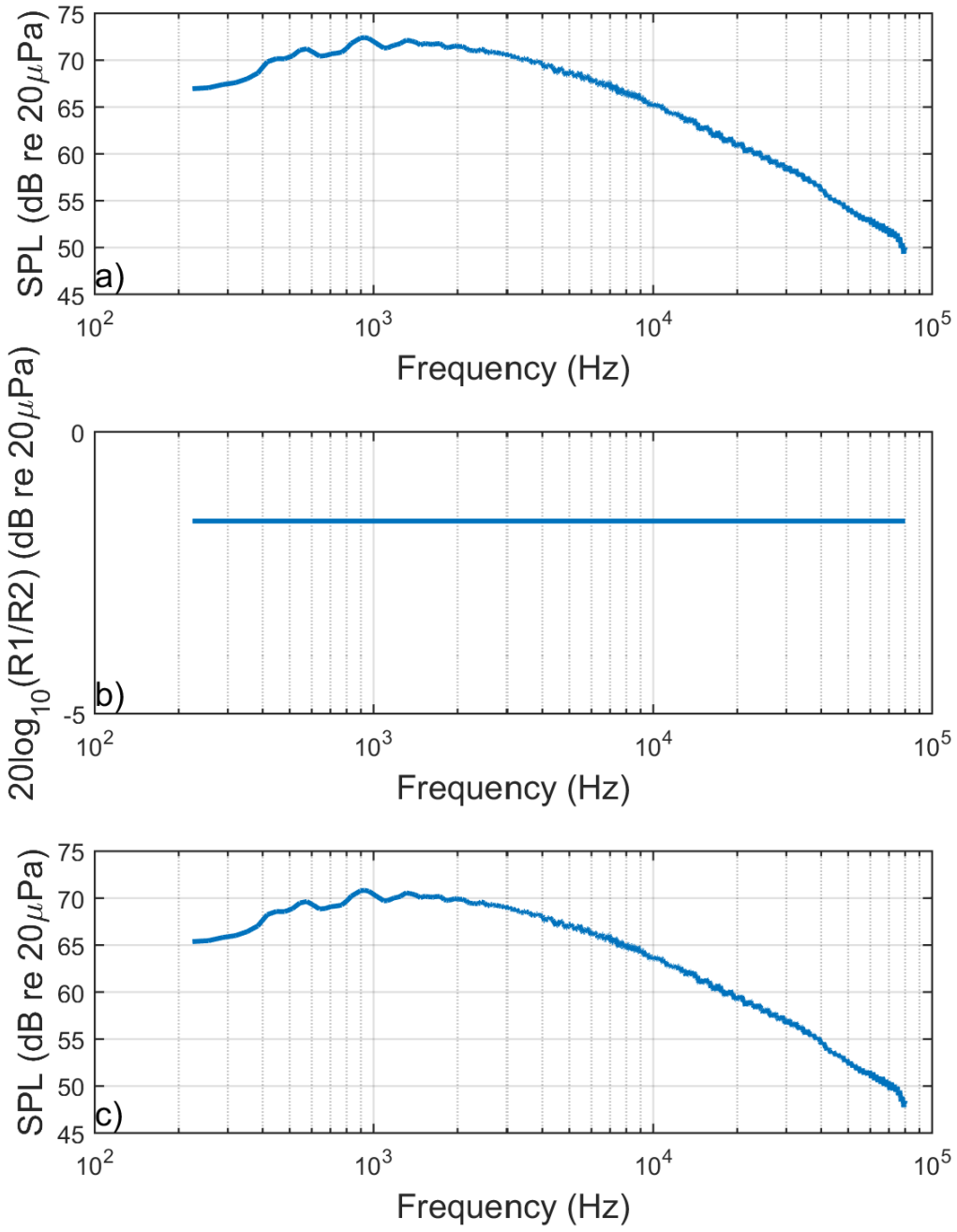

Figure A.5: Application of the distance correction. a) Lossless spectrum, b) distance extrapolation levels, and c) distance corrected spectrum.

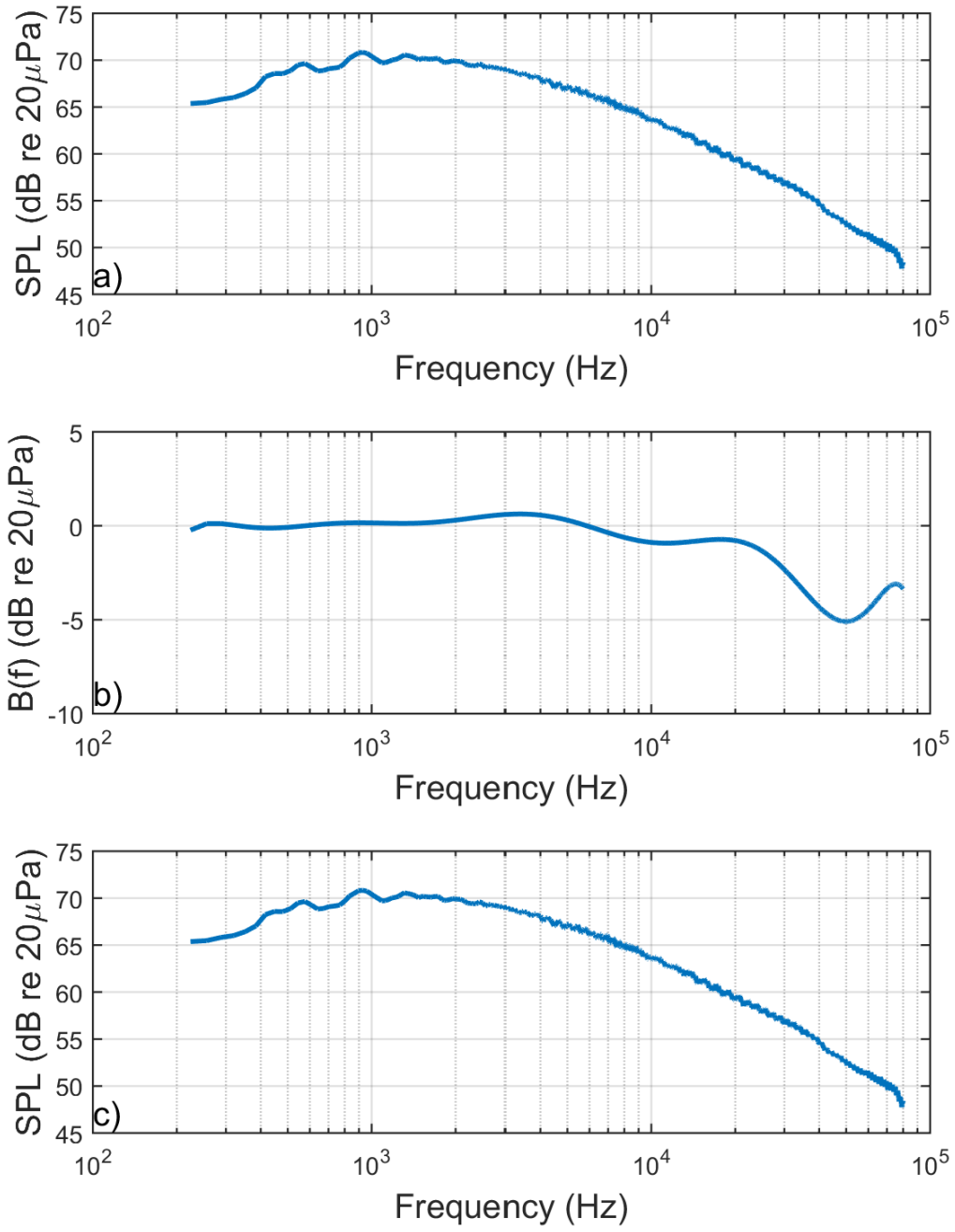

Figure A.6: Correcting for the effects of the foam ball. a) distance corrected spectrum, b) effect of the foam ball, and c) fully corrected spectrum.

The above procedure is the minimal amount of corrections that should be performed on spectra of microphone measurements. Additional processing and corrections can be performed to manipulate the microphone measurements into a form that is desired for the required analysis. One example of this is converting narrowband spectra, such as the spectrum used in the above example, into 1/N-octave band spectra. Narrowband spectra have a constant Δf; while 1/N-octave band spectra have frequency bands that relate to some proportion between the lower and upper limits of the frequency bands. For example, the upper limit of an octave band is two time the lower limit. The standard frequency limits associated with frequency spectra form is readily available in any acoustics textbook. In order to convert narrowband spectra to 1/N-octave band spectra all one has to do is for every 1/N-octave frequency, sum the decibel levels in the narrowband spectra inside of the 1/N-octave band, i.e., all the SPL value associated with frequencies between the lower and upper limits of the band using the equation:

$$SPL_{total} = 10\log_{10}\left(\sum_{i=1}^{N} 10^{\frac{SPL_i}{10}}\right) \quad \text{A.5}$$

Specifically related the jet noise measurements, additional corrections/normalization can be performed. There is much debate about the proper manner to normalize jet noise spectra, so the reader is encouraged to consult the literature as for the best manner to perform these operations.

APPENDIX B

CALCULATION OF THE ATMOSPHERIC ATTENUATION COEFFICIENT

Throughout the study, the acoustic measurements were corrected for the effects of atmospheric attenuation. As shown in Chapter 3, the effects of the losses caused by atmospheric attenuation are added back into the acoustic frequency spectra using the equation:

$$SPL_{corrected} = SPL_{uncorrected} + \alpha(f)R \tag{B.1}$$

where, $\alpha(f)$ is the attenuation coefficient in dB/meters as a function of the frequency and R is distance of the microphone from the source. This attenuation coefficient was calculated using the method laid out in ANSI.S1.26.-1995[61], and the method for this calculation is presented here. The attenuation coefficient is calculated using the equation:

$$\alpha(f) = 8.686\, f^2 \left(\left[1.84 \times 10^{-11} \left(\frac{p_a}{p_r}\right)^{-1} \left(\frac{T}{T_r}\right)^{\frac{1}{2}} \right] + \left(\frac{T}{T_r}\right)^{-\frac{5}{2}} \times \left\{ 0.01275 \left[\exp\left(-\frac{2239.1}{T}\right) \right] \left[\frac{f_{rO}}{f_{rO}^2 + f^2} \right] + 0.1068 \left[\exp\left(-\frac{3352.0}{T}\right) \right] \left[\frac{f_{rN}}{f_{rN}^2 + f^2} \right] \right\} \right) \tag{B.2}$$

where, f is the frequency of the acoustic wave, T is the ambient temperature in Kelvin, p_a is the atmospheric pressure in kilopascals, p_r is the reference pressure of 101.325 kPa, T_r is the reference temperature of 293.15 K, f_{rO} is the vibrational relaxation frequency of oxygen and f_{rN} is the vibrational relaxation frequency of nitrogen. The vibrational relaxation frequencies of oxygen and nitrogen are calculated using the equations:

$$f_{rO} = \frac{p_a}{p_r}\left\{24 + \left[\frac{(4.04\times10^4 h)(0.02+h)}{0.391+h}\right]\right\} \quad \text{(B.3)}$$

$$f_{rN} = \frac{p_a}{p_r}\left(\frac{T}{T_r}\right)^{-\frac{1}{2}}\left(9 + 280h\exp\left(-4.170\left[\left(\frac{T}{T_r}\right)^{-\frac{1}{3}} - 1\right]\right)\right) \quad \text{(B.4)}$$

where, h is the molar concentration of water vapor in the atmosphere. The molar concentration of water vapor in the atmosphere is calculated using the equation:

$$h = h_{rel}\left(\frac{p_{sat}}{p_r}\right)\left(\frac{p_a}{p_r}\right)^{-1} \quad \text{(B.5)}$$

where, h_{rel} is the relative humidity of the air, p_{sat} is the saturation pressure of water given the ambient conditions and p_a is the atmospheric pressure in kPa. The saturation pressure is calculated using the equation:

$$p_{sat} = p_r 10^V \quad \text{(B.6)}$$

where, V is given by the equation:

$$V = 10.79586\left[1 - \frac{T_{01}}{T}\right] - 5.02808\log_{10}\left(\frac{T}{T_{01}}\right) + 1.50474\times10^{-4}\left\{1 - 10^{-8.29692\left[\left(\frac{T}{T_{01}}\right)-1\right]}\right\} + 0.42873\times10^{-3}\left\{-1 + 10^{4.76955\left[1-\left(\frac{T_{01}}{T}\right)\right]}\right\} - 2.2195983 \quad \text{(B.7)}$$

where, T_{01} is the triple-point isotherm temperature of 273.15K. The procedure above was developed to be used for tones, but is applied to broadband signals by calculating the atmospheric attenuation coefficient for each frequency and applying the correction as function of frequency to the broadband spectra.

APPENDIX C

SHIELDING CODE DESCRIPTION

C.1 Shielding Code Description

In Chapter 4, an acoustic shielding code, which was developed by Ahyte and McCulley[39], was used to predict the shielding effects of a baffle, serving as the largest shielding area of a plenum chamber, on jet noise measurements in the forward arc. The basics of this code and the code itself will be presented here. The code uses the solution of a single frequency monopole source being shielded by a half-plane, which was developed by Bowman, Senior and Uslenghi[94].

In this solution, the acoustic velocity potential of an acoustic wave is used as the primary quantity rather than the acoustic pressure. In the far-field these two complex quantities are related using the equation:

$$p = i\omega\rho_a V \tag{C.1}$$

where, p is the acoustic pressure, ρ_a is density of the ambient air, V is the acoustic velocity potential, and ω is the circular frequency, which is related to the frequency of the acoustic wave by:

$$\omega = 2\pi f \tag{C.2}$$

In terms of the velocity potential, the SPL difference caused by the shielding can be expressed by the equation:

$$\Delta SPL = SPl_s - SPL_u = 20\log_{10}\frac{|p_s|}{|p_u|} = 20\log_{10}\frac{|V_s|}{|V_u|} \tag{C.3}$$

where, the subscript *s* refers to the shielded case and the subscript *u* refers to unshielded case. Equation C.3 will cause the ΔSPL values to typically be negative. The unshielded velocity potential is given by the expression:

$$V_u = \frac{\exp(i\omega R)}{kR} \tag{C.4}$$

where *R* is the distance between the monopole and the location in the far-field and *k* is the wave number of the acoustic wave, which is given by:

$$k = \frac{\omega}{a_0} \tag{C.5}$$

where, a_0 is the ambient speed of sound.

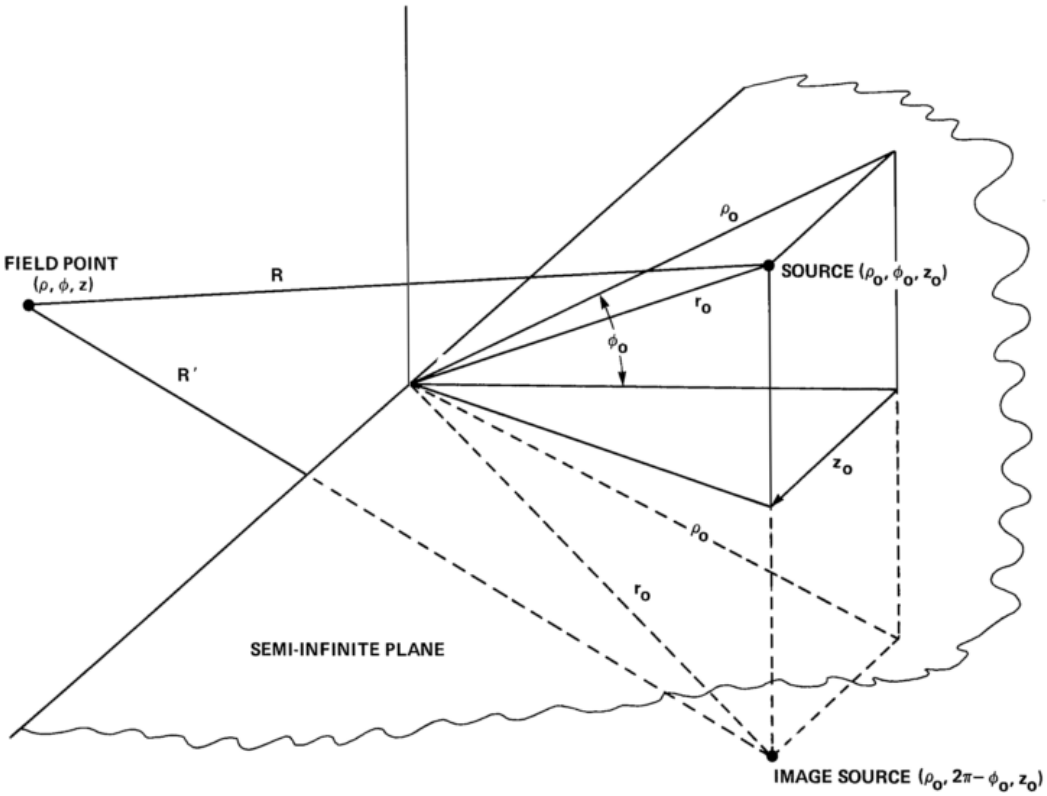

Figure C. 1: Geometry associated with the shielding of a point source by a semi-infinite plane, reproduced from Ahtye and McCulley[39].

Figure C.1 shows the physical configuration of the solution in terms of cylindrical coordinates to the single frequency point source being shielded by the half plane. The z-

axis is positioned at the edge of the half-plane. The distance between the source and far-field is projected don the $z=0$ plane and is given the quantity ρ. The half-plane is located in the $\phi = 0$ plane. As shown in Figure C.1, the coordinates the coordinates of the source are (ρ_0, ϕ_0, z_0), the coordinates of the image source are $(\rho_0, 2\pi - \phi_0, z_0)$, and the coordinates of the point in the far-field are (ρ, ϕ, z). The velocity potential in the shielded case is the expressed in terms of three distances: (1) R, the distance between the source the far-field point, (2) R', the distance between the image source and the far-field point, and (3) R_1, the characteristic diffusion distance. These three distances are given by the equations:

$$R = \sqrt{\rho^2 + \rho_0^2 - 2\rho\rho_0 \cos(\phi - \phi_0) + (z - z_0)^2} \tag{C.6}$$

$$R' = \sqrt{\rho^2 + \rho_0^2 - 2\rho\rho_0 \cos(\phi + \phi_0) + (z - z_0)^2} \tag{C.7}$$

$$R_1 = \sqrt{(\rho + \rho_0)^2 + (z - z_0)^2} \tag{C.8}$$

The solution of the single frequency source being shielded by the half plane makes the following three assumptions, that assume that for the given frequency that the acoustic wave is in the far-field: (1) $k(R_1-R)>>1$, (2) $k(R_1-R')>>1$, and $kR_1>>1$. Given these three assumptions the shielded case velocity potential can be given by the expression:

$$V_s = V_G + V_D \tag{C.9}$$

Where, V_G is the geometrical optics velocity field and V_D is the diffracted velocity field. The geometrical optics velocity field is given by the expression:

$$V_G = \eta(\pi + \phi_0 - \phi)\frac{\exp(ikR)}{kR} + \eta(\pi - \phi_0 - \phi)\frac{\exp(ikR')}{kR'} \tag{C.10}$$

Where, $\eta(\psi)$ is the Heaviside step function, which is given by:

$$\eta(\psi) = \begin{cases} 1, \psi > 0 \\ 0, \omega < 0 \end{cases} \tag{C.11}$$

The diffracted velocity field is given by the expression:

$$V_D = -\sqrt{\frac{2}{\pi k R_1}} \exp\left(-\frac{1}{4} i\pi\right) \left\{ sgn(\pi + \phi_0 - \phi) \frac{\exp(ikR)}{\sqrt{k(R_1+R)}} F\left(\sqrt{k(R_1 - R)}\right) + \right.$$

$$\left. sgn(\pi - \phi_0 - \phi) \frac{\exp(ikR\prime)}{\sqrt{k(R_1+R\prime)}} F\left(\sqrt{k(R_1 - R')}\right) \right\} \tag{C.12}$$

where, *sgn(x)* is the sign function, which is given by:

$$sgn(x) = \begin{cases} 1, x > 0 \\ -1, x < 0 \end{cases} \tag{C.13}$$

and *F* is the Fresnel integral, which is given by:

$$F(\tau) = \int_{\tau}^{\infty} \exp(i\mu^2)\, d\mu \tag{C.14}$$

Ahtye and McCulley[39] cite the suggestion of Conticelli, Di Blasi, and O'Keefe[106], which suggest to apply the above solution of a single frequency source shielded by a half-plane to a quadrilateral shield, each edge of the quadrilateral is extended to plus and minus infinity. Equations C.6 – C.14 are used to calculate the shielded case for each edge. These solutions for each are combined to give the solution for the quadrilateral shield using the equation:

$$\Delta SPL = 20 \log_{10}\left(\frac{\left|\sum_{i=1}^{4} V_{s_i}\right|}{|V_u|}\right) \tag{C.15}$$

It is noted that Equation C.15 does take into account the phase relationship between the solutions for each of the four edges of the quadrilateral.

The original code that was developed by Ahyte and McCulley[39] was written in FORTRAN. This code has been translated into a MATLAB function and used for the

shielding simulation described in Chapter 4. The codes used in this simulation will be presented below.

C.2 Shielding Codes

C.2.1 Main Code Function

This is main MATLAB code that calculates the shielding effects from a rectangular baffle on the noise produced from a single frequency point source:

```
function [theta,dSPL] =
noiseShielding(freq,sourceLocation,micLocation,l,w,dz)
% NOISESHIELDING Calculate noise shielding due to rectangular barrier
%   [theta,dSPL] =
NOISESHIELDING(freq,sourceLocation,micLocation,l,w,dz)
%   calculates the shielding in delta sound pressure level (dSPL) at
each
%   angular microphone location (theta) for a given frequency (freq),
%   cartesian source location (sourceLocation), and microphone traverse
%   location (micLocation) and increment (dz) for a rectangular barrier
%   with a given length (l) and width (w).
%
% INPUTS
%   freq - frequency of noise source [Hz]
%   sourceLocation - [x,y,z] vector of cartesian coordinates of source
[m]
%   micLocation - z coordinate of microphone traverse [m]
%   l - length of barrier in y direction [m]
%   w - width of barrier in x direction [m]
%   dz - increments along the microphone traverse line [m]
%
% OUTPUTS
%   theta - angular position of locations along microphone traverse
[deg]
%   dSPL - change in sound pressure level (shielding) due to barrier
%
% REFERENCES
%   Ahtye & McCulley - Evaluation of Approximate Methods for the
Prediction
%   of Noise Shielding by Airframe Components
%
% See also VELOCITYPOTENTIAL APPROXFRESNEL

% --- VERSION HISTORY ---
% Original 16 Jan 2015
% Modified 18 Jan 2015

% --- AUTHOR ---
% Shane Lympany
% GTRI-ATAS
% slympany3@gatech.edu

%% Prework
```

```
% Functions
% ref: Ahtye & McCulley eq 4-6
fR = @(rho,rho0,dphi,dz) sqrt(rho.^2 + rho0.^2 -
2.*rho.*rho0.*cos(dphi) + dz.^2);
    % Ahtye & McCulley eq 4,5
fR1 = @(rho,rho0,dz) sqrt((rho+rho0).^2 + dz.^2);
    % Ahtye & McCulley eq 6

% Constants
c = 347.412;
    % [m/s] speed of sound
err = 1e-4;
    % allowable error in calculations

% Calculated
k = 2*pi*freq/c;
    % [1/m] wavenumber

% Inputs
xsource = sourceLocation(1);
    % [m] x coordinate of source
ysource = sourceLocation(2);
    % [m] y coordinate of source
zsource = sourceLocation(3);
    % [m] z coordinate of source
zmic = micLocation;
    % [m] z coordinate of mic traverse

% Iteration parameters
% ref: Ahyte & McCulley fig 12
zRightEdge = (w/2-xsource)./zsource .* (zsource+zmic);
    % [m] +x coordinate of right edge of shadow at mic traverse line
zLeftEdge = (w/2+xsource)./zsource .* (zsource+zmic);
    % [m] -x coordinate of left edge of shadow at mic traverse line
maxRightEdge = max(zRightEdge,(zsource+zmic)*tand(60));
    % [m] maximum x coordinate for iteration
minLeftEdge = min(zLeftEdge,(zsource+zmic)*tand(-60));
    % [m] minimum x coordinate for iteration
z = linspace(minLeftEdge,maxRightEdge,1200);
    % [m] vector of microphone location x coordinates
Vs = zeros(length(z),4);
    % [-] shielded velocity potential

%% Case 1 (Top +Y Edge)

% Polar coordinates
% ref: Ahyte & McCulley fig 9
phi0 = atan(zsource./(l/2-ysource));
    % [rad] angle to source
theta = atan2(zmic,l/2-ysource-dz);
    % [rad] temporary angle to mic
phi = 2*pi-theta;
    % [rad] angle to mic
rho0 = abs(zsource./sin(phi0));
```

```
    % [m] projected radius to source
rho = abs(zmic./sin(theta));
    % [m] projected radius to mic
psi = pi - (phi-phi0);
    % [rad] angle difference between mic and source

% Distances
R = fR(rho,rho0,(phi-phi0),z);
    % [m] distance from source to mic
Rprime = fR(rho,rho0,(phi+phi0),z);
    % [m] distance from image source to mic
R1 = fR1(rho,rho0,z);
    % [m] characteristic diffraction distance

% Difference between R and R1
dR = R1-R;
ndx = 2*rho.*rho0.*(1+cos(phi-phi0))./R1.^4 <= err;
temp = rho.*rho0.*(1+cos(phi-phi0))./R1;
dR(ndx) = temp(ndx);

% Difference between R' and R1
dRprime = R1-Rprime;
ndx = 2*rho.*rho0.*(1+cos(phi+phi0))./R1.^4 <= err;
temp = rho.*rho0.*(1+cos(phi+phi0))./R1;
dRprime(ndx) = temp(ndx);

% Velocity potential
Vs(:,1) = velocityPotential(R,Rprime,R1,dR,dRprime,k,psi);

%% Case 2 (Bottom -Y Edge)

% Polar coordinates
% ref: Ahyte & McCulley fig 9
phi0 = atan(zsource./(l/2+ysource));
theta = atan2(zmic,l/2+ysource+dz);
phi = 2*pi-theta;
rho0 = abs(zsource./sin(phi0));
rho = abs(zmic./sin(theta));
psi = pi - (phi-phi0);

% Distances
R = fR(rho,rho0,(phi-phi0),z);
Rprime = fR(rho,rho0,(phi+phi0),z);
R1 = fR1(rho,rho0,z);

% Difference between R and R1
dR = R1-R;
ndx = 2*rho.*rho0.*(1+cos(phi-phi0))./R1.^4 <= err;
temp = rho.*rho0.*(1+cos(phi-phi0))./R1;
dR(ndx) = temp(ndx);

% Difference between R' and R1
dRprime = R1-Rprime;
ndx = 2*rho.*rho0.*(1+cos(phi+phi0))./R1.^4 <= err;
temp = rho.*rho0.*(1+cos(phi+phi0))./R1;
```

```
dRprime(ndx) = temp(ndx);

% Velocity potential
Vs(:,2) = velocityPotential(R,Rprime,R1,dR,dRprime,k,psi);

%% Case 3 (Right +X Edge)

% Polar coordinates
% ref: Ahyte & McCulley fig 9
phi0 = atan(zsource./(w/2-xsource));
alpha = atan((z-w/2+xsource)./zmic);
phi = 3/2*pi - alpha;
rho = abs(zmic./cos(alpha));
rho0 = abs(zsource./sin(phi0));
psi = pi - (phi-phi0);

% Distances
R = fR(rho,rho0,(phi-phi0),dz);
Rprime = fR(rho,rho0,(phi+phi0),dz);
R1 = fR1(rho,rho0,dz);

% Difference between R and R1
dR = R1-R;
ndx = 2*rho.*rho0.*(1+cos(phi-phi0))./R1.^4 <= err;
temp = rho.*rho0.*(1+cos(phi-phi0))./R1;
dR(ndx) = temp(ndx);

% Difference between R' and R1
dRprime = R1-Rprime;
ndx = 2*rho.*rho0.*(1+cos(phi+phi0))./R1.^4 <= err;
temp = rho.*rho0.*(1+cos(phi+phi0))./R1;
dRprime(ndx) = temp(ndx);

% Velocity potential
Vs(:,3) = velocityPotential(R,Rprime,R1,dR,dRprime,k,psi);

%% Case 4 (Left -X Edge)

% Polar coordinates
% ref: Ahyte & McCulley fig 9
phi0 = atan(zsource./(w/2+xsource));
alpha = atan((z+w/2+xsource)./zmic);
phi = 3/2*pi + alpha;
rho = abs(zmic./cos(alpha));
rho0 = abs(zsource./sin(phi0));
psi = pi - (phi-phi0);

% Distances
R = fR(rho,rho0,(phi-phi0),dz);
Rprime = fR(rho,rho0,(phi+phi0),dz);
R1 = fR1(rho,rho0,dz);

% Difference between R and R1
dR = R1-R;
ndx = 2*rho.*rho0.*(1+cos(phi-phi0))./R1.^4 <= err;
```

```
temp = rho.*rho0.*(1+cos(phi-phi0))./R1;
dR(ndx) = temp(ndx);

% Difference between R' and R1
dRprime = R1-Rprime;
ndx = 2*rho.*rho0.*(1+cos(phi+phi0))./R1.^4 <= err;
temp = rho.*rho0.*(1+cos(phi+phi0))./R1;
dRprime(ndx) = temp(ndx);

% Velocity potential
Vs(:,4) = velocityPotential(R,Rprime,R1,dR,dRprime,k,psi);
%% Total Shielding

% Microphone angle locations
theta = atand(z./(zsource+zmic));
    % [deg] angle labeled theta in fig 9

% Shielding
dSPL = 20*log10(abs(sum(Vs,2)));
    % change in sound pressure level (shielding) due to barrier

end
```

C.2.2 Calculation of the Velocity Potential

This code calculates the velocity potential used in the shielding function

```
function Vs = velocityPotential(R,Rprime,R1,dR,dRprime,k,psi)
% VELOCITYPOTENTIAL Compute velocity potential at a location
%   Vs = VELOCITYPOTENTIAL(R,Rprime,R1,dR,dRprime,k,psi) computes the
%   velocity potential Vs (see Ahtye & McCulley eq 10-12).
%
% INPUTS
%   R - distance from source to field point
%   Rprime - distance from image source to field point
%   R1 - characteristic diffraction distance
%   dR - difference between R1 and R (computed in noiseShielding)
%   dRprime - difference between R1 and Rprime (computed in
noiseShielding)
%   k - wavenumber
%   psi - angle difference between mic and source (computed in
noiseShielding)
%
% OUTPUTS
%   Vs - velocity potential at specified location
%
% REFERENCES
%   Ahtye & McCulley - Evaluation of Approximate Methods for the
Prediction
%   of Noise Shielding by Airframe Components
%
% See also NOISESHIELDING APPROXFRESNEL
```

```
% --- VERSION HISTORY ---
% Original 16 Jan 2015
% Modified 18 Jan 2015

% --- AUTHOR ---
% Shane Lympany
% GTRI-ATAS
% slympany3@gatech.edu


% Functions
% fresnel = @(tau) (1/2+1j/2)*sqrt(pi/2)*(1-(1-
1j).*(fresnelc(tau.*sqrt(2/pi)) + 1j*fresnels(tau.*sqrt(2/pi))));
    % fresnel integral
    % note: commented out to improve speed

% Velocity potential terms
term1 = R*sqrt(2)./(sqrt(1j*pi*R1));
w1 = sqrt(k*dR);
term2 = approxFresnel(w1)./sqrt(R1+R);
w2 = sqrt(k*dRprime);
term3 = exp(1j*k*(Rprime-R)).*approxFresnel(w2)./sqrt(R1+Rprime);

% Velocity potential
Vs = zeros(length(R),1);
temp_neg = term1.*(term2+term3);
temp_pos = 1 - term1.*(term2-term3);

% If psi varies with mic position
if isequal(size(R),size(psi))
    Vs(psi < 0) = temp_neg(psi < 0);
    Vs(psi >= 0) = temp_pos(psi >= 0);

% If psi does not vary with mic position
elseif length(psi) == 1
    if psi < 0
        Vs = temp_neg;
    else
        Vs = temp_pos;
    end
end

end
```

C.2.3 Calculation of the Fresnel Integral

This code is used to calculate the Fresnel integral used in the shielding function. MATLAB has functions internally that can calculate this, but they come with large computation times, so for computational efficiency this approximation is used:

```
function F = approxFresnel(tau)
% APPROXFRESNEL Approximate fresnel integral with Taylor series
%   F = APPROXFRESNEL(tau) computes the result of the fresnel integral,
F,
%   for a given input, tau.
%
% INPUTS
%   tau - vector of inputs
%
% OUTPUTS
%   F - vector of results of fresnel integral of tau
%
% REFERENCES
%   Ahtye & McCulley - Evaluation of Approximate Methods for the
Prediction
%   of Noise Shielding by Airframe Components
%
% See also NOISESHIELDING VELOCITYPOTENTIAL

% --- VERSION HISTORY ---
% Original 16 Jan 2015
% Modified 18 Jan 2015

% --- AUTHOR ---
% Shane Lympany
% GTRI-ATAS
% slympany3@gatech.edu


% Constants and preallocation
err = 1e-6;
F = zeros(size(tau));

% Iterate through input vector
for i = 1:length(tau)
    w = tau(i)/sqrt(pi/2);

    % C and S approximately zero
    if abs(w) < 1e-12
        C = 0;
        S = 0;

    % Compute C and S
    else
```

```
    x = w.^2/.636619772368;
    x2 = -x.^2;

    % Asymptotic series computation for C and S
    if x >= 13.1
        x2 = 4*x2;
        term = 3/x2;
        s1 = 1+term;
        n = 8;
        while abs(term) <= err/2
            n = n+4;
            term = term*(n-7)*(n-5)/x2;
            s1 = s1+term;
        end
        term = 0.5/x; % 211
        s2 = term;
        n = 4;
        while abs(term) <= err/2
            n = n+4;
            term = term*(n-5)*(n-3)/x2;
            s2 = s2+term;
        end
        half = -0.5;
        if w >= 0
            half = 0.5;
        end
        x2 = pi*w;
        C = half+(sin(x)*s1-cos(x)*s2)/x2;
        S = half-(cos(x)*s1+sin(x)*s2)/x2;

    % Series computation for C and S
    else
        frs = x/3;
        n = 5;
        term = x*x2/6;
        frsi = frs+term/7;
        while abs(frs-frsi) > err*abs(frs)
            frs = frsi;
            term = term*x2/(n*n-n);
            frsi = frs+term/(2*n+1);
            n = n+2;
        end
        S = frsi*w;
        frc = 1;
        n = 4;
        term = x2/2;
        frci = 1+term/5;
        while abs(frc-frci) > err*abs(frc)
            frc = frci;
            term = term*x2/(n*n-n);
            frci = frc+term/(2*n+1);
            n = n+2;
        end
        C = frci*w;
    end
end
```

```
    % Compute fresnel integral
    Freal = sqrt(pi/2)*(.5-C); % real component
    Fimag = sqrt(pi/2)*(.5-S); % imaginary component
    F(i) = Freal + 1j*Fimag; % complex fresnel integral result
end

end
```

REFERENCES

[1]Lighthill, M. J. "On Sound Generated Aerodynamically. I. General Theory," *Proceedings of the Royal Society of London. Series A, Mathematical and Physical Sciences*, No. 1107, 1952, p. 564.

[2]Lighthill, M. J. "On Sound Generated Aerodynamically. II. Turbulence as a Source of Sound," *Proceedings of the Royal Society of London. Series A, Mathematical and Physical Sciences*, No. 1148, 1954, p. 1.

[3]Lighthill, M. J. "The Bakerian Lecture, 1961. Sound Generated Aerodynamically," *Proceedings of the Royal Society of London. Series A, Mathematical and Physical Sciences*, No. 1329, 1962, p. 147.

[4]Viswanathan, K. "Aeroacoustics of hot jets," *Journal of Fluid Mechanics* Vol. 516, 2004, pp. 39-82.

[5]Viswanathan, K., and Czech, M. "Role of jet temperature in correlating jet noise," *AIAA journal* Vol. 47, No. 5, 2009, pp. 1090-1106.

[6]Tanna, H., Dean, P. D., and Burrin, R. H. "The Generation and Radiation of Supersonic Jet Noise. Volume 3. Turbulent Mixing Noise Data." DTIC Document, 1976.

[7]Lush, P. A. "Measurements of subsonic jet noise and comparison with theory," *Journal of Fluid Mechanics*, 1971, pp. 477-500.

[8]Ahuja, K. K. "Correlation and prediction of jet noise," *Journal of Sound and Vibration* Vol. 29, No. 2, 1973, pp. 155-168.

[9]Viswanathan, K. "Best practices for accurate measurement of pure jet noise," *International Journal of Aeroacoustics* Vol. 9, No. 1, 2010, pp. 145-206.

[10]Ahuja, K. "Designing clean jet-noise facilities and making accurate jet-noise measurements," *International Journal of Aeroacoustics* Vol. 2, No. 3, 2003, pp. 371-412.

[11]Ahuja, K., Milway, S., and Churney, A. "Potential Errors Introduced in the use of Static Engine Noise Data not Acquired in Geometric Farfield," *12th AIAA/CEAS Aeroacoustics Conference (27th AIAA Aeroacoustics Conference)*. American Institute of Aeronautics and Astronautics, 2006.

[12]Harper-Bourne, M. "Jet noise measurements: past and present," *International Journal of Aeroacoustics* Vol. 9, No. 4/5, 2010, pp. 559-588.

[13]Powell, A. "The influence of the exit velocity profile on the noise of a jet," *Aeronautical Quarterly* Vol. 4, No. 4, 1954, pp. 341-360.

[14]Ahuja, K. K. "An experimental study of the effects of upstream obstructions upon subsonic jet noise," *Journal of Sound and Vibration* Vol. 37, No. 2, 1974, pp. 205-234.

[15]Viswanathan, K., and Clark, L. "Effect of nozzle internal contour on jet aeroacoustics," *International Journal of Aeroacoustics* Vol. 3, No. 2, 2004, pp. 103-135.

[16]Zaman, K. B. M. Q. "Effect of nozzle exit conditions on subsonic jet noise." Vol. 17th AIAA/CEAS Aeroacoustics Conference, 2011.

[17]Long, D. F., and Arndt, R. E. A. "Jet noise at low Reynolds number," *AIAA Journal* Vol. 22, No. 2, 1984, pp. 187-193.

[18]Kastner, J., Samimy, M., Hileman, J., and Freund, J. B. "Comparison of noise mechanisms in high and low reynolds number high-speed jets," *AIAA Journal* Vol. 44, No. 10, 2006, pp. 2251-2258.

[19]Bhat, T. "Reynolds number and temperature effects on jet noise," *AIAA Paper* Vol. 3630, 2007, p. 2007.

[20]Proudman, I. "The Generation of Noise by Isotropic Turbulence," *Proceedings of the Royal Society of London. Series A, Mathematical and Physical Sciences*, No. 1116, 1952, p. 119.

[21]Ribner, H. S. "The Generation of Sound by Turbulent Jets," *Advances in Applied Mechanics* Vol. 8, 1964, pp. 103-182.

[22]Ffowcs-Williams, J. E. "The Noise from Turbulence Convected at High Speed," *Philosophical Transactions of the Royal Society of London. Series A, Mathematical and Physical Sciences*, No. 1061, 1963, p. 469.

[23]Lilley, G. "On the noise from jets," *Agard cp-131*, 1974, pp. 13.1-13.12.

[24]Doak, P. E. "Acoustic Radiation from a Turbulent Fluid Containing Foreign Bodies," *Proceedings of the Royal Society of London. Series A, Mathematical and Physical Sciences*, No. 1276, 1960, p. 129.

[25]Goldstein, M., and Rosenbaum, B. "Effect of anisotropic turbulence on aerodynamic noise," *Journal of the Acoustical Society of America* Vol. 57, 1973, pp. 630-645.

[26]Crow, S. C., and Champagne, F. H. "Orderly structure in jet turbulence," *Journal of Fluid Mechanics*, 1971, pp. 547-591.

[27]Tam, C. K., Golebiowski, M., and Seiner, J. M. *On the two components of turbulent mixing noise from supersonic jets*: American Institute of Aeronautics and Astronautics, 1996.

[28]Tam, C. K. W., and Auriault, L. "Jet mixing noise from fine-scale turbulence," *AIAA Journal* Vol. 37, No. 2, 1999, pp. 145-153.

[29]Tam, C. K. W., and Ping, C. "Turbulent mixing noise from supersonic jets," *AIAA Journal* Vol. 32, No. 9, 1994, pp. 1774-1780.

[30]Tam, C. K., Viswanathan, K., Ahuja, K., and Panda, J. "The sources of jet noise: experimental evidence," *Journal of Fluid Mechanics* Vol. 615, 2008, pp. 253-292.

[31]Ahuja, K. K. "An Experimental Study of Subsonic Jet Noise with Particular Reference to the Effects of Upstream Disturbances," *M. Phil.* , 1972.

[32]Barré, S., Bogey, C., and Bailly, C. "Computation of the noise radiated by jets with laminar/turbulent nozzle-exit conditions," *AIAA Paper* Vol. 2443, 2006, p. 2006.

[33]Bogey, C., and Bailly, C. "Influence of nozzle-exit boundary-layer conditions on the flow and acoustic fields of initially laminar jets," *Journal of Fluid Mechanics* Vol. 663, 2010, pp. 507-538.

[34]Bogey, C., and Marsden, O. "Identification of the effects of the nozzle-exit boundary-layer thickness and its corresponding Reynolds number in initially highly disturbed subsonic jets," *Physics of Fluids (1994-present)* Vol. 25, No. 5, 2013, p. 055106.

[35]Bogey, C., Marsden, O., and Bailly, C. "A computational study of the effects of nozzle-exit turbulence level on the flow and acoustic fields of a subsonic jet," *17th AIAA/CEAS Aeroacoustics Conference*, 2011.

[36]Bogey, C., and Marsden, O. "Numerical modelling of jets exiting from the ASME and conical nozzles," *53rd AIAA Aerospace Sciences Meeting*. American Institute of Aeronautics and Astronautics, 2015.

[37]Bogey, C., and Marsden, O. "Influence of nozzle-exit boundary-layer profile on high-subsonic jets," *20th AIAA/CEAS Aeroacoustics Conference*. American Institute of Aeronautics and Astronautics, 2014.

[38]Viswanathan, K. "Instrumentation considerations for accurate jet noise measurements," *AIAA journal* Vol. 44, No. 6, 2006, pp. 1137-1149.

[39]Ahtye, W. F., and McCulley, G. "Evaluation of approximate methods for the prediction of noise shielding by airframe components," *NASA Technical Paper 1004* 1980.

[40]Ahuja, K., and Bushell, K. "An experimental study of subsonic jet noise and comparison with theory," *Journal of Sound and Vibration* Vol. 30, No. 3, 1973, pp. 317-IN1.

[41]Michel, U., and Ahuja, K. K. "On the Scaling of Jet Noise with Helmholtz Number Close to the Jet Axis," *20th AIAA/CEAS Aeroacoustics Conference , Atlanta, GA*, 2014.

[42]Gaeta, R. J., and Ahuja, K. K. "Subtle differences in jet-noise scaling with narrowband spectra compared to 1/3-octave band," *AIAA paper* Vol. 3124, 2003.

[43]Bushell, K. W. "Measurement and Prediction of Jet Noise in Flight," *American Institute of Aeronautics and Astronautics Paper 75-461*, 1975.

[44]Crighton, D. "Basic principles of aerodynamic noise generation," *Progress in Aerospace Sciences* Vol. 16, No. 1, 1975, pp. 31-96.

[45]Bushell, K. "A survey of low velocity and coaxial jet noise with application to prediction," *Journal of Sound and Vibration* Vol. 17, No. 2, 1971, pp. 271-282.

[46]Crighton, D. G. "A Theory of Excess Jet Noise," *Journal of the Acoustical Society of America* Vol. 52, No. 1A, 1972, p. 164.

[47]Crighton, D. G. "The excess noise field of subsonic jets," *Journal of Fluid Mechanics* Vol. 56, No. 04, 1972, pp. 683-694.

[48]Ahuja, K. K., Nance, D. K., Carrigan, J., and Karon, A. "On coherence of jet noise." American Institute of Aeronautics and Astronautics Inc., 2014.

[49]Mendoza, J. M., Nance, D. K., and Ahuja, K. "Source separation from multiple microphone measurements in the far field of a full scale aero engine," *14th AIAA/CEAS Aeroacoustics Conference (29th AIAA Aeroacoustics Conference)*. 2008, pp. 5-7.

[50]Nance, D., and Ahuja, K. "Experimentally Separating Jet Noise Contribution of Large-Scale Turbulence from that of Small-Scale Turbulence," *15th AIAA/CEAS Aeroacoustics Conference (30th AIAA Aeroacoustics Conference), May*. 2009.

[51]Nance, D., and Ahuja, K. "Limitations of the Three-Microphone Signal Enhancement," 2007.

[52]Nance, D. K. "Separating contributions of small-scale turbulence, large-scale turbulence, and core noise from far-field exhaust noise measurements," 2007.

[53]Breen, N. P., and Ahuja, K. "Measuring Jet Noise Source Locations with Acoustic Beamforming."

[54]Chu, W., Laufer, J., and Kao, K. "Noise source distribution in subsonic jets," *Inter-noise 72*, 1972, pp. 472-476.

[55]Laufer, J., Kaplan, R. E., and Chu, W. T. "On noise produced by subsonic jets." 1974, 1974.

[56]Fisher, M., Harper-Bourne, M., and Glegg, S. "Jet engine noise source location: the polar correlation technique," *Journal of Sound and Vibration* Vol. 51, No. 1, 1977, pp. 23-54.

[57]Glegg, S. A. L. "Jet Noise Source Location: A Review," 2000.

[58]Ahuja, K., Massey, K., and D'Agostino, M. "A simple technique of locating noise sources of a jet under simulated forward motion," *AIAA paper*, No. 98-2359, 1998.

[59]Burrin, R. H., Dean, P. D., and Tanna, H. K. "A New Anechoic Facility for Supersonic Hot Jet Noise Research at Lockheed-Georgia," *Journal of the Acoustical Society of America* Vol. 55, No. 2, 1974, p. 400.

[60]Burrin, R., and Tanna, H. "The Lockheed-Georgia coannular jet research facility," *The Journal of the Acoustical Society of America* Vol. 65, No. S1, 2005, pp. S44-S44.

[61]ANSI, S. "26 (1995)," *American National Standard Method for Calculation of the Absorption of Sound by the Atmosphere"(Acoustical Society of America, New York, 1995)*, 1995.

[62]Phillips, O. M. "The intnesity of Aeolian tones," *Journal of Fluid Mechanics* Vol. 1, No. 06, 1956, pp. 607-624.

[63]Martin, J., and Ahuja, K. "Effect of cylinder length on vortex shedding sound in the near field," *Recent Developments in Air-and Structure-Borne Sound and Vibration*. Vol. 1, 1992, pp. 1637-1646.

[64]Ahuja, K., and Blakney, D. "Tone excited jets, part IV: acoustic measurements," *Journal of Sound and Vibration* Vol. 102, No. 1, 1985, pp. 93-117.

[65]Karon, A. Z., and Ahuja, K. "Effect of nozzle-exit boundary layer on jet noise," *AIAA Paper* Vol. 615, No. 2013, 2013, p. 13.

[66]Anderson John, D. *Fundamentals of aerodynamics*: McGraw Hill International, 2005.

[67]Stromberg, J., McLaughlin, D., and Troutt, T. "Flow field and acoustic properties of a Mach number 0· 9 jet at a low Reynolds number," *Journal of Sound and Vibration* Vol. 72, No. 2, 1980, pp. 159-176.

[68]Schlichting, H. *Boundary-layer theory*: McGraw-Hill, 1987.

[69]Zaman, K. "Effect of initial condition on subsonic jet noise," *AIAA journal* Vol. 23, No. 9, 1985, pp. 1370-1373.

[70]Hussain, A. "Coherent structures and studies of perturbed and unperturbed jets," *The role of coherent structures in modelling turbulence and mixing*. Springer, 1981, pp. 252-291.

[71]Hill Jr, W. G., Jenkins, R. C., and Gilbert, B. L. "Effects of the initial boundary-layer state on turbulent jet mixing," *AIAA journal* Vol. 14, No. 11, 1976, pp. 1513-1514.

[72]Browand, F., and Latigo, B. "Growth of the two-dimensional mixing layer from a turbulent and nonturbulent boundary layer," *Physics of Fluids (1958-1988)* Vol. 22, No. 6, 1979, pp. 1011-1019.

[73]Hussain, A., and Zedan, M. "Effects of the initial condition on the axisymmetric free shear layer: Effects of the initial momentum thickness," *Physics of Fluids (1958-1988)* Vol. 21, No. 7, 1978, pp. 1100-1112.

[74]Husain, Z., and Hussain, A. "Axisymmetric mixing layer: influence of the initial and boundary conditions," *AIAA Journal* Vol. 17, No. 1, 1979, pp. 48-55.

[75]Raman, G., Rice, E., and Reshotko, E. "Mode spectra of natural disturbances in a circular jet and the effect of acoustic forcing," *Experiments in fluids* Vol. 17, No. 6, 1994, pp. 415-426.

[76]Raman, G., Zaman, K. B., and Rice, E. J. "Initial turbulence effect on jet evolution with and without tonal excitation," *Physics of Fluids A: Fluid Dynamics (1989-1993)* Vol. 1, No. 7, 1989, pp. 1240-1248.

[77]Russ, S., and Strykowski, P. "Turbulent structure and entrainment in heated jets: The effect of initial conditions," *Physics of Fluids A: Fluid Dynamics (1989-1993)* Vol. 5, No. 12, 1993, pp. 3216-3225.

[78]Xu, G., and Antonia, R. A. "Effects of different initial conditions on a turbulent free jet," *Exp. Fluids* Vol. 33, 2002, pp. 677 - 683.

[79]Bridges, J., and Hussain, A. "Roles of initial condition and vortex pairing in jet noise," *Journal of sound and vibration* Vol. 117, No. 2, 1987, pp. 289-311.

[80]Bogey, C., and Bailly, C. "Investigation of subsonic jet noise using LES: Mach and Reynolds number effects," *AIAA paper* Vol. 3023, 2004, p. 2004.

[81]Schubauer, G. B., and Klebanoff, P. "Contributions on the mechanics of boundary-layer transition," 1956.

[82]Bies, D. A., and Hansen, C. H. *Engineering noise control: theory and practice*: CRC press, 2009.

[83]Martens, S. "Jet noise reduction technology development at GE aircraft engines," *ICAS Paper* Vol. 842, 2002.

[84]Philip, J. M., Dennis, K. M., Russell, W. P., and Matthew, J. K. "Prediction, Experiments and Optimization of High-Speed Jet Noise Reduction Using Fluidic Inserts," *50th AIAA/ASME/SAE/ASEE Joint Propulsion Conference*. American Institute of Aeronautics and Astronautics, 2014.

[85]Viswanathan, K. "Jet aeroacoustic testing: issues and implications," *AIAA journal* Vol. 41, No. 9, 2003, pp. 1674-1689.

[86]Henderson, B., and Bridges, J. "An MDOE investigation of chevrons for supersonic jet noise reduction," *AIAA paper* Vol. 3926, 2010, p. 2010.

[87]Czech, M. J., Thomas, R. H., and Elkoby, R. "Propulsion airframe aeroacoustic integration effects for a hybrid wing body aircraft configuration," *International Journal of Aeroacoustics* Vol. 11, No. 3-4, 2012, pp. 335-367.

[88]Thomas, R., Burley, C., and Olson, E. "Hybrid wing body aircraft system noise assessment with propulsion airframe aeroacoustic experiments," *International Journal of Aeroacoustics* Vol. 11, No. 3-4, 2012, pp. 369-410.

[89]Thomas, R. H., Czech, M. J., and Doty, M. J. "High Bypass Ratio Jet Noise Reduction and Installation Effects Including Shielding Effectiveness," *AIAA Paper* Vol. 541, 2013.

[90]Envia, E. "Emerging community noise reduction approaches," *3rd AIAA Atmospheric Space Environments Conference, 27 - 30 June 2011, Honolulu, Hawaii*, 2011.

[91]Primakoff, H., Klein, M. J., Keller, J. B., and Carstensen, E. "Diffraction of sound around a circular disk," *The Journal of the Acoustical Society of America* Vol. 19, No. 1, 1947, pp. 132-142.

[92]Leitner, A. "Diffraction of sound by a circular disk," *The Journal of the Acoustical Society of America* Vol. 21, No. 4, 1949, pp. 331-334.

[93]Gabrielsen, R. E., and Davis, J. E. "Accuracy of the Kirchoff formula in determining acoustic shielding with the use of a flat plate," *NASA Technical Memorandum - 73261*, 1977.

[94]Bowman, J. J., Senior, T. B., and Uslenghi, P. L. "Electromagnetic and acoustic scattering by simple shapes." DTIC Document, 1970.

[95]Turkdogru, N. *Validity of the point source assumption of a rotor for farfield acoustic measurements with and without shielding*: Georgia Institute of Technology, 2011.

[96]Nark, D. M., Burley, C. L., Tinetti, A., and Rawls Jr, J. W. "Initial integration of noise prediction tools for acoustic scattering effects," *AIAA paper* Vol. 2996, 2008.

[97]Papamoschou, D. "Prediction of jet noise shielding," *AIAA paper* Vol. 653, 2010.

[98]Norum, T. "Screech suppression in supersonic jets," *AIAA Journal* Vol. 21, No. 2, 1983, pp. 235-240.

[99]"Assessing Experimental Uncertainty — Supplement to AIAA S-071A-1999."

[100]"Assessment of Experimental Uncertainty With Application to Wind Tunnel Testing."

[101]Coleman, H. W., and Steele, W. G. "Experimentation and Uncertainty Analysis for Engineers." 2nd ed., John Wiley & Sons, INC., USA, New York.

[102]Nakos, J. T. *Uncertainty analysis of thermocouple measurements used in normal and abnormal thermal environment experiments at Sandia's Radiant Heat Facility and Lurance Canyon Burn Site*: United States. Department of Energy, 2004.

[103]Chung, J. Y. "Rejection of flow noise using a coherence function method," *Journal of the Acoustical Society of America* Vol. 62, No. 2, 1977, p. 388.

[104]"Bruel and Kjaer Microphone Handbook Volume 1: Theory," 1996.

[105]Ahuja, K., Tester, B., and Tanna, H. "Calculation of far field jet noise spectra from near field measurements with true source location," *Journal of sound and vibration* Vol. 116, No. 3, 1987, pp. 415-426.

[106]Conticelli, V., Di Blasi, A., and O'Keefe, J. "Noise shielding effects for engine-over-wing installations," *AIAA Paper* Vol. 75474, 1975, pp. 24-26.

VITA

Aharon Zamir Karon was born in Atlanta, Georgia on February 9, 1987. He attended grade school at the Torah Day School of Atlanta and in 2005 graduated high school from Yeshiva Atlanta. In 2010, he graduated from Georgia Tech with a Bachelor's degree in Aerospace Engineering. In 2012, he graduated from Georgia Tech with a Master's degree in Aerospace Engineering.